Cathode Spot Injection of Dielectric Particles with Applications for Communications Blackout Plasma Depletion

by

Eric D. Gillman

A dissertation submitted in partial fulfillment
of the requirements for the degree of
Doctor of Philosophy
(Nuclear Engineering and Radiological Sciences)
in The University of Michigan
2012

Doctoral Committee:

Professor John Foster, Chair
Professor Alec Gallimore
Professor Ronald Gilgenbach
Isaiah Blankson, NASA

“Science is about what is, and engineering is about what can be.” - Neil Armstrong

“Do all that you have in mind, for God is with you.”–1 Chronicles 17:2

To my grandfather, Donald A. Gillman, who embodied the characteristics of a true Michigan Man more than any other person I have ever known.

ACKNOWLEDGEMENTS

First, and foremost, I would like to thank my advisor, Prof. Foster. I cannot thank Prof. Foster enough for providing me with the opportunity to earn a Ph.D. in his lab. I feel incredibly lucky and privileged to have been a part of building the lab and to see how far it has come since the first day that I walked in. Prof. Foster has been more than any student could ask for in an advisor, mentor, and teacher. He has set an example of what it is to be a great scientist, great teacher, and more importantly, a great human being. He will always be the person that I look up to more than anyone else in my professional life.

I would also like to thank Dr. Isaiah Blankson for his help and guidance during my summer internships at the NASA Glenn Research Center. Without his help and support, this work would not have been possible. This work has truly benefited from his wisdom, expertise, and insight. Prof. Ron Gilgenbach and Prof. Alec Gallimore also deserve special thanks for serving on my committee and for their suggestions and thoughts throughout the course of my graduate studies.

I would like to thank my fellow labmates, Dr. Brandon Weatherford, Brad Sommers, Aimee Hubble, Ben Yee, Kapil Sawlani, Sarah Gucker, and Paul Cummings, who all deserve special recognition. Without all of you, this experience would have been much more stressful, much more difficult, and not nearly as fun as it has been. Thank you for all of your help in the lab and for making sure I didn't take things too seriously.

I would like to thank all of the great teachers that I've had the last 22 years of

my life. Without being intellectually challenged by all of you, I never could have overcome all of the challenges along the way to completing this degree.

Mom, Dad, Cherie, and Kevin, I love you all. Your love and encouragement has been crucial to my success and you deserve the honor and recognition of receiving this degree as much as I do. My Mom and Dad especially deserve credit for all that they have sacrificed. I know how much time and money they have spent to ensure that I received the best education possible. They constantly challenged me to achieve more than I thought I could, but that which they *knew* I was capable of achieving. They have always challenged me not only to work hard, but to be a better person. I am the person that I am today because of you, and for that and more, I will forever be grateful.

Most importantly, I would like to thank my wife, Catherine, for all of her love, support, and encouragement throughout my time as a graduate student. Thank you for dealing with my long work hours, and for dealing with me when I was angry, frustrated, and stressed out. I couldn't have done this without you, and you deserve this degree as much as I do. I love you so much, and I only hope that I can provide you with the same kind of support and encouragement as you strive to achieve your life-long dreams.

TABLE OF CONTENTS

LIST OF FIGURES

Figure

LIST OF TABLES

Table

ABSTRACT

Cathode Spot Injection of Dielectric Particles with Applications for Communications Blackout Plasma Depletion

by

Eric D. Gillman

Chair: John Foster

Vehicles traveling at hypersonic velocities in the atmosphere are readily enveloped by a dense plasma layer that blocks, reflects, and significantly attenuates radio signals typically used for communications. This problem is known as 'radio blackout' and persists for spacecraft reentering the atmosphere, hypersonic test vehicles, and hypersonic missile/defense systems.

The goal of this study is to create a dusty plasma by injecting dielectric particles that will collect many electrons, thereby lowering the electron density. If the electron density of the plasma layer can be significantly lowered, then the cutoff frequency will be lowered, allowing for the transmission of radio signals through the plasma layer.

In this work, the dusty plasma was created by injecting particles into the plasma using cathode spots. Cathode spots form a dense, high flow velocity plume of plasma that emanates from the electrode surface, ejecting dielectric particles into an overhead plasma used to simulate the plasma layer. In the process of clearing powder from the electrode surface, apparent cathode spot motion in the presence of a static magnetic field follows the 'retrograde' or -$\mathbf{J}\times\mathbf{B}$ motion. Particle tracking studies found that

particles were ejected with a greater component of velocity in the horizontal plane in the direction of cathode spot motion, likely due to multiple boosts as the cathode spots and particles traveled together in the same direction on the electrode surface. However, the primary component of velocity was in the vertical direction. The particle ejection velocity distribution had an average and median vertical velocity of 0.66 and 0.5 m/s, respectively, with a maximum ejection velocity of 1.5 m/s. The total particulate mass necessary to achieve depletion of up to 90% was determined by directly dropping microparticles into the discharge. Electron depletion followed an approximately linear relationship, increasing with powder mass flux. Cathode spot injection of particles also resulted in electron depletion greater than 95% as measured by electron saturation current. Depletion may be increased by using particles of optimum size and increasing particle mass flux. It has been shown that this method is capable of depleting the reentry plasma layer.

CHAPTER I

Introduction

This dissertation presents a study for the use of a novel system to inject solid particulate into a plasma, with the purpose of depleting the plasma electron population. This research investigates cathode spots as the method for the injection and dispersion of ceramic particulate into the plasma. While the application of this research is intended for mitigating hypersonic vehicle radio communications blackout, the physical processes associated with cathode spot formation, cathode spot motion, and the velocity distribution of injected particles is also discussed.

1.1 Statement of Problem

Spacecraft reentering the atmosphere and vehicles traveling within the Earth's atmosphere at hypersonic velocities (Mach 8 or greater) become quickly enveloped by a layer of ionized air known as the 'plasma layer'.[101, 16, 57, 91] This plasma layer is formed when air is compressed and heated by a hypersonic shock in front of the hypersonic vehicle. This heating leads to ionization of the surrounding air. The plasma layer, with densities as high as 10^{14} cm^{-3}, may cover the entire surface of the vehicle, particularly during spacecraft reentry.[16, 57, 11, 21, 34, 42, 43, 54, 55, 56, 80, 64, 68, 67, 75, 73, 74, 17, 105, 47, 108, 65, 113, 32, 22, 49, 58, 71, 30, 10, 102, 77] This plasma layer can significantly attenuate and block the sending and receiving of

Figure 1.1: Capsules reentering the atmosphere in the 1960's, such as the Gemini capsule depicted, endured radio blackout.

radio frequency and microwave communication transmissions.[11, 21, 34, 42, 43, 54, 55, 56, 80, 64, 68, 67, 75, 73, 74, 17, 105] The period of time during which reentering spacecraft or hypersonic vehicles are not able to communicate with ground control due to the formation of this plasma layer is known as radio blackout.

1.1.1 Radio Communications Blackout

Spacecraft atmospheric reentry is one of the most critical periods of flight. Because this blackout period can last several minutes, it constitutes a safety issue as telemetry, navigation, command, and control transmissions are terminated.[75, 108] This radio blackout period has been a problem ever since the beginning of manned space missions, during which small, capsule type reentry vehicles were used. For the capsule type spacecraft architectures (Mercury, Gemini, and Apollo), a relatively thick plasma layer enveloped and covered the entire spacecraft, blocking communication signals sent in any direction.[67, 73, 74] The reentry radio blackout period, while undesirable, became a tolerable risk for NASA and the astronauts during the early days of manned spaceflight. The blackout problem to date has not been solved. During the shuttle program, the communication blackout problem was addressed by taking advantage of spatial non-uniformities in the plasma distribution around the

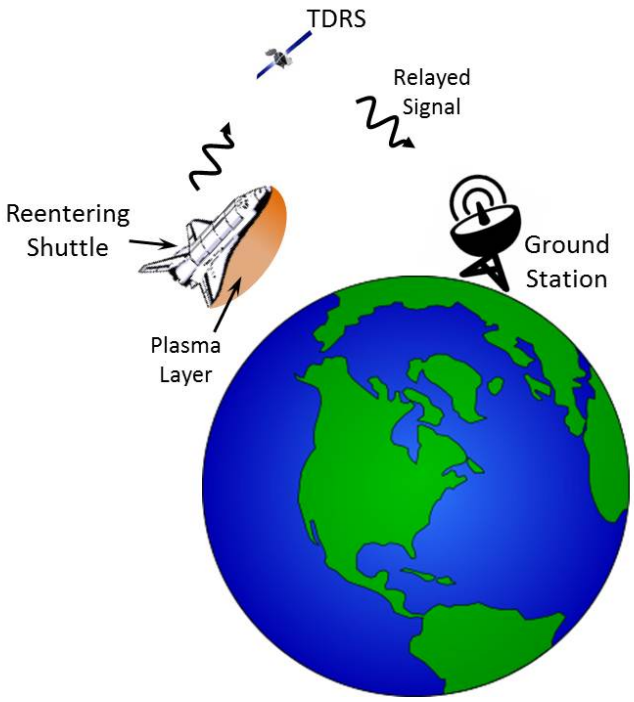

Figure 1.2: The space shuttle utilized TDRS to relay signals, allowing for two-way communication with ground control during reentry.

reentering orbiter. Because the plasma layer formed only on the large underbody of the Space Shuttle, it was possible to transmit radio communications signals upward to the geosynchronous orbiting Tracking Data Relay Satellites (TDRS) during reentry.[67, 73, 74] These satellites relay the signal to ground control centers on the Earth's surface, and vice versa, allowing for two-way communication between NASA ground control and astronauts during atmospheric reentry.[67, 73, 74] However, with NASA's return to the capsule type of spacecraft architecture for the Orion space capsule, the radio communications blackout will again become a problem, and thus is an area of major concern for NASA.[32, 57]

The radio communications blackout is a problem that affects all hypersonic vehicles, not just reentering spacecraft. For example, this issue affects the reception and transmission of telemetry from hypersonic missiles and kinetic kill vehicles. At this time, radio blackout significantly hinders the development of such missile and missile

Electron Density (cm^{-3})	10^9–10^{14}
Collision Frequency (rad/s)	10^8–10^{13}
Electron Temperature (eV)	< 2.2
Pressure (Torr)	0.75–75
Velocity (Mach #)	13–32
Altitude (km)	30–90

Table 1.1: Summary of blackout plasma layer parameters.

defense systems.[32] Communication with unmanned vehicles is a critical task, providing the capability to attain greater targeting accuracy with the use of GPS, and enabling the use of electronic countermeasures such as radar jamming and mission abort functions.[105, 52, 53, 70, 72, 84, 90, 104, 83] For these reasons, NASA and the Air Force have identified radio communications blackout as a problem of great importance for national security.[32, 57]

1.1.2 Plasma Layer Parameters

Mitigation of communications blackout requires, as a starting point, a detailed understanding of the plasma layer, particularly its density and collisionality. The plasma layer itself acts to reflect radiowaves in the frequency bands common for hypersonic vehicle communications. This phenomenon is a consequence of electrons within the plasma responding to the electric field of communication signals in such a way so as to re-radiate incident RF energy in the opposite direction, thereby leading to reflection. This occurs in collisionless plasmas when the frequency of the incident wave is less than the plasma electron frequency:[17]

$$\omega_p = \sqrt{\frac{en_e^2}{\epsilon_0 m_e}} \tag{1.1}$$

where e is the elementary charge, n_e is the electron density, ϵ_0 is the electric constant, and m_e is the electron mass. The plasma electron frequency is dependent solely on physical constants and the electron density.

The shock produced plasma layer pertinent to hypersonic flight has been researched since the 1950's.[4] A great deal of research, especially in the early days of manned space flight was devoted to determining the parameters of the plasma layer, shown in table 1.1. As mentioned above, the electrons, in particular, the electron density has been indicated to be one of the most important parameters of the plasma layer.[55, 98, 46, 30, 87] Most of the plasma layer parameters, including density, depend heavily on the vehicle velocity, altitude, attitude, and trajectory. Vehicle velocities tend to be highest for reentry vehicles, and can range from Mach 13 for reentry from near Earth orbits (304 km to 528 km)[103] and velocities as high as Mach 32 for reentry during lunar missions.[16, 42, 80, 72, 90, 4, 8, 24, 23, 49, 58, 30, 48, 77] The literature states that the plasma layer density varies from 10^9 to 10^{14} cm^{-3} over the course of reentry, with the plasma layer collision frequency being approximately an order of magnitude smaller than the electron density at all altitudes.[16, 57, 11, 21, 34, 42, 43, 54, 55, 56, 80, 64, 68, 67, 75, 73, 74, 17, 105, 47, 108, 65, 113, 32, 22, 49, 58, 71, 30, 10, 102, 77] The plasma layer electron temperature is less than 2.2 eV for most cases.[42, 80] The reentry plasma layer exists for altitudes of approximately 90 km down to about 30 km, with the plasma layer being most severe at lower altitudes as the atmosphere becomes more dense (see figure 1.3).[11, 42, 43, 80, 64, 46, 98, 108, 46, 58, 95] The pressure during reentry ranges from approximately 0.75 Torr to about 75 Torr.[56, 73, 77]

The manned missions during Mercury, Gemini, and Apollo relied on transmission in the VHF (30-300 MHz) and UHF (0.3-3 GHz) bands for voice and telemetry communications. S-band (2-4 GHz) and C-band (4-8 GHz) frequency signals are more commonly used today for communications and radar tracking, respectively. However, GPS signal reception at 1.2 GHz, vital for navigation, has been recognized by the technical community as the most critical frequency band for hypersonic vehicle communication.[57, 43, 73, 47, 108, 65, 113, 46, 80] For the plasma layer densities cited

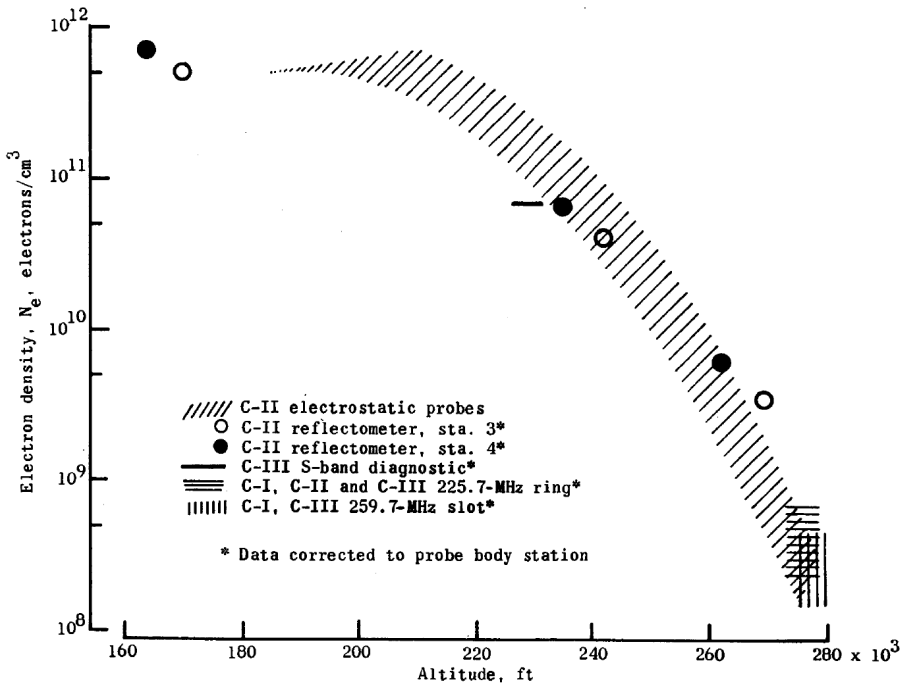

Figure 1.3: Plasma layer density measurements from RAM C-I, C-II, and C-III flight tests. Measurements were performed with electrostatic probes as well as reflectometers and antenna diagnostics.

above, the plasma cutoff frequency ranges from 0.3 to 90 GHz. So all of the currently used frequency bands are below the cutoff frequency, and will encounter blackout for a significant portion of reentry. Figure 1.3 shows the electron density as a function of altitude for RAM C-I, C-II, and C-III test flights.[80] Apollo missions would encounter even more severe plasma conditions.

1.2 Past Communications Blackout Research and Mitigation Approaches

Research on the communications blackout problem has persisted since the beginning of the manned space program, and began with flight tests to determine the plasma layer parameters, followed by testing of proposed techniques for mitigating the problem presented by the plasma layer.

Agency	Flight/Program	Experiments/Objectives
NASA	RAM A-1	Aerodynamic shaping
NASA	RAM A-2	Aerodynamic shaping and magnetic window
NASA	RAM B-1	Multifrequency signal attenuation measurements
NASA	RAM B-2	Water injection
NASA	RAM B-3	Plasma diagnostics (reflectometers)
NASA	RAM C-I	Water injection and plasma diagnostics (electrostatic probes)
NASA	RAM C-II	Plasma diagnostics (reflectometers and electrostatic probes)
NASA	RAM C-III	Water and electrophilic injection and plasma diagnostics
NASA	Fire	Thermal heat transfer and radio signal attenuation measurements
USAF	ASSET	Radio signal attenuation and antenna impedance measurements
NASA	Mercury MA-6	Radio signal attenuation measurements with ablation products
NASA	Gemini GT-3	Water injection on manned mission
USAF	Trailblazer	Plasma diagnostics (antenna impedance, radiometers, electrostatic probes, electroacoustic probes, antenna coupling)

Table 1.2: Summary of all reentry test flights.[4, 104]

1.2.1 Test Flights and Plasma Layer Research

One of the first flight test programs was the radio attenuation measurements (RAM) program at the NASA Langley Research Center.[4] The purpose of this program was to collect information on the plasma layer parameters, and to begin testing preliminary proposed mitigation techniques. The RAM project flew seven successful flights over the course of the decade, beginning in 1960, with the last flights occurring in 1970.[90] Several other test flights sponsored by NASA and the United States Air Force (USAF) flew simultaneously, including Asset (USAF), Fireflight (NASA), Trailblazer (USAF), Mercury MA-6 (NASA), and Gemini 3 (NASA).[104, 107] These flights and the experiments and mitigation methods tested on each flight are given in table 1.2. Most of the plasma layer parameters cited in the literature are a result of these flight test programs, and are still cited today.

Many diagnostic systems had to be developed to accurately measure plasma layer parameters on these test flights. The nature of the environment required new diagnostics and modification of traditional diagnostics. Rakes containing several Langmuir probes at various distances from the vehicle surface were used to measure plasma density as a function of distance from the vehicle surface. However, these rakes had to be retracted at lower altitudes as heating became more intense in the steadily thickening atmosphere.[80, 90, 46, 49, 58, 41] Measurement of signal attenuation, antenna impedance, and antenna coupling from the standard vehicle antennae yielded useful information on the plasma layer. Signal attenuation for antennas sending signals at multiple frequencies provided results similar to a microwave cutoff measurement, allowing for plasma layer density measurement. Furthermore, less intrusive, more innovative and inventive diagnostics such as reflectometers, radiometers, electroacoustic resonance probes, and conductivity probes, along with the above mentioned diagnostics were used to deduce the plasma layer density and density profile throughout the test flight trajectories.[16, 34, 42, 43, 54, 56, 80, 73, 105, 98, 108, 104, 46, 49, 58, 111, 117, 2, 6, 19, 27, 30, 41, 96, 109]

An important result of the measurement of the plasma layer parameters was the ability to create plasma sources in a laboratory setting to simulate the conditions encountered by hypersonic vehicles. The cost of test flights is prohibitively expensive to test every mitigation method. By definitively measuring the plasma layer density, pressure, and plasma temperature for several different conditions allows for greater accuracy in simulating the plasma layer for lab measurements.

Furthermore, the results of the plasma layer measurements allowed for comparison of experimental results with those results yielded from theoretical calculations, or more often currently, results from computational models. Computational models can provide results without any need for expensive experimental equipment, and without the problems encountered in mimicking vehicle reentry in an experimental system.

1.2.2 Methods of Mitigation

Over the course of more than 50 years, an astounding number of ideas for mitigating the communications blackout problem have been proposed. Each of these ideas has had obstacles to overcome, whether technical or practical, and have advantages and disadvantages when compared to each other. Some of the leading mitigation approaches, though certainly not a comprehensive list, include: electrostatic or electromagnetic particle collection, optical communication, relay ejection, high power transmission, low frequency transmission, high frequency transmission, 3-wave/Raman scattering techniques, aerodynamic shaping, magnetic window, and liquid injection.[57, 91, 21, 34, 42, 43, 54, 55, 80, 64, 68, 67, 73, 105, 47, 98, 108, 26, 65, 113, 52, 70, 72, 90, 104, 8, 24, 23, 46, 49, 58, 71, 111, 117, 121, 41, 109, 85, 66, 87, 94, 122, 37, 89, 10, 95, 114, 102, 3, 9, 48, 51, 82] Table 1.2 lists several of the earliest mitigation methods, which to date have achieved the best results and are widely regarded as the leading methods for mitigating radio communications blackout today. The three mitigation methods that are widely considered to be the most viable options are: aerodynamic shaping, magnetic window, and liquid injection.[57, 105, 47, 104]

Aerodynamic shaping was the most obvious mitigation technique, and in general does not require additional hardware. This mitigation technique takes advantage of the properties of attached shocks on sharp-nosed bodies, which generally speaking, result in relatively thin plasma layers. If the wavelengths of radio communication signals are considerably longer than the plasma layer thickness, transmission of communication signals through the thin plasma layer may be possible. The cutoff frequency holds for plasma layers that are thick relative to the communication wavelength. The longest wavelength transmitted on reentering spacecraft during the early days of manned spaceflight was 10 m (VHF at 30 MHz), significantly longer than the thickness of the plasma layer. However, modern spacecraft use GPS signals with a wavelength of 25 cm (1.2 GHz), and S-band with a wavelength of approximately 13

cm (2.3 GHz). These much shorter wavelengths are on the order of the plasma layer thickness. Therefore, the attenuation for signals of this frequency is still significant. Additionally, maintaining a sharp leading edge to maintain a thin plasma layer while minimizing spacecraft heating was not trivial. This intense heating that takes place on the leading edge of such sharp features was the most significant problem with this mitigation method. There is currently no method for addressing this issue without the use of an active cooling system. Using an ablative shield, a common passive cooling method, however, will not be able to maintain the sharp leading edge necessary for this approach.

Aerodynamic shaping requires sharp-nosed vehicle bodies that present unrealistic vehicle design constraints. For example, spacecraft capsules are designed to use the vehicle's blunt face to take advantage of aerodynamic braking, creating a bow shock that stands in front of the vehicle, creating a relatively thick plasma layer. Still, several innovative ways to address this problem have been investigated, such as the use of a remote antenna assembly (RAA), shown in figure 1.4.[57, 91, 67, 73, 105, 47, 98, 26, 90, 4, 24, 46, 111, 122, 37, 10, 95] An RAA is attached to the front of a vehicle, providing a sharp point where the resulting plasma layer tends to be very thin, and contains an antenna for sending signals through this resulting plasma layer. This method, however, does require an active cooling system, which, again adds more mass and complexity to the spacecraft. Another idea, shown in figure 1.5 is the use of a gas spike, in which a burst of air is injected in front of the vehicle, modifying the blunt shock into a more narrow shock similar to that of sharp-nosed bodies.[57, 91, 67, 73, 105, 47, 98, 26, 90, 4, 24, 46, 111, 122, 37, 10, 95] This method carries with it the added advantage that, not only is the body not subjected to the high temperatures of sharp leading edges, but the gas spike itself tends to reduce vehicle heating. However, experiments using this method have had mixed results, and have shown that this method may be ineffective at lower altitudes.[98]

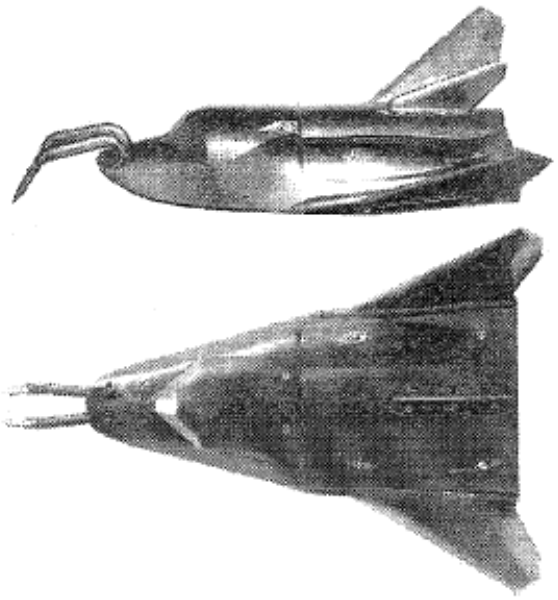

Figure 1.4: A remote antenna assembly (RAA), creating a shock similar to that on a sharp-nosed body, may transmit through a thin plasma layer created by the attached shock.[10]

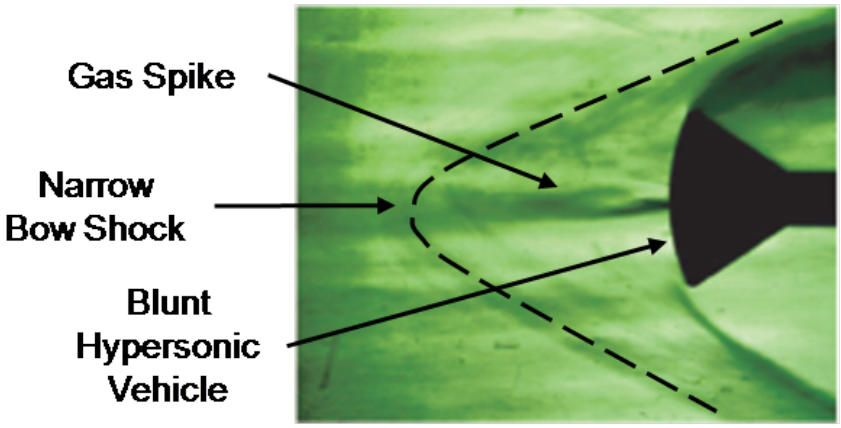

Figure 1.5: A gas spike modifies the shock in front of a blunt body, and may mitigate heating problems.[26]

In an unmagnetized plasma such as that of a reentry vehicle plasma layer, electromagnetic waves propagate as ordinary waves with a cutoff at the plasma frequency. In the presence of a magnetic field, the dispersion relation is modified. Depending on the orientation of the propagation vector with respect to the magnetic field, the cutoff frequency can be significantly less than the plasma frequency. By introducing a magnetic field, this effect may be exploited, thereby allowing the passage of communication signals below the plasma electron frequency.

These magnetic modes include R/L waves if the magnetic field is oriented along the transmission path, as well as the extraordinary wave modes if the magnetic field is oriented transverse to the direction of wave transmission. Figures 1.6 and 1.7 show the dispersion relation for the extraordinary wave and R/L waves, respectively. Note that by definition, the plasma frequency, ω_p, will always be between ω_L and ω_R.[17]

$$\omega_L = \frac{1}{2}\left(-\omega_c + \sqrt{\omega_c^2 + 4\omega_p^2}\right) \tag{1.2a}$$

$$\omega_R = \frac{1}{2}\left(\omega_c + \sqrt{\omega_c^2 + 4\omega_p^2}\right) \tag{1.2b}$$

where ω_c is the electron cyclotron frequency. Notice that there are several propagation modes that exist below the plasma frequency, for the extraordinary wave, L-wave, and R-wave. The red regions indicate areas where wave propagation is not possible. The extraordinary wave has a region below ω_p, starting at ω_L, where wave propagation is possible. Furthermore, the whistler wave mode for the R-wave exists below ω_c, the electron cyclotron frequency. Furthermore, above the ω_L cutoff, the L-wave may propagate.

Magnetic field penetration through the plasma layer is required to assure wave propagation out of the plasma. If the magnetic field penetrates only a short distance through the plasma layer, then the signal will be reflected at the point where the cutoff frequency matches the wave frequency. The magnetic field strength required

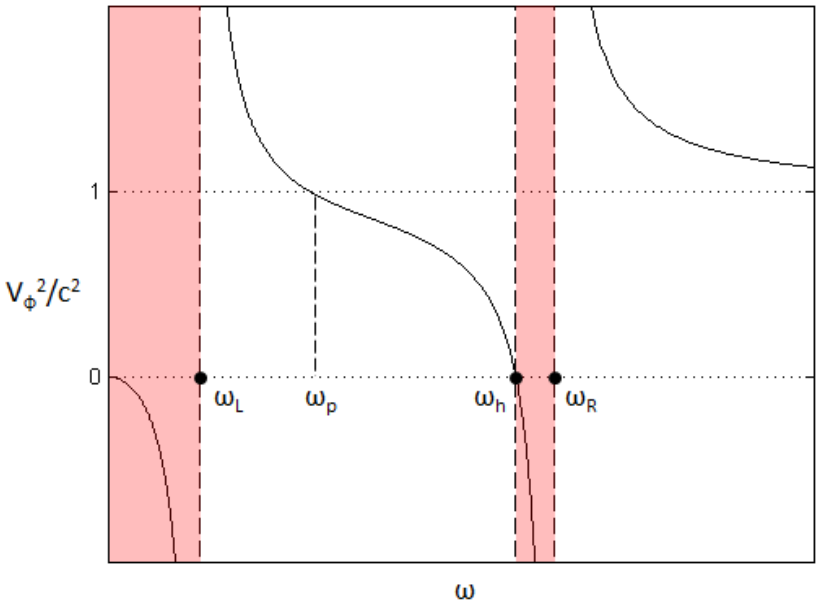

Figure 1.6: The extraordinary wave dispersion relation.

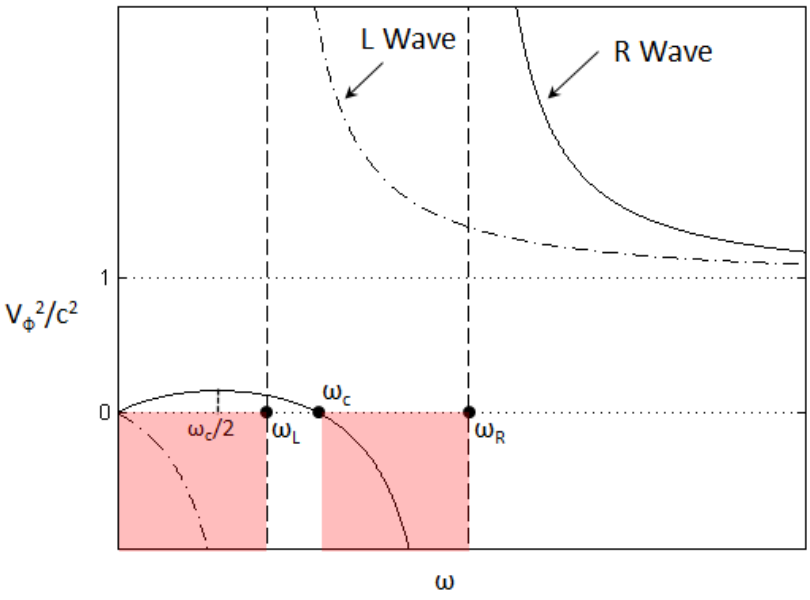

Figure 1.7: The dispersion relation for the R-wave (solid line) and L-wave (dashed line).

to give rise to propagation in these alternative modes span anywhere from a few hundred Gauss up to tens of kGauss, depending on plasma sheath properties.[98, 52, 102] Permanent magnets are a natural option for supplying the necessary magnetic flux density. They are compact and do not require an external power source. Permanent magnets, however, do have disadvantages. They represent added mass, and the magnetic field drops off rapidly with distance, which leads to reduced penetration. Furthermore, permanent magnets have temperature limits. Above the Curie temperature, magnets lose their magnetization. This occurs at $\sim$400 C for samarium cobalt magnets. As was mentioned earlier, heating of hypersonic vehicles is a problem that requires serious consideration, and in this case, renders the use of conventional permanent magnets not possible. Meanwhile, electromagnets require heavy, power consuming systems and heavy iron cores. The mass required for electromagnets is estimated to be around 25 kg/kGauss, making this approach impractical, given the hefty price tag for space vehicle mass ($10,000/kg).[73, 74, 76]

Liquid quenchant injection has shown a great deal of promise, and has been successfully tested on several flights, including the only active mitigation method to be flown on a manned space mission (Gemini 3).[54, 105, 47, 108, 90, 104, 83, 46, 121, 107, 51] The liquid quenchant mitigation approach relies on the injection of a liquid into the plasma layer during reentry to reduce the plasma layer electron density. Thereby reducing the cutoff frequency and lowering the attenuation of communication signals. While this method has not shown the capability to entirely mitigate the radio blackout problem, it has shown significant effectiveness in reducing the radio blackout period during reentry of the Gemini 3 spacecraft.[54, 105, 47, 108, 90, 104, 83, 46, 121, 107, 51]

Liquids investigated to quench the plasma layer include water as well as electrophilic liquids such as sulfur hexafluoride, carbon tetrachloride, trichloroethylene, freon, or other fluorocarbons.[91, 43, 55, 80, 105, 47, 108, 8, 23, 46, 49, 58, 71, 117, 121, 95, 3, 48, 51, 18] Injection of water cools the plasma and more importantly, the

water droplet surfaces provide a surface for electron-ion recombination. This extra surface area for plasma recombination has been cited as the most important effect of the water spraying.[108] Meanwhile, electrophilic liquids, in addition to providing a recombination surface, also have a high electronegativity, thereby creating negative ions by capturing electrons. Water will attach to electrons through means of dissociative attachment, whereby attaching an electron causes the water molecule to disassociate. By combining an electron with a molecule or atom to create a negative ion, the electron density and cutoff frequency is reduced. Since the negatively charged ions are many times heavier than a single electron, they are not able to react to a communication signal whose frequency is significantly greater than the negative ion response time.

Electrophilic liquids have shown greater effectiveness in causing recombination, attaching electrons, and ultimately reducing the plasma layer cutoff frequency.[105, 71, 117, 3] However, while the electrophilic liquid's high reactivity is beneficial for blackout mitigation, this reactivity causes environmental concerns for the same reason (reactivity with ozone, etc.)[3] Further drawbacks regarding liquid quenchant mitigation is, again, the significant mass added by carrying this liquid on board the spacecraft. However, rather than having constant liquid injection, short bursts of liquid injection several times during flight is a feasible approach. The short burst could quench the plasma layer long enough for the hypersonic vehicle to transmit essential telemetry and receive navigation signals before the plasma layer recovers and radio blackout resumes.

All of the proposed mitigation methods have significant drawbacks or technological hurdles that need to be overcome before they can credibly be implemented as a solution to communication blackout. Whether the drawback is significant mass or design complexity, this problem poses a serious hurdle for hypersonic flight, critical to national defense. Current hypersonic vehicles usually use a combination of aero-

dynamic shaping and high power to attempt to transmit through the plasma layer. However, even using these approaches, several very recent hypersonic test flights have failed due to loss of signal from the vehicle due to the plasma layer.[92, 120] It is likely that a full solution to the problem may require a combination of several approaches, however, no sufficient solution or combination of solutions has yet been established.

1.3 Proposed Approach

The main focus of this research is to study and quantify the interaction of cathode spot injected solid quenchant material with a background plasma—with the overarching goal being to investigate this approach as a means to blackout plasma mitigation. The background plasma is intended to roughly simulate the plasma layer experienced by hypersonic vehicles. By ejecting ceramic powder into the background plasma, a dusty plasma is formed. The basis of this investigation relies on the collection of electrons by the ceramic particles, which leads to a reduction in the free electron density. Each injected ceramic powder particle will act like an electrically isolated surface, collecting many electrons in the process of charging to the plasma's local floating potential. The particles also provide a surface for electron-ion recombination.

While the proposed methodology is inherently a quenchant approach, it differs from the liquid quenchant approach in several ways. This approach, in contrast to electrophilic liquid quenchants, does not rely on a chemical reaction to collect electrons. Instead, it relies on high electron mobility and the natural tendency of electrons to electrostatically "stick" to ceramic surfaces with sufficient binding thereby removing them from the plasma. As such, similar to water injection, this approach provides a plasma loss surface for electron-ion recombination after already collecting many electrons in reaching the steady state plasma floating potential—which naturally develops as a consequence of mobility differences between electrons and ions.

The advantages of using solid ceramic particles, such as reduced quenchant mass

and reduced material reactivity, are significant , but present a challenge in the method of injection. Liquid injection systems require tankage, temperature control, and injection systems that must survive reentry. Injecting solid quenchants are likely to suffer from injection issues, though in principle this can be achieved using fluidized bed approaches. But again, tankage, compressed gas, and delivery nozzles not only add to mass and complexity, but must also survive the reentry flight.

This research investigates the method of injecting solid particles by means of cathode spot arcs. A cathode spot is formed by placing a layer of ceramic particles on an electrode surface. The layer of particles could be loose or incorporated in an ablation dielectric coating. When in the presence of the background plasma above the electrode, the electrode is biased to large negative voltages, and intense, violent cathode spot arcs form on the electrode surface. The arc forces powder particles up into the overhead plasma, making the background plasma a dusty plasma.

The research performed herein ejects powder from an electrode surface laden with loose powder. So a method of practical implementation will be required that could endure a space mission and last until atmospheric reentry at the end of the space mission. Several possible means of practically implementing this method will be commented on.

In order to assess the feasibility of this approach, the cathode spot dynamics of this system had to be studied and quantified. Characterization of cathode spot operation on the surface of an electrode was therefore the first step in this study. The cathode spots are operated in the presence of a magnetic field, and analysis of cathode spot movement on the electrode surface, electrode erosion, and the role of the powder and background plasma in cathode spot formation was studied. Further measurements are made to evaluate the potential for powder ejection and rate of removal from the electrode surface. A high frame rate camera and expanded laser beam are used to deduce the mechanism of energy transfer from cathode spot arcs to the powder

particles, and the distribution of initial velocities at the time of particle ejection from the electrode surface. Measurements were made to investigate the amount of particle dispersion that would be required to significantly deplete a simulated background plasma electron population. Further measurements are made regarding the effect that both the cathode spot and the ejection of powder by cathode spots has on the electron density of a background plasma discharge. These results along with the consequences in the context of both radio communications blackout and other possible applications are presented herein.

1.4 Scope of Dissertation

The research presented and discussed herein is intended to provide a benchmark for plasma electron population depletion. Optimization was not the goal of this research, nor was significant time spent improving this approach. Rather, a basic understanding of the process and proof of the feasibility of this approach was the main focus. This research is intended to expand knowledge regarding cathode spot behavior and the potential as use for particle ejection, as well as provide a strong starting point for further research on this approach for blackout mitigation.

CHAPTER II

Wave Propagation, Cathode Spots, and Particle Depletion

2.1 Plasma Dispersion Relation

Waves propagating at frequencies below the plasma electron frequency, ω_p, are reflected by electron motion canceling out the incident wave. This result is a consequence of the plasma dispersion relation. To better understand the physics associated with the propagation of electromagnetic waves through a plasma, the dispersion relation neglecting plasma collisions as well as the dispersion relation including collisional effects will be derived and presented in this section.

2.1.1 Non-Collisional Model

Electromagnetic waves incident on a plasma surface are reflected, because in the low frequency limit ($f < \omega_p$), the plasma behaves like an ideal conductor. The electrons in the plasma can respond and act to cancel out and excite a wave in the opposite direction of the incident wave, resulting in reflection. At high frequencies ($f > \omega_p$), the electrons can't respond, so the plasma acts more like a dielectric, allowing waves to propagate through the medium.

Assuming that the plasma layer surrounding a hypersonic vehicle is non-collisional

and non-magnetic, the dispersion relation can be simply derived, beginning with two of Maxwell's Equations:

$$\nabla \times \mathbf{E} = -\frac{\partial \mathbf{B}}{\partial t} \tag{2.1a}$$

$$\nabla \times \mathbf{B} = \mu_0 \mathbf{J} + \mu_0 \epsilon_0 \frac{\partial \mathbf{E}}{\partial t} \tag{2.1b}$$

where $\mathbf{E}$ is the electric field, $\mathbf{B}$ is the magnetic flux, $\mathbf{J}$ is the free current, μ_0 is the magnetic constant, and ϵ_0 is the electric constant. The result after combining these equations, removing $\mathbf{B}$, and assuming a transverse electromagnetic wave with E and J varying as $\exp(ikx - i\omega t)$ is:

$$k^2 E = i\omega\mu_0 J + \omega^2 \mu_0 \epsilon_0 E \tag{2.2}$$

where k is the wavenumber, and ω is the wave frequency (in rad/s). Note that the only difference thus far between a wave propagating in vacuum (or air) and a plasma, is the addition of the term containing the free current, J. The free current in a plasma can be written as:

$$J = -e n_e v_e \tag{2.3}$$

where v_e is the electron velocity. The velocity of free electrons can be found using the fluid model for electrons, and since J varies as $\exp(ikx - i\omega t)$, and e and n_e are constant, v_e must also vary as $\exp(ikx - i\omega t)$:

$$\dot{v_e} = -\frac{e}{m_e} E \tag{2.4a}$$

$$-i\omega v_e = -\frac{e}{m_e} E \tag{2.4b}$$

$$v_e = -i\frac{e}{m_e \omega} E \tag{2.4c}$$

So then the free current substituted into equation (2.2), after canceling terms and

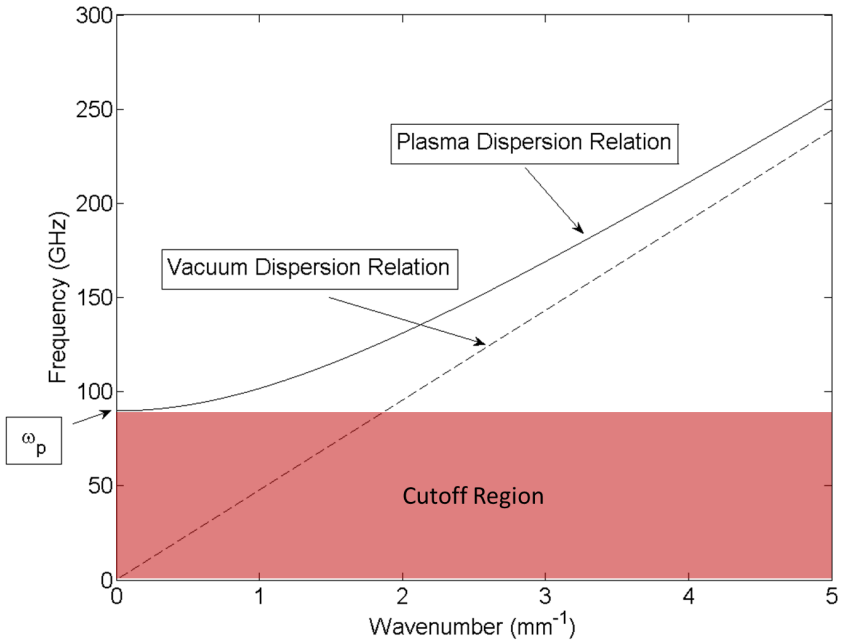

Figure 2.1: The dispersion relation for electromagnetic waves in a collisionless plasma and in a vacuum. Waves of any frequency can propagate in vacuum, however, the plasma dispersion relation has a minimum cutoff frequency, ω_p, below which waves will not propagate through the plasma layer.

rearranging becomes:

$$\omega^2 = c^2k^2 + \frac{n_e e^2}{\epsilon_0 m_e} \tag{2.5a}$$

$$\omega^2 = c^2k^2 + \omega_p^2 \tag{2.5b}$$

where, again, ω_p is the plasma electron frequency. Equation (2.5b) is known as the dispersion relation for a collisionless plasma. Figure 2.1 shows that for waves propagating in vacuum, any frequency of wave can propagate. For high frequency signals, the plasma dispersion relation approaches that of the vacuum dispersion relation. However, at low frequencies, the plasma dispersion relation has a minimum that is determined by the plasma density. The minimum, or cutoff frequency is the plasma electron frequency, ω_p. For any signal below the cutoff frequency, the electrons

in the plasma are able to oscillate to cancel the incident wave, and give rise to a wave in the opposite direction, resulting in reflection of the signal. So spacecraft trying to send a communication signal through an overly dense plasma layer will be reflected, and similarly, ground communication signals trying to propagate through the plasma layer to the spacecraft will also be reflected.

2.1.2 Collisional Model

The above collisionless plasma model provides a relatively straightforward way of analyzing the communications blackout problem caused by the presence of the plasma layer around a hypersonic vehicle. In reality, there will always be some collisions in a plasma, and in some instances, these collisions may have an important effect on the properties of wave propagation through the plasma layer.

The derivation of the dispersion relation in a collisional plasma model follows the same as that above until equation 2.4a. This equation does not take into account the effect of collisions. A term is added to (2.4a), to give us the electron fluid velocity with collisions:

$$\dot{v_e} = -\frac{e}{m_e}E - \nu v_e \tag{2.6a}$$

$$-i\omega v_e = -\frac{e}{m_e}E - \nu v_e \tag{2.6b}$$

$$v_e = \frac{e}{m_e(\nu - i\omega)}E \tag{2.6c}$$

where ν is the collision frequency. Substituting this value into (2.3), the free electron current becomes:

$$J = \frac{n_e e^2}{m_e}\frac{E}{(\nu - i\omega)} \tag{2.7}$$

and substituting this value into (2.2):

$$c^2k^2 = i\frac{\omega\omega_p^2}{(\nu - i\omega)} + \omega^2 \tag{2.8}$$

which can be simplified to obtain the dispersion relation for a collisional plasma medium:

$$\omega^2 = c^2k^2\left[1 - \frac{\omega_p^2}{\nu^2+\omega^2} + i\frac{\omega_p^2\,(\nu/\omega)}{\nu^2+\omega^2}\right]^{-1} \tag{2.9a}$$

$$\frac{c^2k^2}{\omega^2} = 1 - \frac{\omega_p^2}{\nu^2+\omega^2} + i\frac{\omega_p^2\,(\nu/\omega)}{\nu^2+\omega^2} \tag{2.9b}$$

The most important thing to note from equation 2.9b, is that if ν is zero (that is, if the plasma is assumed to be collisionless), then the collisionless dispersion relation, equation 2.5b, is recovered. However, as long as $\nu \neq 0$, then equation 2.9b is not entirely real. Therefore, the wavenumber, k is not entirely real, but made of both real and imaginary parts.

$$k = k_r + ik_i \tag{2.10}$$

It is also known that E varies as $\exp(ikx)$ when the time dependency is removed, so then the electric field can be represented as:

$$E = E_0\exp(i(k_r + ik_i)) = E_0\exp(ik_r - k_i) = E_0\exp(ik_r)\exp(-k_i) \tag{2.11}$$

where k_i must be positive and real. The k_i is dependent on ω_p, ν, and ω. From equation 1.1 ($\omega_p = \sqrt{en_e^2/\epsilon_0 m_e}$), it is clear that ω_p must be positive and real, and from general convention, the frequency values ν and ω must also be positive real values. Therefore, k_i must always be a real and positive. The resulting expression for the electric field has a sinusoidally varying portion dependent on k_r and an exponentially decaying portion dependent on k_i. This expression shows that for large k_i, the electric

field will vanish rapidly as the electromagnetic wave travels through the dense plasma layer. Obviously if the electric field vanishes, then the electromagnetic wave, or communication signal vanishes. This k_i factor is the attenuation coefficient. Rybak worked this derivation out and plotted the attenuation coefficient.[105]

$$\alpha_p = k_0 \left(\frac{\sqrt{K_r^2 + K_i^2} - K_r}{2} \right)^{\frac{1}{2}} \tag{2.12}$$

where $k_0 = \omega/c$ and K_r and K_i are defined as:

$$K_r = 1 - \frac{\omega_p^2}{\omega^2 + \nu^2} \tag{2.13a}$$

$$K_i = \frac{\omega_p^2 \left({}^{\nu}/_{\omega}\right)}{\omega^2 + \nu^2} \tag{2.13b}$$

The blackout plasma parameters are discussed in section 1.1.2 on page 4, and are presented in table 1.1.

There are several interesting features to notice about the attenuation coefficients in figure 2.2. Larger attenuation coefficients mean larger attenuation as a signal travels through the plasma layer. Collisions have been taken into account for this situation, yet when the wave frequency is greater than the plasma frequency, the attenuation coefficient for all cases still rapidly and significantly drops. So there is still an effective cutoff at the plasma frequency, despite particle collisions. The most significant effect that particle collisions have on the plasma dispersion relation is that for highly collisional plasmas, where $\nu \approx \omega_p$, the attenuation coefficient drops for frequencies significantly below the cutoff frequency. Mentioned earlier, on pg. 9, low frequency transmission is one possible way of mitigating the radio blackout period. However, this approach requires a dense, highly collisional plasma layer throughout the duration of reentry and/or hypersonic flight, and still has a higher attenuation coefficient than frequencies just slightly above the cutoff frequency.

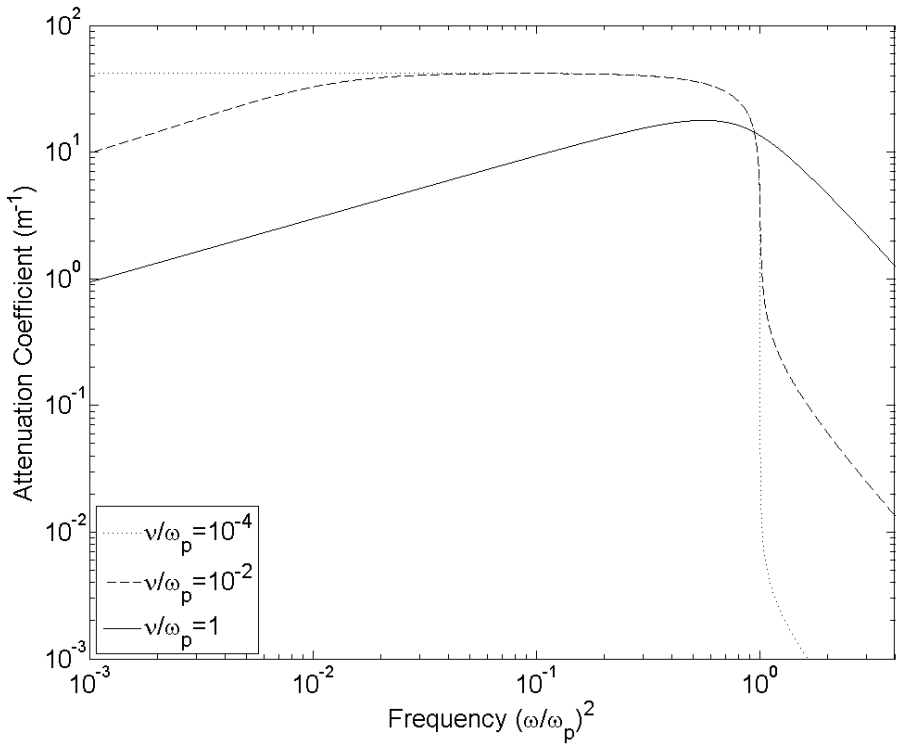

Figure 2.2: This figure shows the attenuation coefficient, or the imaginary portion of the wavenumber, k_i, from equation 2.9b. The plot shows the attenuation for various frequencies and collision rates, normalized by the plasma frequency.

2.2 Cathode Spot Arcs

Momentum transfer via a cathode spot arc plume is a novel method that is used in this dissertation research to eject powder from the surface of a metal electrode. Such quenchant powder injection enables the depletion of a reentry plasma. Therefore, an understanding of cathode spot arc phenomena is necessary, as it is an integral part of this dissertation work.

2.2.1 What Are Cathode Spot Arcs?

A cathode spot, strictly speaking, is a very localized arc discharge formed on the surface of a negatively biased electrode by a cathode spot arc. In a looser sense, the term 'cathode spot' often refers to the spot left on the electrode surface, as well as the cathode spot arc itself. This terminology will be used for the remainder of this work to conform to the standard in current literature.

Cathode spots are short-lived, intense vacuum arcs that are initiated on the surface of a metal cathode surface. In many cases, cathode spot arcs are initiated in ultra high vacuum systems, so the arc current is carried, for the most part, not by background ionized gas, but by cathode material that has been molten, vaporized, ionized, and ejected from the cathode surface.[14, 15] In this way, it is said that cathode spots 'burn' on or into the electrode surface. The result is a very violent and energetic jet or plume of ionized electrode material being pushed away from the cathode surface. These energetic cathode spot plasma jets have flow velocities of up to 10^4 m/s, and can have densities as high as 10^{20} cm^{-3}![14, 15, 45, 29, 61, 100, 20, 28] The current density emanating from cathode spots ranges from 10^9 to 10^{12} A/m^2.[20, 14, 61, 15] As a result of electrode material being ejected from the cathode surface, a spot is etched into the cathode where the spot burned, thus the term 'cathode spot'. The lifetime of these cathode spot arcs tend to be very short, on the order of one to tens

Parameter	Typical Cathode Spot Values
Lifetime	2–25 µs
Size	10–500 µm
Density	10^{20} cm^{-3}
Flow Velocity	10^{4} m/s
Pressure	1–50 atm
Current	1–1000 A
Current Density	10^{9}–10^{12} A/m^{2}

Table 2.1: Summary of typical cathode spot parameters.[14, 20]

of microseconds.[14, 15] The cathode spot dies as electrode heating can no longer be maintained. However, new cathode spots can be ignited in very quick succession, resulting in many cathode spots burning and extinguishing if supplied with a voltage pulse lasting for hundreds of microseconds or more. Typical parameters cited in the literature for cathode spots are given in table 2.1. These parameters are not so-called shot-to-shot variations in a given experimental setup, but rather are dependent on several factors such as electrode material, electrode surface conditions, background pressure, and many others.

Cathode spots tend to form at small, microscopic protrusions on the cathode surface, where the electric field is intensified. It is theorized that cathode spots are initially ignited by field emission at these microscopic protrusions.[14, 86, 61] Localized ohmic heating of these protrusions lead to vaporization of electrode material. These electrons, when emitted, are accelerated away from the cathode surface, where they subsequently collide and ionize the electrode vapor.[13] The resulting positively charged ions then accelerate back to the cathode surface, colliding and depositing kinetic energy, converted to thermal energy in the electrode surface. Repetition of this process heats the electrode near the protrusion and gives rise to thermionic emission of electrons from the cathode surface. At this point, the cathode spot has been 'ignited'. Electrons are being emitted, ionizing atoms that then bombard the cathode surface and continue to heat the cathode surface. This intense heating of the cathode

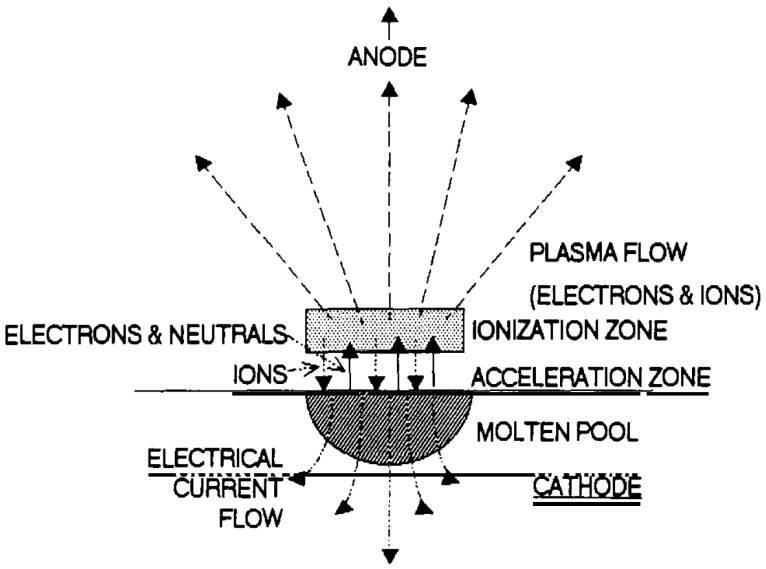

Figure 2.3: This schematic from Boxman 1992 [13], shows the basic process of cathode spot ignition.

at the cathode spot location results in the electrode material itself becoming liquefied, vaporized, and ionized, giving rise to the dense and energetic ionized cathode spot plume. This cathode spot plume emanates from a pool of molten electrode material on the electrode surface. At some point, the spot loses enough heat and has vaporized the initial protrusion on the cathode that provided the intense electric field to initiate this entire process, and the cathode spot can no longer be maintained. The spot collapses because it has become too large to maintain the heat required to continue melting, vaporizing, and ionizing the electrode material. The spot is extinguished.

There are two main types of cathode spots, known simply as type 1 and type 2 cathode spots.[14, 15] Type 1 cathode spots tend to form spuriously, at seemingly random times and in random places on the electrode surface, when the conditions for ignition are favorable. Type 1 cathode spots seem to jump from place to place on the electrode surface without regard to the location of the previous spot, because they will reignite anywhere on the electrode surface. However, type 2 cathode spots will preferentially ignite nearby previous spots where the cathode is still warm from the

thermal energy deposited from the previous, now extinct, cathode spot.[14, 15] Type 2 cathode spots rely on the thermal energy to reignite, and often times, a protrusion has been formed on the edge of the crater of the previous spot, providing all that is required for ignition of another cathode spot. In this way, type 2 cathode spots will ignite, burn, extinguish, and reignite at nearby locations over and over again. This results in type 2 cathode spots leaving continuous etched tracks in the cathode surface. This behavior gives rise to the apparent motion of the cathode spots moving across the electrode surface in a seemingly continuous way. Both type 1 and type 2 cathode spots have been observed in the experiments performed and described herein.[33, 35]

2.2.2 Cathode Spot Motion

The motion of cathode spot arcs on the surface of an electrode, particularly the nature of the motion of type 2 cathode spots in static magnetic fields has been a subject of great debate and intense research. This behavior is of particular interest to this project because a magnetic field is used to affect the occurrence and motion of cathode spots on a quenchant-laden electrode. Intuitively, one would expect that type 2 cathode spots would travel in the Amperian direction, $\mathbf{J}\times\mathbf{B}$. However, many have reported observing cathode spot arcs moving in the -$\mathbf{J}\times\mathbf{B}$, or 'retrograde' direction.[33, 35, 86, 100, 29, 7, 123, 112, 62] It has been observed that retrograde motion is usually observed at low background pressures less than a few Torr.[100, 86] Many theories attempt to explain this cathode spot motion, but no general consensus has been reached to clearly explain these observations. Several possible theories exist regarding the cause of retrograde motion: (1) self magnetic field effects; (2) asymmetric space charge; (3) asymmetric plasma confinement; and (4) ion motion.

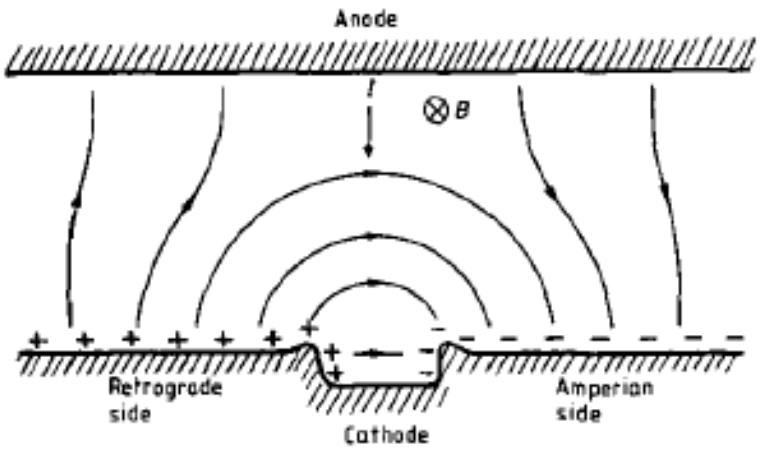

Figure 2.4: Some believe asymmetric space charge in the cathode spot vicinity accounts for retrograde motion.[86]

2.2.2.1 Self-magnetic Field Effects

Robson observed that while the arc itself bent in the Amperian direction, the self magnetic field caused by this bending could explain retrograde motion at low pressures, and Amperian motion at higher pressures. As the pressure rose, the Amperian bending of the arc became less pronounced, therefore reducing the self-imposed magnetic field due to the cathode spot arc, reverting to Amperian motion.[100]

2.2.2.2 Asymmetric Space Charge

Others believed that as ions and electrons were spewed from the cathode spot, the individual ions and electrons would follow Amperian motion, with the ions moving to the 'retrograde' side and electrons to the 'Amperian' side (figure 2.4). From this separation of charge, a Hall electric field in the cathode spot vicinity was produced. The cathode spot forming on the negatively biased electrode would move towards the direction of the largest potential drop, towards the ions, and in the retrograde direction.[86]

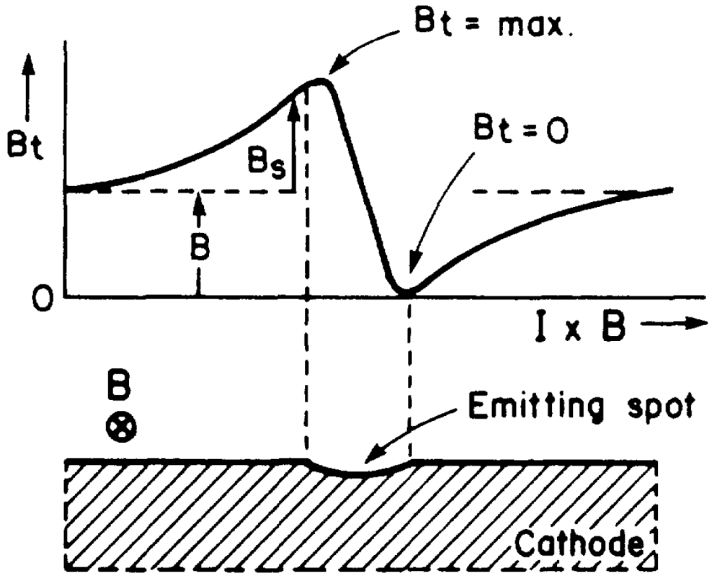

Figure 2.5: The self-imposed magnetic field can cause an asymmetry leading to retrograde motion.[29]

2.2.2.3 Asymmetric Plasma Confinement

Another theory takes into account both self-magnetic fields and asymmetry near the cathode spot to explain the retrograde motion. The self-magnetic field caused by current flowing into the cathode spot induces a magnetic field on the cathode spot. This magnetic field, when in the presence of a transverse magnetic field, will add to the static field on the retrograde side, and reduce the field on the Amperian side of the cathode spot (figure 2.5). This asymmetric magnetic field will affect plasma diffusion, acting to confine the plasma on the retrograde side, while allowing free diffusion on the Amperian side. The plasma on the Amperian side will quickly diffuse away from the spot, while the plasma on the retrograde side will diffuse more slowly. While the plasma on the retrograde side slowly diffuses away, heat is continually being deposited by ions bombarding the electrode surface near the cathode spot.[29] Therefore, the type 2 spots that are dependent on thermal energy will preferentially form on the retrograde side. Cathode spots revert to Amperian motion at higher pressures due to

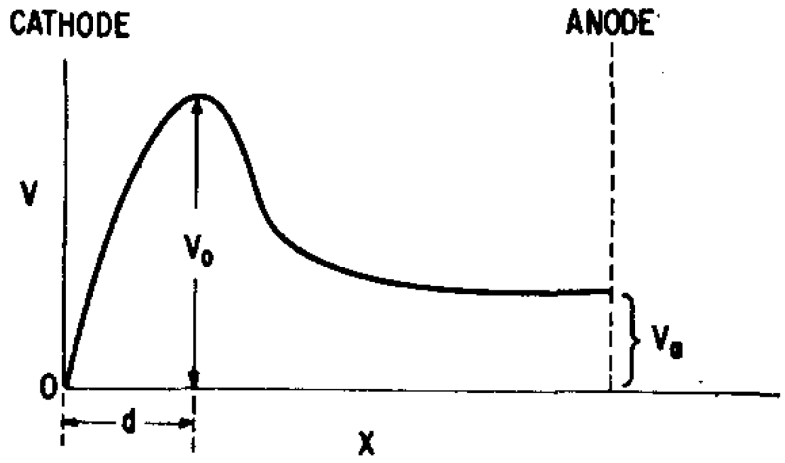

Figure 2.6: A diagram of the proposed electric potential between the cathode and anode directly above a cathode spot.[28]

reduced diffusion on the Amperian side caused by collisions with neutral atoms.[29]

2.2.2.4 Ion Motion

It has been observed in many instances that ions are ejected from the cathode spot and eventually reach the anode, opposite of the expected motion of a positive ion. However, positive ions flowing in this opposite direction would change the sign of the current, and therefore, cause retrograde motion of a cathode spot arc. Measurements of positive ions reaching the anode at velocities greater than the anode-cathode potential is explained by the proposed potential hump theory.[28] This theory proposes that low energy electrons and neutral atoms emitted from the cathode spot travel some distance from the cathode, with the electrons gaining energy. Once these electrons have gained enough energy, many neutral ions can be ionized, created many positive ions. Meanwhile, many energetic electrons continue past this region, creating a region of positive ions, where neutrals continue to be ionized. The ions created in this region will have a positive potential, creating a potential hump between the cathode and anode, shown in figure 2.6. Ions on the left side of the potential hump will be accelerated back to the cathode to continue heating the cathode, while those

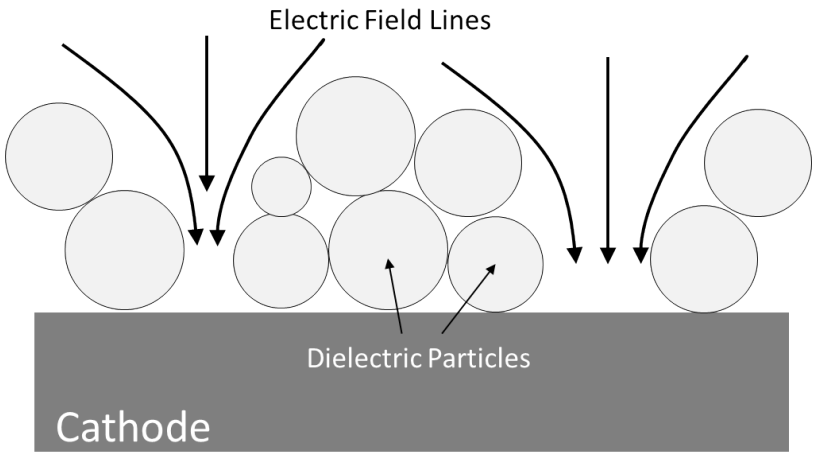

Figure 2.7: Electric field intensification due to dielectric particles on the electrode surface enhances cathode spot formation.

to the right of the potential hump will be accelerated away from the cathode, towards the anode with an energy greater than the anode-cathode potential difference.

2.2.3 Cathode Spots For Particle Acceleration

The intense electric field required to initiate field emission for cathode spot formation can be created by a high voltage provided to an electrode. The use of a dielectric material placed on top of the electrode may help to intensify the electric field at the electrode surface, as shown in figure 2.7, particularly at surface imperfections and protrusions.[61, 33] In these experiments, the electrode that cathode spots are ignited on is covered in a layer of dielectric powder to enhance cathode spot formation, and to provide the particles that will be injected into the overhead plasma.

2.2.3.1 Why Use Cathode Spots?

Cathode spot plume qualities are ideal for the acceleration and dispersal of dielectric microparticles. Cathode spots plumes tend to be very high pressure and high density. The pressure at the electrode surface of a cathode spot has been cited to range from 1 atm to 50 atm.[20, 86] The high pressure conditions of the plasma plume

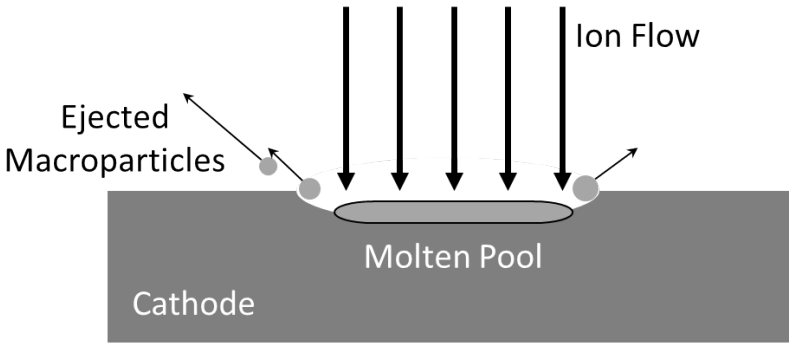

Figure 2.8: Schematic depicting macroparticle ejection from cathode spots.

will push back on the electrode where the cathode spot is burning. If the cathode spot has created a pool of molten electrode material, this pressure will push back on the molten metal material. This high pressure, as well as explosive eruption will eject small droplets of the molten cathode spot material as 'macroparticles'. [123, 14, 15] These macroparticles have been cited to be ejected at velocities from 10–800m/s, and particle radii ranging from 0.1 µm to about 100 µm.[13, 25, 28, 100, 14, 15, 61] Figure 2.8 depicts how ions streaming back to the electrode will exert pressure on the molten material in the cathode spot, causing the macroparticles to be ejected.

This high pressure acting on the cathode spot at the electrode surface may not eject all molten metal, but may push some of the molten metal material out of the spot as it bares down into the electrode surface. In this way, the molten material piles up on the electrode surface next to the cathode spot crater that has been bored into the electrode surface. The results of this mechanism following the ignition of a cathode spot is shown in figure 2.8. This is the type of protrusion that can lead to subsequent cathode spot ignition. These protrusions, in addition to the heating of the electrode as a result of the previous spot, leads to type 2 cathode spots forming near this previous spot that has since extinguished.[13, 61, 86]

Cathode spots plumes, in addition to having high pressure, have extremely high flow velocities, on the order of 10^4 m/s.[61, 29, 45, 14] That is almost Mach 30! This high flow velocity makes cathode spots an extremely attractive method for entraining

and subsequently ejecting dielectric microparticles at potentially high velocities.

2.2.3.2 Cathode Spot Acceleration Mechanism

The mechanism by which cathode spots accelerate and eject dielectric microparticles is multifaceted, and it is not exactly clear how much each mechanism is responsible for particle acceleration. The main mechanisms by which particles are accelerated is by cathode spot plume pressure and flow velocity, as well as particle charging and electric field ejection.

Cathode spot plume pressure is high enough to eject molten metal from the site of the cathode spot at extremely high velocities. Dielectric powder with particle sizes on the same order of the molten metal droplet size will be much lower in mass. Therefore, despite laying on top of the cathode spot (rather than residing *in* the spot crater), dielectric particles may be ejected a relatively high velocities as well. However, there is a fundamental difference in that the macroparticles are heated to a molten state, and then ejected from the plume pressure. Still, the pressure from the cathode spot plume will act on the bottom of the dielectric particles, pushing them up and into the overhead plasma. The cathode spot plume pressure will be dissipated somewhat due to free expansion of the cathode spot plume from the electrode surface.

Since the cathode spot plumes will be emanating from the electrode surface and pushing up on the dielectric particles, the cathode spot plume flow velocity is an important factor in the ejection of dielectric particles. This spot plume can travel at extremely high, supersonic velocities, in fact, as measured with optical methods, retarding potential analyzers (RPA's), current collecting probes, and momentum pendulums.[14, 28] The plume velocity, combined with the plume density (10^{20} cm^{-3}), will impart a portion of its energy and momentum to the dielectric particles in the vicinity of the cathode spot.

Particles, when ejected into the plasma, will quickly charge to a negative potential.

The negative charge associated with the ejected dielectric particles, along with the electric field in the plasma sheath will act to accelerate the particle up and away from the electrode. However, once the particle has left the sheath and entered the quasi-neutral bulk plasma, there will no longer be an electric field to accelerate the charged particle. The dielectric particle will travel in a ballistic trajectory. The process by which particles charge will be discussed in the next section.

2.3 Powder and Depletion

The entire purpose of initiating cathode spots is to eject dielectric particles from the electrode surface into an overhead plasma with the ultimate purpose being that they will reduce the electron density of the overhead plasma.

2.3.1 Particle Charging Processes

This method of plasma depletion relies on the charging of dielectric particles when ejected from the electrode. This section will discuss the method of particle charging as well as the time required for dielectric particles to charge.

2.3.1.1 Particle Charging

Each powder particle in a plasma acts as an electrically isolated or floating object. Powder particles in a plasma discharge will collect ion and electron current, charging to the plasma floating potential in the process. Since electron mobility is typically much greater than that of the plasma ions, particles will collect a net negative charge. Charge is collected until the ion and electron current to the particle surface becomes equal. Hence the particle has reaches the plasma floating potential, and the electron

and ion current to the particle surface are:[17]

$$0.61en_e\sqrt{\frac{kT_e}{m_i}} = \frac{1}{4}en_e \exp\left(\frac{e(V_f - V_p)}{kT_e}\right)\sqrt{\frac{8kT_e}{\pi m_e}} \tag{2.14}$$

If it is assumed that the particles are approximately spherical, then the charge on the particle can be calculated from the formula for a spherical capacitor:[44]

$$C_d = 4\pi\epsilon_0 r_d \tag{2.15}$$

where ϵ_0 is the electric constant, r_d is the dust particle radius, and C_d is the capacitance of the spherical particle. Equation 2.15 can be used in the relation that relates charge and capacitance:[78]

$$Q_d = C_d V_d = 4\pi\epsilon_0 r_d V_f \tag{2.16}$$

where Q_d is the net charge on the particle and V_d is the particle potential. So for a particle 22.5 µm in radius (or 45 µm in diameter) and a nominal floating potential of -5 V, the particle would collect almost 80,000 electrons!

2.3.1.2 Particle Charging Time

The time that it takes particles to fully charge once they are injected into the plasma is an important parameter that will have a first order effect on local plasma depletion. Particles that charge fast will deplete the plasma near the ejection site, whereas particles that charge more slowly will collect charge and deplete the plasma along the particle's full trajectory after being ejected.

The particle charging time can be found by taking the time derivative of the

particle charge:[78]

$$\frac{dQ_d}{dt} = -I_{e0} \exp\left(\frac{Q_d}{C_d T_e}\right) + I_{i0}\left(1 - \frac{Q_d}{C_d T_i}\right) \tag{2.17}$$

where I_{e0} and I_{i0} are the electron and ion current entering the Debye sphere around the particle. The capacitance of the particle may be assumed to be that of a sphere (given in equation 2.15), but is expressed as simply C_d here to simplify equations. For a particle that has no initial net charge, the ion current term (the second term in equation 2.17) is small compared to the electron current (first term). Therefore the particle charge as a function of time can be found to be approximately:[78]

$$Q_d(t) = -I_{e0} t \tag{2.18}$$

Equating this to equation 2.16 and solving for the particle charging time:[78]

$$\tau \sim \frac{C_d V_f}{I_{e0}} = \frac{4\pi\epsilon_0 r_d V_f}{I_{e0}} \tag{2.19}$$

It is important to note here that I_{e0} may depend on the particle size relative to the Debye length. If $r_d >> \lambda_D$, then the usual expression for the electron saturation current may be used:[78]

$$I_{e0} = \frac{1}{4} e n_e \sqrt{\frac{8kT_e}{\pi m_e}} 4\pi r_d^2 \tag{2.20}$$

However, if $r_d << \lambda_D$, then orbital motion limited (OML) theory must be taken into account, and the charging time may be slightly longer.

Assuming again that a particle 22.5 µm in radius is immersed in a plasma with T_e = 3 eV, density $n_e = 10^{10}$ cm^{-3}, and floating potential of -5 V, the particle charging time will be approximately 4.24 ns.

2.3.2 Powder Requirements For Plasma Depletion

The purpose of ejecting powder particles is to deplete the plasma. However, in order to successfully deplete the plasma electron population, several material factors must be taken into account. Furthermore, the particle dispersion method must also meet several requirements. These factors and considerations are discussed below.

2.3.2.1 Macroparticle Considerations

It has been shown that droplets of molten electrode material can be ejected from cathode spot sites. The mechanism behind macroparticle ejection from cathode spots was discussed earlier. These molten macroparticles, when ejected from the cathode spot on the electrode will undergo charging and current collection in a similar fashion to the ceramic dielectric particles when ejected.[13] So, in many cases, the macroparticles ejected from cathode spots, even without the presence of dielectric powder, likely also contributes to the depletion of the plasma electron population. However, in experiments presented herein, few macroparticles are ejected as compared to the number of dielectric powder particles ejected. Also, experiments show that the dielectric powder is the main component causing electron population depletion, so macroparticle depletion is neglected in these studies.

2.3.2.2 Temperature Considerations

The dielectric particles will experience intense heat as they are ejected from the cathode spot site as the surface there is molten. Since the melting temperature of steel is around 1300 to 1500 degrees Celsius, the dielectric material used should remain in the solid state over this temperature range.[5] After a particle is ejected by a cathode spot, the particle will be bombarded by ions and electrons as the particle traverses through the overhead plasma. Both, exposure to the cathode spot-derived plasma jet, as well as electron and ion bombardment in the overhead plasma will heat

Material	**Dielectric Constant**	**Melting Temperature (°C)**	**Boiling/Sublimation Temperature (°C)**
Alumina (Al_2O_3)	9.0 - 10.1	2100	3000
Aluminum Nitride (AIN)	9.2	2200	2500
*Boron Nitride (BN)	4.3	*	*2600 – 2800
Silicon Nitride (Si_3N_4)	10	1800	1900
Titanium Dioxide (TiO_2)	80 - 100	1850	2900
* Material dissociates at the temperature listed, but does not melt or boil			

Table 2.2: Summary and comparison of ceramic material properties.[40, 38, 99, 1]

the particle. Therefore, it is important that the particle used is able to withstand high temperatures without melting or thermionically emitting electrons, as well as maintain a low secondary electron coefficient.

Most metals that have melting temperatures above the melting temperature of stainless steel will easily thermionically emit, and will have relatively high secondary electron emission coefficients. These are several reasons why macroparticle ejection may not have as significant of an effect on the plasma electron population, and are neglected herein. However, ceramic dielectric particles have extremely high melting temperatures, will not easily thermionically emit electrons due to a large band gap, and have relatively low secondary electron emission coefficients when bombarded by electrons at energies of a few eV. Alumina (Al_2O_3) powder, readily available from Goodfellow, has a melting temperature of 2100 degrees Celsius and a continuous use temperature of 1700 degrees Celsius.[40] Both the melting point and continuous use temperature are well above the melting point of steel. Furthermore, the melting point, or temperature above which alumina will exist in a gaseous phase is 3000 degrees Celsius.[40] These properties and the properties of a few other possible candidate materials are shown in table 2.2. Alumina was the ceramic material selected because it was readily available, and for its combination of high melting point, high boiling point, and high dielectric constant.

2.3.2.3 Particle Ejection Velocity Requirement

Particles must be ejected from the electrode with enough velocity to penetrate through the depth or thickness of the plasma layer surrounding a hypersonic vehicle. Penetration of the plasma layer is required to deplete the plasma layer beginning near the spacecraft surface at the antenna location, where the wave will be launched. This penetration must extend to the plasma layer depth where the signal can travel unimpeded. That depth will be edge of the plasma layer, or the depth where the plasma layer cutoff frequency is below the signal frequency (for $\sim$ 1 GHz, $n_e \sim 10^{10}\text{cm}^{-3}$). The thickness of this plasma layer will depend on many factors related to the specific vehicle and flight parameters such as vehicle shape, velocity, and altitude, just to name a few. However, as an approximation, the plasma layer thickness has been shown to be on the order of several centimeters, but can vary depending on a variety of parameters such as vehicle shape, angle of attack, velocity, altitude, etc.[108, 64, 47, 105, 49]

If it is assumed that particles will follow a ballistic trajectory, then the required initial injection velocity in the vertical direction can be calculated. So, for particles to penetrate to a plasma layer thickness of 10 cm, an initial ejection velocity of approximately 1.40 m/s would be required. A particle ejected at 1.0 m/s would penetrate more than 5cm, and an injection velocity of 0.7 m/s results in a penetration of 2.5 cm. Figure 2.9 shows the plot of penetration depth versus initial injection velocity, assuming a value of $g = 9.81$ m/s.

However, in actual reentry situations, particle penetration will most likely not be ballistic. The particle trajectory will be affected significantly by flow around the vehicle. The flow around the vehicle will vary depending on vehicle shape, velocity, angle of attack, altitude, boundary layer thickness, etc.

Regardless, greater penetration into the plasma layer can be achieved with greater velocity, and it would seem intuitive that lighter, less dense, and smaller particles may

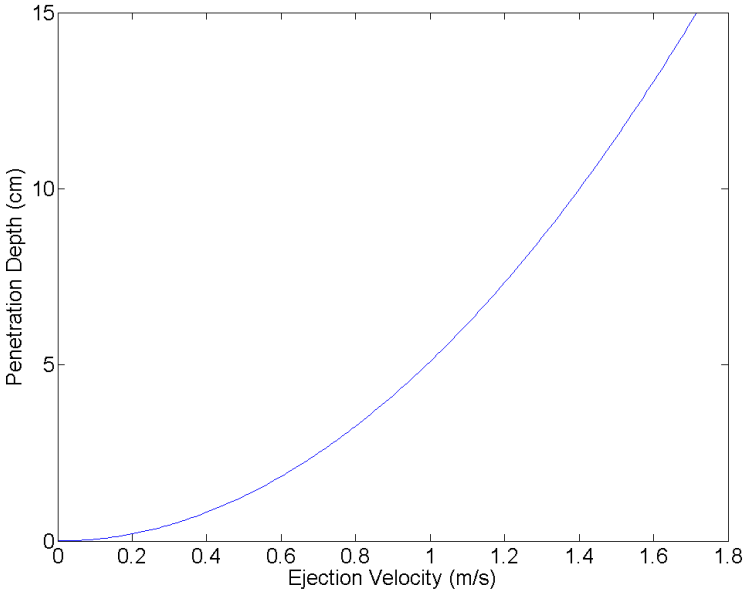

Figure 2.9: A plot showing the penetration depth achieved for particles ejected with various initial velocities in the vertical direction, assuming a ballistic trajectory.

be injected at higher velocities. Therefore, the material chosen for these studies was aluminum oxide (Al_2O_3), or alumina, readily available from Goodfellow. The density of alumina is relatively low, 3.9 g/cm^{-3}.[39]

2.3.2.4 Electrical Properties

It is important that the dielectric powder that is used for these experiments have a high dielectric constant. Cathode spot ignition depends on a strong electric field at the electrode surface, where the dielectric powder is placed. Therefore, a dielectric powder with a high dielectric constant will help to enhance cathode spot ignition on the surface of the electrode, as shown in figure 2.7.[61, 33] The dielectric constant for alumina is approximately 10, which is relatively high for ceramic materials.[38]

2.3.2.5 Particle Size Trade Study

Particle size and density are also important parameters to consider. Charge removal from the plasma is highly dependent on the size of the particle. While total charge accumulated by the particle increases with size, so does particle mass. Therefore these two parameters must be carefully considered and balanced to obtain the optimum particle size .

The total charge collected is a function of the particle capacitance and particle charge collected, given in equations 2.15 and 2.16, respectively. So large particles will collect more charge than smaller particles, therefore removing more electrons per particle from the overhead plasma. However, the number of particles ejected is just as important to the overall charge removed from the plasma. The total charge removed by a group of particles will be determined by:

$$Q_{tot} = Q_d N_p \tag{2.21}$$

where Q_{tot} is the total charge collected by N_p powder particles, Q_d is the charge collected by a single dust particle, and N_p is the total number of particles injected into the plasma. So in addition to the size of each particle, the total number of particles injected will also be important.

It is assumed that each cathode spot plume exerts a fixed force on the powder particles as it emanates from the electrode surface. Therefore, it may be a reasonable assumption to assume that for a given dielectric powder coverage, each cathode spot will eject a fixed mass of powder. In this case, particle mass also becomes a significant factor. The mass of each powder particle can be determined by particle radius and material density. For a particle 22.5 µm in diameter and made of alumina, the particle

mass is 0.186 µg. The total mass of a group of N_d powder particles is:

$$M_d = N_d \frac{4}{3} \pi r_d^3 \rho_d \tag{2.22}$$

where ρ_d is the mass density of the powder material. Solving for the number of particles, N_d and substituting this and equation 2.16 into equation 2.21, the following is obtained:

$$Q_{tot} = 4\pi\epsilon_0 V_f r_d \frac{3M_d}{4\pi r_d^3 \rho} = \frac{3\epsilon_0 V_f M_d}{\rho_d r_d^2} \tag{2.23}$$

So assuming that each cathode spot ejects a fixed mass of powder, the total charge collected by powder particles is inversely related to the square of the particle radius. This clearly suggests that smaller particles will collect more electrons from the overhead plasma. This is due to the smaller mass of each particle, allowing for the ejection of more particles in the fixed mass injection limit.

In addition, the surface area of particles acts as a loss surface for the overhead plasma in that it allows ions and electrons to recombine to form neutral gas particles, thereby also reducing the electron density in the overhead plasma. In fact, Schroeder and Russo [108] showed that ion-electron recombination on the surface of water droplets injected into the plasma flow during the reentry of Gemini 3 was the main mechanism for reducing the plasma layer cutoff frequency. Therefore, the powder particle surface area is also an important factor to be considered, and is dependent on the particle radius squared if the powder particles are assumed to be spherical. So the additional loss area for the overhead plasma when particles are injected is:

$$SA_{tot} = N_p SA_d = \frac{3M_d}{\rho r_d} \tag{2.24}$$

where SA_d is the surface area for each particle. So, for a fixed mass of powder ejected, the total particle surface area, or plasma loss area is inversely proportional to the

particle radius. This calculation also suggests that the smallest possible particle size will be advantageous for plasma depletion. However, if the particles are too small, then the particle ejection velocity may be high, and residence time in the plasma may be too low to collect sufficient charge.

In experiments, two readily available alumina particle sizes are used. The larger particles have a mean diameter of 45 µm, and the smaller particles have a diameter no larger than 0.1 µm. According to the equations above, and assuming each spot ejects a constant mass of particles, the smaller particles will collect more than 200,000 times more electrons in the process of charging, and provide a loss area more than 450 times as large as the 45 µm particles.

However, several considerations must be taken into account. To begin, our previous assumption of fixed mass ejection of powder, regardless of particle size, may not be valid. A more reasonable assumption may be that each cathode spot clears a given area of the electrode of powder. Here, the cathode spot and associated plume are a fixed size, and therefore, only extend a given distance from the center of the spot, clearly only the powder in this area of the electrode will be ejected.

In this case the so-called 'packing' density of the powder must be considered. The packing density is the mass density of the powder, including the interparticle space in the volume. The 45 µm diameter powder has a packing density of approximately 0.96 g/cm^3, and the 0.1 µm diameter powder has a packing fraction of approximately 0.099 g/cm^3, an order of magnitude smaller. The volume of powder cleared from the electrode surface will be:

$$V_s = \pi r_s^2 t \tag{2.25}$$

where r_s is the radius of the cathode spot ($\sim$ 0.5 mm), and t is the thickness of the powder layer, about 1 mm in this case. Then the total number of particles cleared

by one cathode spot is:

$$N_d = \frac{3V_s\rho_p}{4\pi\rho_d r_d^3} = \frac{3r_s^2 t\rho_p}{4r_d^3\rho_d} \tag{2.26}$$

where ρ_p is the packing density of the powder. The total charge carried out of the discharge by powder particles, assuming fixed volume ejected, then is:

$$Q_{tot} = N_d Q_d = \frac{3\pi\epsilon_0 V_f r_s^2 t\rho_p}{r_d^2\rho_d} \tag{2.27}$$

The cathode spot size and powder layer will be the same, but the packing fraction and dust particle radius will vary. In the limit of constant volume of powder ejected, the 0.1 micron powder will remove about 2×10^4 times the total charge as the 45 micron powder. This is in contrast to the 0.1 micron powder collecting a factor of 2×10^5 more charge for the fixed mass case. The 0.1 micron powder will also have a surface area 45 times larger than the 45 micron powder. While there are still more factors to be considered and discussed below, the constant volume assumption seems like the most valid model for assessing particle ejection and charge collection.

Another factor that must be considered is particle clumping. Van der Waals forces can lead to particle clumping. Remnant water vapor on particle surfaces also leads to clumping—typically associated with hydrogen bonding.[59, 119] The 45 micron powder, shown in figure 2.10 consists of particles that are almost all 45 µm in diameter, and have consistent size and shape. However, in figure 2.11, the 0.1 micron powder particles tend to clump together into particles that are much larger than even the 45 micron powder particle size. Several of these particles are nearly 500 µm in diameter! However, in addition to large clumps, there are also intermediately sized particles that are significantly smaller than the 45 µm. This 0.1 micron powder, in experiments and as shown in figure 2.11, was sifted through a fine wire mesh to reduce especially large powder clumps.

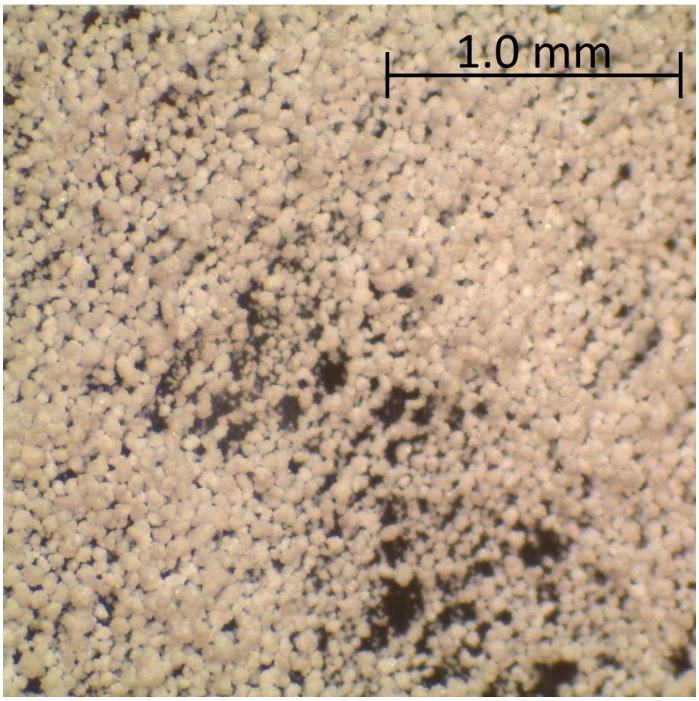

Figure 2.10: Microscope image at 35× of 45 micron diameter powder. Almost all particles are separate and approximately 45 µm in diameter.

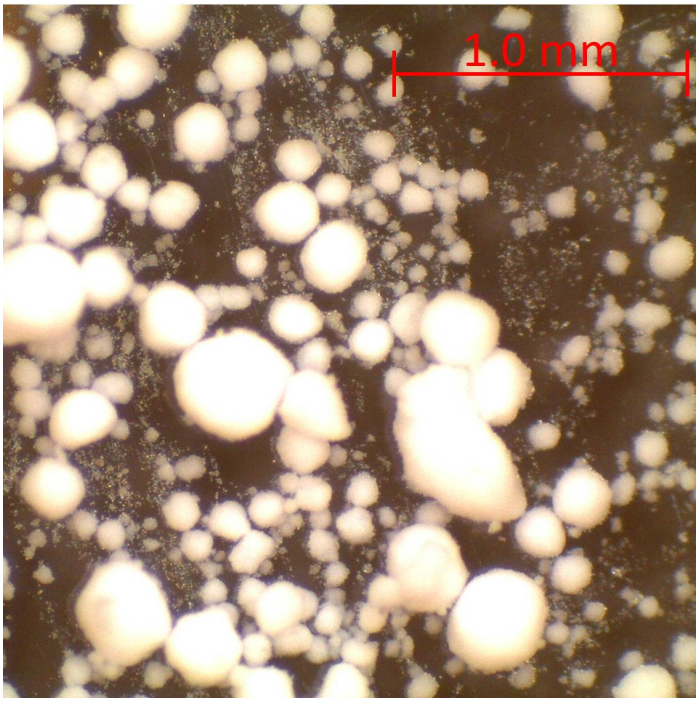

Figure 2.11: Microscope image at 35× of 0.1 micron diameter powder. Most particles have clumped together into particles that are significantly larger than 0.1 µm in diameter.

2.3.2.6 Particle Flux Required

The density of the plasma layer can be as high as 10^{14} cm^{-3} for hypersonic vehicles.[16, 57, 11, 21, 34, 42, 43, 54, 55, 56, 80, 64, 68, 67, 75, 73, 74, 17, 105, 47, 108, 65, 113, 32, 22, 49, 58, 71, 30, 10, 102, 77] The cutoff frequency for this density is well above the cutoff frequency for the lowest and most important signal, GPS (1.2 GHz).[57, 43, 73, 47, 108, 65, 113, 46] The required amount of powder required to deplete the plasma can be estimated, and is an important parameter for this study.

The electron density of the plasma layer must be lowered such that the cutoff frequency is below the wave frequency. For a conservative calculation, it is required that the cutoff frequency be 1 GHz or less, corresponding to an electron density of 1.23×10^{10} cm^{-3} or less. Then the number of electrons that need to be collected to reach this density is:

$$n_e' = n_{e0} - n_{e1} \tag{2.28}$$

where n_{e0} is the initial electron number density of the plasma layer, and $n_{e1} = 1.23 \times 10^{10}$ cm^{-3}, the plasma density corresponding to a cutoff frequency of 1 GHz. So n_e' is the number of electrons per cubic centimeter that must be collected by dust particles. The number of electrons collected by each particle is:

$$N_e' = \frac{Q_d}{e} = \frac{4\pi\epsilon_0 r_d V_f}{e} \tag{2.29}$$

Then the dust particle number density required to deplete the plasma electron population can be calculated:

$$n_d = n_e'/N_e' = \frac{(n_{e0} - n_{e1})\, e}{4\pi\epsilon_0 r_d V_f} \tag{2.30}$$

Figure 2.12 shows a plot of the required particle density to deplete an initial plasma layer electron density to allow passage of a 1 GHz communication signal. The plasma

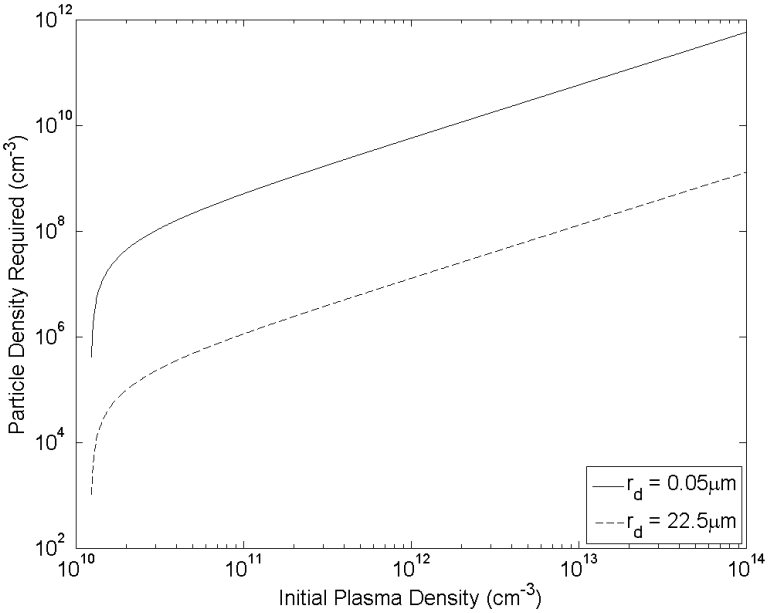

Figure 2.12: The particle density required to deplete the initial plasma layer to a plasma frequency below 1 GHz.

floating potential is assumed to be -5 V, and lines are plotted for both 22.5 µm and 0.05 µm radius particles. The density of powder particles required goes up to 1.27×10^{9} cm^{-3} and 5.76×10^{11} cm^{-3} for particles with radii of 22.5 µm and 0.05 µm, respectively. The plasma must be depleted to *below* the cutoff frequency, so a slightly higher particle density than shown in figure 2.12 is required to allow transmission. Fewer particles are required if the particle is larger, because the particle capacitance increases with particle size, allowing for the collection of more electrons. However, as discussed above, smaller particles may be desired for greater ease of injection and increased number of particles injected. The above calculation takes into account only the net charge collected by each powder particle. However, the electron depletion in a plasma may be enhanced by the surface area of powder particles providing recombination sites. Even after the particle has reached the plasma floating potential, continuous ion and electron currents, given by equation 2.14, are incident on the particle surface. Therefore, ions and electrons may continuously recombine at the particle surface to

create a neutral gas particle, further depleting the electron population. Obviously, this calculation does not take into account recovery of the plasma by further ionizations. However, as the electron density is decreased, ionizing collisions will become less likely due to fewer available electrons to participate in these ionizing collisions.

2.3.2.7 Window Size

The concept being investigated will provide a 'window' through the dense plasma layer that is void of almost all electrons. This window will act as a virtual waveguide, providing a volume extending from the vehicle body to beyond the thickness of the plasma layer that electromagnetic waves will be able to travel through. This window will be responsible for transmitting signals from the spacecraft antenna, as well as receiving signals from ground control. The plasma around the window will be highly conductive, similar to the walls of a metal waveguide. So if it is assumed that all electrons in the window are absorbed then the electric and magnetic fields for waveguide propagation can be derived beginning with Maxwell's equations.[44] The lowest cutoff frequency in a waveguide is in the TE_{10} mode. The lowest frequency for a waveguide with the largest dimension a, is:

$$f_{10} = \frac{c}{2a} \tag{2.31}$$

where f_{10} is the cutoff frequency for the TE_{10} mode, and c is the speed of light. Since one of the most important frequencies for hypersonic vehicles, and the lowest frequency is GPS signals just above 1 GHz, a waveguide is required that can carry 1 GHz or higher frequency waves. Solving equation 2.31 for the waveguide dimension, a, and setting $f_{10} = 1$ GHz, the waveguide dimension must be at least 15 cm. Therefore, the window size must be 15 cm wide in one dimension. While this size scale is larger than that studied herein, it is important to keep this in mind for the

practical application of this method. Also, since some residual electrons may not be collected, and the plasma surrounding the window will have some finite conductivity, the equation may be slightly modified from the ideal vacuum waveguide equation given above.

2.3.3 Previous Plasma Depletion Experiments

Several experiments have been performed in the past that have investigated the effect of powder particles on the plasma electron population.[82, 85, 81, 12] Experiments have reported various levels of plasma electron population depletion, used various particles sizes and powder materials, and have used different methods of powder injection.

One of the first experiments used tungsten oxide (WO_3) particles 3 µm in diameter, ejected by using a shock tube. The shock expelled dust into the plasma that was created by the shock wave. The electron density was reduced by a factor of three according to microwave interferometry measurements.[85] Tungsten oxides of various chemical compositions and sizes were also injected and studied by Madson.[82] In these experiments, the tungsten oxide powder was injected by using a heated oven and gas flow, and microwave interferometry was again used as a diagnostic. Once again, significant electron population depletion was observed. Another study using an oven to heat and inject particles into a plasma discharge reported plasma electron density reduction of approximately 85% using microwave cavity measurements.[12] Kaolin and aluminum oxide powder are used in another study and are dispensed by means of a rotating drum into a quiescent plasma source. The electron density is monitored with a Langmuir probe biased at the electron saturation current, and almost total disappearance of electron current is reported, as seen in figure 2.13.[81].

Past experiments have demonstrated the feasibility of depleting a plasma electron

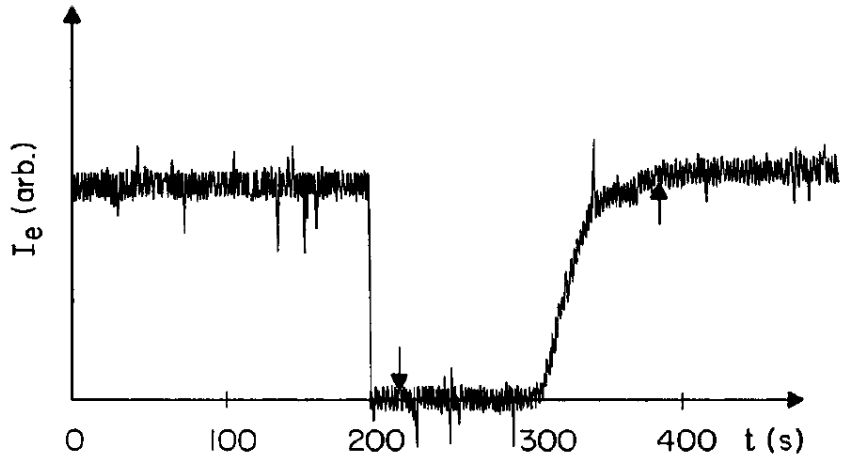

Figure 2.13: The electron saturation current drops upon the introduction of powder to the plasma discharge.[81]

population through the introduction of small powder particles of varying size and material. These observations serve as the basis of this approach where depletion is actively driven through the injection of dielectric particles into a plasma using cathode spots.

CHAPTER III

Vacuum Facilities, Plasma Sources, and Diagnostics

Testing for this work was performed at the University of Michigan in the Plasma Science and Technology Lab (PSTL). The vacuum facilities, associated diagnostics, and devices used for this research are discussed and presented in this chapter.

3.1 Vacuum Facilities

All experiments were performed in vacuum chambers at pressures between 75 and 500 mTorr, with base pressures of 10^{-5} Torr or lower to produce stable, efficient, and low power plasma sources for the overhead plasma. Furthermore, high vacuum systems allowed for more stable cathode spot operation.

3.1.1 GEC Cell

The initial cathode spot characterization phase and the density depletion studies were performed in the Gaseous Electronics Conference(GEC) reference cell, shown in figure 3.1. The GEC cell is a vacuum system that was originally designed to standardize experiments aimed at understanding and developing materials plasma processing techniques.[93] The cylindrical vacuum chamber is approximately 25.1 cm

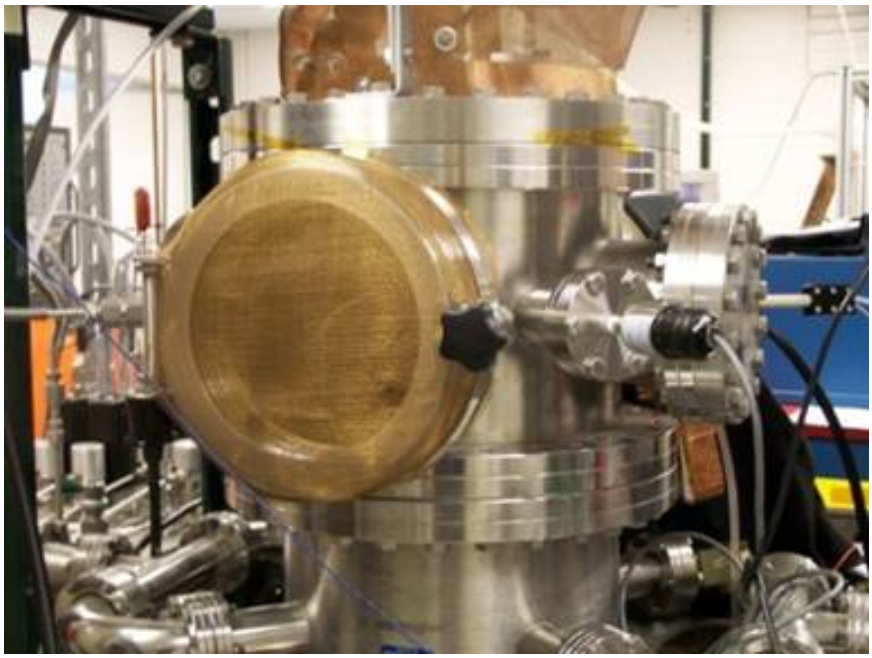

Figure 3.1: The Gaseous Electronic Conference (GEC) vacuum chamber reference cell is shown.

in diameter and 22.2 cm tall.[93] The vacuum chamber is evacuated by an Alcatel 5402CP turbomolecular pump at 400 L/s. This pump is controlled by an Alcatel CFF 450 Turbo controller, and is backed by a Pfeiffer Duo 005M roughing pump that pumps at 1.67 L/s. The roughing pump was directly connected to the chamber to reach roughing pressures before the turbo was turned on. The vacuum system is capable of reaching base pressures of 10^{-6} Torr.

Feedstock gas was input into the vacuum system using an MKS 1179 flow controller which had an upper flow limit of 50 sccm on N_2, or 72.5 sccm on argon. The gas flow rate was read out with an MKS 247C 4-channel readout. Gas was fed into a tube connected to the chamber and allowed to freely diffuse into the chamber volume. A closed-loop throttle valve located upstream of the turbopump allowed for precision control of the gas pressure. The chamber pressure was measured using a Lesker KJL-6000 thermocouple at roughing pressures, and a KJL G075N ion gauge for high vacuum. Both pressure gauges were controlled by a KJL 4500 that provided pressure

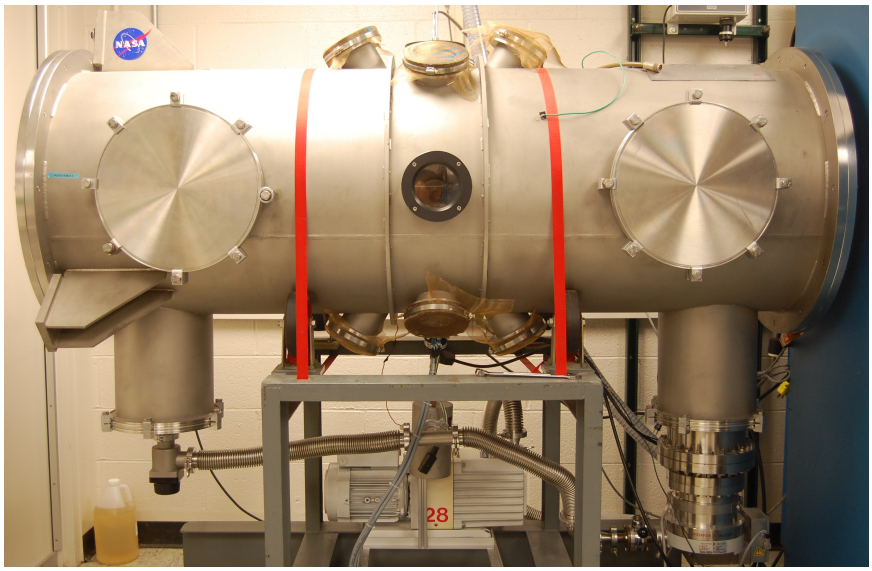

Figure 3.2: The 'Rocket Chamber' vacuum facility.

readout. A closed loop water cooling system featuring a NESLAB Merlin M75 chiller cooled in series both the inductive discharge antenna, discussed in section 3.2.1 (pg. 58), and turbopump.

3.1.2 Rocket Chamber

The vacuum facility dubbed the 'Rocket Chamber' is shown in figure 3.2. This cylindrical chamber is 64 cm in diameter and 190 cm long. The chamber is evacuated with an air-cooled Pfeiffer TMU 521 P turbomolecular pump at 520 L/s on N_2 and backed by an Edwards 28 rotary vane roughing pump. A separate roughing line connected the roughing pump directly to the chamber for evacuation down to about 100 mTorr at almost 11 L/s. Base pressures in the 10^{-7} Torr range were reached with the turbopump before testing began. This vacuum chamber was outfitted with eight 13 cm diameter viewports. The viewports, which provided excellent view factors of the experiment, were utilized in the particle velocimetry measurements presented in chapter V.

Argon gas was fed into the chamber using an MKS Type 1159B flow controller

Figure 3.3: The 'Bessie' vacuum facility.

capable of flowing 50 sccm of N_2, corrected to 72.5 sccm for argon. An MKS Type 246 readout was used to read the flow rate of argon. Pressure in the chamber was measured with a KJL-6000 thermocouple connected to a KJL 205BM readout down to about 10 mTorr. At pressures below 10 mTorr an MKS 943 cold cathode pressure gauge with an I-MAG head was used to readout pressure.

3.1.3 Bessie

The vacuum facility shown in figure 3.3, referred to as 'Bessie', has an inner diameter of 45 cm and height of 62 cm. Mounted on the side of the chamber was a Pfeiffer-Balzers TPU170 turbomolecular pump, controlled by a Pfeiffer-Balzers TCP 121, that would pump at 170 L/s. The turbopump was also backed by a Pfeiffer Duo

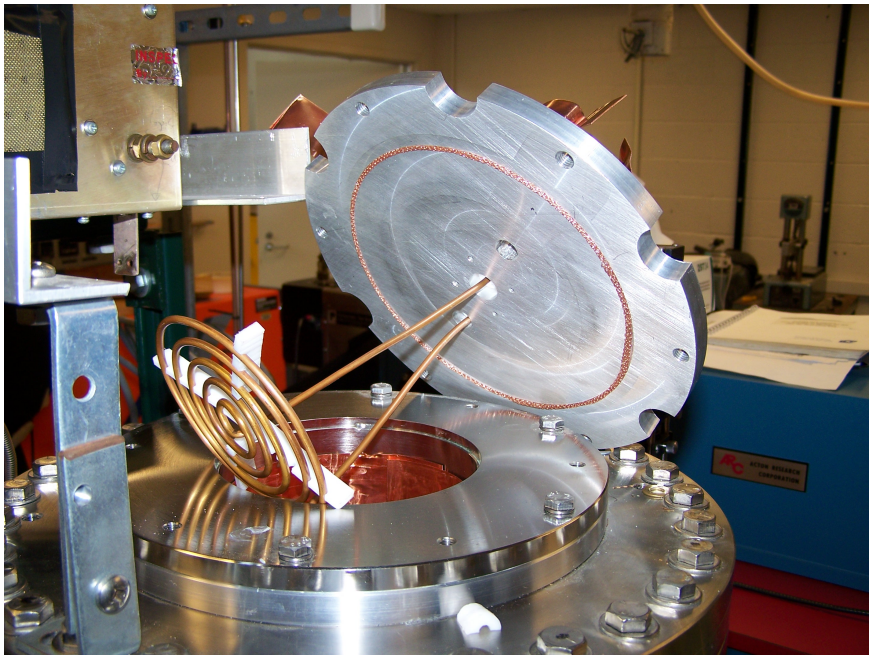

Figure 3.4: The GEC cell RF planar spiral water-cooled antenna is shown.

005M rotary vane roughing pump and cooled by a closed loop water system connected to a NESLAB RTE-111 chiller. Base pressure in this chamber was on the order of 10^{-5} Torr.

Argon gas was supplied to the vacuum system through a gas feed system consisting of a VACOA MV-25 needle leak valve and was measured using an Omega FMA1802 mass flow meter capable of measuring up to 10 sccm of N_2, or 14.5 sccm of argon. Chamber pressure was measured by a KJL-6000 thermocouple and KJL G100F ion gauge, both controlled by a KJL 4500 controller that provided pressure readout.

3.2 Plasma Sources

Each vacuum system had a background plasma discharge source to provide the 'overhead' background plasma for experiments. Those sources are discussed below.

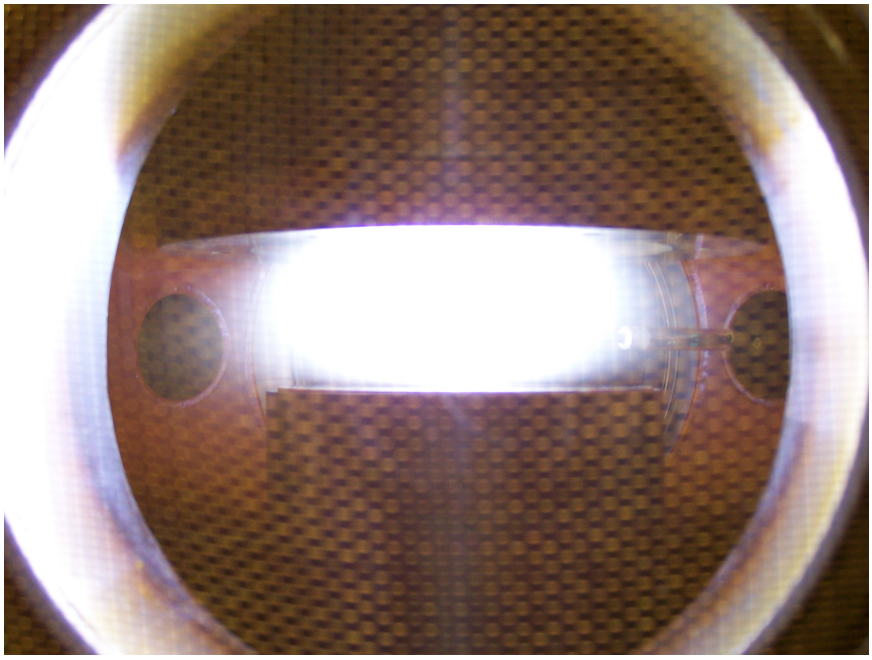

Figure 3.5: The GEC cell operating in the inductive mode on argon gas.

3.2.1 GEC RF Source

The background plasma in the GEC cell was generated using a water-cooled hollow copper tube, 0.32 cm in diameter, formed into a planar spiral coil antenna approximately 10 cm in diameter, shown in figure 3.4. The antenna was mounted on the atmosphere side of a 2.5 cm thick vacuum quartz window. In this manner, RF power is coupled into the main chamber. The antenna was excited using an ENI ACG-5 13.56 MHz, 500 W RF power supply through an ENI MW-5D-01 matching network. The GEC plasma source was capable of producing an RF discharge in the capacitive or inductive mode. Figure 3.5 shows the GEC cell operating in the inductive mode on argon. Plasma densities as high as 10^{12} cm^{-3} were achieved on argon gas. In this work, only the spiral antenna is utilized.

3.2.2 RF Stand-Alone Plasma Source

A 10 cm laboratory model thruster based on the GEC source described above, was built and tested previous to this work. RF power was supplied to the antenna at 13.56

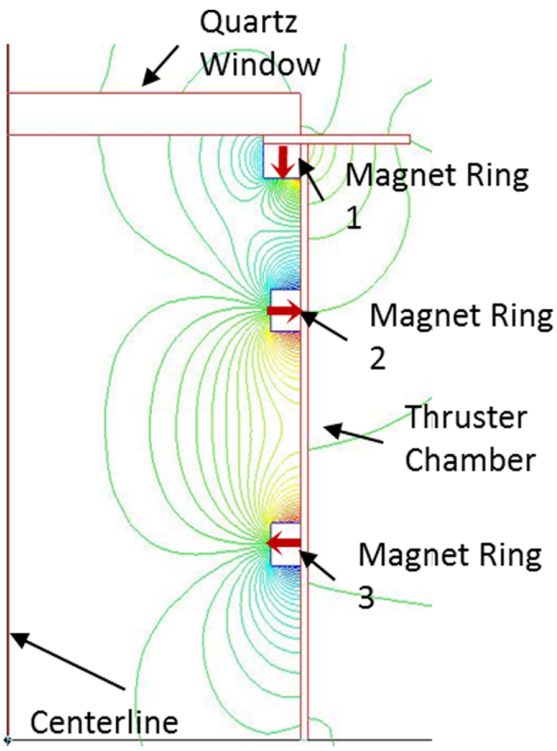

Figure 3.6: The magnetic circuit of the thruster discharge confines the plasma, allowing for more efficient plasma production and operation. The red arrows indicate the direction of magnet polarity.

MHz by a CCA Electronics HFS-1500D, 1500 W RF power supply through a manually operated matching network. In addition to a hollow copper tube spiral antenna, the source can contained three rings of permanent Samarium-Cobalt magnets to aid in plasma confinement for efficient source production. The magnetic circuit for this source is shown in figure 3.6. The thruster design is shown in figure 3.7, and actual tested hardware is shown in figure 3.8. The thruster operating in the inductive mode is shown in figure 3.9. For these tests, the grid was removed to allow the plasma to flow freely out into the vacuum chamber, providing the background plasma for these experiments.

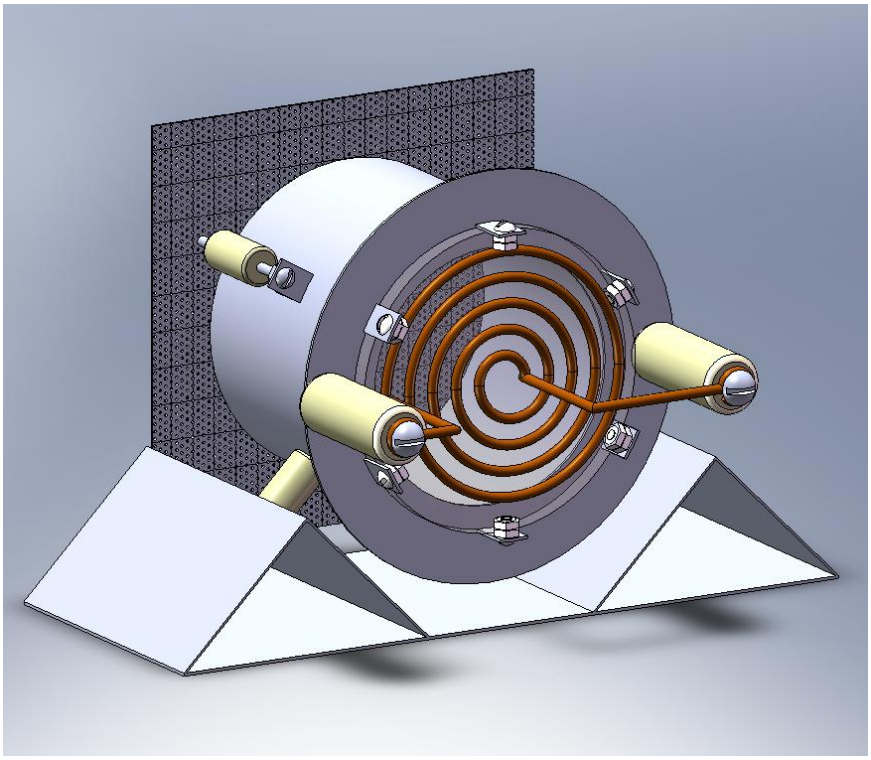

Figure 3.7: The design of the thruster discharge chamber.

3.2.3 Glow Discharge

A glow discharge was initiated in the 'Bessie' vacuum facility using two electrodes, 10 cm in diameter, with the faces polished to a mirror finish. These electrodes are shown in figure 3.10. Figure 3.11 shows the discharge operating on argon at 350 mTorr and 40 mA. The negatively biased cathode electrode surface on the left is partially blocked by a planar Langmuir probe inserted into the positive column region of the discharge to perform diagnostic measurements. The glow discharge was initiated by a Hewlett-Packard 6521A DC power supply capable of providing 1 kV and 200 mA, and was used as the background plasma for experiments.

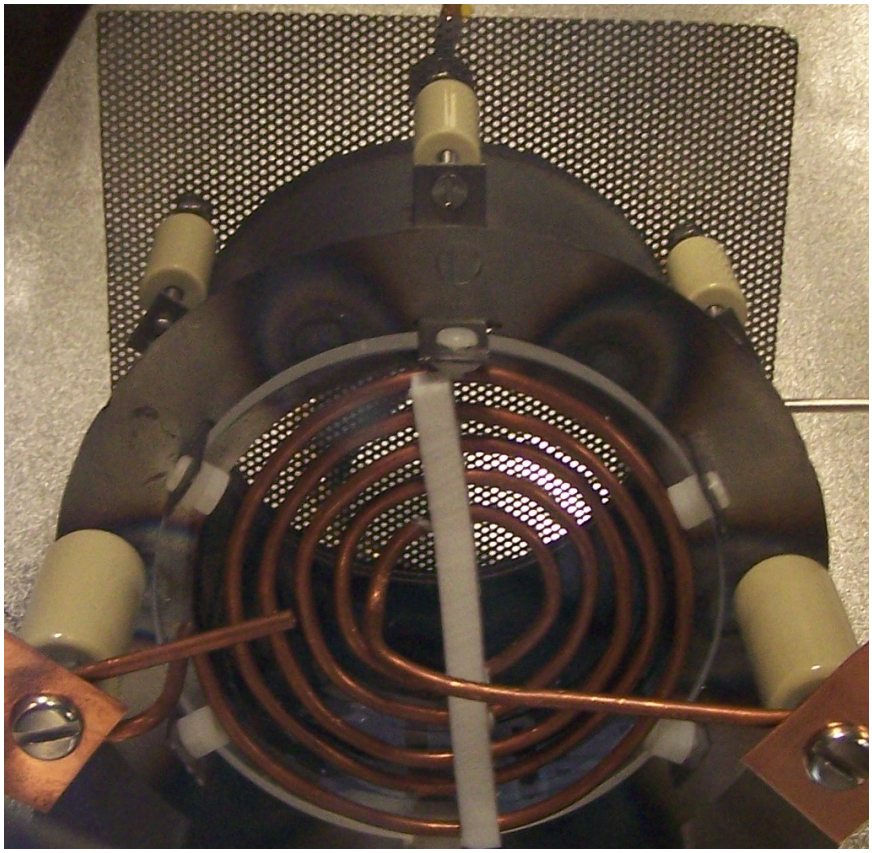

Figure 3.8: The actual thruster hardware after fabrication and assembly.

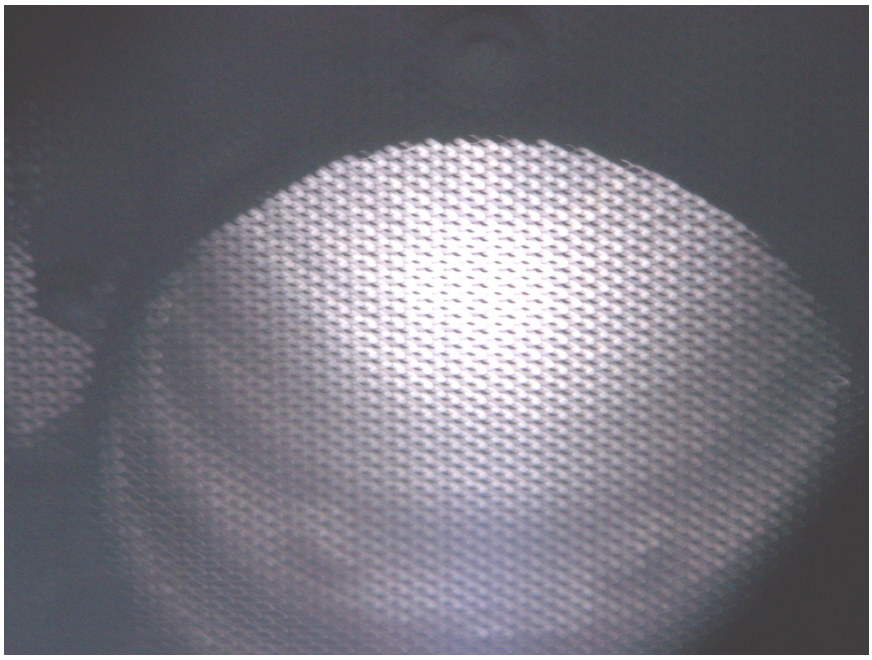

Figure 3.9: The thruster operating in the inductive mode. The grid was removed for these tests to allow plasma to flow out of the chamber.

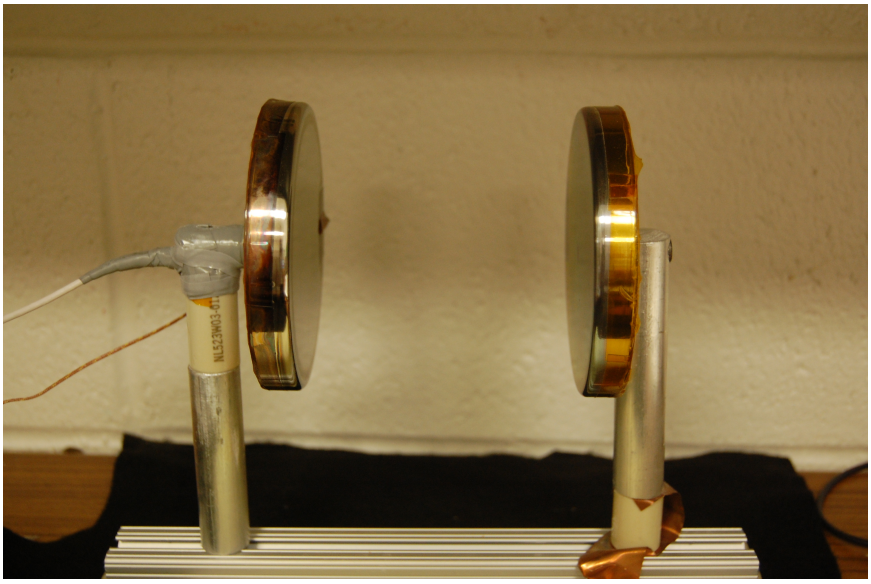

Figure 3.10: Electrodes 10 cm in diameter were used to initiate a glow discharge.

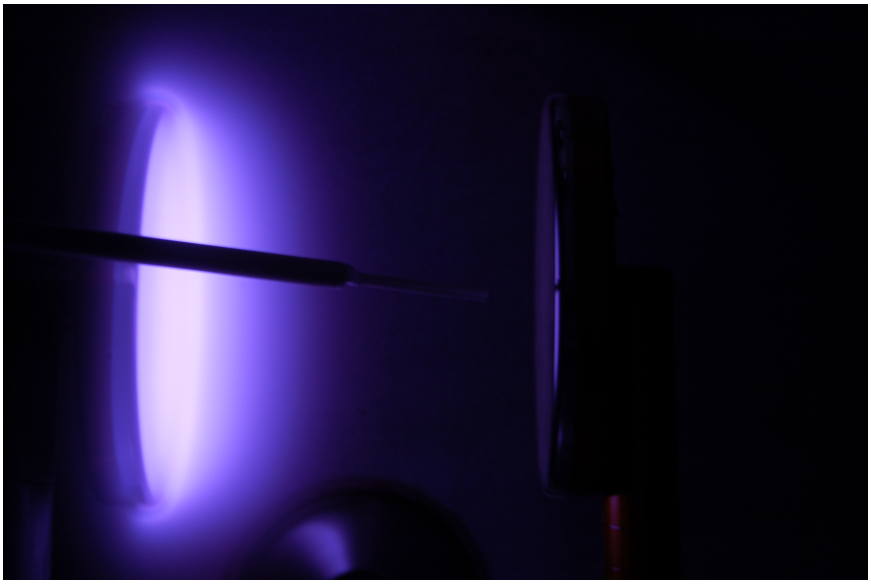

Figure 3.11: The glow discharge operating on argon at 350 mT and 40 mA. A planar Langmuir probe partially blocks the cathode on the left.

3.3 Diagnostics

Several diagnostic instruments were used in this investigation to study and to quantify many cathode spot and background plasma parameters, in particular, changes in background plasma density.

3.3.1 Initial Characterization Diagnostics

A Scientific Systems RF compensated 'Smartprobe' Langmuir probe system was used to measure the GEC cell plasma source parameters. The Smartprobe system consists of a Langmuir probe mounted on a standard 7 cm conflat flange, and the probe is 20 cm long so that the tip was centered in the middle of the GEC cell. The probe also contained electronics and a reference probe to account for the 13.56 MHz oscillations in plasma potential caused by the RF radiation. The reference probe plugged into a filtering box and then both the probe output and filtering box output were connected to the Scientific Systems probe box. This black box was then connected to a PC via RS-232 port. Smartsoft software installed on the PC was the user interface through which the user specified Langmuir probe sweep parameters, initiated Langmuir probe sweeps, and analyzed resulting data. The automated system also allowed for the collection of EEDF's, cleaning of the probe tip, and the analysis of acquired data. The specifics of Langmuir probe analysis can be found in section 3.3.4.2, on page 77.

A Redlake MotionPro HS-4 high frame rate camera was used to image cathode spot jets initiated on the electrode surface. This camera was capable of capturing images at a rate greater than 5000 frames per second at full resolution (512 x 512 pixels), and a rate exceeding 140,000 frames per second at lower resolution (16 x 512 pixels). The software used to control and capture images, Motion Studio, was provided by the manufacturer. The camera was connected to a PC via USB. The software provided a

user interface where the user could set camera settings such as frame rate, exposure time, number of frames captured, and initiate camera acquisition sequences. After images were captured and stored on the camera's internal memory, the Motion Pro software allowed to user to download the captured images. The software also allowed the user to examine and playback captured images in slow-motion for more detailed analysis.

A Tektronix TDS 640A oscilloscope was used for measuring the voltage and current of cathode spots, as well as for diagnostics. The TDS 640A is a 500 MHz scope with a maximum sampling rate of 2 GS/s. The high frequency and high sampling rate was required to resolve the high frequency waveforms associated with cathode spots. This oscilloscope was used with a variety of probes, depending on the measurement requirements. The electrode voltage was monitored using a Tektronix P6015A high voltage probe or Tektronix P5205 High Voltage Differential probe. The P6015A was capable of measuring up to 20 kV. The P5205 was capable of measuring up to 1300 V between leads, up to 1000 V from ground. The P5205 was also used for measuring voltage across a resistor connected in series with the electrode to calculate cathode spot current. For low voltage signals, such as Langmuir probe voltage and current, Tektronix P2220 probes were used. This oscilloscope and associated probes were used for the duration of experiments carried out herein.

3.3.2 Particle Imaging Velocimetry/Tracking Diagnostics

Particle imaging velocimetry (PIV) and particle tracking measurements were performed in the 'Rocket Chamber' vacuum facility, using the RF thruster plasma source. The Redlake high frame rate camera along with an expanded laser beam imaged particles traveling through the overhead plasma discharge after being ejected by a cathode spot arc. A solid state Laserglow Brightline laser (LBD-650-ND-25), providing 25 mW of beam power in the red region of the visible spectrum, along with optics to

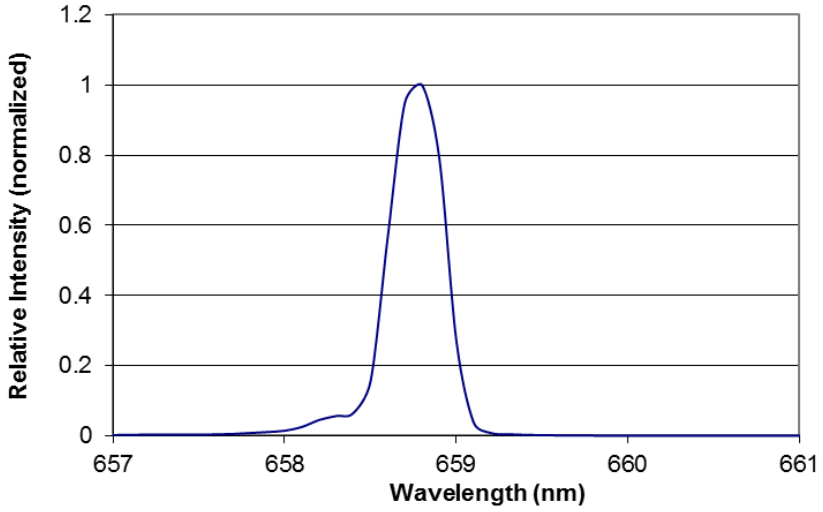

Figure 3.12: The solid state, 25 mW Laserglow Brightline laser output as measured by an Acton Research scanning spectrometer.

expand the laser beam was used to illuminate particles ejected from the electrode surface. The laser was controlled by a 3 V, 500 mA DC power supply. The laser output was centered near 658.8 nm. The laser output is shown in figure 3.12. The laser wavelength determines the minimum size of particles that may be resolved in these measurements. In this diffraction limited case, the smallest particles that can be imaged is approximately half of the wavelength ($\sim$ 325 nm).

The laser and associated beam expanding optics, mounted in the Rocket Chamber are shown in figure 3.13. The laser system was mounted vertically to provide a cylindrical zone of illumination terminating at the surface of the electrode. A narrow optical bandpass filter centered at 656 nm with a full-width half-maximum (FWHM) of 10 nm was used to filter out the all wavelengths with the exception of scattered laser light. Camera and camera lens settings were adjusted to allow for clear observation of ejected powder particles. This required allowing enough light into the camera to clearly observe particles, while minimizing background radiation from the overhead plasma discharge and the broad spectrum of light produced by cathode spot arcs.

An Ocean Optics USB2000 spectrometer was used in conjunction with an optical

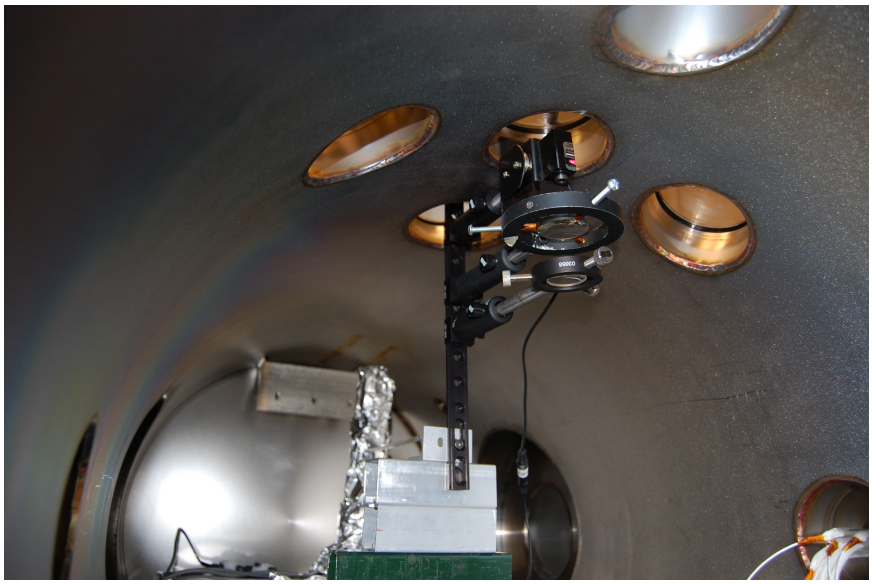

Figure 3.13: A laser combined with beam expanding optics was used to illuminate particles for PIV measurements.

fiber and wide-view lense to analyze cathode spot plume optical emissions. The spectrometer was setup to integrate over large time periods during which many cathode spots were initiated on the electrode surface. While the cathode spot arcs were by far the brightest phenomenon, some light was also collected from the overhead plasma source.

3.3.3 Dust Shaker Device

In order to quantify the mass of dielectric powder required to deplete a background plasma of modest density, a mechanical powder disperser was fabricated. This 'shaker' device was used to drop powder into the plasma discharge at a steady rate. This shaker device, shown in figures 3.14 and 3.15 consisted of a metal cone hopper region that had two vibrating motors attached. These motors produced vibrations that felt similar to a cell phone on vibrate, and were obtained from www.allelectronics.com, part #DCM-382. Monel-wire cloth mesh from McMaster-Carr with opening sizes varying from 74 µm to 279 µm, and around 30% open area, was placed at the bottom

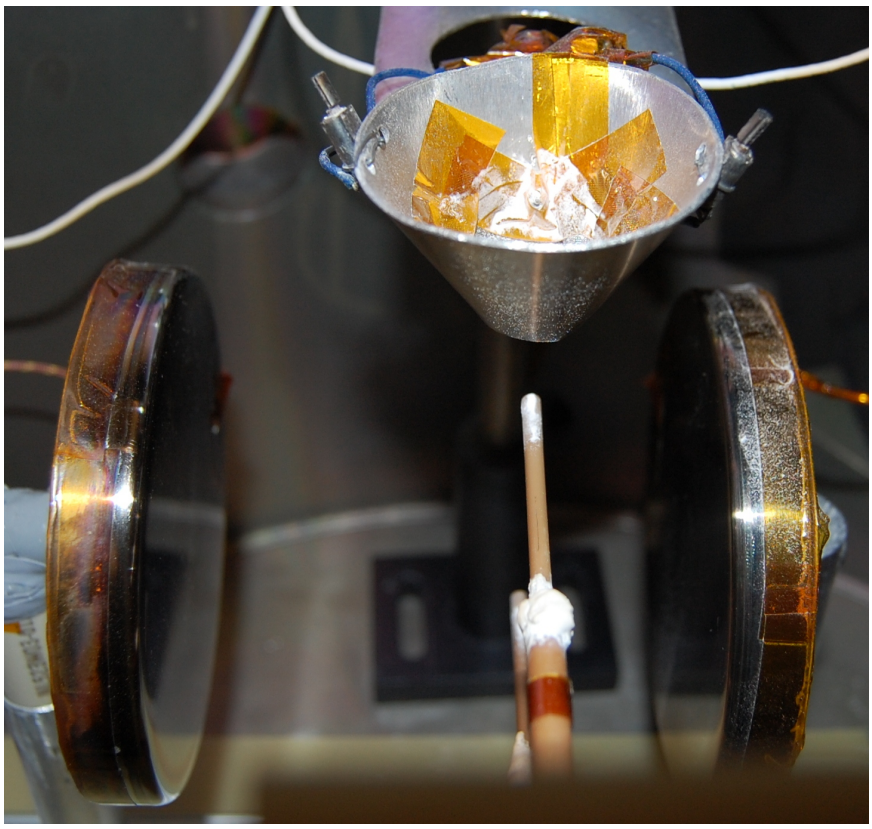

Figure 3.14: The shaker device situated over the Langmuir probes in the positive column region of the glow discharge after a test.

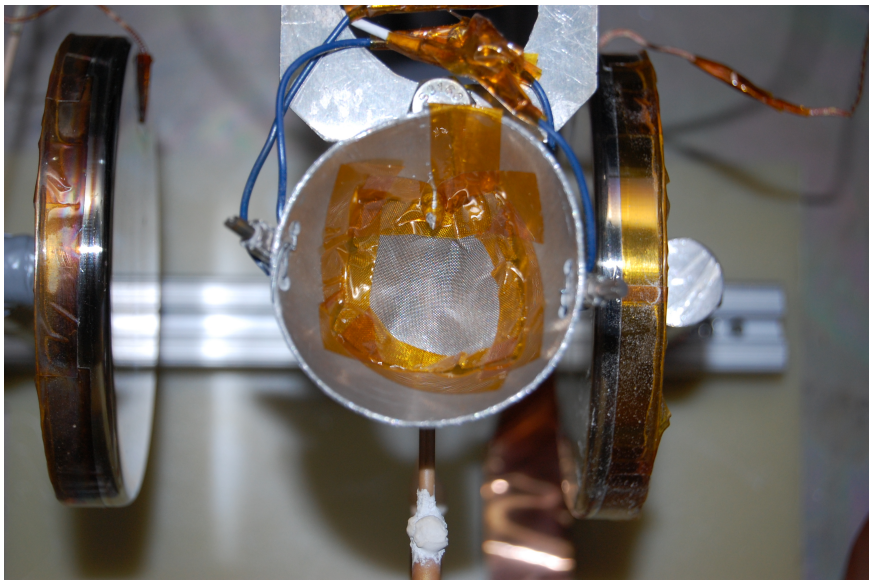

Figure 3.15: The shaker device from above with the vibrating motors and mesh at the bottom of the hopper to control powder dispersion.

opening of the cone hopper. This mesh controlled the rate of release of 45 µm size powder particles from the shaker opening at the bottom of the cone hopper. When the vibrating motors were actuated, the powder in the hopper shifted and resulted in powder falling from the shaker device into the discharge at a relatively fixed rate. The voltage to the motors was varied to increase or decrease the intensity of vibration, along with mesh opening size, and therefore vary the rate of powder dropped from the shaker device. Two planar Langmuir probes were used to measure the glow discharge electron density as a function of time before, during, and after the powder was dropped into the discharge. Langmuir probe theory is discussed in depth in section 3.3.4.2.

3.3.4 Cathode Spot Ejection Density Depletion Diagnostics

The final phase of study for this dissertation consisted of measuring the extent of electron population depletion in an overhead plasma via cathode spot arc injection of powder. One challenging aspect of this study was that of finding a suitable diagnostic– capable of measuring electron density in a plasma discharge with very fine time and spatial resolution. The spatial and time resolution required was estimated to be on the order of 1 cm and a few milliseconds, respectively, based on the size of cathode spot plumes and cathode spot particle time-of-flight measurements. Several diagnostics were considered including triple probes, microwave interferometry, and microwave cutoff frequency measurements. While triple probes provide great time resolution, the ion saturation current is collected, yielding the ion density, from which quasi-neutrality is assumed. In these experiments, quasi-neutrality is maintained by the negative charge collected on the dielectric particles, but the electron density is not directly measured with a triple probe. Concerns regarding the spatial resolution of microwave interferometry and microwave cutoff frequency measurements might have been overcome with precisely positioned and closely spaced antennas, however, the

time resolution for these measurements was limited with the available equipment. However, the hairpin resonance probe and Langmuir probe were chosen and used in experiments discussed in chapter VI.

3.3.4.1 Hairpin Resonance Probe Diagnostic

A hairpin resonance probe is a resonant structure that can be used as a plasma diagnostic for measuring plasma electron density. The hairpin resonance probe was first developed by Stenzel in 1976.[115] These probes are provided with a signal of varying frequency, and the probe response is measured. When the probe is provided with a particular frequency signal, known as the resonant frequency, a standing wave is initiated in the probe tip. At this frequency, the hairpin probe acts similar to a quarter wavelength antenna, with the electric field from the probe having a negligible effect on the surrounding plasma.[96, 106] The probe is shaped like the letter 'U', with one end of the probe shorted, and the other end open. When resonating, the voltage minimum is located at the shorted end, and the oscillating voltage maximum is located at the open end. The minimal interaction between the electrical signal and surrounding medium will affect the hairpin probe resonant frequency, dependent on the relative dielectric constant of the medium.

There are two main methods commonly used to couple a high frequency signal to a hairpin resonance probe tip. The directly coupled hairpin resonance probe is directly connected to the signal source and is the easiest to implement because it provides the strongest signal response. However, this method is difficult for use in an RF plasma where the sheath voltage will vary with the RF plasma potential in the same way that Langmuir probe signals are affected by variations in RF plasma potential.[106] Therefore, a method of coupling known as inductive coupling is shown schematically in figure 3.16, and is used in these experimental efforts. In the inductively coupled case, a small loop directly connected to the varying signal source couples the varying

frequency signal through electromagnetic induction into the 'U'-shaped hairpin section of the probe. Since the hairpin section of the probe is no longer directly connected to ground, the hairpin is allowed to float with the plasma potential, creating a time constant sheath voltage and capacitance, therefore reducing measurement error, and mitigating the challenges commonly associated with many RF plasma diagnostics.

Hairpin resonance probes can be operated in the transmission mode or reflection mode.[96, 106] In the transmission mode, a variable frequency signal is sent to the hairpin probe, and a receiving device placed nearby the hairpin probe detects the transmitted signal. However, this process is dependent on the receiving device proximity to the hairpin probe, as well as the fidelity of the receiving device and associated return signal hardware. For these reasons, the reflection mode of operation is used herein. In this operation mode, a signal of varying frequency is sent to the hairpin resonance probe, and the minimum of reflected power as a function of signal frequency is measured to find the probe resonant frequency.

A Hewlett-Packard 8753E Network Analyzer, with a frequency range up to 6 GHz is employed to supply the frequency varying signal to the hairpin probe. The network analyzer is also used to measure the reflected power and probe response, yielding the hairpin probe's resonant frequency.

The hairpin resonance probe is similar to a parallel wire transmission line antenna with one end shorted, and the other end open.[115, 106] The resonant frequency of the basic mode is determined by the physical dimensions of the probe:[106]

$$f_r = \frac{c}{2\left(2\ell + w\right)\sqrt{\epsilon}} \tag{3.1}$$

where f_r is the resonant frequency of the hairpin probe, c is the speed of light, ℓ is the length of the probe, w is the width of the probe, and ϵ is the relative dielectric constant of the surrounding medium. In vacuum, $\epsilon = 1$. In the limit of a long and

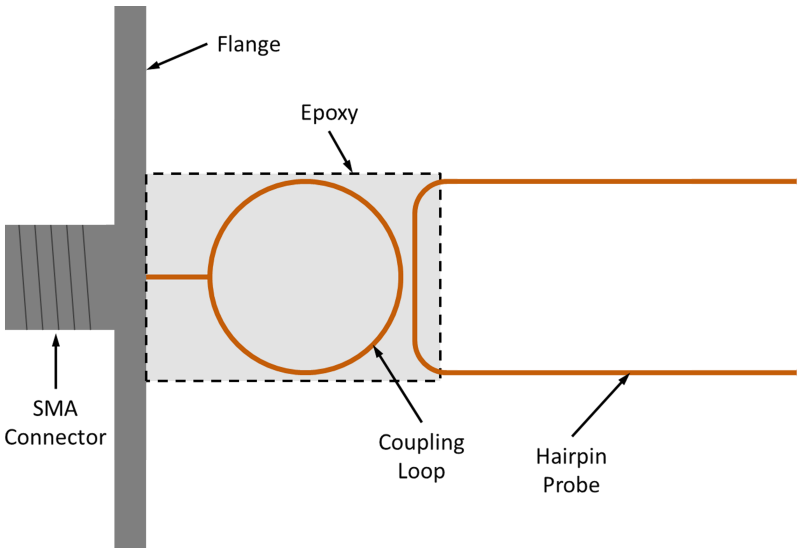

Figure 3.16: A schematic of an inductively coupled hairpin resonance probe.

narrow hairpin resonance probe, this equation reduces to:[115, 96, 74]

$$f_r = \frac{c}{4\ell\sqrt{\epsilon}} \tag{3.2}$$

where the width of the probe is dropped due to the insignificance compared to the probe length in a long and narrow hairpin resonance probe. For the case here, the more precise equation, equation 3.1, will be used.

At high pressure, where electron-neutral collisions are important, the dielectric constant of a plasma is:[106]

$$\epsilon = 1 - \frac{f_p^2}{f\left(f - i\frac{\nu_{en}}{2\pi}\right)} \tag{3.3}$$

where ν_{en} is the electron-neutral collision frequency, and $f_p = \sqrt{n_e e^2/\pi m_e}$ is the plasma frequency. In the work performed here, the plasma can be assumed to be collisionless, so the dielectric constant becomes:[106, 96]

$$\epsilon = 1 - \frac{f_p^2}{f^2} \tag{3.4}$$

and is valid when $f > f_p$. Then the frequency components can be related by:[106, 96, 115]

$$f_r^2 = f_0^2 + f_p^2 \tag{3.5}$$

where f_r is the resonant frequency of the hairpin probe in the presence of a medium, and f_0 is the resonant frequency of the probe in vacuum. Then this equation can be solved for the electron density:

$$n_e = \frac{f_r^2 - f_0^2}{8978^2} \tag{3.6}$$

where n_e is the electron density in cm^{-3}, and f_r and f_0 are in Hz.

However, in the above derivation, the plasma sheath that forms around the hairpin resonance probe has not been accounted for. Although the voltage across the sheath, and therefore sheath size, is constant due to the inductively coupled construction of the probe, the sheath volume has relatively few electrons compared to the bulk plasma. Therefore, if the sheath around the hairpin probe constitutes a significant portion of the volume between the probe tips, then the probe will significantly underestimate the actual electron density. To correct for this, equation 3.5 can be rewritten as:[106, 96]

$$f_r^2 = f_0^2 + \varsigma_s f_p^{'2} \tag{3.7}$$

where $f_p^{'}$ is the corrected plasma frequency, and ς_s is the sheath correction factor, the ratio of $f_p^2/f_p^{'2}$. The correction factor is derived by assuming the sheath to be a cylindrical volume around each arm of the hairpin probe, extending with radius of r_{sh}, with a dielectric constant of unity. The sheath is assumed to be totally void of electrons ($\epsilon = 1$), and the plasma between the sheaths to have a dielectric constant ϵ_p. In actuality, the dielectric constant for the sheath volume will be slightly below unity since some electrons are present in the sheath volume unless the floating potential is several times greater than the electron temperature. However, to maintain a reasonably simple calculation for the correction factor, the dielectric constant within

the sheath is assumed to be unity. The resulting electron density calculated will be the upper limit of the electron density. Then treating the resonance probe as a transmission line model, and following the derivation of Piejak [96], the capacitance per unit length in cgs is:[106, 96]

$$C_1 = \frac{\epsilon_p}{4\left(ln\left(\frac{w}{r_{sh}}\right) + \epsilon_p ln\left(\frac{r_{sh}}{r_{wire}}\right)\right)} \tag{3.8}$$

where r_{sh} is the plasma sheath radius and r_{wire} is the radius of the hairpin resonance probe wire. Then effective capacitance per unit length is:

$$C_1^{eff} = \frac{\epsilon}{4ln\left(\frac{w}{r_{wire}}\right)} \tag{3.9}$$

Using equations 3.8 and 3.9 with equation 3.4, and assuming that the hairpin width is much larger than the wire and sheath radii, the sheath correction factor is:[106, 96]

$$\varsigma_s = 1 - \frac{f_0^2}{f_r^2}\frac{ln\left(\frac{r_{sh}}{r_{wire}}\right)}{ln\left(\frac{w}{r_{wire}}\right)} \tag{3.10}$$

Since in this study, the sheath and wire radius are less than a third of the hairpin probe width for all cases, the above expression is valid for the sheath correction factor. In this case, the sheath extends to a radius r_{sh}, which is defined as $r_{sh} = r_{wire} + \lambda_D$, where λ_D is the Debye length. However, since λ_D and the sheath correction factor are both a function of density, the equations that depend on density (equations 3.10 and 3.11) must be solved iteratively to find an appropriate sheath correction factor.

$$n_e = \frac{f_r^2 - f_0^2}{\varsigma_s 8978^2} \tag{3.11}$$

The above derivation is valid even in a magnetic field, as long as $\omega_p^2 \gg \omega_c^2$ or the

resonance frequency, $\omega_r^2 \gg \omega_c^2$ (according to Stenzel):[115]

$$\epsilon_\perp = 1 - \frac{\omega_p^2}{(\omega^2 - \omega_c^2)} \approx 1 - \frac{\omega_p^2}{\omega^2} = \epsilon_\parallel \tag{3.12}$$

where $\epsilon_\perp$ and $\epsilon_\parallel$ are the dielectric constants in the directions perpendicular and parallel to the probe tips, and ω_c is the cyclotron frequency of electrons. Others have also stated that as long as $\omega_r \gg \omega_c$, then the magnetic field effects are negligible and can be neglected.[63] Also, if the probe resonance wavelength is much longer than the probe width, then the magnetic field will have a negligible effect. Karkari also argues that regardless of the cyclotron frequency, if the propagation vector of the resonance probe is parallel to the magnetic field, then, since the dispersion relation for ordinary waves is unchanged from a non-magnetized wave in plasma, the applied magnetic field has no effect.[63] Still others have shown that for a system with a cyclotron frequency greater than 3.5×10^{10} rad/s and plasma frequency of less than 5.70×10^9 rad/s, that the dielectric constant is approximately equal to unity above ~ 1.5 GHz.[74]

In our experiments, the magnetic field was near 300 Gauss at the hairpin resonance probe location, resulting in a cyclotron frequency of 5.28×10^9 rad/s. Our hairpin probe resonates near 1.85 GHz, or 1.16×10^{10} rad/s. Therefore, according to Stenzel and Karkari, the plasma density should be greater than approximately 7.9×10^{10} cm^{-3} for magnetic field effects to be negligible, which is not the case for all plasmas investigated here.[115, 63] According to Lemmer, however, the magnetic field can be neglected in all instances for our case since the resonant frequency is several GHz, and the magnetic field is only 300 G. Since our probe is not oriented directly parallel to the magnetic field lines, and opinions contradict as to whether or not the magnetic field can be neglected for our case, an additional correction factor for magnetic field effects is taken into account:

$$f_r^2 = f_0^2 + \varsigma_B \varsigma_s f_p'^2 \tag{3.13}$$

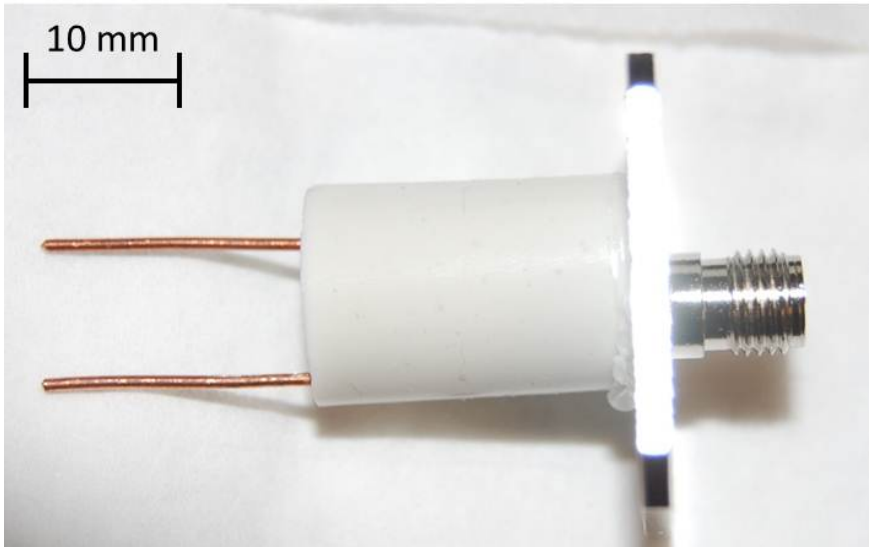

Figure 3.17: An inductively coupled hairpin resonance probe mounted on an SMA flange.

where ς_B is the correction factor for the magnetic field effects, and is:[36]

$$\varsigma_B = \left(1 - \frac{f_{ce}^2}{f_r^2}\right)^{-1} \tag{3.14}$$

where f_{ce} is the electron cyclotron frequency. Then the equation for density, including both magnetic field and sheath effects can be written as:

$$n_e = \frac{f_r^2 - f_0^2}{\varsigma_B \varsigma_s 8978^2} \tag{3.15}$$

The magnetic correction factor for these studies is ~ 1.25, and is taken into account for all calculations. If this correction factor were neglected, the electron density would be overestimated.

An inductively coupled hairpin resonance probe, shown in figure 3.17, was built for use in these experiments. The coupling loop and hairpin portion of the probe were epoxied together in Dow-Corning Silastic J RTV Silicone epoxy. This epoxy has a dielectric constant of 2.94 at 100 Hz and 2.79 at 100 kHz. The dielectric properties of the epoxy provided greater coupling between the loop and hairpin after the epoxy

containing the loop and hairpin is set. The coupling loop was soldered to the open end of an SMA flange, and the hairpin probe was positioned relative to the coupling loop before the molding fixture was filled with epoxy. The coupling loop and hairpin probe were fashioned from copper wire, 0.81 mm in diameter, because copper wire was readily available, has high conductivity, and has been shown to provide superior frequency response.[106] The hairpin probe was 15.4 mm long and 7.4 mm wide. Since the probe width is almost half of the length, equation 3.1 is used to find the the expected probe resonance in vacuum, 3.92GHz.

Although the hairpin resonance probe used in these experiment was expected to resonate near 4 GHz, the probe actually resonated near 1.85 GHz. There are several possible reasons to explain this discrepancy. The hairpin resonance probe is located inside of the vacuum chamber, so the high frequency signal must go through a vacuum feedthrough. So the cable is connected to an adapter, connected to one side of the vacuum flange, then connected through another adapter and cable to the other side of the vacuum flange. Furthermore, the other end of the cable is then connected to the probe flange. The hairpin probe also in the immediate vicinity of a magnetic field, a large metal disc (the electrode), and an RF antenna. Furthermore, Sands [106] discusses the many difficulties associated with manufacturing the probes, noting that nicks and scratches on the metal surface can significantly affect probe response. Copper was used for this probe because it was readily available and had a high conductivity. However, copper is also more susceptible to nicks, scratches, and surface contamination. Finally, the hairpin probe is inductively coupled to the network analyzer system. The location of the hairpin section of the probe with respect to the coupling loop affected the frequency at which the hairpin resonated. The hairpin and coupling loop were held in place when epoxied together, but there may have been a slight shift as the epoxy was applied and dried. However, before used for testing the hairpin probe electron density measurements are compared to Langmuir

probe measurements, a proven diagnostic, to ensure measurement accuracy.

3.3.4.2 Langmuir Probe Diagnostics

Langmuir probes are one of the most commonly used plasma diagnostics in existence, and was proposed and used by Langmuir as early as 1926.[88] A Langmuir probe typically consists of either a planar or cylindrical metal conductor which is exposed to the plasma environment for the purpose of charged particle collection. By varying the probe bias and recording the response–the collected current–an I-V characteristic is obtained. From this curve, plasma parameters such as potential, temperature, and density can be made, provided some assumption is made regarding the electron energy distribution function.

Analysis of the IV characteristic is greatly simplified if certain plasma conditions prevail. First, the sheath that forms around the probe must be collisionless. That is, particles that enter the sheath will not undergo a collision with another particle before contacting the probe surface. The electron population is Maxwellian in nature. It is implicitly assumed that the probe does not significantly disturb the plasma discharge beyond the sheath. Furthermore, if the probe is immersed in a magnetized plasma, depending on the probe orientation, particle flux to the surface may be significantly impeded such that further considerations must be taken into account.[116]

There are two methods of analysis for cylindrical probes that depend on the probe and plasma dimensions. If the probe diameter is significantly larger than the Debye length ($r_p/\lambda_D \gg 1$), then the thin-sheath method of analysis is valid, and cylindrical probes can be treated as planar probes. However, if the probe diameter is much smaller than the Debye length ($r_p/\lambda_D \ll 1$), then the equations must be modified to account for Orbital Motion Limited (OML) analysis. In OML conditions, not all particles that enter the sheath will be collected at the probe surface, some particles may enter the sheath, but exit along parabolic or hyperbolic trajectories. The col-

$\mathbf{T}_e$ **(eV)**	$\mathbf{n}_e$ **(cm^{-3})**	λ_D **(mm)**	r_p/λ_D	
			$r_p = 0.23mm$	$r_p = 0.19mm$
2	3×10^8	0.61	0.38	0.31
2.7	2.5×10^8	0.77	0.30	0.25
5	2×10^7	3.7	0.06	0.05
1.5	1.5×10^{10}	0.074	3.09	2.56
1	3×10^{10}	0.04	5.36	4.43

Table 3.1: Debye length scaling with typical plasma parameters and associated probe parameters.

lected current depends on particle initial angular momentum and energy. The current typically takes on a square root of the voltage dependence. Between thin sheath and OML, Laframboise has expanded the analysis equations in terms of the ratio of probe radius to Debye length, allowing for a range of ratios to be properly analyzed.[69] For the probe data obtained herein, the commercial Smartprobe wire radius is 0.19 mm, and the lab fabricated probe wire radius is 0.23 mm. The ratio of probe radius to Debye length for plasma parameters typical for the studies herein, shown in table 3.1, ranges from 0.05 to 5.36. The thin-sheath method is altered, taking into account OML theory when necessary, but the thin-sheath method is valid in many cases.

Figure 3.18 shows a typical Langmuir probe trace, denoting the regions and points of particular interest. The total current collected by the probe is the sum of the ion and electron current:

$$I = I_{i^+} + I_e \tag{3.16}$$

where I_{i^+} is negative by convention and is the ion current, and I_e is the electron current and is positive. In the ion saturation region, the probe is biased sufficiently negative relative to the plasma potential so that most electrons are repelled, and only ions are collected. This ion saturation current is:[78, 118]

$$I_{s,i^+} = -en_s u_B A_p \tag{3.17}$$

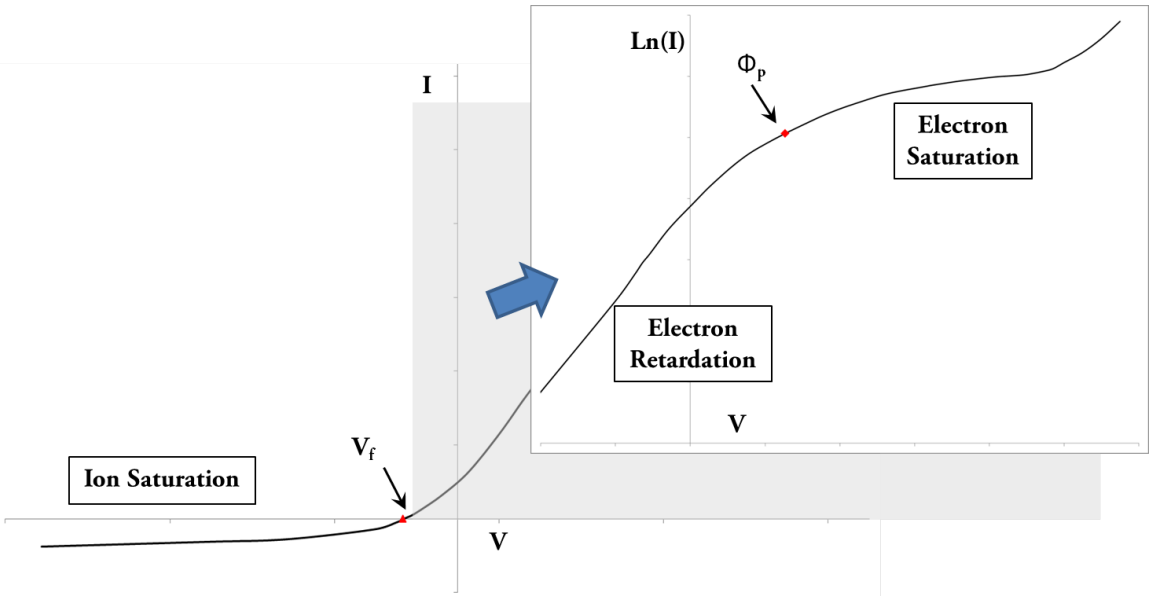

Figure 3.18: A typical Langmuir probe IV characteristic, with each region of interest labeled. The inset shows the natural log of current plotted.

where n_s is the ion density at the sheath edge, u_B is the ion Bohm velocity, and A_p is the probe surface area. The bulk plasma density beyond the presheath region can then be found using the Boltzmann relation, and the ion saturation current becomes:

$$I_{s,i^+} = -0.61 e n_i A_p \sqrt{\frac{k_B T_e}{M_i}} \tag{3.18}$$

where n_i is the bulk ion density, T_e is the electron temperature, and M_i is the ion mass. The ion saturation current is collected by the probe until the probe is biased positive relative to the plasma potential, at which point the ion current is only a very small portion of the total current.

As the probe voltage is raised, the probe begins collecting electron current in addition to the ion saturation current. So the electron current is the total current plus the magnitude of the ion current.[78, 118]

$$I + |I_{s,i^+}| = I_{e^-} = \frac{1}{4} e n_e A_p \sqrt{\frac{8 k_B T_e}{\pi m_e}} \exp\left(\frac{-e\left(\Phi_p - V\right)}{k_B T_e}\right) \tag{3.19}$$

The point where the ion and electron current to the probe is equal is called the floating potential, V_f. Since the electrons are significantly less massive than the ions, and tend to be warmer, the electron current is significantly higher than the ion current. The electron current reaches saturation at the plasma potential, Φ_p. The plasma potential is usually identified as the 'knee' in the curve, or the point where the curvature becomes negative (where $d^2I/dV^2 = 0$) and the sheath vanishes. This point on the IV curve is shown in figure 3.18. The electron saturation current is:

$$I_{s,e^-} = \frac{1}{4} e n_e A_p \sqrt{\frac{8 k_B T_e}{\pi m_e}} \tag{3.20}$$

Biasing the probe beyond the plasma potential drives the probe further into the saturation region. Because the sheath tends to expand with increasing bias voltage, the current also increases and thus, the current does not actually saturate. Owing to the increased current collection at bias voltages above the plasma potential, the probe tends to perturb the plasma discharge.

Once a simple Langmuir probe sweep has been acquired, the ion and electron density, electron temperature, plasma floating potential, and plasma potential can be found. The floating and plasma potential can be found as described above. The slope of the current between about the floating potential and the plasma potential reveals the electron temperature:[78, 118]

$$ln\left(\frac{I_e}{I_{s,e^-}}\right) = \frac{-e\left(\Phi_p - V\right)}{k_B T_e} \tag{3.21}$$

So by fitting a line to the slope of the natural log of the electron current, the electron temperature can be found ($T_e = e/\left(k_B * slope\right)$). Then the ion and electron saturation current equations (3.18 and 3.20) can be solved for the ion and electron densities:

$$n_i = \frac{I_{s,i^+}}{0.61 e A_p} \sqrt{\frac{M_i}{k_B T_e}} \tag{3.22}$$

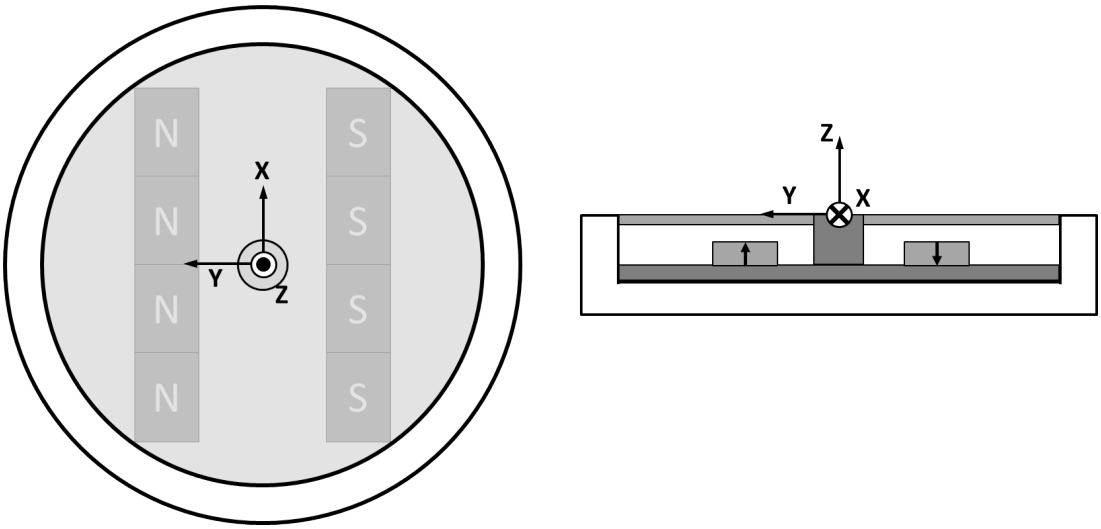

Figure 3.19: A schematic of the electrode used to initiate cathode spots, with an overhead view (left) and side view (right), and associated axes definitions.

$$n_e = \frac{4I_{s,e^-}}{eA_p}\sqrt{\frac{\pi m_e}{8k_B T_e}} \tag{3.23}$$

Langmuir probes are employed for a variety of the experiments performed herein, in various capacities, depending on the application.

3.4 Cathode Spot Electrode

The electrode on which cathode spots were ignited was the heart of most experiments performed in this work. While this device was fairly straightforward, it is necessary to discuss the specifications of this device.

3.4.1 Dimensions and Materials

A scaled schematic of the electrode on which cathode spots were ignited is shown in figure 3.19. Also shown are the axes definitions used for the remainder of this work. Notice that the x-axis is along the magnet rows, while the y-axis is across the magnet rows, and the z-axis is the vertical direction. The origin is at the very center of the electrode.

The top electrode is a non-magnetic steel disk, 8.9 cm in diameter. A set screw 1 cm in diameter in the center of the top electrode holds the electrode in position. This set screw is attached to the bottom of a magnetic steel disk, also 8.9 cm in diameter. The gap between these disks is just large enough to fit two rows of samarium-cobalt magnets. These magnet rows consist of four magnets each, aligned end-to-end, with the left row having all four magnets with the north pole facing up, and all four magnets in the right row with the south pole facing up. The magnet rows were attached magnetically to the bottom disk. The magnet rows were approximately 7.2 cm long. The inside of the magnet rows are separated by 1.75 cm. They were pushed as far away from each other as possible while remaining parallel and within the diameter of the electrode. This entire two-disk assembly was set inside of a machined mica cup, 2 cm tall and 10.4 cm in outside diameter. The inside of the cup was approximately 1.25 cm deep, just deep enough to house the two-disk assembly. The mica cup allowed the electrode to be electrically isolated from the surrounding chamber. A small hole (not pictured in figure 3.19), was drilled into the side of the mica cup. A wire carrying the high voltage signal was fed through the hole and attached to the two-disk assembly. In some cases, a small alumina rod of known diameter was placed in the center of the electrode to provide a size scaling when using the high frame rate camera. An image of the actual device is shown in figure 3.20.

3.4.2 Power Supplies and Pulsers

In order to initiate cathode spots on the surface of the electrode, a high voltage power supply was required. For many experiments, the Hewlett-Packard 6521A power supply, capable of supplying up to 1 kV and 200 mA of current was used. In the last phase of experiments, precise timing and control of cathode spot ignition and extinction was required, therefore a high frequency pulser was used. The pulser was a Velonex 350, with a V-1097 plug-in module capable of supplying up to 4 kV of

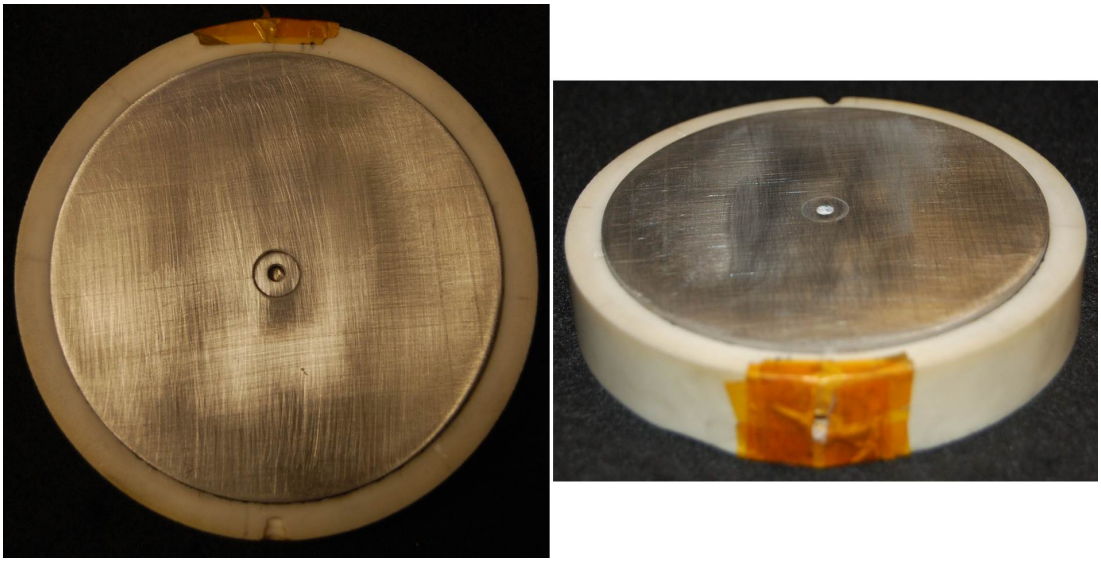

Figure 3.20: An actual image of the electrode used to initiate cathode spots. An overhead view on the left, and a side view on the right.

voltage and over an amp of current. The pulser is capable of producing voltage pulse widths down to 100 ns and repetition rates up to 100 kHz. The pulser outputs a negative voltage pulse (required to initiate cathode spots), and had a rise time of approximately 50 ns. The pulse width was variable up to about 300 µs. A voltage pulse from the Velonex pulser is shown in figure 3.21.

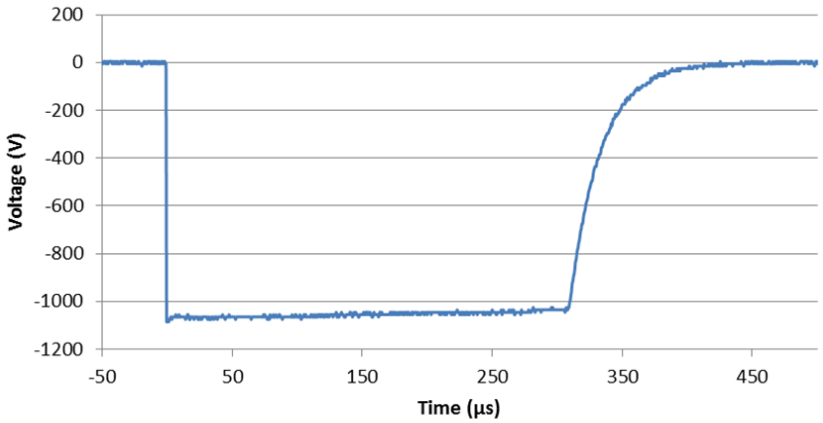

Figure 3.21: A typical voltage pulse supplied by a Velonex 350 pulser.

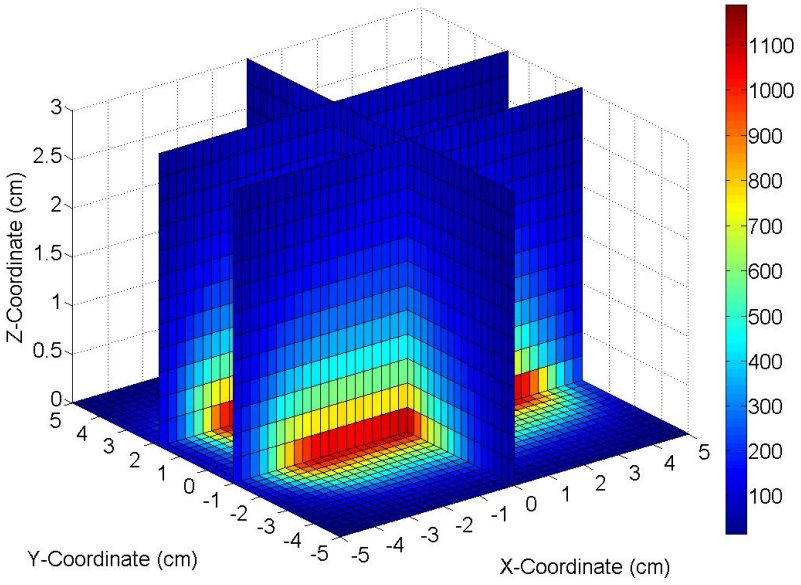

Figure 3.22: A three-dimensional plot of magnetic flux magnitude (in Gauss).

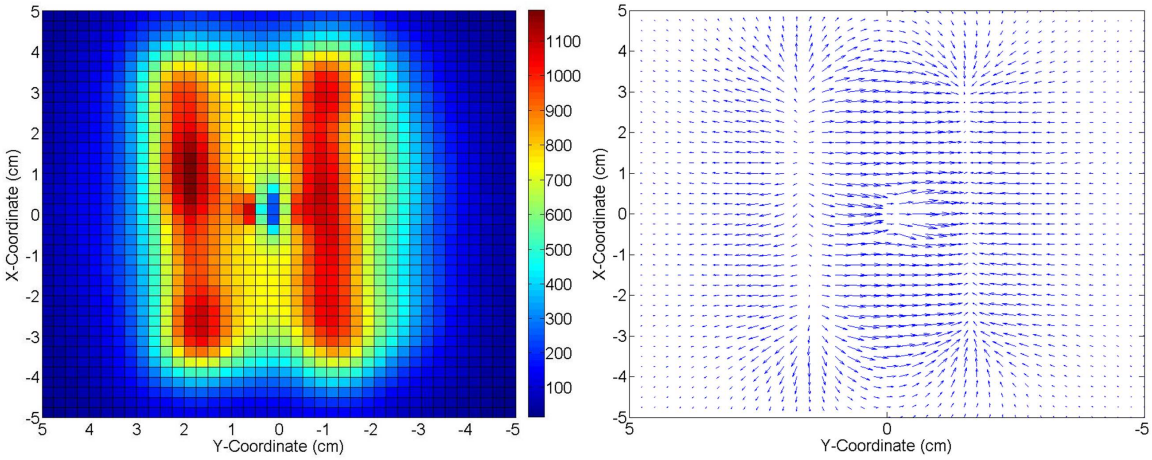

Figure 3.23: A plot of magnetic flux magnitude (left) and vector field (right) in the X-Y plane at the electrode surface (z = 0 cm).

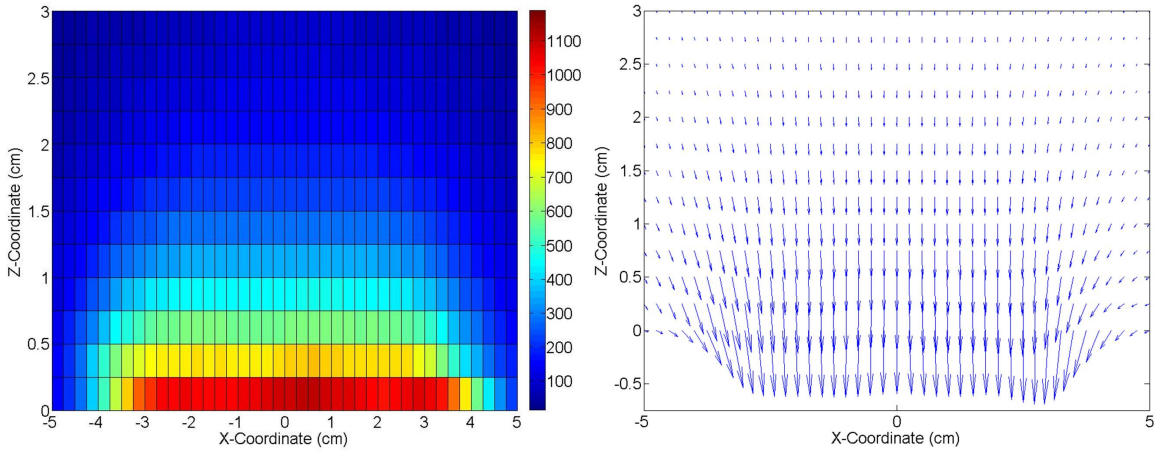

Figure 3.24: A plot of magnetic flux magnitude (left) and vector field (right) in the X-Z plane over the right magnet row.

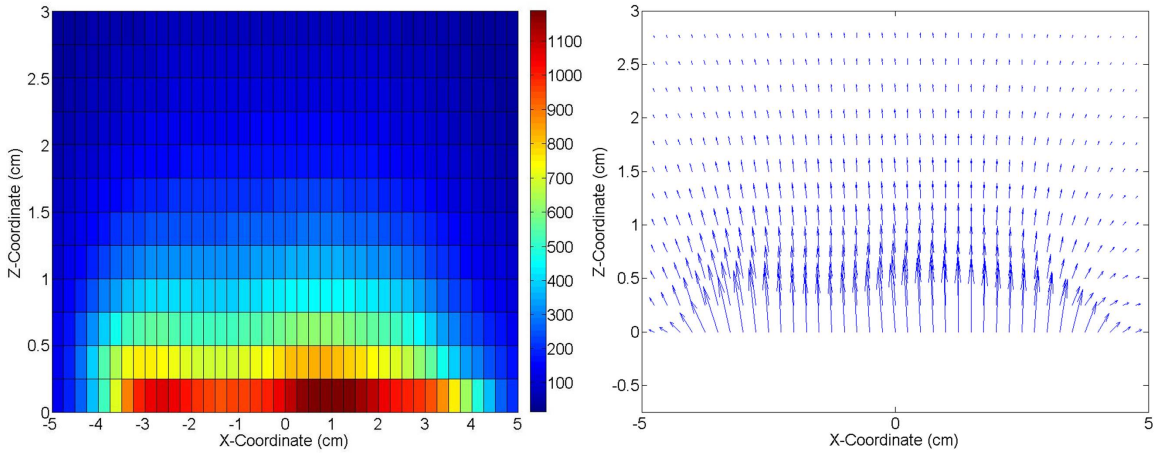

Figure 3.25: A plot of magnetic flux magnitude (left) and vector field (right) in the X-Z plane over the left magnet row.

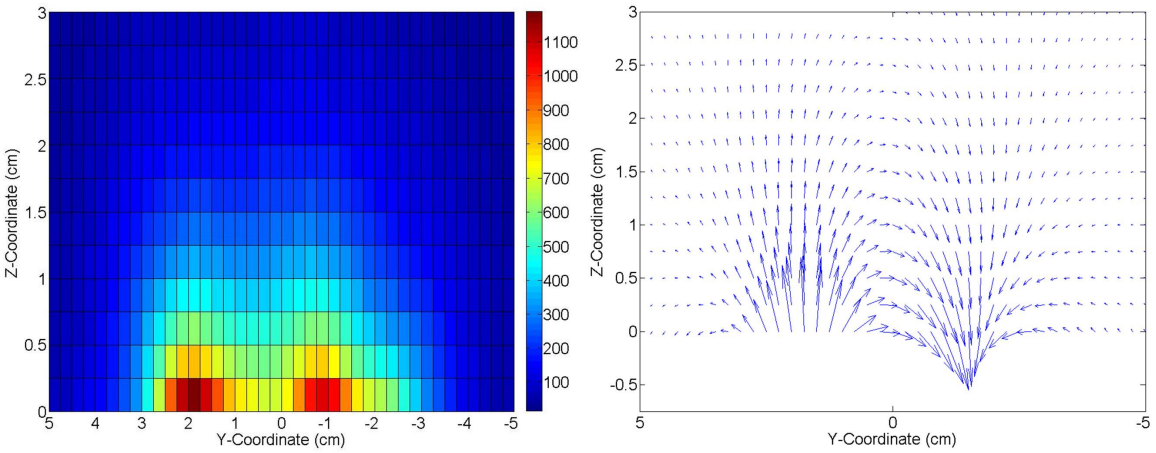

Figure 3.26: A plot of magnetic flux magnitude (left) and vector field (right) in the Y-Z plane at x = 1 cm.

3.4.3 Magnetic Configuration

The magnetic field above the electrode was mapped out precisely using a Velmex 3-axis motion system and Lakeshore 475DSP Gaussmeter. Sweeps were taken in a square grid pattern 10 cm by 10 cm in the horizontal plane, by 3 cm in the vertical direction, with 2.5 mm steps in each dimension. Three of these sweeps were taken to map out the magnetic field components in all three dimensions. See figure 3.19, for the axis definitions. All magnetic flux measurements are in Gauss.

A three-dimensional plot showing the magnitude of magnetic flux in the X-Z plane directly over each of the magnet rows, in the X-Y plane at the surface of the electrode, and in the Y-Z plane at the center of the electrode is shown in figure 3.22. The units for magnetic field are in Gauss. Figure 3.23 shows the magnetic flux magnitude and associated vector plot in the X-Y plane on the electrode surface. This is the magnetic field that influences apparent cathode spot motion and plume phenomena. The average magnetic field at the electrode surface is 409 G, with a maximum of 1,188 G, occurring directly over the magnet rows. For all plots, the magnetic field relatively insignificant more than 1.5 cm above the electrode surface, with the magnetic field

falling to less than 200 G. Notice that near the axis origin, the magnetic field is slightly modified due to the magnetic screw located in the center of the electrode. This slight modification does not appear at $z \geq 0.5$ cm.

Figures 3.24 and 3.25 show both the magnitude and vector plot of the magnetic flux above the magnet row on the right and left, respectively, in figure 3.19. So figure 3.24 (3.25) is the plot over the magnet row with the south (north) pole facing upwards. These plots are viewing the electrode across the magnet rows, in the y-direction. Note that, for both magnet rows, the magnetic field is mostly in the vertical direction, with a very small component in the horizontal direction above the magnet rows. However, at the ends of each magnet row, the horizontal component is larger than the vertical component. Directly over each magnet row, the magnitude of the magnetic flux is approximately constant, with little variation.

Figure 3.26 shows the magnitude and vector plot of magnetic flux as viewed in the Y-Z plane, along the magnet rows (in the x-direction). The vector plot shows the magnetic flux lines connecting from the left magnet row to the right magnet row, creating a significant transverse component of the magnetic flux in the center of the electrode, between the magnet rows.

CHAPTER IV

Initial Cathode Spot Characterization

Initial experiments were carried out to characterize cathode spot arcs on the surface of an electrode covered in alumina powder, as well as their interaction with a background plasma and static magnetic field.

4.1 Experimental Setup

The majority of the experiments in this chapter were carried out in the GEC cell, using the GEC cell RF plasma source. Cathode spots were initiated by biasing the electrode to large negative voltages with the HP 6521A DC power supply. A 500 MHz Tektronix TDS 640A oscilloscope with two Tektronix P5202 high voltage differential probes was used to capture current and voltage waveforms of cathode spots. A 500 Ω, 100 W Ohmite wire-wound resistor was connected between the power supply and ground, and was used to measure cathode spot current. The full experimental setup is shown in figure 4.1. Argon gas flowed into the chamber to reach a nominal operating pressure of approximately 100 mTorr for all experiments. With 100 W of RF power and almost 0 W reflected, an inductively coupled discharge was initiated to provide the overhead or 'background' plasma required for these experiments. The overhead plasma was strongly magnetized due to the placement of two rows of permanent magnets under the electrode surface, as shown in figure 4.2.

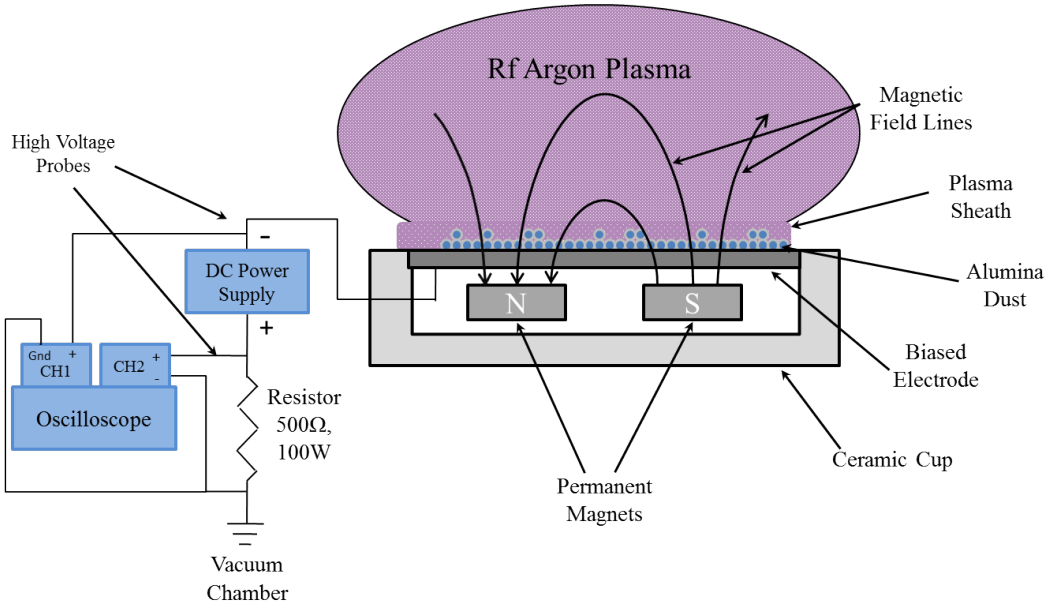

Figure 4.1: The experimental setup for the initial characterization of cathode spots in the GEC cell.

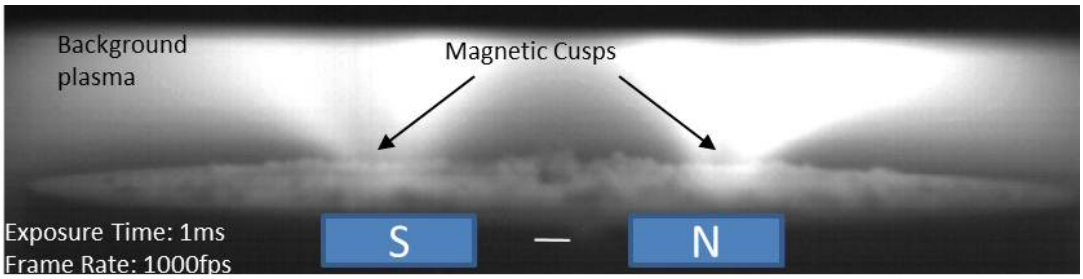

Figure 4.2: The GEC cell operating in the inductively coupled mode on argon at 100 mTorr background pressure and 100 W of RF power. Notice the highly constrained plasma in the magnetic cusp regions located over the magnet rows.

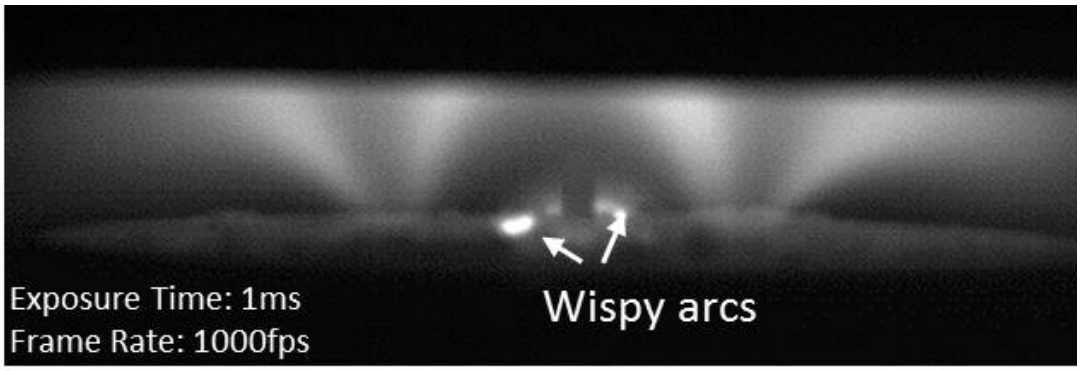

Figure 4.3: Small, wispy arcs are produced when the electrode is biased to modest voltages of -100 V. The arcs are indicated by the arrows.

4.2 Current and Voltage Characterization

4.2.1 Cathode Spot Initiation Conditions

Cathode spots were initiated at electrode bias voltages as small as -100 V. At these low voltages, the cathode spots appear as very small, 'wispy' arcs, as shown in figure 4.3, and may be a mechanism for charge transfer along the dielectric layer's surface. The image was captured with a 1 ms exposure time at 1000 frames per second, and in the center of the electrode is a small piece of alumina tubing, 3 mm wide and 5 mm tall, used for size scaling. The magnetic field produces a strong magnetic cusp structure in the overhead plasma, as shown in figure 4.2, and is visible in figure 4.3 as well. This magnetic structure may lead to charge build-up on the dielectric layer. The magnetic cusp structure will trap charged particles, particularly electrons, and will constrain electrons from flowing uniformly to the surface of the dielectric layer. Therefore, the magnetic cusps will act to channel electrons to the electrode surface directly over the magnet rows. These small, wispy arcs may be a mechanism by which voltage build-up along the dielectric layer surface is relieved.

By increasing the magnitude of the bias voltage supplied to the electrode beyond -100 V, cathode spots became more violent, intense, and more frequent. Increasing the voltage led to intensification of the electric field at the electrode surface, and

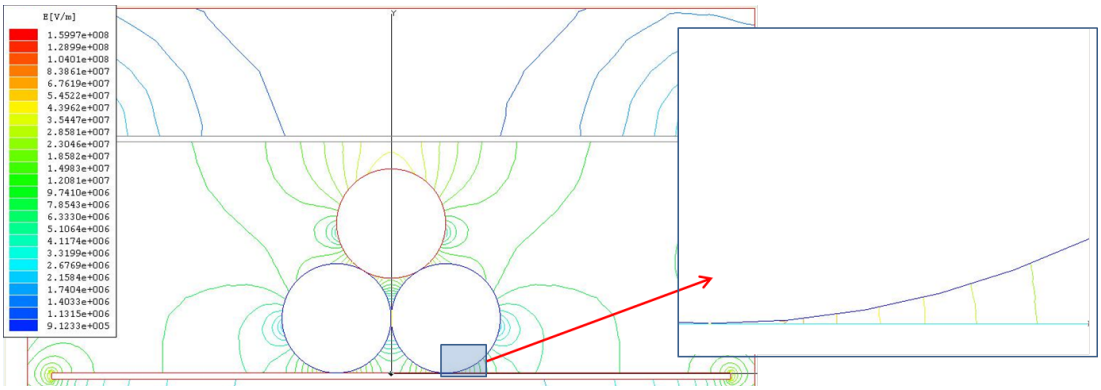

Figure 4.4: The electric field is intensified around three dielectric particles on top of an electrode. Notice in the inset that electric fields are as high as 10^8 V/m.

further augmented field enhancement due to microscopic protrusions and the dielectric powder layer. The cathode spots were observed to bore through the aluminum oxide powder placed on the surface of the electrode. Alumina (Al_2O_3) powder, available from Goodfellow, with a mean diameter of 45 µm was placed on the electrode surface in a layer $\sim$ 1 mm thick.

Cathode spots continued to occur as long as a sufficient voltage bias was applied to the electrode, the overhead plasma discharge was on, and an appreciable amount of alumina powder remained on the electrode. Once the majority of the powder was cleared, the initiation of cathode spots ceased, despite an applied voltage on the electrode. It was evident that the dielectric powder played an important role in intensifying the electric field at the electrode surface, leading to cathode spot formation. Figure 4.4 demonstrates that the addition of dielectric particles acts to intensify the electric field on the surface of an electrode. The bottom surface is set at a bias of -400 V to simulate the DC bias applied to the electrode. The top electrode in this model is set to 0 V to simulate the fixed potential of the overhead plasma. The particles on the electrode are 45 µm in diameter to simulate the alumina particles, approximated as spheres. In regions of close contact between the electrode and dielectric particles, electric field intensities as high as 10^8 V/m are possible. This

electric field is the calculated field for a smooth electrode surface. In reality, every electrode will have microscopic protrusions that will lead to further intensification of the electric field beyond that calculated here.

The point where the electrode, dielectric particle, and vacuum meet form triple points. It has been shown that intense electric fields, as predicted here, combined with the specific triple point geometry encountered here, can lead to significant multiplication of field emitted electrons.[60] These field emitted electrons can multiply by striking the dielectric at high energy, due to the associated high electric field, initiating secondary electron emission. This process can lead to the initiation of cathode spots on the electrode surface, ultimately resulting in a cathode spot arc forming and ejecting the powder above the cathode spot up into the overhead plasma. Once injected into the overhead plasma, these particles are charged to a negative potential.

Not only was sufficient ceramic powder required on the electrode surface for cathode spot initiation, but the background plasma was also required to initiate cathode spots. It is presumed that the background plasma completes the electric circuit between the electrode and ground via the chamber walls. The chamber walls are at least 10 cm away from the electrode surface. Therefore, significantly higher voltage is required to strike an arc to the grounded chamber walls without the presence of the background plasma. However, when the inductive discharge is on, the high conductivity of the background plasma essentially brings the ground anode closer to the electrode surface, thereby, with the initiation of a cathode spot arc, providing a closed loop between electrode and ground. The background plasma acts as an effective anode in these experiments.

4.2.2 Cathode Spot Waveform Analysis

Several waveforms, typical of cathode spots ignited on the electrode surface in these experiments are shown in figures 4.5 and 4.6. The average magnetic field

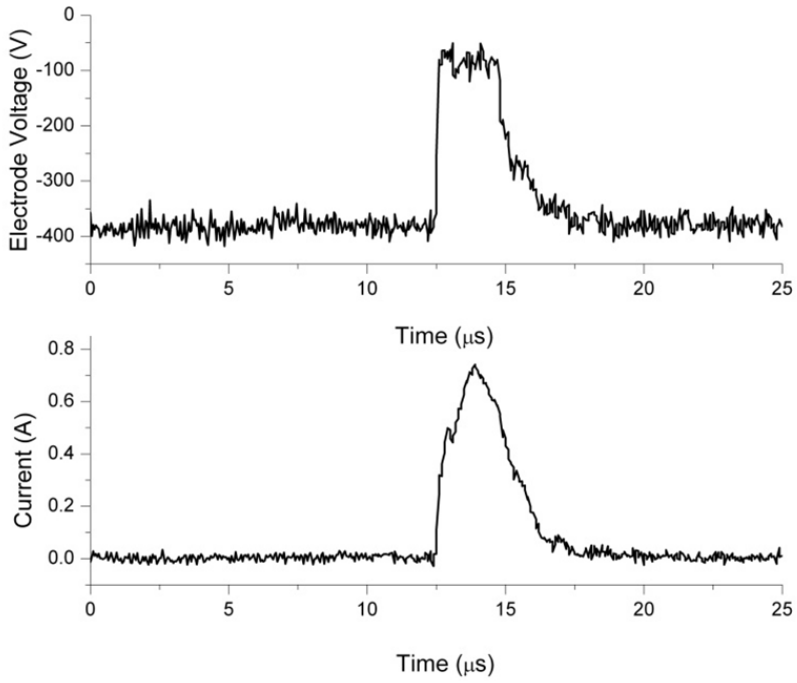

Figure 4.5: A typical current and voltage waveform captured during experiments indicates peak current and voltage of $\sim$ 1 A and $\sim$ 70 V, respectively.

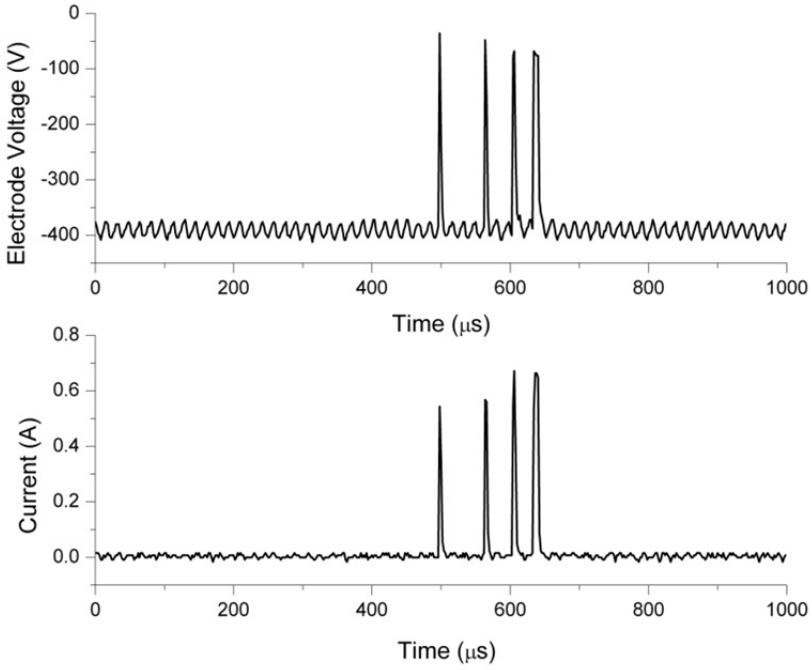

Figure 4.6: Current and voltage traces showing multiple spots forming in quick succession on the electrode surface. Also note voltage baseline oscillations.

strength on the electrode surface was around 400 Gauss. A sample of approximately 20 waveforms were collected and analyzed. The voltage while cathode spots were burning was between -65 and -80 V, with an average burning voltage of -70 V. Typical arc current peaks were around 1 A. Therefore, the maximum arc power was approximately 70 W. While type 1 spots are known to have cathode spot burning voltages of no more than 20 V, type 2 cathode spots have been observed in some cases to have burning voltages of greater than 25 V.[15] However, a high effective impedance between the electrode and grounded anode wall would account for the higher than normal burning voltages observed here. In true vacuum arc experiments, an anode electrode is usually located a couple of centimeters away. While the overhead plasma acts as a virtual anode in our experiments, it has finite conductivity, and the true anode (the chamber wall), is still over 10 cm away. Therefore, the potential drop between the overhead plasma and anode walls will add to the effective impedance when compared to typical cathode-anode configurations. In addition, the dielectric powder layer, while intensifying the electric field at the electrode surface to initiate cathode spots, may also increase the effective impedance between the electrode and anode by limiting the available electrode area. Lastly, the magnetic field in the vicinity of the electrode constrains electrons by trapping them on field lines. In order to reach the anode, electrons must traverse across the magnetic field lines near the electrode surface where the average magnetic field strength is over 400 G, and the maximum field strength is over 1100 G. Therefore, the magnetic field also increases effective impedance between the plasma and anode walls. These factors account for the unusually high cathode spot burning voltages.

The full width half maximum (FWHM) of the cathode spot bursts are measured from the voltage and current waveforms. The cathode spot lifetimes are between 2 and 25 μs for the samples collected here. These timescales are in line with the lifetimes observed in the literature. Figure 4.6 shows four successive cathode spots within a

period of about 150 µs. It is possible that this is due to cathode spot splitting or multiple cathode spot activity. Also of interest in this figure are the oscillations in the baseline, particularly for the voltage waveform. The frequency of these oscillations are approximately 550 kHz, well below the RF frequency of the plasma source (13.56 MHz). These oscillations are not evident in all waveforms, and may be a result of prearc or underdeveloped cathode spot bursts.

4.3 High-Speed Imaging

Images of cathode spot operation were captured with a high frame rate camera, allowing observational analysis of cathode spot plumes in a static magnetic field.

4.3.1 High-Speed Imaging Methods

High frame rate imaging was required to accurately observe the behavior of cathode spots on the electrode surface. Apparent cathode spot plume characteristics and motion on the electrode surface with the naked eye was not nearly sufficient. The high frame rate camera was used to image Cathode spots at varying frame rates, with exposure times usually increased to the maximum allowed to capture as much light as possible in the short time between successive images. However, at these high frame rates, the relatively dim background plasma (when compared to cathode spot plumes) is usually not visible. For these experiments, the camera was positioned in two distinct configurations, relative to the electrode, as shown in figure 4.7. In actuality, due to the viewport constraints of the GEC cell, the camera remained stationary for all tests and the electrode was rotated between tests to obtain images in the two configurations. In the 'across the cusp configuration', the axis of the camera was aligned perpendicular to the magnet rows under the electrode surface, in the negative y-direction. In this configuration, the magnetic cusp structure of the plasma discharge was not evident, nor was very much information gained regarding plume

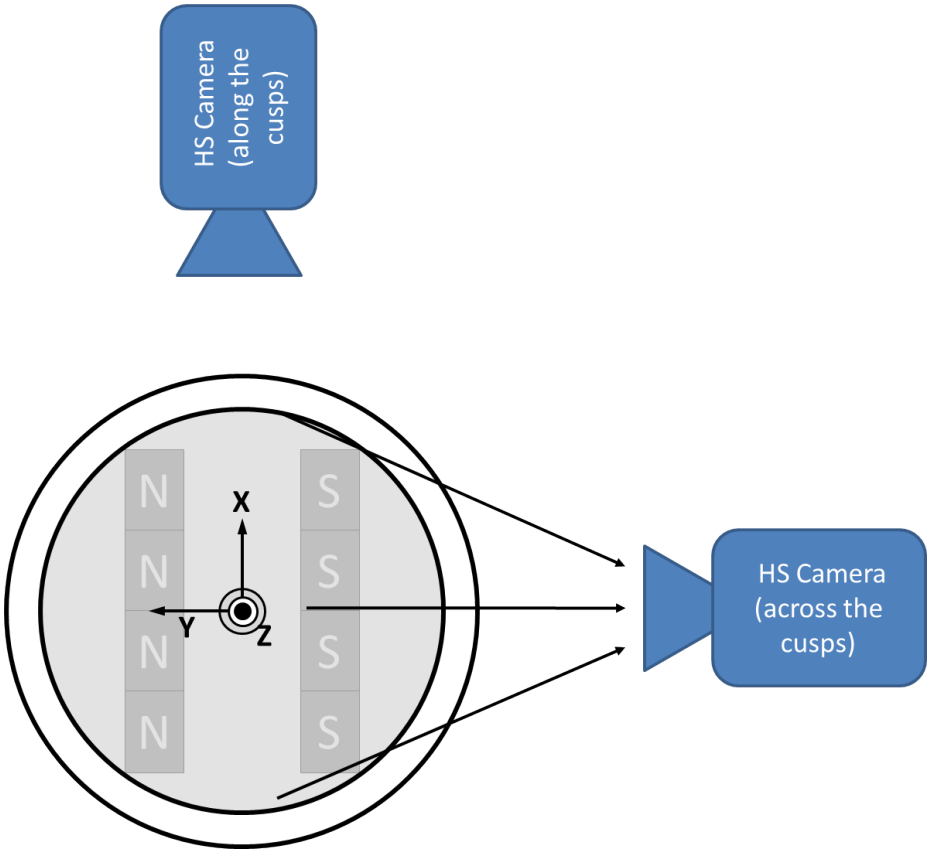

Figure 4.7: The high speed camera was oriented in two configurations, referred to as 'across' or 'along' the cusps, during experiments.

interaction with the static magnetic field. However, when the axis of the camera is situated parallel to the magnet rows (in the positive x-direction), in the 'along the cusp' configuration, the plasma structure in the magnetic cusps was clearly evident, as was cathode spot plume interaction with the static magnetic field. In later experiments, mentioned in section 4.5 and more in-depth in chapter V, the 'across the cusp' configuration resulted in several critical observations.

4.3.2 Cathode Spot Plume-Magnetic Field Interaction

Figure 4.8 shows the time evolution of a cathode spot plume imaged across the magnetic cusps. These images were captured at 5000 frames per second (fps), with a maximum exposure time of 200 µs. Notice in the first image, that the cathode spot plume has just formed, and has not reached the full intensity or brightness of that in the second and third images. This series of images has captured type 2 cathode spots. While in the images, the cathode spot and associated plume appear to be continuous, they are, in fact discrete cathode spots igniting, dying out, and reigniting every 2 to 25 µs. Since the image exposure is 200 µs, several cathode spots have likely formed, died out, and then reignited nearby during this single image. This is typical of type 2 cathode spots, as subsequent cathode spots form at the edge of a previous spot that has since been extinguished. The cathode spot plume in this first image may appear less bright because the first cathode spot formed just at the end of the exposure time, because fewer spots occurred during this particular 200 µs exposure, or because the cathode spots that formed during this first image were simply less intense cathode spots. If inspected closely, the images show that the cathode spot plume actually is moving slowly to the left in the images.

It is evident from figure 4.9, that cathode spot plumes are strongly affected by the static magnetic field present near the electrode surface. These images were captured in the 'along the magnetic cusp' configuration. The magnetic field above the electrode

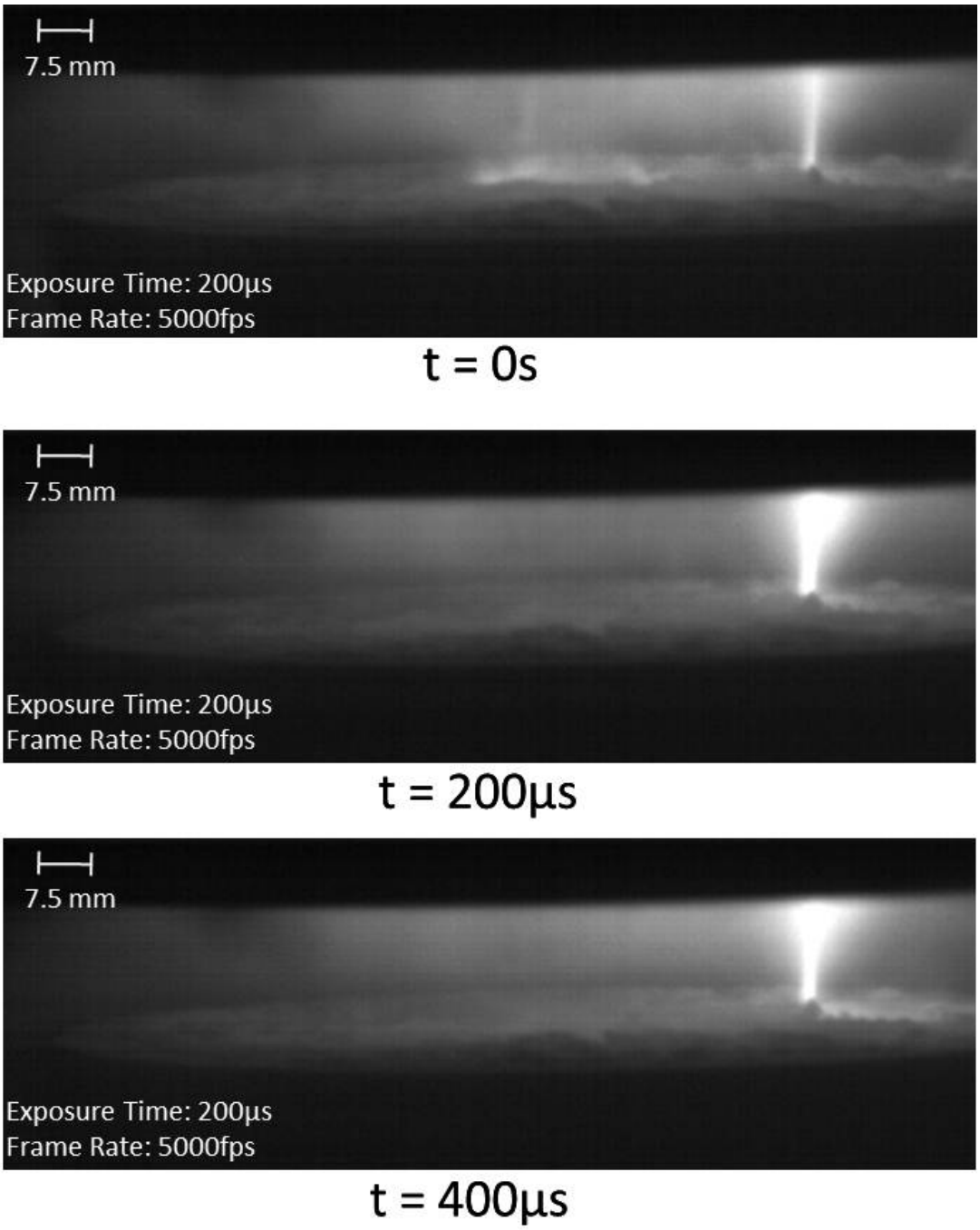

Figure 4.8: Time evolution of a cathode spot plume imaged in the 'across the cusp' configuration.

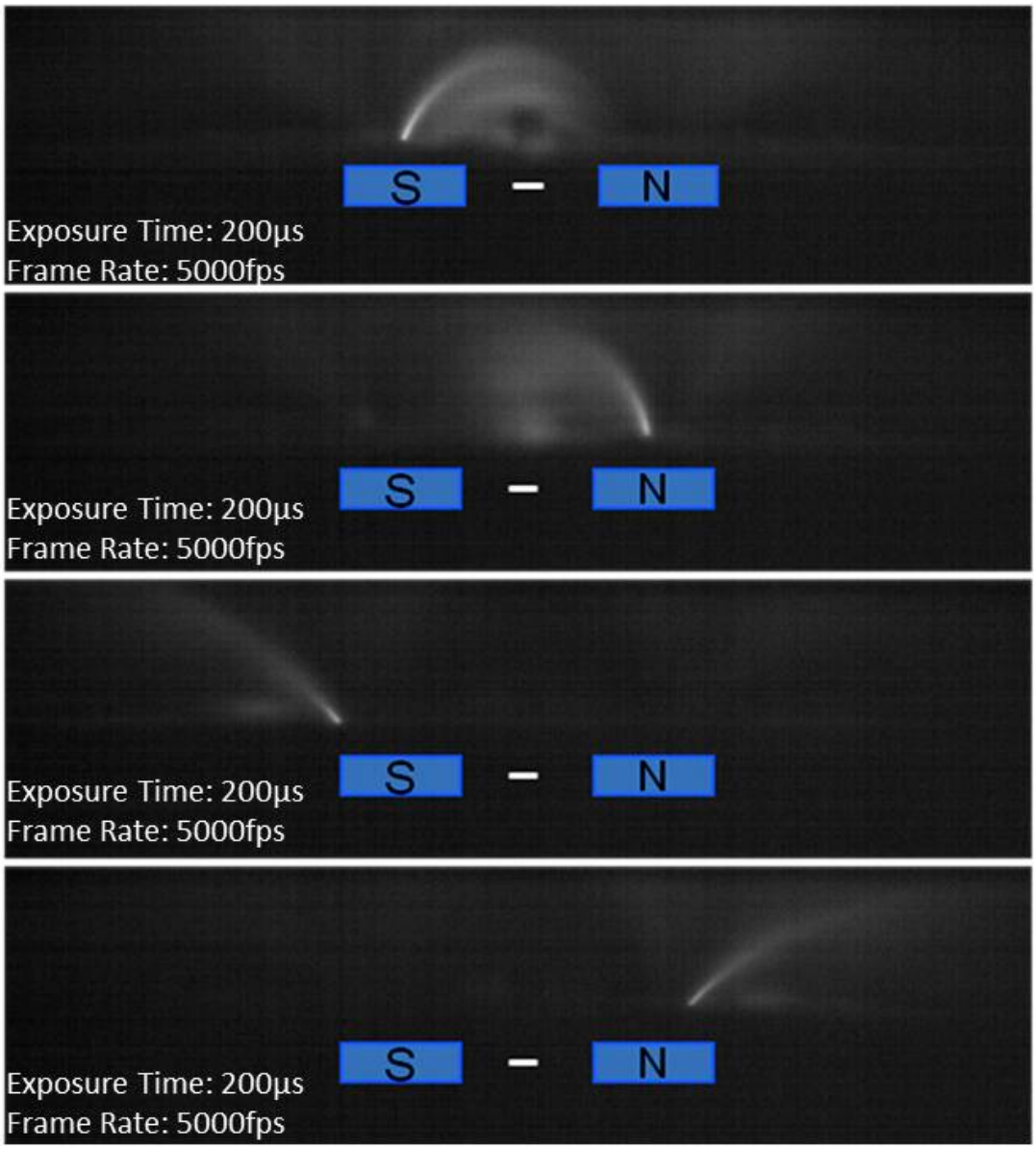

Figure 4.9: Cathode spots imaged along the magnet rows show the strong plume attachment to magnetic field lines.

in this configuration is most similar to figure 3.26, only the orientation of the electrode is rotated 180 degrees, so the polarity of the magnets is flipped. It is clear that the charged particles in the plume that are being emitted from the cathode spot are strongly bound to magnetic field lines. The top two images show cathode spots that have formed on the inside edge of the magnet row, where the field lines from the magnet rows arch over and across to the opposite magnet row. However, before the plume reaches the surface of the electrode at the opposite magnet row, the plume has expanded and become diffuse. In the bottom two images, cathode spots have formed on the outer edges of the magnet rows, and in these cases, the magnetic field lines send the cathode spot plumes outward from the center of the electrode.

The cathode spots eject metal vapor which is ionized by energetic electrons, forming these plumes that emanate from the electrode surface. So the cathode spots are essentially loading the magnetic field lines with charged particles. These charged particles are strongly constrained by the magnetic field lines, and the magnetic field lines may act to redistribute charge on the electrode or dielectric layer surface by guiding charge to the opposite magnetic cusp, as shown in the top two images in figure 4.9. While the cathode spot plumes are expected to be composed primarily of ionized metal vapor, energetic electrons ejected from the cathode spot may also ionize a portion of the background argon gas. Therefore, it is suspected that the cathode spot plumes are composed of both ionized metal vapor, as well as a small portion of ionized background argon gas. This hypothesis will be investigated further with spectral data presented in chapter V.

The images in figure 4.10 were captured at 17,900 fps, with an exposure time of 56 µs, again captured along the magnetic cusps. In these images, multiple cathode spot plumes are simultaneously visible. It may be possible, and due to the low exposure times may even be *likely*, that these spots are not only simultaneously visible, but are also simultaneously burning. It is, however, possible that within the 56 µs exposure

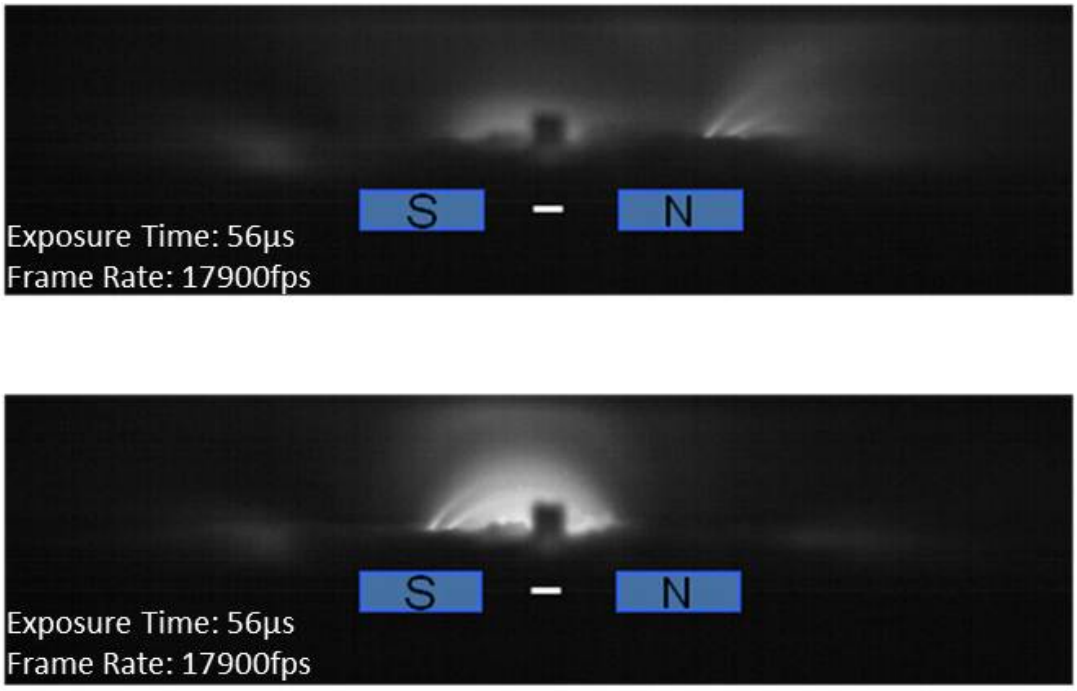

Figure 4.10: Images demonstrate multiple cathode spots burning on the electrode surface.

time of these images, that a cathode spot was ignited, then died out, and then a subsequent cathode spot was formed nearby, in a similar fashion to the waveform shown in figure 4.6. However, due to the long exposure time compared to the cathode spot lifetime, the image may have captured two separate cathode spots in the same image. Due to cathode spots potentially lasting as long as 25 µs, however, it is still possible that these cathode spots were burning on the electrode simultaneously. Therefore it is unclear as to whether the multiple cathode spots imaged are actually burning simultaneously, or are separated in time by less than 56 µs. Regardless, cathode spot plume -magnetic field interaction, similar to that in previous images, is observed here as well.

4.4 Powder Removal

Throughout these experiments, it has been observed that the ignition of cathode spots ejects alumina powder particles from the electrode surface. Several observations regarding this dielectric powder removal are discussed in the following section.

4.4.1 Qualitative Analysis

On an electrode loaded with a layer of alumina powder approximately 1 mm thick, cathode spot activity would occur consistently with an overhead plasma and supplied voltage bias for about 30 minutes. During cathode spot operation, cathode spots would etch tracks into the electrode surface, in the process ejecting powder primarily in the vertical direction, up into the overhead plasma. During this 30 minute period, a significant amount of dielectric powder was removed. After this 30 minute period, cathode spot activity would become sparse, as observed visually as well as by oscilloscope waveforms. This reduction in cathode spot activity was directly related to the amount of powder that remained on the electrode surface. Cathode spots would preferentially form in particular regions on the electrode surface due to magnetic field effects. This phenomenon will be discussed in more detail in section 4.5.

While cathode spots resulted in powder ejection primarily in the vertical direction, there was at least some significant horizontal component of velocity provided to particles, as particles were observed post-test at substantial distances away from the electrode. Figure 4.11 shows the inside of the GEC chamber with powder scattered all the way to the chamber walls, more than 10 cm away from the electrode! However, in this case, powder particles may have been ejected and deflected off of the window just a few centimeters above the electrode, and then scattered horizontally. Regardless, as powder was ejected primarily in the vertical direction, a significant portion of the

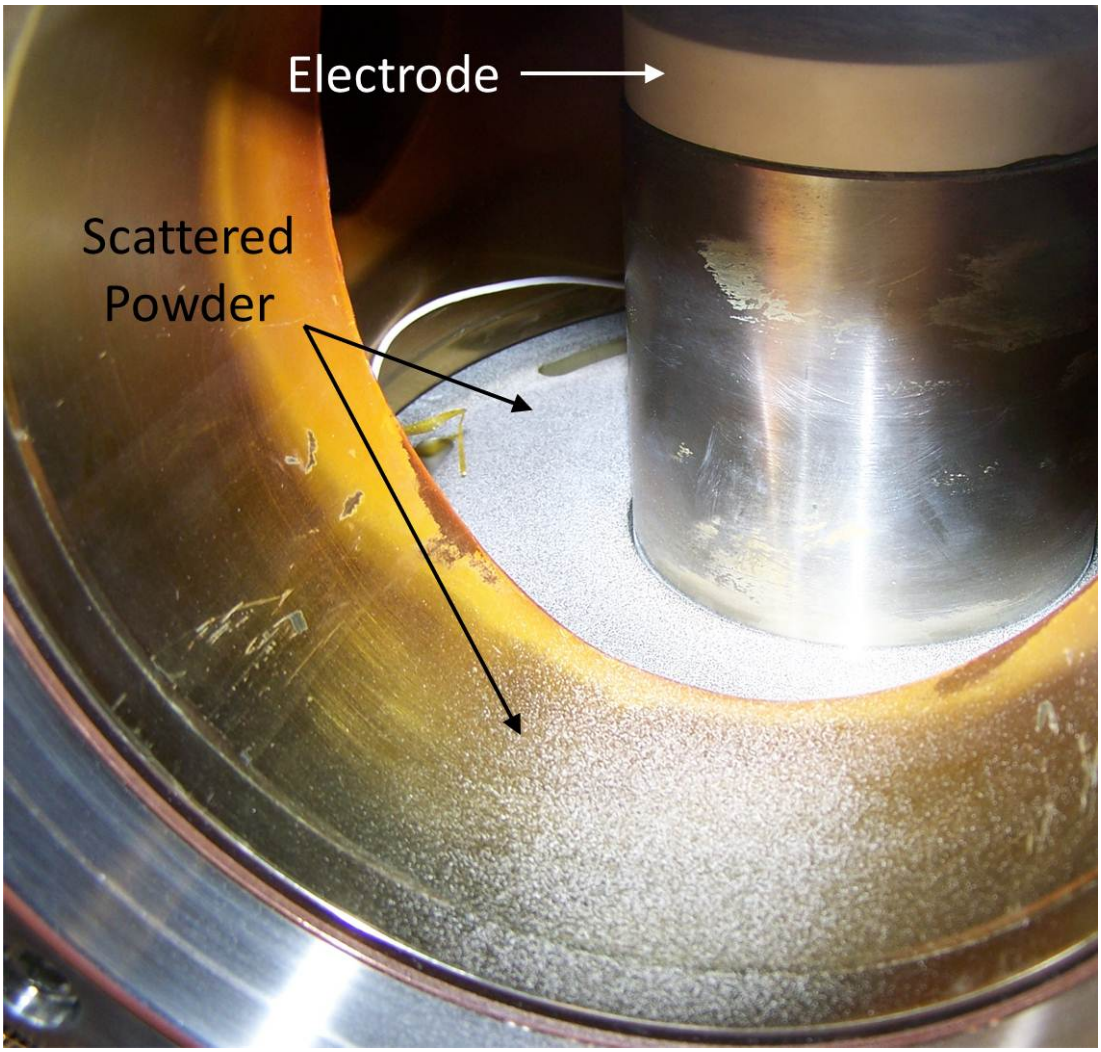

Figure 4.11: Alumina powder is scattered from the electrode surface all the way to the chamber walls, more than 10 cm away!

powder would return to the electrode surface. In this way, powder particles may be ejected multiple times within a short time period. Each particle will collect charge over the course of its trajectory through the overhead plasma, and in redepositing on the electrode surface, may redistribute charge on the electrode and/or dielectric layer surface.

The charged dielectric powder particle Larmor radius can be estimated. Assuming the particles charge as spherical capacitors in the overhead plasma with a floating potential of -5 volts, a particle velocity component perpendicular to the magnetic field at ejection of 1.5 m/s, and a magnetic field of 1100 Gauss, then an estimate of the Larmor radius can be estimated to be 20 cm. However, the magnetic field will be drastically reduced to below the maximum of 1100 Gauss as the dielectric particle moves away from the electrode surface, and, as will be shown in chapter V, the *maximum* ejection velocity will be 1.5 m/s. Furthermore, this ejection velocity will be directed primarily vertically, along the magnetic field lines on the magnet cusps, providing the particle with a much smaller component perpendicular to the magnetic field line on average. Therefore, the estimated Larmor radius of 20 cm is an *extremely* conservative estimate, with the dielectric particles' Larmor radii more likely being on the order of several meters, rather than tens of centimeters.

Since these large dielectric particles will have Larmor radii much larger than the scale of the experiment performed herein, the particles will be, in contrast to ions and especially electrons, loosely coupled to the magnetic field. Therefore these particles may redeposit charge on the electrode/dielectric powder layer areas between or outside of the magnet rows that have a deficiency of electron charge due to tightly bound electrons streaming to the surface at the magnet cusps. Regardless, figure 4.11 shows that cathode spots are capable of ejecting significant amounts of dielectric powder, and transporting the powder particles over large distances.

4.4.2 Witness Plate Powder Flux Measurements

The rate at which dielectric particles are removed from the electrode is an extremely important factor as it determines the capability of this system in terms of the degree of electron depletion. A sufficient supply of free dust particles in the reentry plasma layer must be available for electrons to attach to for maximum electron depletion. Since the dust particle trajectories are, for the most part, ballistic, the dust particles will eventually fall out and leave the plasma, carrying with it the charge that it has collected. In steady state, the rate at which dust particles are leaving the plasma will be equal to the rate at which dust particles are being ejected into the plasma since particle trapping is not expected. Therefore, the rate of dust injection is very closely related to the rate of electron removal. Assuming that the electron production rate does not increase, the electron density depletion will increase with an increasing rate of dust ejection. However, as the electron population is depleted through collection on dust particle surfaces, the electron production rate will most likely decrease due to a decrease in electron-impact ionization collisions, further augmenting electron depletion.

Measuring and analyzing the rate of dust removal is not trivial. A large portion of dust mass returns to the electrode, due to gravity, after having been ejected. It has been observed that dust particles are ejected in the vertical direction with little, if any, component of velocity in the horizontal direction. Therefore, many particles simply ascend and fall back down, landing on the electrode in the vicinity of the initial ejection. Electrons removed from the plasma therefore precipitate on the electrode in the form of returning charged dust particles. Images captured verify that a very significant portion of the ejected dust particles return to the electrode surface. As a lower limit to the mass ejection rate, due to powder returning to the electrode surface, the difference in powder mass on the electrode before and after a test yield a mass ejection rate of approximately 0.12 g/min (2.0 mg/s). Only a few particles that have

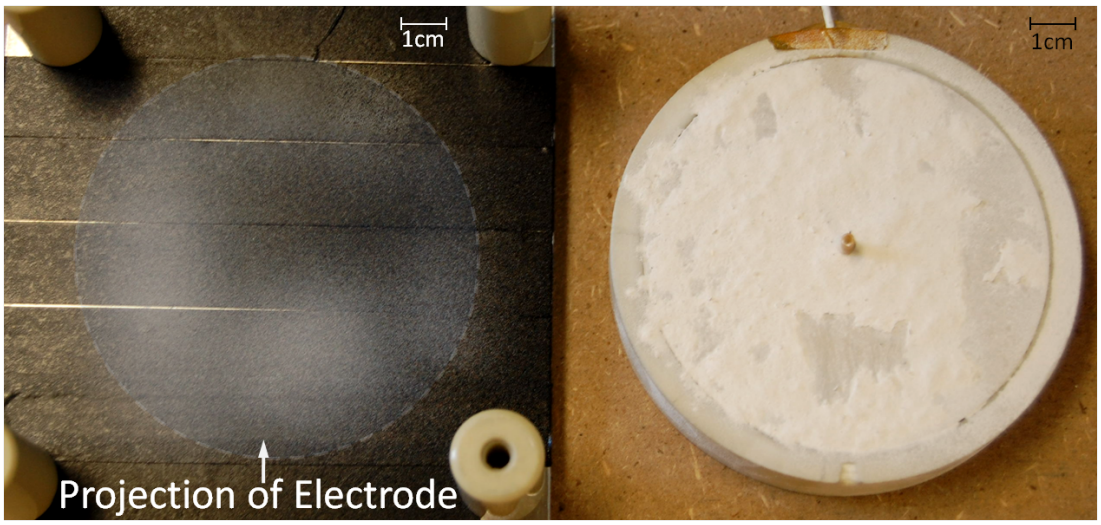

Figure 4.12: The witness plate covered with carbon tape (left) and the electrode (right) after a test run with a portion of the dust transferred from the electrode to the witness plate.

unusually large velocities will not return to the electrode surface.

An alternative method of ascertaining particle injection rates was also implemented. This method featured physically capturing ejected particles before they return to the electrode. This was achieved by placing a target or 'witness plate', containing double sided carbon tape typically used in electron beam applications, 1.8 cm above the electrode. However, since the space between the electrode surface and quartz window in the GEC cell is so limited, these experiments were performed in the rocket chamber, using the associated RF thruster discharge source. By measuring the mass of ceramic powder on the witness plate after a test, it is possible to more accurately estimate the injection rate. This test was carried out at (the same conditions as all previous tests) for a period of 30 seconds. The difference in mass was 0.1 g, leading to an estimated ejection rate of 0.20 g/min (3.3 mg/s).

Several interesting observations were made regarding the witness plate with carbon tape beginning with the pattern of dust deposited on the capture plate as compared with a post test image of the biased electrode. In figure 4.12, the plate with the carbon tape is shown on the left, and the electrode with powder removed after the

test is on the right. The carbon tape on the witness plate is naturally black, so areas that have collected more dust appear white. The electrode surface is naturally gray, so the areas of the electrode that have been cleared of dust are gray, while the white areas are still covered by alumina powder. It is clear that there are areas in which the dust is almost completely cleared from the surface of the electrode. While the area of the witness plate that collected dust is larger than the cleared electrode area, it was observed that the areas do correspond very well—the witness plate is a mirror image of the electrode. That is, when flipped so that the witness plate collection surface faces the electrode, as in the test, the areas of greatest dust depletion on the electrode correspond to the areas of greatest dust deposition on the witness plate.

4.5 Cathode Spot Motion/Erosion

Type 2 cathode spots depend strongly on thermal energy deposited into the electrode surface from previous spots to reignite. Therefore, type 2 spots have a strong tendency to form near previously formed cathode spots that are now extinct. This tendency is due, in addition to thermal energy deposited by previous spots, to protrusions that are commonly formed near the edge of a crater from the previous spot. These protrusions are caused from molten electrode material in the cathode spot being pushed to the side by the pressure of the cathode spot plume, and subsequently cooling. The protrusion results in electric field intensification near the edge of the previous cathode spot, leading to subsequent cathode spot formation.

Due to the limited lifetime of cathode spots, and rapid reformation of a cathode spot nearby, type 2 cathode spots are associated with an apparently continuous motion across the surface of an electrode. In reality, however, a cathode spot is ignited, burns for a short time (< 25 µs), dies out, and then reforms nearby, moving across the electrode in a discrete, step-wise method.

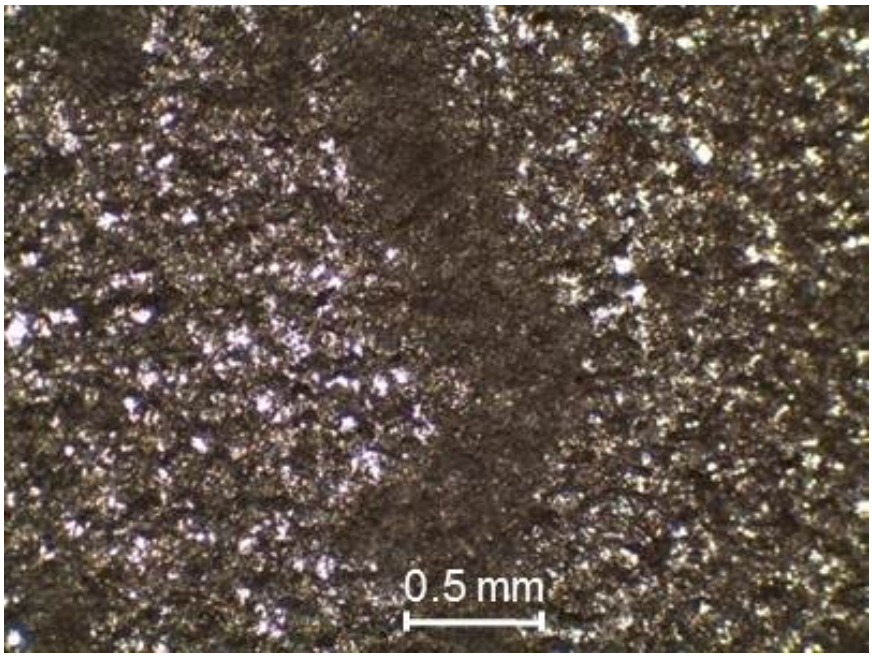

Figure 4.13: A continuous track is etched into the electrode surface by a type 2 cathode spot.

4.5.1 Electrode Erosion

In the process of melting, vaporizing, and ionizing electrode material, the electrode is eroded. This erosion is minimal, but is an important characteristic of cathode spots. The majority of this erosion is the result of molten electrode macroparticle ejection.[14, 61]

Inspection of the electrode post-test revealed continuous cathode spot tracks etched into the electrode surface, as shown in figure 4.13. This type of continuous cathode spot track is typical of type 2 cathode spots. Because type 2 cathode spots reform on the edge of previously extinct cathode spots, the craters form on top of and next to each other, creating a continuous track that is etched into the electrode surface. The darkened region denotes the erosion track. The width of this continuous track is approximately 500 µm.

The current density of these cathode spots can be estimated by assuming that the cathode spot crater is a circular cross section on the surface of the electrode, 500

µm in diameter. Therefore, assuming a peak current of 1 A, the current density is over 5×10^6 A/m^2. While this current density is lower than that of cathode spots cited in the literature (10^9-10^{12} A/m^2), the track size used in these calculations is the upper limit for the cathode spot size. The actual cathode spot size may be smaller. Side-to-side cathode spot motion would tend to widen the track. Furthermore, these cathode spots tend to be low current cathode spots, partly due to high impedance between the electrode and the chamber walls, further adding to a reduction in current. Therefore, a spot size smaller than the track width and the high impedance reconciles the difference in estimated cathode spot current density.

4.5.2 Magnetic Field Effects

The formation of type 2 cathode spots and associated motion can be significantly affected by a static magnetic field. During experiments, type 2 cathode spots appeared to be racing across the surface of the electrode. These spots were actually making discrete, step-wise movement as a cathode spot would die out, followed by another cathode spot on the edge of this previous spot, a mere few microseconds later. These cathode spots led to the continuous tracks shown and discussed above.

However, over the course of many cathode spots, and over the course of many experiment trials, these cathode spots repeatedly etched tracks into the electrode and cleared powder from the electrode surface in regular patterns. It was apparent that these tracks were due to the magnetic circuit geometry present on the electrode surface. Others have observed the importance of magnetic fields on cathode spot motion, and have observed motion in both the traditional, Amperian direction ($\mathbf{J}\times\mathbf{B}$), as well as the 'retrograde' direction ($-\mathbf{J}\times\mathbf{B}$).[7, 29, 33, 35, 62, 86, 100, 112, 123]

Figure 4.14 shows the electrode after a test, with the magnetic field vectors overlaid on top. The magnetic field lines on the electrode surface go from left to right (negative y-direction), and is strongest in the center with a highly transverse component.

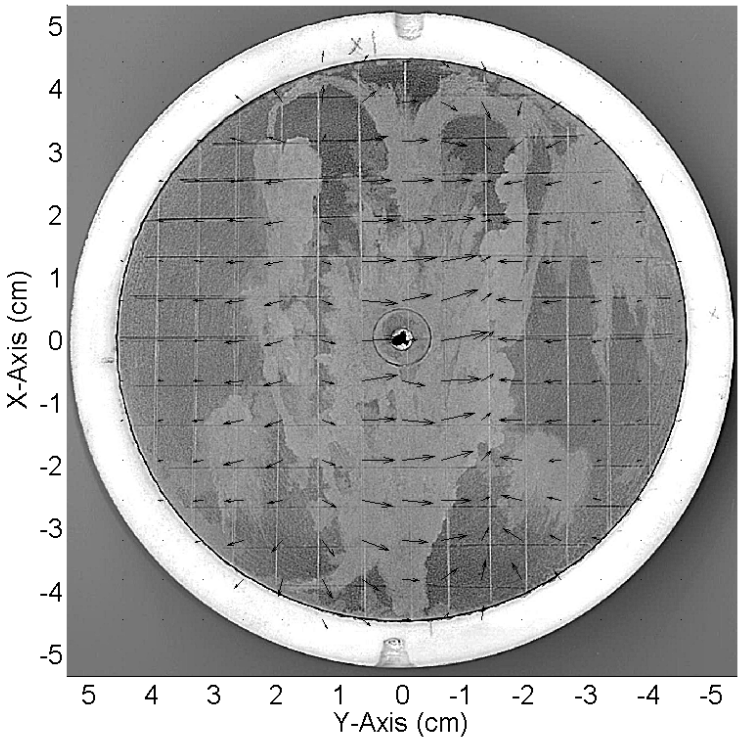

Figure 4.14: Posttest image of the electrode with the static magnetic field lines overlaid.

The current vector for cathode spots is directed in the negative z-direction, or directly into the electrode. As the charged particles are ejected from the cathode spot on the electrode, the plume is initially oriented in the positive z-direction, until the charged particles become trapped and begin to bend with the magnetic field lines. However, the cathode spot itself is rooted at the electrode surface, therefore the magnetic field component that the cathode spot sees is the transverse component on the electrode surface. Since the cathode is biased negatively, the direction of conventional current is into the electrode. Since the main component of current will be in the vertical direction, $\mathbf{J}$ is in the negative z-direction. When the $\mathbf{J}\times\mathbf{B}$ force lines are plotted, as shown in figures 4.15 and 4.16, they will be strongest in the center of the electrode, pointing in the negative x-direction. On the outside of the magnet rows, the force lines will be pointing in the positive x-direction. These force lines on the outside are not as strong as those in the middle, due to the lower transverse magnetic field. The $\mathbf{J}\times\mathbf{B}$ force will decrease from the outside of the magnet row towards the edge of the electrode due to the steadily decreasing magnetic field. However, the $\mathbf{J}\times\mathbf{B}$ force field lines at the end of the magnet rows curl around due to the field lines now bending primarily in the y-direction. Therefore, a swirl pattern develops at both ends of each magnet row.

In figure 4.16, the areas that are more white are areas that were untouched by cathode spots, where the layer of alumina powder is virtually intact. However, the gray areas of the electrode are areas where cathode spots have ejected the white alumina powder, and the gray electrode surface is exposed. Figure 4.15 shows the electrode after the powder has been removed from the electrode surface. The areas of the electrode that are light gray are areas that have been eroded by cathode spots, while the dark gray areas were covered by the powder and did not experience cathode spot formation. It is obvious that the gray areas of figure 4.16 correspond to the light gray areas in figure 4.15. In other words, areas where the powder was cleared from

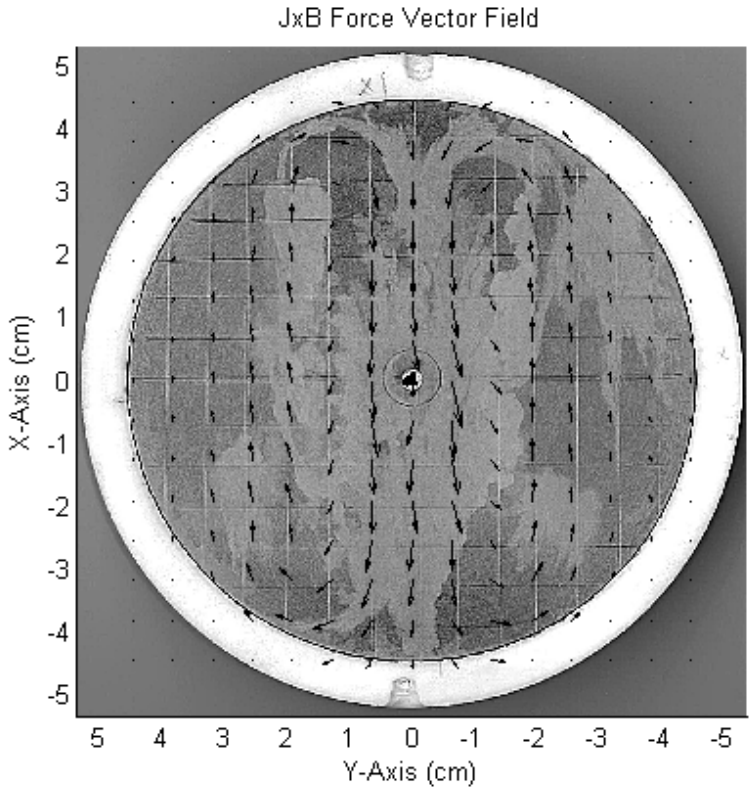

Figure 4.15: Posttest image of the electrode with the $\mathbf{J}\times\mathbf{B}$ force lines plotted, after the powder has been removed.

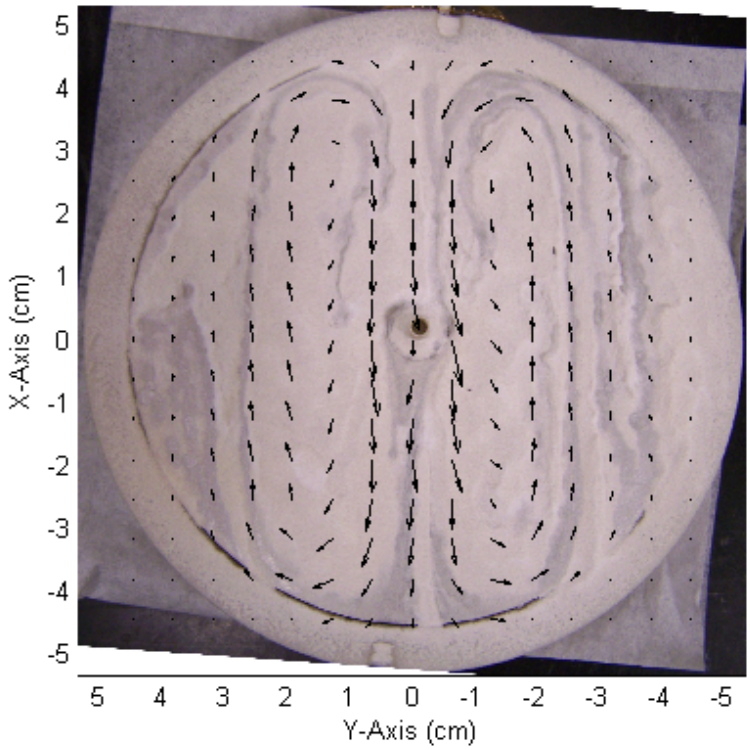

Figure 4.16: Posttest image of the electrode with the $\mathbf{J}\times\mathbf{B}$ force lines plotted, before the powder is removed.

the electrode surface clearly correspond to areas where cathode spots formed.

In figures 4.15 and 4.16, it is easy to see that the cathode spot tracks follow along the $\mathbf{J}\times\mathbf{B}$ force lines almost identically, especially in the regions where the $\mathbf{J}\times\mathbf{B}$ force lines are strongest. There are several lines of continuous cathode spot tracks where alumina powder has been cleared from the electrode, especially close to the magnet rows. Most notably, the cathode spot tracks follow the $\mathbf{J}\times\mathbf{B}$ force lines in the swirl regions at the end of the magnet rows almost *exactly*. However, it is impossible to tell from these images which direction along the $\mathbf{J}\times\mathbf{B}$ force lines the cathode spots traveled. That is, these images do not reveal whether cathode spots were traveling in the Amperian or retrograde direction. Studies performed later on will reveal the direction of cathode spot motion.

Regardless, it is very clear that the $\mathbf{J}\times\mathbf{B}$ force plays an important role in the motion of type 2 cathode spots on the electrode surface. It is also important to note that the regions of the electrode where the majority of the powder has been cleared exists in the regions near the magnet rows, where the $\mathbf{J}\times\mathbf{B}$ force is the strongest, as well as where the transverse magnetic field is strongest on the electrode surface. The cathode spot tracks along the $\mathbf{J}\times\mathbf{B}$ force lines almost encircle the magnet rows, but rarely if at all move directly on top of the magnet row. Directly over each magnet row, the transverse magnetic field is very small, and the field is directed primarily vertically, as shown in figure 3.26. The majority of alumina powder was removed from areas with a strong transverse magnetic field.

4.5.3 No Magnetic Field Case

For comparison, the same tests were run after removing the magnet rows. In this case, the overhead plasma density was uniform, and cathode spot behavior, in general, was found to be similar in nature. Cathode spot lifetimes were similar, with cathode spots lasting a few to tens of microseconds. However, cathode spot initiation

did not begin until a bias voltage of -130 V, compared to -100 V with the applied magnetic field. Furthermore, the cathode spot burn voltage was slightly lower, closer to -40 V, compared to -70 V for the applied magnetic field case. The cathode spot plumes in the B = 0 case did not bend as the applied field case plumes bent, and were more spherical in shape. Since in the B = 0 case, there was no magnetic field to trap electrons and ions in the plume emitted from the cathode spot, the ionized vapor particles were emitted in a more isotropic way, creating a more spherically shaped plume, emanating in every direction.

The absence of lateral flashovers suggests that the potential gradient on the surface of the dielectric powder layer is not as great. With the applied magnetic field, the highly nonuniform overhead plasma deposited a greater amount of charge on the dielectric layer surface directly above the magnet rows, creating a potential difference that led to lateral flashover of cathode spots. However, in the B = 0 case, the overhead plasma is highly uniform, leading to uniform charging of the dielectric powder layer, and eliminating the potential gradient that led to lateral flashovers. This reduced potential gradient on the dielectric layer in the B = 0 case may have led to a greater required bias voltage to initiate cathode spots. Since the potential difference on the dielectric layer is more uniform, the potential between the electrode and dielectric surface layer charge must be increased through means of an increase in supplied electrode voltage.

Once cathode spots were ignited, there was a significant difference observed in the burning voltage of cathode spots. While this burning voltage of -40 V is still higher than values cited in the literature, it is significantly less than in the applied magnetic field case. This suggests that even in the B = 0 case, the high impedance due to the distance to the anode walls, as well as the dielectric powder layer limiting the exposed electrode area, lead to a higher burning voltage than normal. However, the difference between burning voltage for the applied magnetic field and B = 0 case could also

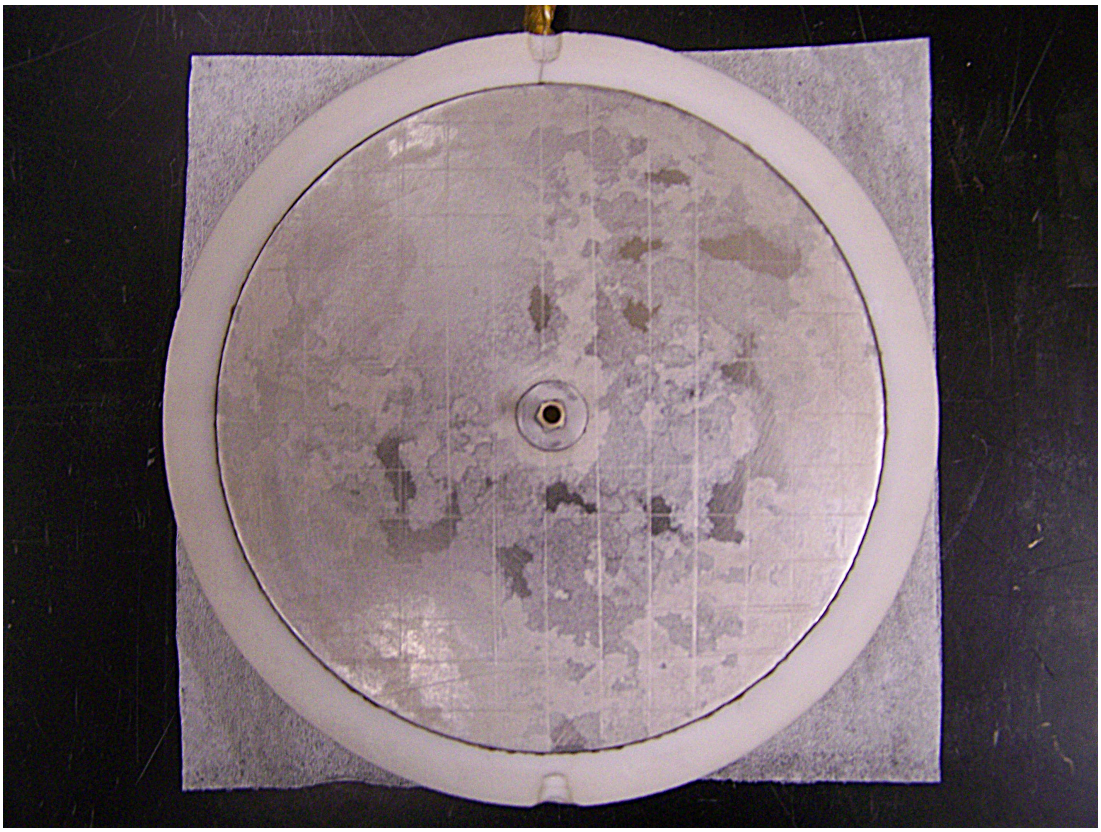

Figure 4.17: Posttest image of the electrode surface with the permanent magnet rows removed, that is, with no applied magnetic field.

be explained by the applied magnetic field increasing the effective impedance. By trapping charged particles on the field lines, the impedance to the grounded chamber walls was increased, as electrons would have to travel across magnetic field lines to reach the anode chamber wall. This could have led to a higher burning voltage in the case of the applied magnetic field. It is suspected that the application of stronger magnetic fields would lead to higher burning voltages due to greater particle trapping and increased impedance, while weaker magnetic fields would decrease the burning voltage.

Figure 4.17 shows the electrode surface following the test case with no applied magnetic field. The lighter gray areas indicated areas that were cleared of powder, while the dark areas indicate areas that were untouched by cathode spots. Cathode

spots behaved similarly in the B = 0 case, in that cathode spots became less frequent as alumina powder was removed from the electrode. However, as the image shows, there is no regular pattern associated with cathode spot formation or regions of powder removal. The cathode spots formed at seemingly random locations on the electrode surface, and followed no particular pattern or direction. In this case, cathode spots were forming in regions that were most favorable based solely on electrode surface conditions. Unlike in the applied magnetic field case, there was no particular electrode region that was more favorable for powder removal. Rather, the cathode spots were not constrained by a magnetic field. It may be important to note that some areas of the electrode surface in figure 4.17 appear lighter than others. This suggests that cathode spots processed particular locations on the electrode surface multiple times.

4.5.4 Implications of Magnetic Field Effects

The implications of these experiments are far-reaching. The ability to control cathode spot formation, cathode spot motion, and regions of powder removal on the electrode is a significant improvement compared to experiments where cathode spot formation occurs in random locations on the electrode surface. For the application of blackout mitigation, the ability to control cathode spot formation and motion leads to control of the areas of powder removal. Thereby, it may be possible to modify the magnetic circuit configuration to maximize the amount of powder ejected from the electrode. Controlling regions of the electrode that are cleared of powder provides greater flexibility, allowing the user to tailor the magnetic circuit and associated cathode spot formation to their specific requirements and needs. On a more basic level, constraining cathode spot movement may provide for more regular cathode spots, with less variation on a shot-to-shot basis.

CHAPTER V

PIV and Particle Tracking Studies

This chapter presents experiments to determine the velocity at which dielectric particles are injected into an overhead plasma by cathode spot formation at the surface of an electrode covered in dielectric powder. These experiments provide a great deal of insight into energy transfer from localized cathode spot plumes to the dielectric particles, as well as provide important information regarding the potential use of this mechanism for ejecting particles for radio blackout mitigation applications. Measurements of the rate of powder injection, directionality and magnitude of ceramic particle injection, and the velocity distributions of ejected particles are presented.

5.1 Experimental Setup and Procedure

These experiments utilized a solid-state laser with beam expanding optics in conjunction with a high speed camera fit with a notch filter to image dielectric particles ejected from the electrode surface. Details on this equipment can be found in chapter III. These experiments were performed in the Rocket Chamber. Alumina (Al_2O_3) powder, with mean particle diameters of 45 µm in diameter, was placed on the electrode surface in a layer approximately 1 mm thick. The background plasma was created with the RF stand-alone plasma source, also discussed in chapter III. The plasma was allowed to flow out over the electrode from the discharge can, located

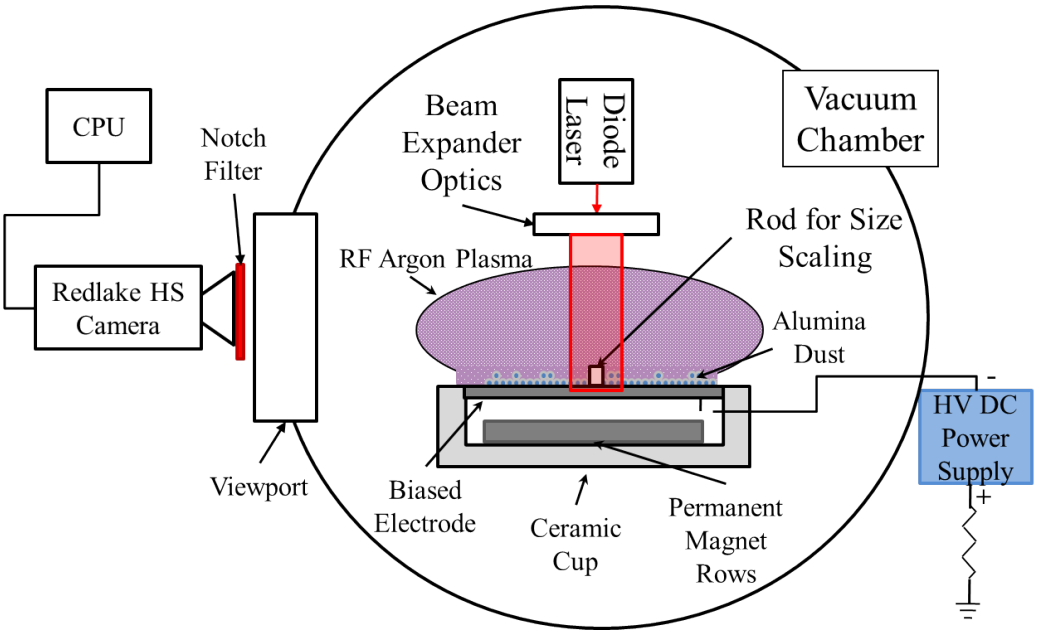

Figure 5.1: Experimental setup for these experiments, depicting the vacuum chamber, electrode, laser illumination, high frame rate camera, and associated systems.

approximately 10 cm away. The RF plasma source was operated nominally in the capacitive regime at 125 W, with 10 sccm of argon flow. The neutral gas pressure in the vacuum chamber was 125 mTorr.

The experimental setup is shown in figure 5.1 , excluding the Langmuir probe and plasma source to clearly depict the laser, camera, and electrode system and geometry. The same HP 6521A DC power supply and Ohmite 500 Ω ballast resistor from previous tests were used to provide the electrode with a -900 V bias to initiate cathode spots for these experiments. The laser and associated beam expanding optics produced a cylindrical interrogation region approximately 2 cm in diameter. The notch filter blocked all light except that in the wavelength region of the laser. Camera settings were optimized to image as many particles as possible, including being able to identify even the most dimly lit particles. The camera was setup so that the surface of the electrode was barely visible in the bottom of the collected images. The camera lens was focused on the center of the interrogation region, and every image

included the center of the electrode, where a piece of alumina tubing was located for size scaling. Most sequences of ejected particles were collected at 2000 fps, with an exposure time of 497 µs. The camera and electrode were again setup for imaging in two configurations, as shown previously in figure 4.7. This allowed for imaging in the X-Z and Y-Z planes.

5.2 Plasma Characterization at the Electrode Surface

Collecting background plasma parameters was important for these studies to accurately determine what effect, if any, the background plasma would have on the trajectory of particles ejected from the electrode surface as they traveled through the background plasma.

5.2.1 Langmuir Probe Measurements

The background plasma parameters were measured with a Langmuir probe placed directly over the center of the electrode, 2 cm above the surface. To avoid RF plasma perturbations, only the ion saturation portion of the I-V characteristic was collected. This portion of the I-V trace was impervious to the RF oscillations of the overhead plasma, due to the slow ion response time. The inverse of the ion frequency is the characteristic ion response time, 3.0 µs (330 kHz), and is long compared to the RF oscillation period of 0.074 µs (13.56 MHz). The ion motion was considered to be unperturbed by the RF oscillations. A background plasma with a density of approximately 10^8 cm^{-3} was produced 2 cm above the electrode surface, assuming a nominal electron temperature of 2 eV (typical for these types of discharges).[78]

5.2.2 Cathode Spot Spectra

Time-integrated emission spectra were collected from cathode spot plumes and the associated overhead plasma using the Ocean Optics 2000 spectrometer. The

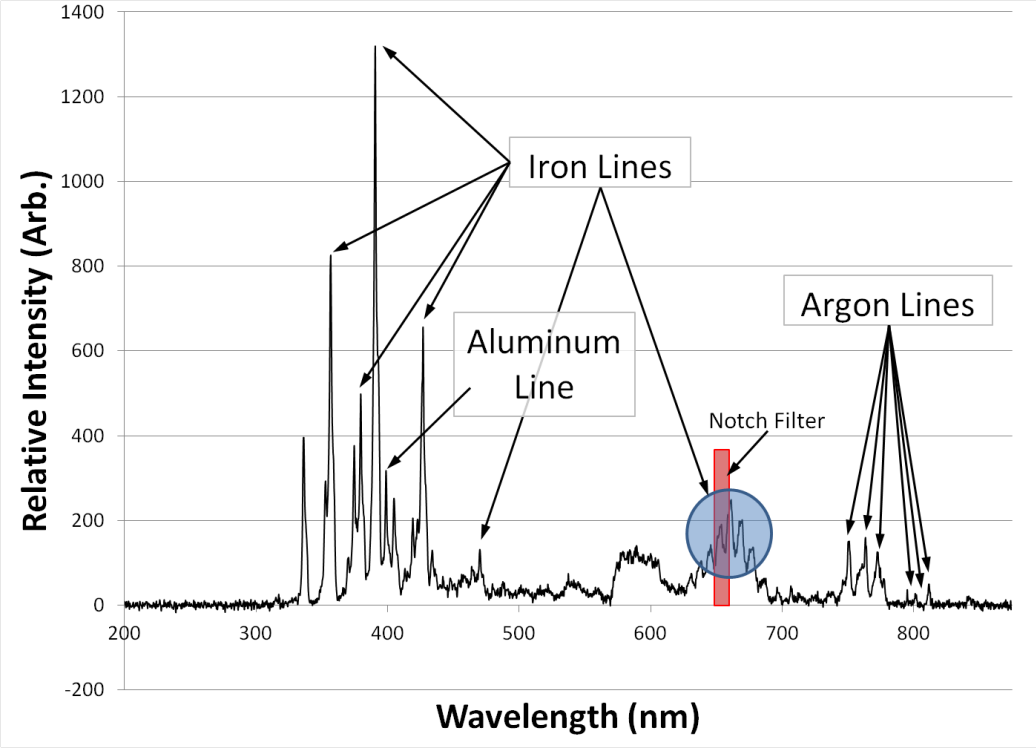

Figure 5.2: Cathode spots spectra captured over long integration times shows a broad emission spectrum with many iron and argon lines.

collected emission spectra were corrected by subtracting the background plasma and laser light emission from the measured emission during cathode spot operation. This allowed for discrimination of the emission due to the cathode spots alone. This correction also yields insight into the interaction of the cathode spot plasma plume with alumina powder particles, the argon gas, and the background plasma. Spectra were taken with very long integration times, 3.5 seconds, with acquisitions covering many cathode spot events. The wavelength range is very wide, so the resolution of the spectral measurements is limited to $\pm \sim 0.35$ nm. The resulting corrected spectrum collected is shown in figure 5.2. The pass region of the notch filter, used later on for PIV measurements, is also highlighted in the figure.

Cathode spot plumes are expected to consist primarily of vaporized and ionized electrode material, with some ionization of the background gas. The electrode that cathode spots are formed on is steel. Several iron lines are pointed out, and these

lines are the strongest lines present on the spectrum. Many atomic iron lines match with lines in the collected spectrum, shown in table 5.1. There are many instances in which a line is present in the measured spectrum, and there are multiple strong iron lines predicted near the measured line. For example, for the 390.52 nm line, there are strong tabulated lines for iron at 390.65 nm and 390.29 nm. In this case, it is likely that both lines contribute to the measured line at 390.52 nm, due to the limited spectrum resolution. These results confirm that indeed, the cathode spot plumes are composed largely of the electrode material. No emission line from iron, carbon, or argon could be found to account for the line at 336 nm. It is possible that this peak is due to an alloyed metal, but no common alloying metals had strong lines at this wavelength. Nitrogen does have an emission line at 336 nm. However, the chamber was pumped down to base pressures on the order of 10^{-5} Torr for each test, therefore no significant amount of background nitrogen gas is expected.

It is important to note that there are several lines present in the spectrum that may indicate the presence of aluminum. It has been shown that the temperature of the electrode at a cathode spot site can be as high as 4000 K.[15, 14] This temperature is well above the melting and boiling temperature of alumina. Therefore, it is possible that not only are cathode spots and the associated plume melting and vaporizing electrode material, but the cathode spot may also be melting, vaporizing, and even decomposing alumina into its basic atomic elements of aluminum and oxygen. Several aluminum lines may be present in the spectrum, and are included in table 5.1.

The pass region of the bandpass or notch filter used on the camera during PIV image capture is indicated. It is important to note that there are several iron lines associated with the cathode spot plumes that are located in this region. Therefore, it is expected that while most of the cathode spot plume light will be filtered, the cathode spots will still be visible, even with the use of the notch filter. However, the intensity of light collected from the cathode spots will be reduced significantly since

Measured Emission Line (nm)	NIST Data [97]	
	Emission Line (nm)	**Atom**
811.51	811.53	Ar I
801.11	801.48	Ar I
795.06	794.82	Ar I
772.20	772.42	Ar I
	772.38	Ar I
763.90	763.51	Ar I
750.31	750.39	Ar I
675.15	675.02	Fe I
667.29	667.80	Fe I
660.20	660.91	Fe I
653.75	654.62	Fe I
645.66	646.27	Fe I
469.90	469.14	Fe I
426.82	427.18	Fe I
	427.12	Fe I
398.66	394.40	Al I
	396.15	Al I
390.52	390.65	Fe I
	390.29	Fe I
379.51	379.50	Fe I
356.68	357.03	Fe I
	356.54	Fe I

Table 5.1: Measured and tabulated spectral lines associated with iron (Fe), argon (Ar), and aluminum (Al).

the strongest wavelengths of emission are removed via use of the notch filter.

Detection of argon emission lines between 750 nm and 815 nm, despite removing the background plasma spectrum, indicates cathode spot driven background gas excitation. This suggests that interaction of the cathode spot plasma plume with the background gas leads to further ionization. This would likely be due to direct interaction between the cathode spot plume and/or cathode spot emitted electrons, resulting in further ionization of the background plasma or neutral gas. The spectra provides ample evidence that cathode spot plumes stemming from the electrode surface interact with the background plasma and/or background argon gas to excite and lead to further ionization of argon, beyond that achieved during steady-state operation of the plasma source.

The ability of cathode spot plumes to lead to further background gas ionization may have an important effect on the proposed use of this method for blackout mitigation. If the cathode spot plume leads to further ionization of background gas, this would impede transmission through the plasma layer. However, as will be shown in the images presented in section 5.4, the particles that are responsible for plasma depletion reside in the background plasma well beyond the cathode spot lifetime. That is, the cathode spot is ignited, emitting an intense plasma plume that adds to background plasma ionization, while also emitting dielectric particles. Before the dielectric particles fully charge or travel any significant distance, the cathode spot dies out. Argon that was ionized and excited by the cathode spot plume will begin recombining and de-exciting back to the neutral ground state, leaving only the overhead plasma. During and continuing well after these processes occur, the dielectric particles traverse through the overhead plasma, collecting many electrons. Therefore, cathode spot plumes may lead to an increase in plasma density that will then be reduced immediately following cathode spot extinction, while the dielectric particles remain present in the overhead discharge to deplete the electron population.

In the region between 645 nm and 675 nm, iron lines overlap, causing a broad region of intense light emission. There is a similar region just below 600 nm, but without the resolved peaks. It is possible that this is a region of molecular emission lines, close together so that our spectrum resolution was not fine enough to pick out specific peaks.

The spectrum results indicate, as presumed earlier, that cathode spot plumes are composed primarily of vaporized and ionized steel (iron), but also have a significant amount of ionized argon.

5.3 Witness Plate Observations

Witness plate experiments, like that carried out to determine particle flux from the electrode surface in chapter IV, utilized the same apparatus, outfitted with the same carbon tape, and also placed 1.8 cm above the electrode surface. Several other interesting results, in addition to the particle flux, regarding ejected particle morphology and dielectric particle ejection velocity, were observed in these experiments.

5.3.1 Melted Particles

In several instances, after witness plate experiments were performed, microscopic inspection of the witness plate and electrode revealed the presence of large particles, suggestive of melted alumina. A microscope image of a seemingly transparent particle captured on the witness plate during an experiment is shown in figure 5.3. The particle in the figure is approximately 500 µm long. Figure 5.4 shows a similar particle, approximately 1.5 mm in length, that may have been too heavy to be collected by the witness plate. For the experiments performed here, the 45 µm diameter particles are used, and very little clumping of particles has been observed with these particles, as shown by the other particles visible in figures 5.3 and 5.4. Therefore, some other mechanism is causing the large particles observed.

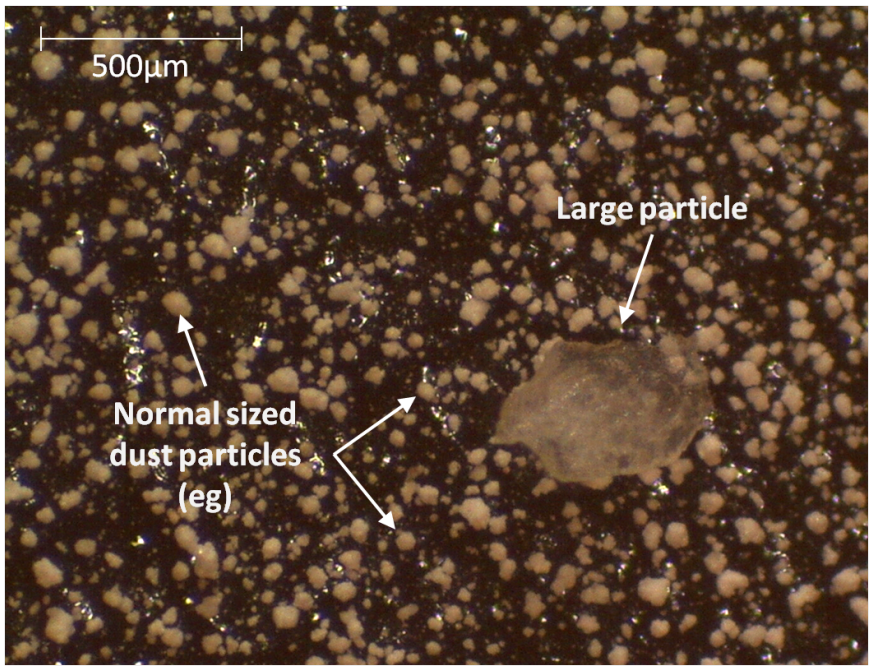

Figure 5.3: Microscope image taken at 35× magnification of witness plate. The large particle is indicated as well as a few of the other, normal sized (45 µm diameter) alumina dust particles.

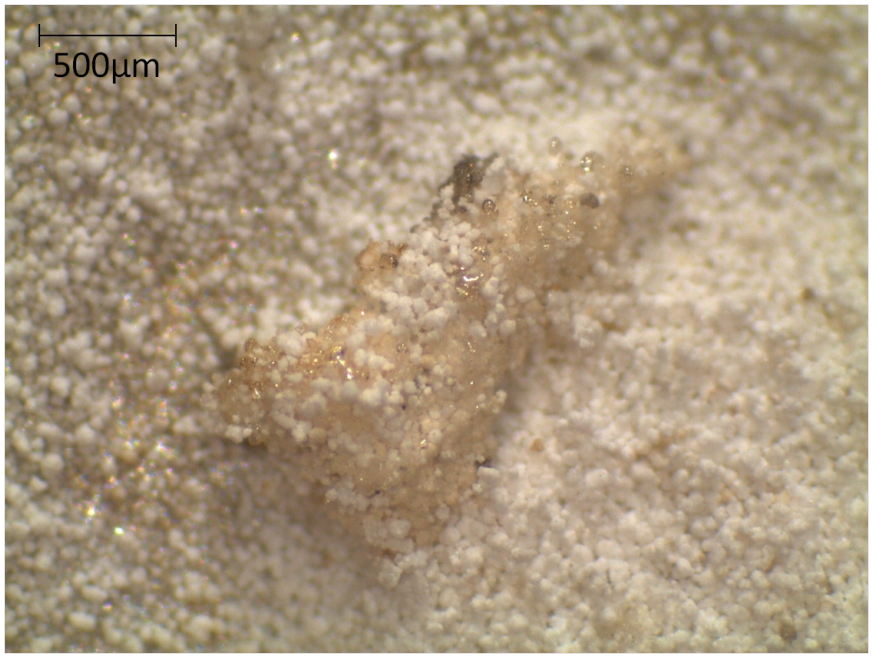

Figure 5.4: Microscope image of one of several very large particles found to be present on the electrode surface.

These particles could indicate that several alumina particles were heated to temperatures exceeding their melting temperature (2100 °C) and then fused together to result in one large particle when cooled.[40] The possibility of aluminum lines present in the spectrum in section 5.2.2, suggests that alumina particles may not only be melted. Alumina molecules may also be broken down into the basic atomic elements of aluminum and oxygen by the heating associated with cathode spot formation. Presumably the melting is a consequence of energy transfer between the cathode spot arc and the surrounding powder. Therefore, the particles would most likely melt and fuse together on the electrode surface near the cathode spot before, or during the impulse imparted by the cathode spot plume. In this vicinity of the cathode spot, many powder particles are present, and particles could clump together from simple collisions or electrostatic mechanisms. The particles would likely cool rather quickly after being injected into the overhead plasma. In addition, these large particles may become so large and massive that the particle is not necessarily ejected, but may simply be moved aside so that the electrode is clear as the cathode spot burns on the electrode surface. Conventional plasma sprayers utilize ceramic powder injected into an arcjet, where the ceramic is melted and deposited on a substrate downstream.[50] The physics observed here may be similar to particle melting for plasma sprayers.

A few particles of this morphology, such as those shown in figure 5.3, and the particle in figure 5.4 itself, were found on the electrode as well. The particles found on the electrode were generally larger than that found on the witness plate, and therefore it is hypothesized that these particles, if ejected, were unable to reach, or due to the particle mass, were unable to stick to the witness plate. The large particles found on the electrode were usually covered in alumina dust, probably due to subsequent ejection of dust that landed back on the electrode surface, on top of the large particles.

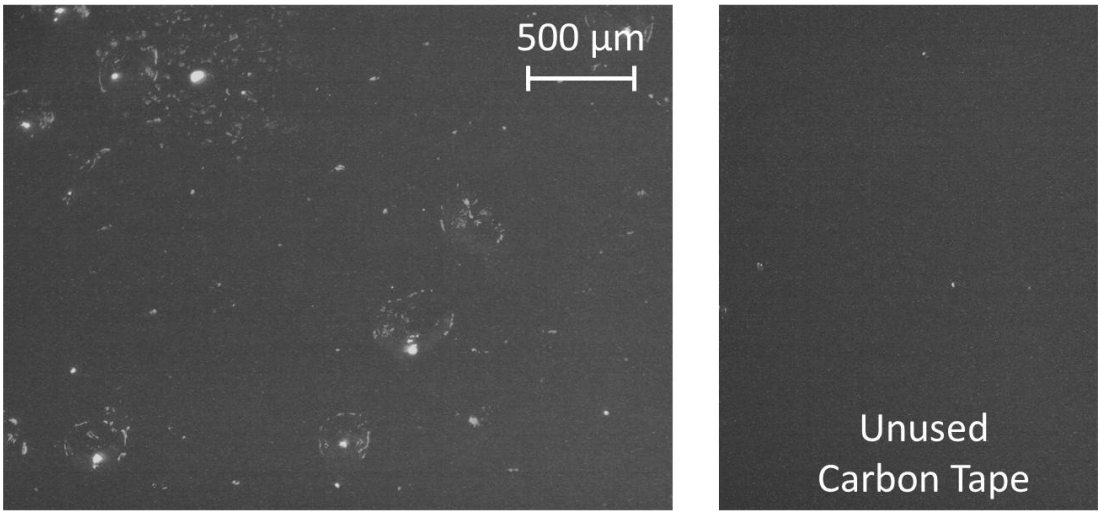

Figure 5.5: Microscope inspection of the witness plate posttest (at 35×) shows impact craters on the carbon tape (left). A pretest image of the carbon tape is shown on the right.

5.3.2 Macroparticle Ejection

Upon further inspection of the witness plate, most notably at the edges of the witness plate, near where little or no dust powder was collected, small impressions had been made on the carbon tape surface. Figure 5.5 shows a sample of unused carbon tape (right) whose surface is relatively smooth and free of irregular dimples, contrasted with the tested carbon tape sample on the left. Figure 5.6 shows a similar image at a lower zoom, again depicting impressions or impact craters on the carbon tape. These craters were significantly more prevalent on the edges of the witness plate, where very few dust particles were present or captured. In the case of figure 5.5, no dust particles were captured in this region. This suggests that dust particles ejected from the edge of the electrode and/or dust particles with a large horizontal velocity component may have reached the witness plate near the edge and impacted the witness electrode. But perhaps because of the low impact angle or velocity, did not become embedded in the carbon tape. Rather, they had sufficient velocity to impact the witness plate and create an impression only to then bounce off of the

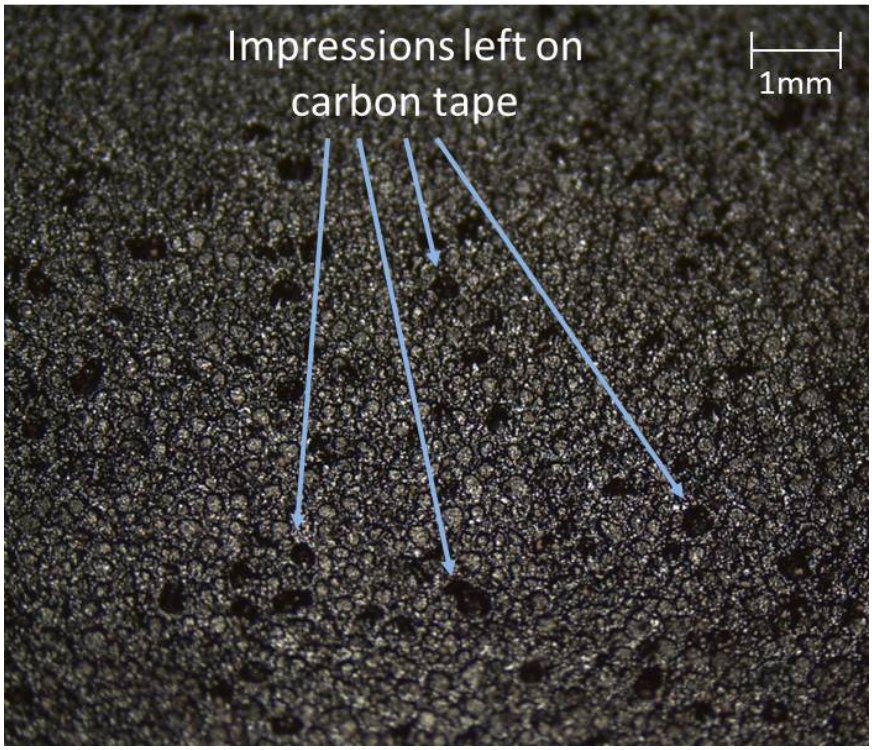

Figure 5.6: Another image depicting many impact craters on the witness plate carbon tape.

witness plate. The only evidence of their presence is the impact craters left on the witness plate.

However, this phenomenon could have also been caused by so-called 'macroparticles' of molten electrode material that were ejected at very high velocities. It has been shown that these macroparticles have a tendency to be ejected at small angles with respect to the electrode plane, approximately 10 to 30 degrees.[15, 14] Assume that a macroparticle is ejected at the center of the electrode with a nominal velocity and angle for macroparticle ejection of 500 m/s and 20 degrees, respectively. Assuming a ballistic trajectory, shown to be valid later on, the macroparticle will impact the capture plate 105 µs after being ejected, 5 cm radially outward from where it was ejected. This is just beyond the radius of the electrode (4.5 cm), precisely where these impact craters predominantly appear. These impact craters are most apparent on the capture plate between 4.5 cm radially outward from the center of the electrode

and the edge of the witness plate.

Macroparticles have been cited to have diameters as large as 200 µm.[13, 25, 28, 100, 14, 15, 61] In the images shown above, the impact craters left on the carbon tape are between 100 and 400 µm. While many of these craters are larger than the expected size of macroparticles, these craters are significantly larger than the dielectric powder diameter (45 µm). The crater size may be larger than impacting particles. It is presumed that whatever particles are creating these impact impressions are traveling at a small angle with respect to the surface ($< 30°$), almost parallel. Therefore, it may be reasonable to assume that these particles may impact and drag along the surface of the carbon tape before being cooled and being captured or reflected off of the tape. Furthermore, the carbon tape is a soft material that may easily deform. Furthermore, it is suspected that these particles impart a large majority of their kinetic energy in the carbon tape. So the impact craters on the carbon tape may be similar to that observed on a larger scale like that from meteoroids impacting a surface, where the crater of region of damage to the surface is actually much larger than the impacting object itself. Although no metal deposits were readily observed on the witness plate, particle cooling, small particle size, and relatively limited microscope capabilities may have prevented detection. Therefore, it seems as though this curious occurrence could be explained as impacts by macroparticles.

5.3.3 Horizontal Particle Velocity Estimates

During testing, the witness plate is flipped so that the face with the sticky carbon tape is facing downwards towards the face of the electrode. Figure 5.7 shows the witness plate, where the white areas indicate more dense particle collection. The more gray areas on the electrode surface indicate areas where powder has been removed, exposing the gray steel. Since the witness plate is flipped over, the witness plate is a mirror image of the electrode in terms of areas of powder collection (removal on the

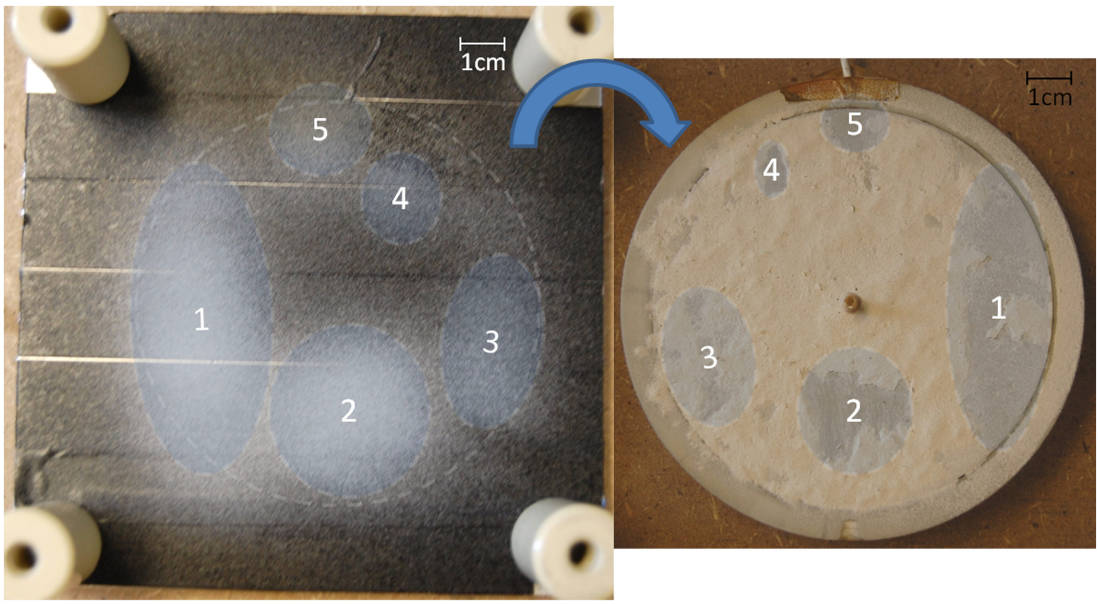

Figure 5.7: The witness plate (left) and electrode (right) after a test. Areas of the witness plate that collected powder correspond to areas of the electrode cleared of powder.

electrode).

Areas on the electrode cleared of dust are somewhat smaller than the corresponding areas on the witness plate. As the dust particles travel primarily vertically from the electrode to the witness plate, many dust particles also travel at least a small distance horizontally. By analyzing the magnification of the areas indicated in figure 5.7, a rough estimate of the ratio of horizontal to vertical velocity can be obtained. The horizontal velocity component is about 6.4% of the vertical component. It is also noted that the horizontal component of velocity along the magnet rows (x-direction) is about 7.0% of the vertical velocity compared to 5.5% for the horizontal component across the magnet rows (y-direction). This suggests that there is a preferential horizontal direction for dust ejection. This phenomenon is discussed further after PIV results confirm this observation.

5.4 Captured PIV Images

Images were captured using the high frame rate camera, and a laser with beam expanding optics was used to illuminate ejected particles. Several sequences of these images are presented herein, as well as the methods used to track and calculate the velocity distribution of ejected particles.

5.4.1 Particle Tracking and Image Velocimetry Methods

Figure 5.8 shows an example of a sequence that is 66.5 ms long that was captured with the high frame-rate camera. This sequence was imaged in the XZ-plane, at 2000 fps, with a maximum exposure time of 497 µs. A total of 133 images comprise this entire sequence, but only a few were selected at various intervals to show specific features. First notice that the large, bright oval region is the laser interrogation region projected on the electrode surface. Anything in the cylindrical volume above this area will be observable. Furthermore, in the first image shown, a cathode spot is visible approximately one centimeter to the right of the laser interrogation region. This cathode spot appears to be relatively dim because the notch filter removes a large portion of the light emitted from the cathode spot plume. In images one through four, the cathode spot is visible. The cathode spot is a type 2 cathode spot that ignites, burns out, and reignites at locations adjacent to previous spots. Within each single image, the cathode spot is burning, dying out, and reigniting several times, with lifetimes on the order of microseconds. This cathode spot continues to move closer and closer to the laser interrogation region until, in images four and five, the cathode spot finally enters the interrogation region and burns out for the duration of this sequence. The cathode spot is visible for only a small portion of this sequence, less than 12.5 ms, and travels approximately 12.5 mm. The 'velocity' of the cathode spot traveling across the electrode surface, based on the distance it traveled during

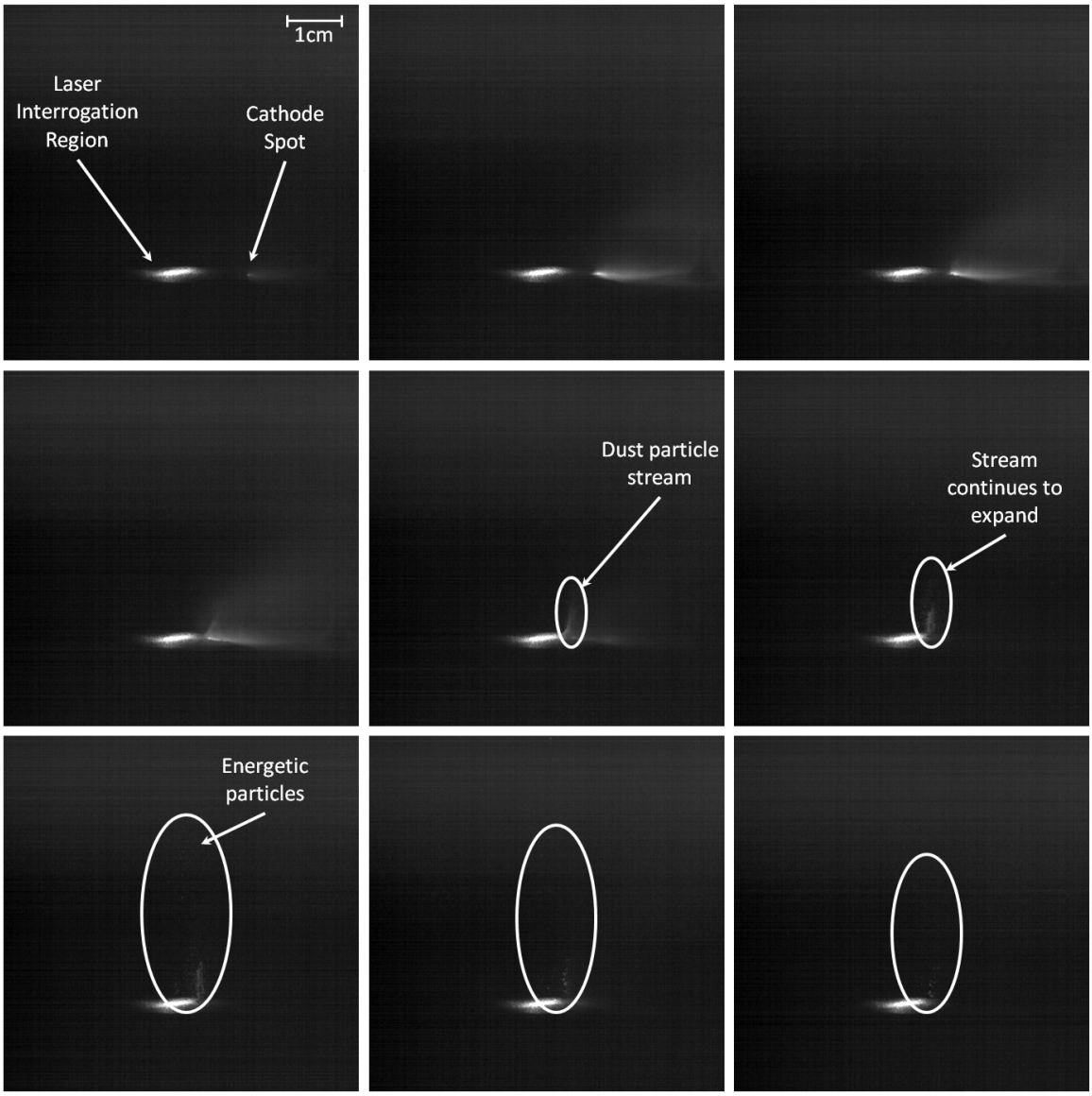

Figure 5.8: A sequence of images captures at 2000 frames per second with maximum exposure time. The order of images starts in the top row, reading from left to right, then the second row reading from left to right, etc.

this time period was approximately 1.0 m/s. This measured velocity is consistent with type 2 cathode spot velocities reported in the literature.[15, 14, 31, 110]

If the cathode spot is assumed to have a footprint of about 0.5 mm in diameter (see chapter IV), and subsequent cathode spots ignite on the edge of the previous spot, one radius (0.25 mm) away, then during this sequence approximately 50 cathode spots occurred over the course of etching the 12.5 mm track in the electrode surface. In the process of moving across the electrode, 50 cathode spots have been formed and extinguished, moving in a step-wise fashion, but etching a continuous track in the electrode surface. It is estimated then, that a cathode spot occurred once every 250 μs on average. Therefore, each image will capture approximately two cathode spots. Cathode spots are observable in every image captured during the first 12.5 ms of this sequence. There also may have actually been more than 50 cathode spots ignited since there may have been some small cathode spot motion in the axis perpendicular to the -$\mathbf{J}\times\mathbf{B}$ direction. From this data, it is likely that the cathode spots are only burning for a small fraction of the time during which the images are captured. However, while the cathode spots are burning, a large amount of light is captured so that when integrated over the exposure time, the cathode spot is still extremely bright and clearly visible.

Beginning in the fourth image, and definitely by the fifth image in figure 5.8, it becomes clear as the cathode spot enters the laser interrogation region, that a plume of powder is being ejected at the spot location. The cathode spot, as it moves along the surface of the electrode continues kicking up dielectric powder from the electrode surface, producing a stream of powder emanating from the root of the cathode spot. This stream becomes more visible in subsequent images after the cathode spot has died out. After the cathode spot has died out, the powder particles have already been accelerated by the cathode spot, and these particles continue to follow a trajectory into the overhead plasma, as can be seen in images five through nine. Because it

may be difficult to see the particles, the white oval has been added to images to show the location of the main stream of powder. The stream continues to expand, as the particles that have been imparted a large velocity continue to travel away from the slower particles. Eventually the particles begin to slow down due to the force of gravity and eventually fall back to the electrode surface, as shown in images eight and nine in figure 5.8. Also visible is a stream of energetic particles that leads the primary stream of particles. These particles are more faint, but still visible. It is clear from observing the particles ejected, that all particles travel primarily in the vertical direction, with a very small component of velocity in the horizontal direction.

In this sequence, figure 5.8, the camera was positioned at the positive y-axis, looking in the negative y-direction. The interrogation region is centered near x = 2.5 cm, y = 0.5 cm. In section 4.5, the $\mathbf{J}\times\mathbf{B}$ force is shown to have a significant effect on the apparent motion of type 2 cathode spots on the electrode surface. However, in those previous experiments it was unclear if spots were moving in the Amperian or retrograde ($-\mathbf{J}\times\mathbf{B}$) direction. Figures 4.15 and 4.16 show the patterns scribed into the electrode following $\mathbf{J}\times\mathbf{B}$ force lines, but it was unclear whether the direction of motion was Amperian or retrograde. It becomes apparent in this sequence of images, that this cathode spot is in fact moving in the retrograde direction. If the cathode spot were moving in the Amperian direction, it would be moving from left to right, in the opposite direction, in the images.

Motion in the retrograde direction has been observed by many others, and was previously discussed in section 2.2.2 on page 29.[33, 35, 86, 100, 29, 7, 123, 112, 62] The conditions for this experiment are consistent with those who have observed retrograde motion. The background pressure in the chamber is relatively low ($\sim$ 125 mTorr), and the magnetic field is relatively low ($<$ 1200 G) at all locations on the electrode surface.[100, 29, 15, 14] The experiment conditions are similar to those performed in the GEC cell, therefore it may be reasonably assumed that cathode spots were also

traveling in the retrograde direction in all of these experiments.

Figure 5.9 shows a sequence of images captured at only 1000 fps, with a maximum exposure time of 997 µs. This particular sequence of images was taken at a relatively low frame rate; most images analyzed for the PIV results were taken at 2000 fps. By imaging at a slower frame rate, the exposure time can be increased, therefore increasing the brightness and the visibility of particles, so that particle can be observed more readily. However, the settings for the electrode, powder layer, overhead background plasma, and actual cathode spots that were ignited remained the same. Several sequences of images similar to that shown in figure 5.9 are captured. Therefore, through detailed analysis of image sequences captured at 1000 fps, it has been verified that cathode spots typically eject and form 'fountains' of dielectric particles similar to figure 5.9, where many particles emanate from a previous cathode spot. Similar to the previous sequence shown, only a few images were selected at somewhat constant time intervals to give the reader an idea of how the images evolve over time.

The first image in this sequence (top left), shows a cathode spot burning. By the time that the cathode spot burns out, and the plume diffuses and is dissipated, the particles have already been given their initial ejection velocity. However, due to the short lifetime of the cathode spots, the particles have not traveled any significant distance until several images after the cathode spot has died out. The second image in this sequence shows the particles as they travel away from the original cathode spot. This plume continues to expand as those particles with greater velocities travel farther ahead of the main pack. By the fourth image, it is clear that the fountain contains particles with a distribution of velocities. The particle velocities are directed primarily in the vertical direction. In images five and six, another cathode spot strikes, before particles from the previous spot have even begun to fall back to the electrode surface. In image seven, the particles ejected from the first spot are beginning to slow down due to the force of gravity. However, a new stream of particles is beginning

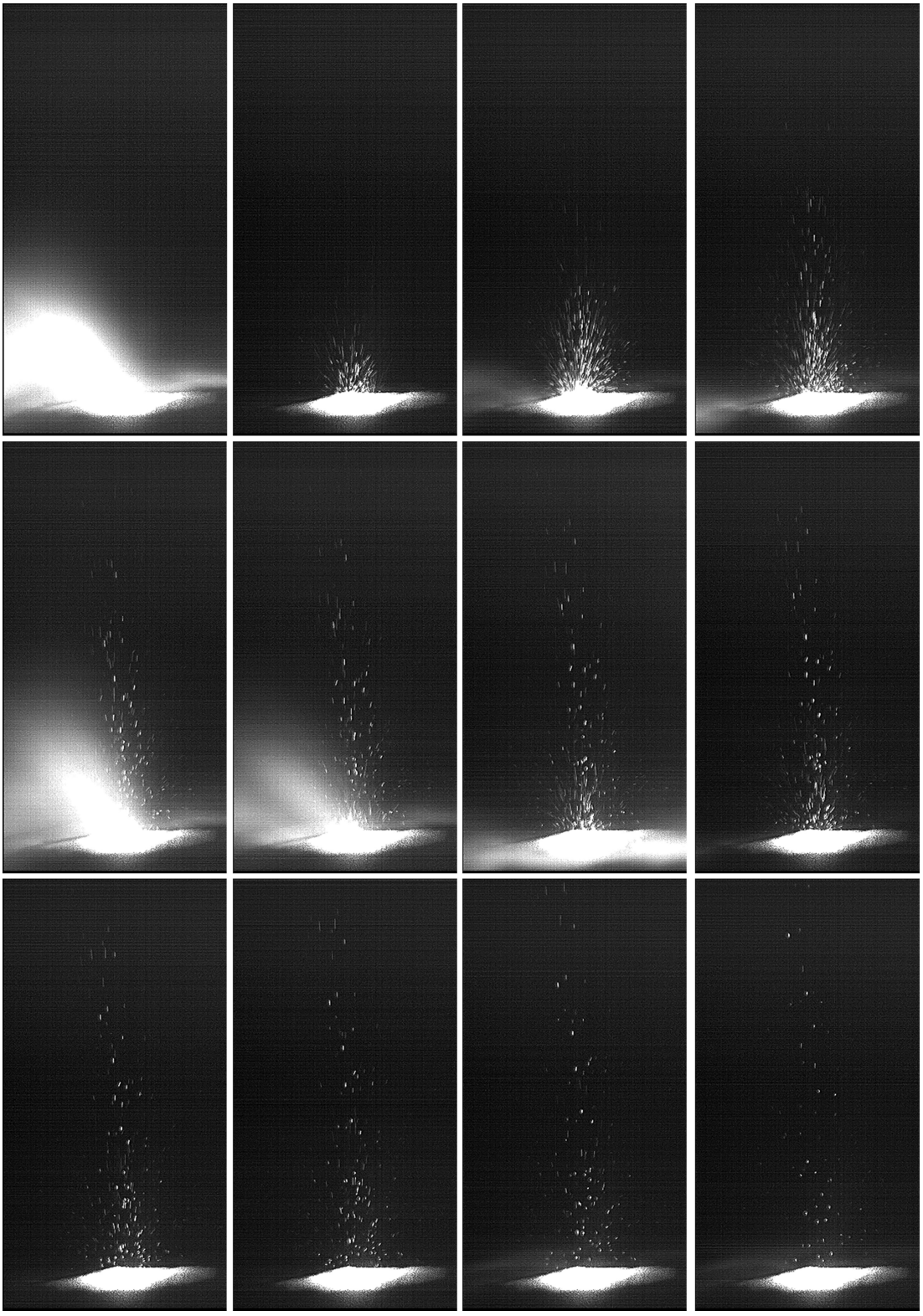

Figure 5.9: A sequence in which a cathode spot creates an intense and bright fountain of dust particles emanating from the electrode surface.

to travel outward, ejected from the second cathode spot. These particles appear as streaks initially, as the first particles that are observed are high velocity particles. Another consequence of imaging at slower frame rates and longer exposure times is that fast particles tend to leave streaks, as the fast particles move some non-trivial distance during the exposure time. Eventually, in image nine to the end, the particles reach their peak height above the electrode, and begin to fall back to the electrode surface. The images show that many particles fall back to the electrode in the same vicinity of the initial cathode spot.

The sequence shown in figure 5.9 shows the particles when they are ejected, along with many particles falling back to the electrode surface. If it is assumed that these particles follow a ballistic trajectory, with only the force of gravity acting on these particles, an estimate of the particle velocity can be made from the time of flight. All particles are assumed to have been ejected from the initial cathode spot, and most particles can be followed for the duration of their trajectory to confirm this. The particle time of flight ranges from 50 to 200 ms for all visible dust particles that return to the electrode. Therefore, assuming a ballistic trajectory, the vertical velocity is estimated to be between 0.25 m/s and 1.0 m/s. Most particles are observed to fall back to the electrode in the same vicinity of the electrode. Assuming that particles are ejected in approximately the middle of the interrogation region, the particles would have to travel 1 cm horizontally during the time of flight to escape from the interrogation region. Therefore, since most particles are visible when they fall back to the electrode, it is estimated that the horizontal velocity is between 0.05 m/s and 0.2 m/s. The next sections will provide more detailed analysis that support these estimates.

5.4.2 Equations of Motion

Over the course of the trajectory of an ejected dielectric particle, the velocity will change substantially. The velocity will range from the velocity at the initial point of injection, to approximately zero as the particle reaches the highest point in its trajectory. So, as a standard for all particles tracked, the particle velocity at the moment of initial ejection will be calculated. It has been shown from the collection of several sequences of images, shown above, that dielectric particles are ejected primarily in the vertical direction, and often return to the electrode in the direct vicinity of the initial ejection site. No observations of dust grain formation have been observed. In these experiments, it is unlikely for dust grains to form due to the relatively large particle size (45 µm diameter). The lower limit on the size of particles that can be imaged due to the diffraction of light is on the order of half of the wavelength of laser light used.[79] All particles over approximately 325 nm in diameter will be visible. However, any particles below this size will not be observable, and is a source of error in these measurements. Given the average particle diameter of 45 µm, very few particles are expected to fall below this limit. However, it is not entirely clear what forces will act on the dielectric particles over the course of the particle trajectory.

Electromagnetic forces will have very little effect on particle motion once the particle leaves the sheath at the surface of the electrode. It is possible that the electric field between the dielectric surface layer and edge of the sheath may act to accelerate charged dielectric particles, in addition to the momentum transfer from the cathode spot plume–particle interaction. However, in these experiments, the sheath is expected to be on the order of one Debye length ($\sim$ 1.0 mm). Therefore, the particle trajectories are observed when the particles are well beyond 1 mm from the electrode, and therefore well beyond the distance required for the plasma to shield the electrode electric field. Furthermore, when the particles are more than one millimeter

from any other particle, the electric field from other particles can be neglected. When particles are closer than 1 mm, which was observed for the slow particles in figure 5.8, the electric field between particles is small and is mostly due to small differences in collected charge. However, because all particles are expected to be charged to approximately the plasma floating potential, these electric fields will be small, and can also be neglected.

The only gravitational force of Earth is affecting particle trajectories, where g = 9.81 m/s^2. Furthermore, the overhead plasma above the electrode is assumed to be approximately uniform with no significant temperature gradients or variation, so thermophoretic forces can be neglected. Also, radiation from the plasma is assumed to be small enough, such that radiation pressure will be negligible. However, the effects of ion and neutral drag require more careful consideration.

Ion and neutral particles can affect dust particle motion in three ways: 1) direct ion impact collisions; 2) electrostatic Coulombic collisions with ions; and 3) neutral and ion fluid flow. Obviously, the first two forces can only be due to ions. Consider that for these first two cases, the dust particle mass for 45 µm diameter particles is more than 10^{15} times larger than an argon ion's mass. Therefore neither of these two forces will have a large effect on the particle trajectory. The neutral drag force due to fluid flow will not be a significant force on the particle trajectory in these experiments because the plasma is not flowing, and the pressure is so low inside the vacuum chamber that there will be essentially no 'wind' resistance. Furthermore, the estimated Larmor radius for particles is beyond larger than the size scale of these experiments. Collisions between particles on the surface just before launching are likely a dominant energy transfer mechanism. Once airborne, however, collisions were not observed to occur. So ejected particles will have a ballistic trajectory, with only gravity acting on the particles.

Therefore, conservation of energy was used to calculate the initial velocity im-

parted to a particle at the time that it was ejected, since no energy will be extracted from the system during particle flight. Using simple classical mechanics, this can be written as:

$$\epsilon_d = \frac{1}{2} m_d \left[v_x(t)^2 + v_y(t)^2 + v_z(t)^2 \right] + m_d g z(t) = constant \tag{5.1}$$

where ϵ_d is the total energy of the dust particle, $v_x(t)$, $v_y(t)$, and $v_z(t)$ are the velocity of the dust particle in the x, y, and z-directions as a function of time, respectively, g is the gravity constant (9.81 m/s^2), and $z(t)$ is the vertical distance above the electrode as a function of time. The dust particle energy is a constant since as the particle moves in the plasma, friction and drag are neglected, and so the particle will only slow down due to gravity, which adds to the particle energy in the form of potential energy. Therefore, the x and y velocities will remain constant throughout the particle trajectory. Considering the particle energy only in the vertical direction:

$$\epsilon_{dz0} = \frac{1}{2} m_d v_{z0}^2 = \frac{1}{2} m_d v_z(t)^2 + m_d g z(t) \tag{5.2}$$

where the subscript '0' denotes values at the time of ejection. The coordinates are setup so that, at the point of ejection, all particles' z-coordinate is zero at the surface of the electrode. From this equation, the initial ejection velocity can be solved for:

$$v_{z0} = \sqrt{v_z(t)^2 + 2 g z(t)} \tag{5.3}$$

By obtaining the particle position and velocity as a function of time, the particle's initial ejection velocity can be calculated.

5.4.3 Particle Tracking Algorithm

Identifying and tracking dust particles traveling through the overhead plasma was a difficult and time-consuming task. An algorithm utilizing particle brightness, and previous frames to judge expected position and velocity was implemented to assist in tracking the ejected particles after being initially identified manually. The algorithm was tested by comparing measurements to manual particle tracking. The algorithm, however, was limited to tracking relatively isolated particles, and sequences with a large number of particles close together still had to be manually tracked. However, many particles were still tracked using the algorithm. Particle position in pixels was obtained, and a small piece of alumina tubing was utilized for size scaling to convert pixel location to position.

Therefore, particle position as a function of time was obtained. Since the frame rate of the camera was known, the time between images is known (2000 fps = 500 µs). From this information, a particle's instantaneous velocity was easily calculated. The cathode spot plume lasted for only a few microseconds, and was extremely localized, so that subsequent cathode spots were considered to have no effect on particles ejected from previous cathode spots once they left the near-cathode spot area.

5.5 Particle Ejection Velocity Distributions

It was observed in the sequences of images collected above, that many particles were ejected from each cathode spot, and that the velocity of these particles varied greatly. Up until this point, only rough estimates of particle velocity have been made. In this section, the particle distribution functions are determined more precisely, using the standard method outlined above.

5.5.1 Horizontal Velocity Measurements

Very little information has been revealed regarding the particle velocity in the horizontal direction. An estimate of particle velocity in the x and y-directions was made in section 5.3.3 as a percent of the vertical velocity. Since the witness plate was 1.8 cm away from the electrode surface, and the particle trajectories are ballistic, the lower limit of the velocity of particles collected on the witness plate can be estimated. Using the conservation of energy equations above, the particle velocity in the vertical direction must have been:

$$v_{0z} = \sqrt{2gz_{max}} \tag{5.4}$$

where z_{max} is the maximum vertical height above the electrode reached by a particle ejected at v_{0z} from the electrode surface. Setting z_{max} equal to 1.8 cm, the distance between the electrode surface and witness plate, v_{0z} is 0.59 m/s. So particles must be ejected at a velocity greater than 0.59 m/s to be collected by the witness plate. Now that the lower limit of the vertical velocity of particles collected on the witness plate is known, the horizontal velocity components can be estimated. The average estimated horizontal velocity was found to be about 6.4% of the vertical velocity, yielding a horizontal velocity estimate of 0.038 m/s. Keep in mind, however, that this is the lower limit of horizontal velocity. If particles were traveling faster in the vertical direction, then the horizontal velocity will subsequently also be larger.

5.5.1.1 X-Direction Velocity Distribution

Many sequences of images were collected and analyzed by particle tracking while the camera was viewing cathode spots in the XZ-plane. The distribution of particle velocity in the x-direction is given in figure 5.10. The mean and median velocity in the x-direction for particles was 0.29 and 0.26 m/s, respectively. The distribution for the particle component of velocity in the x-direction is centered around zero, and has

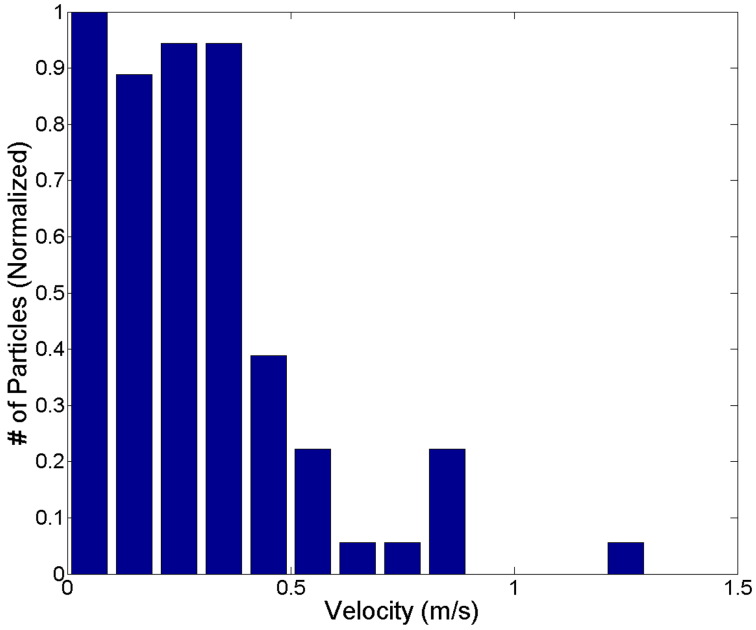

Figure 5.10: The distribution of the x-component of velocity imparted to particles ejected from the electrode. All values are normalized.

a somewhat Gaussian shape, trailing off significantly beyond 0.5 m/s.

5.5.1.2 Y-Direction Velocity Distribution

Images taken with the camera viewing the electrode in the YZ-plane, and the image analysis resulted in the distribution shown in figure 5.11. The distribution of the y-component of particle velocities is again centered at zero. However, it is interesting to note that, in contrast to the x-component distribution, the y-component distribution drops off drastically beyond 0.1 m/s. The average and median for the y-component of velocity is 0.17 m/s and 0.08 m/s, respectively. This is a significant difference between the x and y-direction distributions that were expected to be almost identical. The x-direction velocity distribution has a much more significant high energy tail that comprises a significant fraction of particles in the overall distribution.

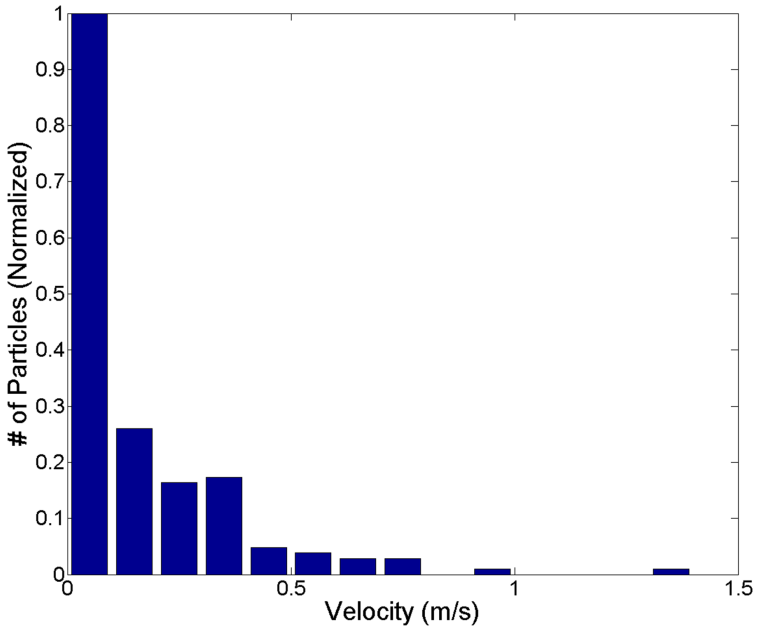

Figure 5.11: The y-component of velocity imparted to particles ejected from the electrode.

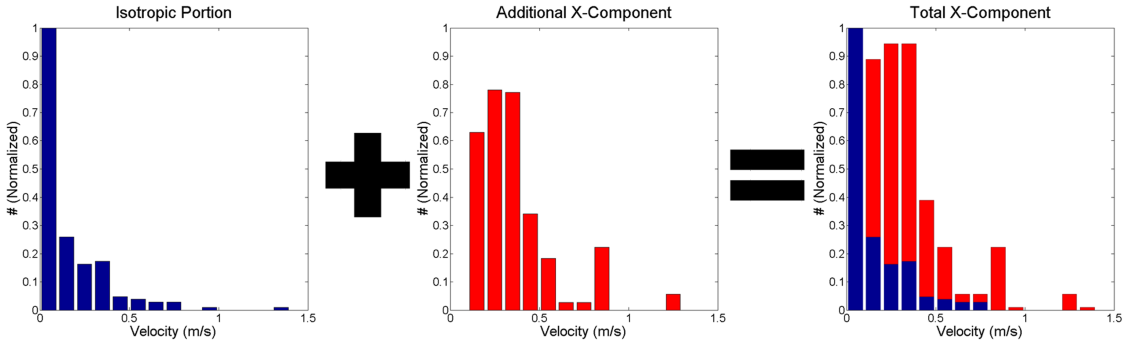

Figure 5.12: The isotropic (left) and high-energy tail (center) portions that make up the total x-component velocity distribution (right).

5.5.1.3 Non-isotropic Horizontal Particle Ejection

Experiments herein have shown that type 2 cathode spots have been generated on the electrode, and tend to move in the retrograde, or -$\mathbf{J}\times\mathbf{B}$ direction on the electrode surface. Cathode spots moving in the retrograde direction primarily move in the positive or negative x-direction on the electrode surface, as they move parallel to the rows of magnets. Only at the very ends of the magnet rows do the cathode spots move any significant distance in the y-direction. However, type 1 cathode spots have been observed to form on the electrode surface as well.

Inspection of figure 5.10 suggests that the distribution of velocity in the x-direction may be broken down into two components, as shown in figure 5.12. The first component of the distribution (figure 5.12, left) is a distribution that is the same shape as the y-direction distribution (figure 5.11). The second component (figure 5.12, center), comprises the high-velocity tail from figure 5.10. The second component of the distribution is derived by the subtraction of the y-direction distribution from the x-direction distribution. The x-direction and y-direction distributions were assumed to be identical since isotropic particle dispersion is expected in the horizontal plane. However, the differences between these two distributions suggest that there is an additional factor that contributes to and accounts for the high energy tail in the x-direction. The distribution for this additional contributor peaks between 0.2 and 0.4 m/s, and has a mean and median between 0.3 and 0.4 m/s. The distribution has a bell-shaped curve, similar to the vertical velocity distributions presented below.

Before data analysis, it was presumed that if particle dispersion in the horizontal plane was not isotropic, that it would be due to magnetic field effects on the plume. The thought was that cathode spot plumes bending and following along the magnetic field lines, as shown in chapter IV, would preferentially transfer more energy to particles in the y-direction. This would cause the particles to have a higher y-component of velocity. However, the opposite is observed, with particles gaining a

greater x-component of velocity.

The presence of the seemingly two distributions for the x-direction is most likely due to two related causes: 1) cathode spot type; and 2) type 2 cathode spot motion. In the YZ-plane of view, particle motion in the x-direction was not visible, as particle motion in the x-direction was into and out of the page. However, in the XZ-plane of view, type 2 cathode spots moving and the ejection of powder with a significant velocity component in the x-direction became visible. The first distribution shown in figure 5.12 (left), is the result of expected isotropic particle dispersions in the horizontal plane. This isotropic dispersion was most likely and commonly caused by type 1 cathode spots. The type 1 cathode spot will occur once at some random electrode location, one that is favorable for cathode spot formation. After this type 1 cathode spot dies out, another spot does not reignite nearby anytime soon, if ever. This cathode spot will eject powder isotropically in the x and y-directions. Type 2 cathode spots move mostly along the magnet rows in the x-direction, lending itself to be the most likely additional contributor of this high-energy tail in the x-direction. These cathode spots moving along the magnet rows have been observed to have a so-called 'snowplow' effect, building up a small pile of powder in front of the spot as it moved. As the spot moved in the retrograde direction on the electrode surface, powder was preferentially directed in the same direction as the cathode spot, resulting in a small pile at the end of a type 2 cathode spot's continuous track on the electrode surface. This is the mechanism that is suspected to have occurred many times, giving a large portion of particles a larger x-component of velocity.

A type 2 cathode spot will ignite, eject particles, extinguish after a few microseconds, and then reignite nearby as it moves in the retrograde direction (primarily along the magnet rows, in the x-direction). However, before dust particles ejected by the previous spot can move more than a few microns and leave the vicinity of the previous spot, a subsequent cathode spot forms. This subsequent spot will likely occur on the

edge of the previous spot, only a short distance from the original particle ejection site. Therefore, this spot will likely occur at a location in the vicinity of some powder particles that have just been ejected, and that are traveling in the same direction as the cathode spot. This second spot may be capable of giving particles ejected with some component of velocity in the x-direction a second boost. This could happen several times as the particle continues to travel along with the cathode spots in the retrograde direction, and the particle may get boosted multiple times. Each time the particle gets boosted again, the x-component of its velocity is increased. Once the type 2 cathode spots stop reigniting, or the particle gains enough energy to outrun the cathode spot plume's realm of influence, the particle follows a ballistic trajectory. Type 2 cathode spots have a tendency to move at velocities of 0.1 to 1.0 m/s on the surface of the electrode, primarily in the x-direction, and the distribution of the x-component of particle velocities has been shown to have approximately the same magnitude (figure 5.12, center).[15, 14, 31, 110]

It should also be noted that, while the exact magnitude of the horizontal velocity components is, in most cases, larger than the 0.05 to 0.2 m/s estimated from witness plate experiments on page 139, it is comparable. Also, the horizontal velocity estimates were clearly stated to be a lower limit to the velocity components, as particles were assumed to be traveling in the vertical direction at the minimum velocity required to reach the witness plate (0.59 m/s). As will be shown in the next section, these particles obtain vertical components of velocity greater than this. Furthermore, witness plate measurements also estimated that the x-direction component of velocity would be slightly larger than the y-component of velocity, as was shown to be the case here.

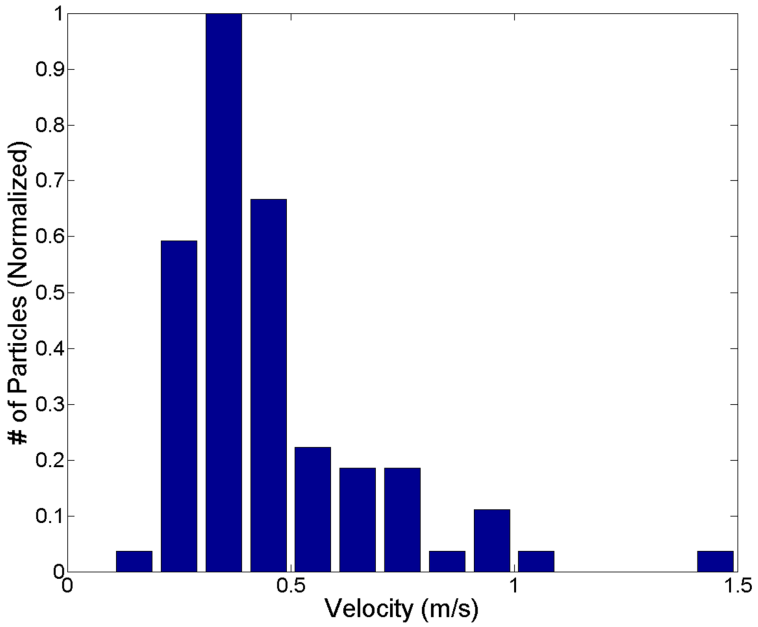

Figure 5.13: The vertical component of particle initial ejection velocity when viewed in the XZ-plane of view.

5.5.2 Vertical Velocity Measurements

While the x and y-components of the particle velocity are of interest, the most important parameter for this application is the vertical component of particle velocity. This vertical component of velocity will determine the depth to which particles are able to penetrate the plasma layer.

5.5.2.1 Vertical Velocity Distribution in X-Z and Y-Z Plane

Figure 5.13 shows the vertical component of velocity only for those instances in which the camera is positioned to observe the XZ-plane. The mean for this distribution is 0.54 m/s, and the median is 0.40 m/s. The distribution of velocity is positive for all values, as the main component of velocity imparted to particles is in the vertical direction. This distribution appears to have a Maxwellian type of shape to the distribution, with a majority of particles being ejected with velocities below 0.5 m/s,

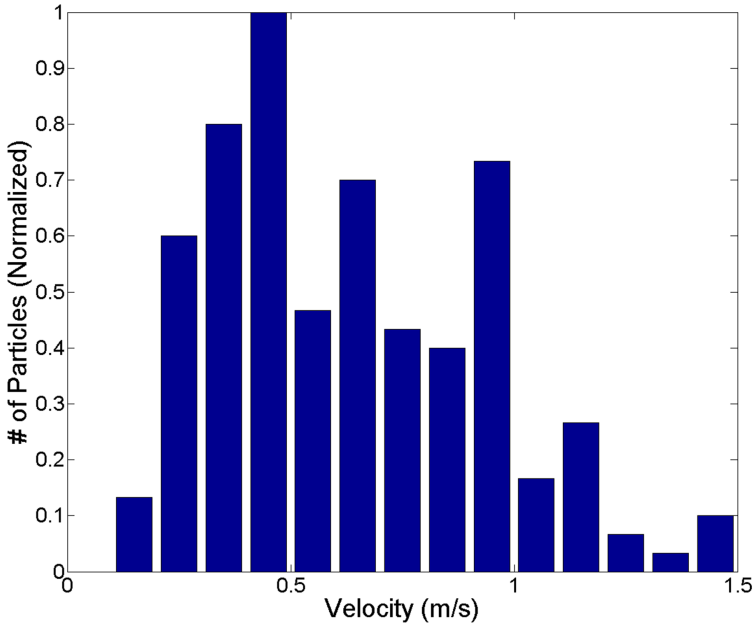

Figure 5.14: The vertical component of particle initial ejection velocity when viewed in the YZ-plane

but with a tail that trails off beyond 1 m/s.

When the camera is positioned to observe the YZ-plane, the resulting distribution has a mean and median of 0.72 m/s and 0.61 m/s, respectively. This distribution is shown in figure 5.14. The distribution has a Maxwellian type of shape, however, once again there is a large disparity between the distribution in the XZ and YZ-planes. The distribution of the vertical component of particle velocity when viewed in the YZ plane has a much greater mean and median, and has a significant portion of particles ejected with velocities ranging from 0.5 to 1.5 m/s.

It is possible that the discrepancy in the shape of the distributions and vertical velocity given to particles when viewed in the XZ and YZ-plane may also be related to the cause of the non-isotropic particle dispersion in the horizontal plane. It may be possible that each cathode spot exerts a fixed impulse on the powder layer, and therefore, only transfers a fixed amount of kinetic energy to dielectric particles. Consider a case where a type 1 cathode spot disperses powder isotropically in the horizontal

plane, giving some small amount of kinetic energy to particles in the horizontal direction, and depositing a majority of kinetic energy in the vertical direction. Now, consider a second case in which a type 2 cathode spot is moving rapidly across the electrode surface, imparting a relatively large amount of kinetic energy to particles in the x-direction. Therefore this cathode spot, as a result, may deposit a slightly lower amount of kinetic energy to particles in the vertical direction since a large portion was transferred to particles in the horizontal plane. Particles in this second case get a large velocity in the x-direction, and smaller velocity component in the vertical, or z-direction. Meanwhile, in the first case, the opposite is true—particles receive a large vertical velocity component and a small horizontal component of velocity. Sequences such as those described in the second case are more readily observed in the XZ-plane since the type 2 cathode spots move primarily in the x-direction, and the x-component of particle velocity cannot be viewed in the YZ-plane. Therefore, the vertical velocity as observed in the YZ-plane is greater than the vertical velocity in the XZ-plane.

5.5.2.2 Total Vertical Velocity Distribution

The distribution shown in figure 5.15 is the distribution of the vertical component of velocity for all particles at the time of ejection from the electrode surface. The mean and median for the distribution is 0.66 m/s and 0.50 m/s, respectively, with the most common velocity being between 0.30 and 0.40 m/s. Therefore, the vertical component of the initial particle velocity at the time of injection is clearly the largest and most significant component of ejection.

Of particular note, is that most particles are ejected with vertical velocity components between 0.2 and 1.0 m/s. A range of 0.25 to 1.0 m/s was estimated in section 5.4.1, on page 139. This range was estimated from particle time of flight as observed in the second sequence of particle ejection presented above, and the estimate assumed

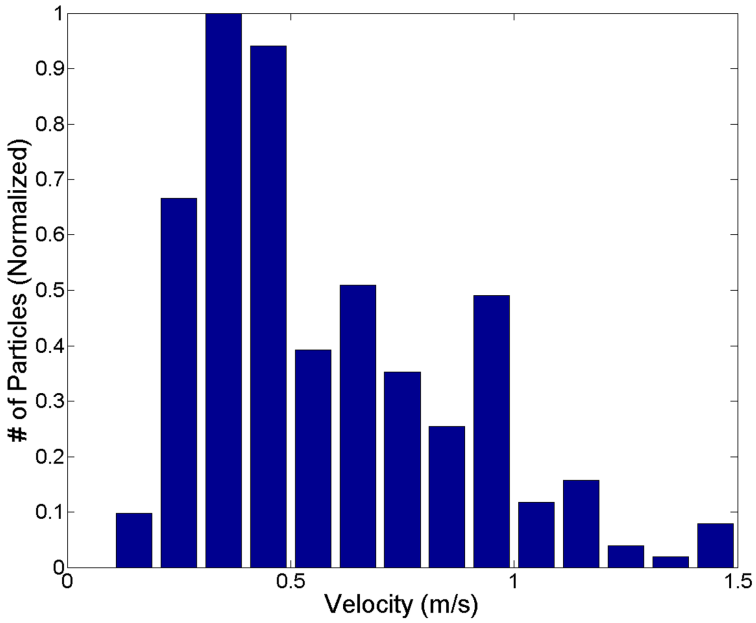

Figure 5.15: Distribution of the vertical component of particle velocity at the time of particle ejection from the electrode surface.

Direction	**Mean (m/s)**	**Median (m/s)**	**Mode (m/s)**
x	0.29	0.26	0.0 to 0.1
y	0.17	0.08	0.0 to 0.1
z	0.66	0.50	0.3 to 0.4
Total	0.74	0.60	0.4 to 0.5

Table 5.2: Summary of statistical values for the distributions presented above.

that particles followed a ballistic trajectory.

Figure 5.16 shows the distribution of velocities for particles at the time of ejection from the electrode surface. For this measurement, only two components of velocity are included since it is presumed that any particles with a large component of velocity into or out of the page will quickly exit the interrogation region. The mean and median for this distribution is 0.74 m/s and 0.60 m/s,respectively. The most likely velocity of a particle at the time of injection is between 0.4 and 0.5 m/s. Table 5.2 lists the mean, median, and most common velocity component for particles in each direction.

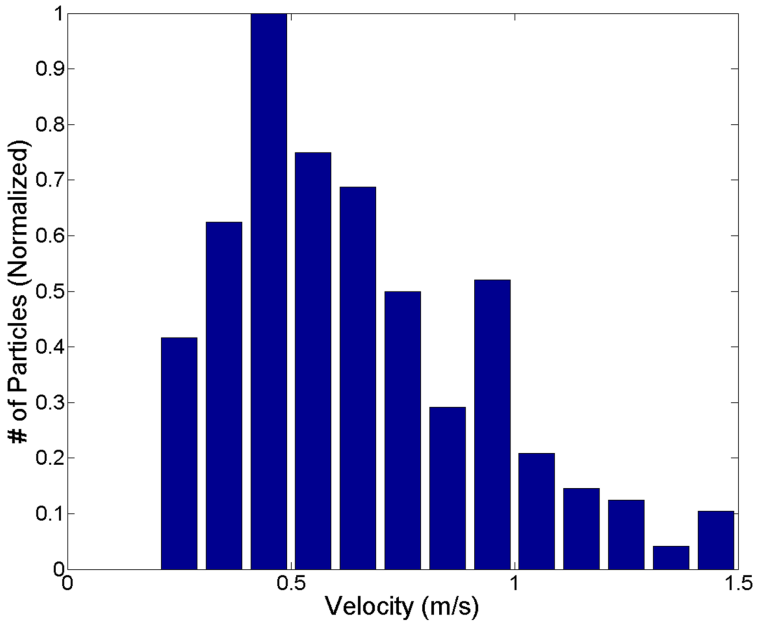

Figure 5.16: Distribution of the total particle velocity (horizontal and vertical components) at the time of particle ejection from the electrode surface.

The high pressure of the cathode spot plume, emanating from the cathode spot at a very high flow rate, creates a pressure that is the main mechanism of dielectric particle acceleration. A calculation to determine the cathode spot pressure required to accelerate particles to the velocities measured above can be performed. The cathode spots last on the order of 2 to 25 µs. Then from the maximum velocity of 1.5 m/s, the approximate acceleration can be calculated:

$$a_d = \frac{v_d}{\Delta t} \tag{5.5}$$

where a_d is the acceleration of the dielectric dust particle, v_d is the final particle velocity after being accelerated by the cathode spot plume for the duration of the cathode spot lifetime (2 to 25 µs). Then the acceleration must be 60,000 to 750,000 m/s^2, depending on the cathode spot lifetime. Since the average particle size and mass is known (45 µm and 1.86×10^{-10} kg), the force can then be easily calculated.

The pressure of the cathode spot is then a function of the force and area on which the force is exerted:

$$P_{sp} = \frac{F_{sp}}{A_d} = \frac{m_d a_d}{\pi r_d^2} \tag{5.6}$$

where P_{sp} is the pressure of the cathode spot, F_{sp} is the force of the spot, A_d is the area over which the force is applied, assumed to be the cross-sectional area of a 45 micron diameter particle. Then the cathode spot pressure is found to be no more than 87.75 kPa, or 658 Torr. This is the upper limit for cathode spot pressure, which assumes a cathode spot that lasts for only 2 µs and accelerates a particle to 1.5 m/s. The lower limit of cathode spot pressure is just barely above the background gas pressure (less than 4 mTorr above the background gas pressure), and assumes a cathode spot that lasts for 25 µs and accelerates a particle to just 0.1 m/s.

Therefore, even the cathode spot pressure calculated is likely lower than the actual cathode spot pressure. The calculation above assumes that there is perfect transfer of kinetic energy of the gas plume to the particle. In reality, the efficiency of this process will be less than perfect, meaning that cathode spot pressure may be higher than the estimated value.

Using the cathode erosion rate ($\sim$ 40 to 284 µg/C), cathode spot lifetime (2 to 25 µs), and cathode spot plume flow velocity (10^4 m/s), a crude calculation of cathode spot pressure can be performed.[15, 14] The resulting estimated cathode spot pressure is around 100 atmospheres. This estimate is in agreement with cathode spot pressure cited in the literature ($\sim$ 1 to 50 atm).[14, 20]

This calculation overestimates the cathode spot pressure since the erosion rate for a stainless steel electrode would be significantly less than that for a copper electrode. Therefore, the latter calculation of pressure provides an upper limit for the cathode spot pressure observed in these experiments.

5.6 Implications

The distributions of the particle velocity at the time of ejection from the electrode surface have been presented and discussed. These results may have an important effect on the end application, radio blackout mitigation.

5.6.1 Particle Mass Flux Rate

In order to deplete the electron population in the reentry plasma layer, a sufficient amount of powder must be ejected from the electrode surface. In previous experiments the witness plate was placed 1.8 cm above the electrode surface, and the mass of powder collected on the witness plate yielded the mass flux from the electrode surface. However, several particles are ejected without sufficient velocity in the vertical direction to reach the witness plate at an altitude of 1.8 cm above the electrode. In order to reach an altitude of 1.8 cm above the electrode, a velocity of at least 0.59 m/s must be obtained. However, a significant portion of particles will not have the vertical component of velocity required to reach the witness plate. Therefore, the mass ejection rate of 3.3 mg/s measured previously in chapter IV is significantly underestimated. To simplify this calculation, lets assume that any particle ejected at a velocity below 0.60 m/s, was not captured by the witness plate. Then, the distribution in figure 5.15 shows that only about 40% of all particles will reach the witness plate. This means that 60% of the particles that were ejected would fall back to the electrode surface. Correcting for the percentage of particles that were ejected, but never reached the witness plate, the actual mass ejection rate of particles from the electrode is closer to 8.4 mg/s. Therefore this is a significant difference from the previously estimated 3.3 mg/s, which vastly underestimated the mass ejection capability of this method.

5.6.2 Particle Penetration Depth

For quenchant methods to be successful, at least two requirements must be met: 1) the number of quenchant particles must be sufficient to deplete plasma to the desired level; and 2) ejected quenchant particles must penetrate the plasma layer thickness to form a dielectric channel through which the electromagnetic communication waves can propagate. If the particles cannot penetrate through the thickness of the plasma layer, then radio transmissions will traverse through the plasma layer until the cutoff frequency is encountered. At this point, the signal will be reflected. Therefore, it is important that particles are able to deplete the plasma layer through the entire thickness of the plasma layer.

Using the particle distribution data and assuming a ballistic particle trajectory, estimates can be made for particle penetration depth into the plasma layer. From the vertical velocity distribution presented, particles ejected at 1.5 m/s may be able to penetrate roughly 11.5 cm into the plasma layer. With an average vertical particle ejection velocity of 0.66 m/s, the average penetration of particles into the plasma layer will be over 2.2 cm.

A large amount of experimental data from the RAM test flights, as well as more recent computer modeling data predicts the plasma layer density as a function of thickness for several different flight conditions.[108, 64, 47, 105, 49] Our proposed approach matches or exceeds the penetration of other past liquid injection methods.[108, 64, 47, 105, 49] The injection depth may be improved with greater cathode spot current and particle size optimization, if required. However, the current injection method is capable of launching dust particles to depths in the plasma layer beyond the peak electron density region, approximately 2 to 3 cm from the vehicle surface, as shown in figure 5.17.[80]

During actual reentry and hypersonic vehicle flights, particle trajectories will not be ballistic, and additional factors such as ionized plasma flow, vehicle shape, angle of

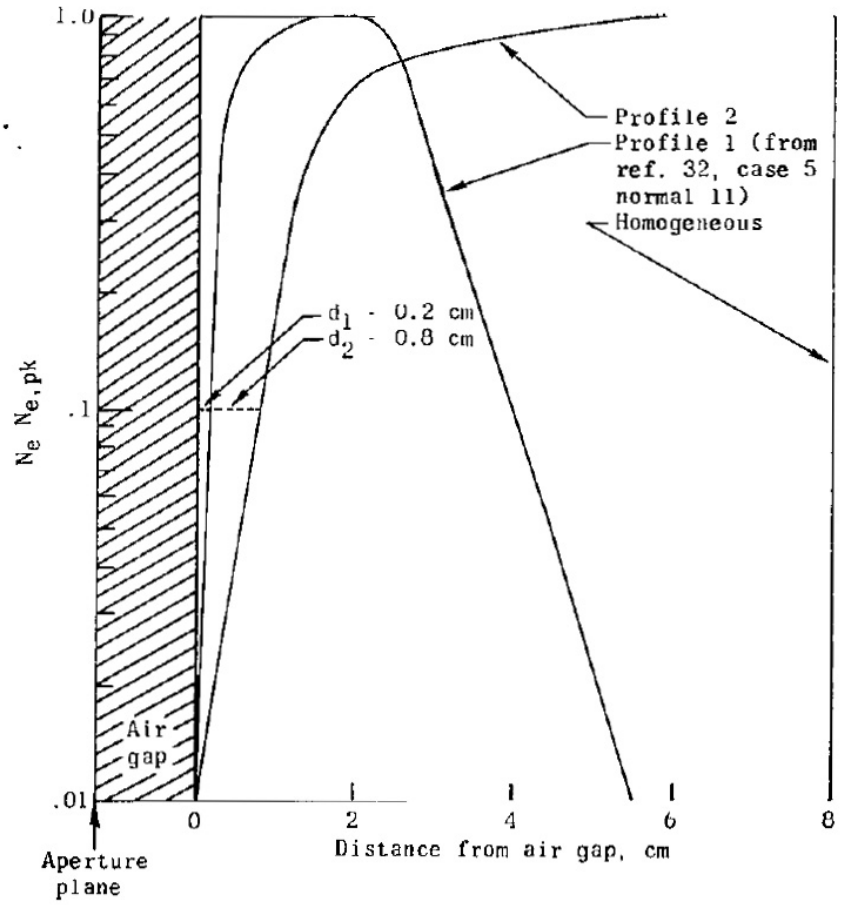

Figure 5.17: Electron density profile from RAM C-II (profile 1) and RAM C-I (profile 2) flights.[80]

attack, antenna placement and orientation, and varying pressure and velocity along the vehicle trajectory will effect the particle trajectory after injection. While the flow around the vehicle may be hypersonic, the boundary layer in contact with the vehicle surface will be stationary, providing a very thin layer in which the flow around the vehicle will be significantly below the vehicle velocity. Furthermore, the injection site could be placed at a stagnation point on the vehicle, where the flow will be static or much slower than the vehicle velocity over a somewhat larger region. It has been shown, however, that in this static situation, this injection method may be sufficient to penetrate the hypersonic plasma layer and is comparable to other systems previously used. Air flow and drag forces may distort the dielectric channel. If particles are injected into regions where flow around the vehicle is minimized, distortion of the dielectric channel may be minimized. Further testing, beyond the scope of this work, is required to verify and determine flow effects on the particle penetration depth.

Furthermore, the results discussed previously have again demonstrated the significant effect that an applied static magnetic field can have on cathode spot formation, powder dispersion, as well as the velocity and directionality of these particles. In the case of this application, it may be beneficial to reduce the horizontal component of velocity imparted to particles if it will result in a greater vertical component of velocity. The vertical velocity component is what determines the particle penetration in this case. Adjusting the magnetic circuit may affect the directionality of ejected particles, and will most likely affect the areas of the electrode that are cleared of powder, as has been shown in the experiments presented herein.

CHAPTER VI

Density Depletion Measurements

The underlying goal of this research is to investigate plasma electron depletion via dispersion of dielectric powder into a plasma discharge. The actual mass required to achieve meaningful depletion is assessed by means of controlled, mechanical particle dispersion into a plasma discharge. Following these experiments, cathode spot driven depletion experiments were carried out. The capacity of dispersion via cathode spots is compared with the required dispersion as determined by the mechanical shake tests.

6.1 Dust Shaker Measurements

Experiments presented herein are performed with a mechanical dust shaker device, described in chapter III, used to disperse dielectric powder into a plasma discharge. The plasma response, specifically the density of the plasma electron population, is then measured. The goal is to determine the amount of dielectric powder required to significantly deplete the plasma electron population. For these experiments, two planar Langmuir probes are used to measure electron saturation current in the positive column region of a glow discharge.

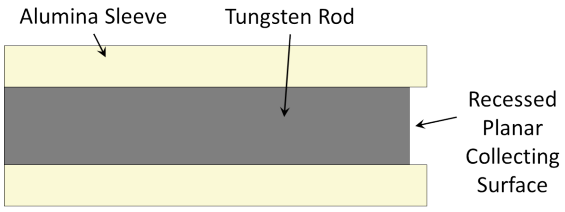

Figure 6.1: A schematic of the planar probes slightly recessed in the alumina sleeve.

6.1.1 Glow Discharge Characterization

The glow discharge used as the plasma source in this section is described in chapter III, and is initiated in the 'Bessie' vacuum facility. A relatively quiescent plasma source was required to carefully detect the plasma response to dust powder dispersion.

This plasma was initiated by biasing a 10 cm diameter electrode negative relative to a grounded anode, separated by 10 cm. A 500 Ω ballast resistor was used to measure discharge current. Approximately 10 sccm of argon was fed into the discharge chamber, resulting in a background pressure of 350 mTorr. A discharge was sustained with a discharge voltage between 450 and 500 V, and constant current of 40 mA.

Two planar Langmuir probes, 1.6 mm in diameter were used for initial plasma characterization and subsequent electron depletion measurements. The surface of the planar probes was slightly recessed in the alumina tubing, as shown in figure 6.1, in an attempt to prevent excessive collection of powder on the probe surface. The recessed current collecting surface will have little effect on the traditional Langmuir probe IV trace and probe operation. The shaker device was placed 3 cm from the surface of the grounded anode electrode, directly above the discharge column. One probe was placed approximately 1 cm directly below the shaker opening, and one probe was placed in the center of the positive column discharge approximately 6 cm below the shaker opening, also directly below the shaker. Figures 6.2 and 6.3 show a schematic and actual image of the experimental setup, respectively. The probe located in the middle of the discharge will be referred to as the 'middle' probe, and

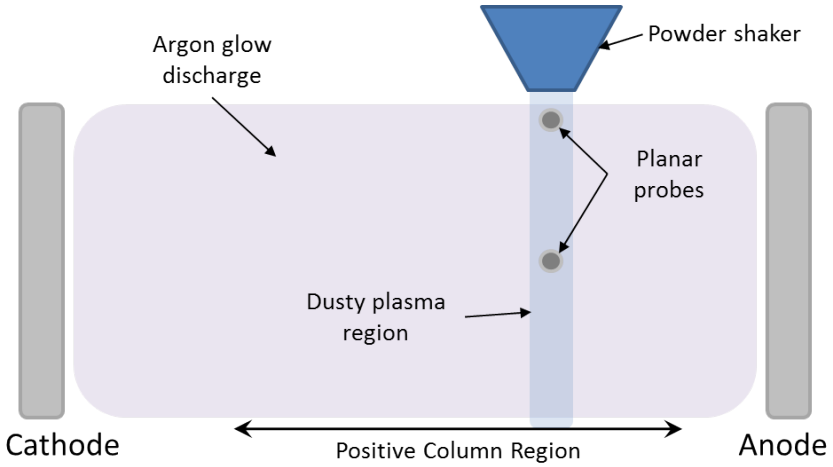

Figure 6.2: A schematic of the experimental setup, with two planar Langmuir probes placed in the positive column region of a glow discharge, directly below the shaker device.

the probe located nearest to the shaker device opening will be referred to as the 'top' probe.

The probes were located so as to be in the center of the column of powder dropped from the shaker. While some falling powder was deposited on the top probe, shown in figure 6.7, this amount was very small over the course of the shaker tests. The majority of powder passed by both the top and bottom probes. Furthermore, the middle probe was used primarily for characterization of the glow discharge (without powder dispersion), to ensure a stable operating glow discharge before shaker tests. The top probe was the primary probe for measuring plasma depletion.

A Langmuir probe sweep with the middle probe provides a very smooth Langmuir probe trace, shown in figure 6.4 and reveals typical plasma parameters for these operating conditions, shown in table 6.1. The plasma density is approximately 2.0 to 3.1×10^{8} cm^{-3}, with an electron temperature of approximately 2.5 to 3.0 eV. The plasma potential ranges from approximately -14.5 to -12.0 V and the floating potential -17.0 to -15.0 V, both with respect to ground. The discharge parameters were in this range for all experiments presented.

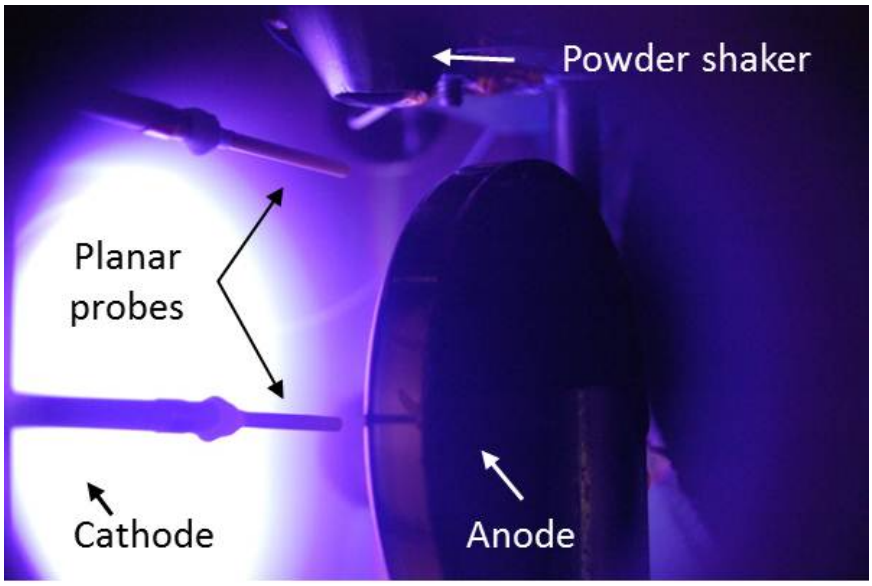

Figure 6.3: An image of the experimental setup with the glow discharge operating.

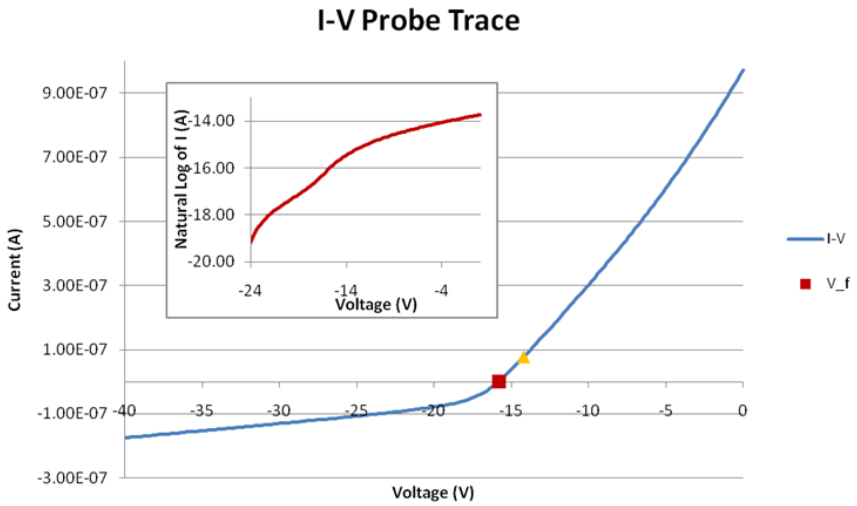

Figure 6.4: An example of a probe sweep in the positive column region of the glow discharge.

Discharge Current (mA)	40
Discharge Voltage (V)	450 to 500
Ion Density (cm^{-3})	2.0×10^8 to 3.1×10^8
Electron Temperature (eV)	2.5 to 3.0
Floating Potential (V)	-17.0 to -15.0
Plasma Potential (V)	-14.5 to -12.0

Table 6.1: Typical parameters of the glow discharge operating on argon at 350 mTorr.

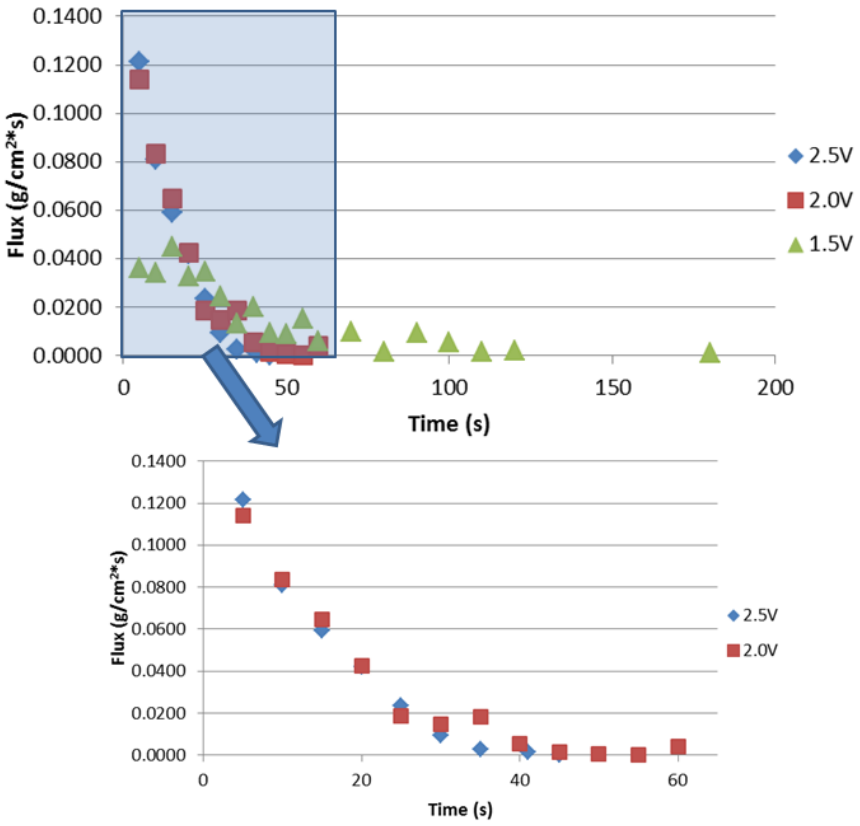

Figure 6.5: A plot of the mass flux of powder from the shaker as a function of time for varying voltages supplied to the vibrating motors.

6.1.2 Shaker Performance

The shaker device was described previously in chapter III. This shaker device was the instrument used to disperse powder into the glow discharge, rather than cathode spots. Using the shaker device allowed for measurement of the effect of dust dispersion on the plasma discharge, separate from the effect that cathode spots themselves would have on an overhead discharge. For these experiments, only 45 µm diameter alumina powder was used.

The rate at which powder was dropped into the discharge from the shaker device was determined by two factors: 1) the voltage supplied to the shaker vibrating motors, and 2) the amount of powder remaining in the shaker hopper.

Figure 6.5 shows the mass flux rate of dielectric powder dropped from the shaker device as a function of time. For each measurement, the hopper is loaded with powder. The vibrating motors are then supplied with a dc voltage for five seconds, during which the shaker drops powder into a collecting cup. The mass of powder dropped into the collecting cup is then measured and averaged over the five second time period. This procedure is repeated until the shaker device hopper is empty. This test was repeated several times for each vibrating motor voltage. In this way, the shaker powder flux was calibrated.

When the vibrating motors are supplied with a greater voltage, the intensity of the vibration of the conical hopper is greater, thereby shifting more powder, resulting in more powder dropping through the wire mesh at the bottom of the hopper. Figure 6.5 shows the powder dropped for three different voltages, with 2.5 V being the maximum allowable voltage for the hopper motors. The mass flux rate is slightly higher when the motors are supplied with 2.5 V compared to when the motors are supplied with 2.0 V. However, when the motors are supplied with only 1.5 V, the powder flux is significantly lower during the first 20 seconds. However, beyond 20 s, all voltages resulted in similar flux rates since the 2.5 V and 2.0 V cases had less powder left in the hopper after 20 s. Regardless, for all cases, the shaker mass flux rate exponentially decreased with time. The mass flux rate provided by the shaker ranged from 0.04 to 0.12 g/cm^2-s at the start of the shaker to approximately zero once all the powder had been dropped from the hopper.

As the amount of powder remaining in the hopper was reduced, there was less powder to be dropped through the mesh. Furthermore, there was less pressure from the mass of powder in the hopper above pushing the powder through the mesh at the bottom of the hopper. This resulted in the reduction of mass flux rate with time. Another possible mechanism that reduced powder mass flux rate was clogging of mesh holes. While mesh hole size was selected to reduce mesh clogging, at the end of tests,

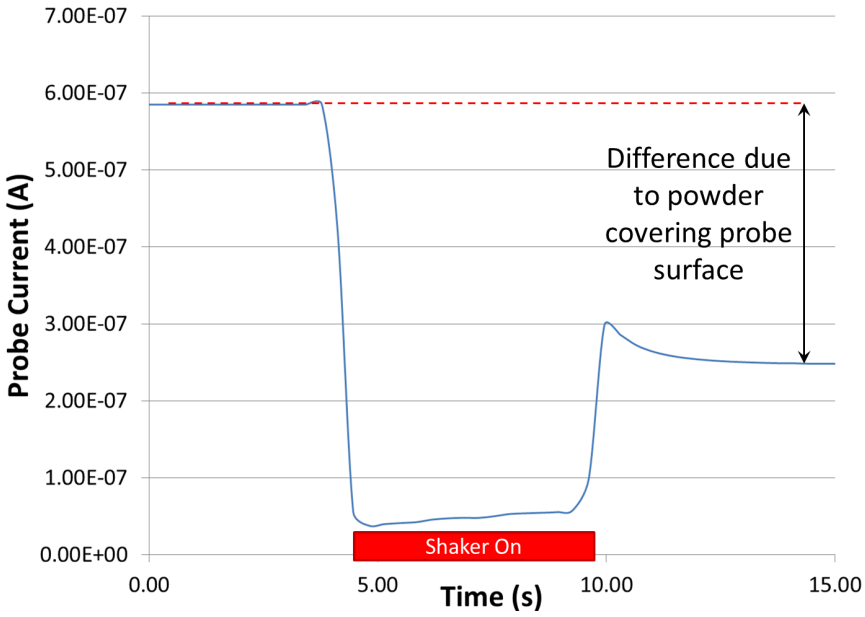

Figure 6.6: A typical current trace from a Langmuir probe biased at electron saturation before, during, and after shaker operation.

it became apparent that some portion of the mesh holes had become clogged. These holes were cleared before every test with compressed air.

6.1.3 Response to Dust Dispersion

The observations of the probe and plasma discharge response to dust dispersion with the shaker device are discussed below.

6.1.3.1 Probe Response and Correction

During tests, the glow discharge was initiated, and a Langmuir probe trace was taken to find the initial plasma discharge parameters. Then the Langmuir probes were biased just above the plasma potential to collect the electron saturation current. While the electron saturation current was collected, the shaker device was turned on for a short period of time, dropping powder into the discharge, and then was turned off, stopping the dispersion of powder. A typical trace of the electron saturation current as a function of time is shown in figure 6.6. Notice that while the shaker is

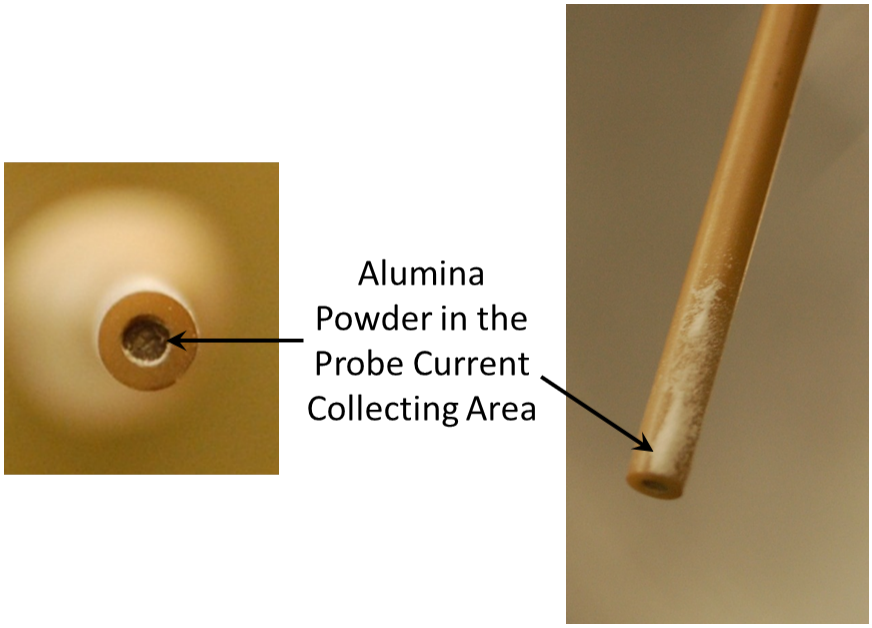

Figure 6.7: The planar probe after a test, with alumina powder on and near the current collecting surface.

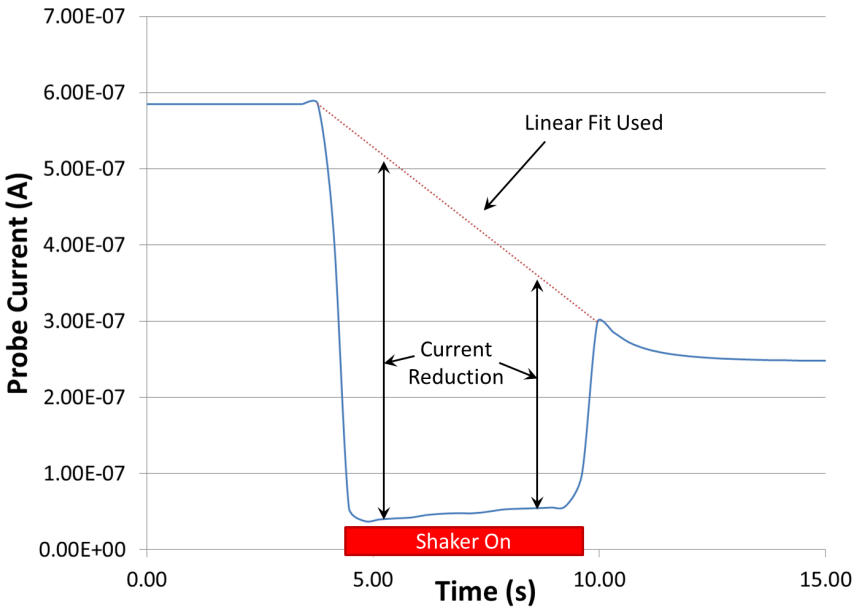

Figure 6.8: A typical current trace showing the linear fit used to determine current reduction.

on, the current collected at the planar probe surface drops drastically, and then is fairly steady while the shaker remains on. The electron saturation current collected by the planar Langmuir probe is proportional to the electron density, shown in equation 3.20 in chapter III on page 80. So figure 6.6 indicates that while the shaker is on, the electron population in the discharge is reduced, leading to a reduction in the electron density, and therefore, a reduction in the electron saturation current to the Langmuir probe.

Once the shaker is turned off, the current recovers. However, the collected current never fully recovers to the initial value before the shaker was turned on. This is because, despite the recessed surface of the planar probes, the probe current collecting surface still collects some dielectric powder, as shown in figure 6.7. Therefore, this powder shields a portion of the area of the planar probe, effectively reducing the probe's current collecting area, and the amount of collected current. Despite the reduced current to the probe surface, the plasma parameters, particularly the electron density, after the shaker is turned off actually *do* fully recover, returning to the same value as before the shaker was turned on.

The electron saturation current to the probe is proportional to the probe current collection area. Since the parameter of interest is the ratio of current while the shaker is on (depleted current) to the current when the shaker is off (steady state current), a correction can be made if an assumption is made. It must be assumed that the probe surface continues to collect powder on the probe surface at a constant rate while the shaker is on. As shown in figure 6.8, once the shaker is turned on, and before the shaker is turned off, the depleted current remains approximately constant. However, if the discharge is operated in steady state (with no powder dispersion), but somehow the probe surface area was reduced at a constant rate, one would expect the steady state probe current collected to look something like the dashed red line in figure 6.8.

This linear fit is an approximation to what the current to the probe surface would

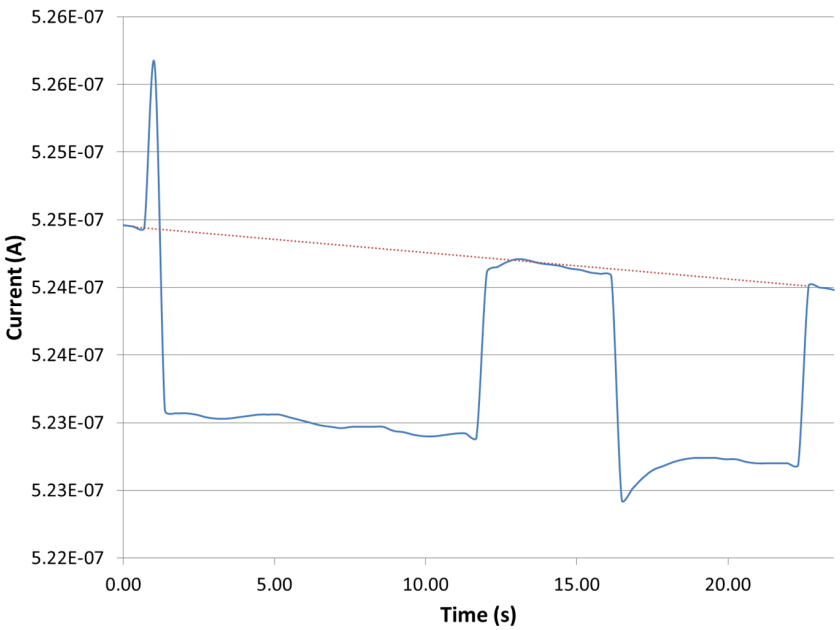

Figure 6.9: The shaker is turned off between about t = 12 s and t = 17 s. This shows that the linear fit model is a good approximation for the discharge steady state probe current collected.

be if the shaker were turned off at any given time and the discharge returned to the steady state condition. While this approximation may not be precise, it provides a relatively good measure of the difference between the steady state electron current and depleted electron current.

To test this approximation, a test was run where the shaker was turned on for 10 seconds, then turned off for 5 seconds, then turned on again for 5 seconds. If the linear fit is a good model for the steady state current collected, then the current should follow the linear fit when the shaker is turned off. The current collected by the probe during this test is shown in figure 6.9. As can be seen, the current returns to approximately follow the linear fit when the shaker is turned off. The steady state current when the probe was turned off was expected to be constant. However, residual powder still falling through the plasma and collecting on the probe surface, or the plasma still attempting to recover from the dust dispersion may account for the slight decrease in probe current during the time when the shaker is turned off. Despite this,

the linear fit is a good approximation for the steady state discharge current collected by the probe.

Now, if the rate of powder mass flux dispersed into the discharge remains constant and the probe surface collects powder at a constant rate, then one would expect the collected current to continue dropping while the shaker is on, as the probe surface area is reduced. However, recall from section 6.1.2, that the mass flux rate of powder from the shaker is rapidly decreasing as powder is dispersed. Therefore, the rate of powder being dropped from the shaker at t = 5 s in figure 6.8, is more than the rate of powder being dropped from the shaker at t = 9 s. However, as figure 6.8 shows, the amount of current being collected while the shaker is on is approximately constant. The electron saturation current collected during powder dispersion should be proportional to the powder mass flux rate. Therefore, the ratio of steady state current to depleted current if the shaker were turned off at t = 5 s would be greater than the ratio of current when the shaker is turned off at t = 9s. If the ratio of currents collected is calculated using the current of the dashed red line as the steady state current, then the current ratios follow the expected trend. The resulting ratio of steady state (no powder) current to depleted (powder dispersed) current when using the linear fit as the steady state current, is plotted versus time in figure 6.10. As expected, the current ratio decreases for the longer that the shaker is turned on, because as the shaker is on, the powder mass flux rate is decreasing, resulting in a decrease in the current ratio. This is also another example proving that the linear fit for the steady state discharge current collected by the probe is a good approximation.

However, rather than reporting results as current ratios, the parameter will be converted to a depletion percentage for the remainder of this section.

$$\text{Electron Depletion } \% = 100 \times \left(1 - \frac{I_d}{I_0}\right) \tag{6.1}$$

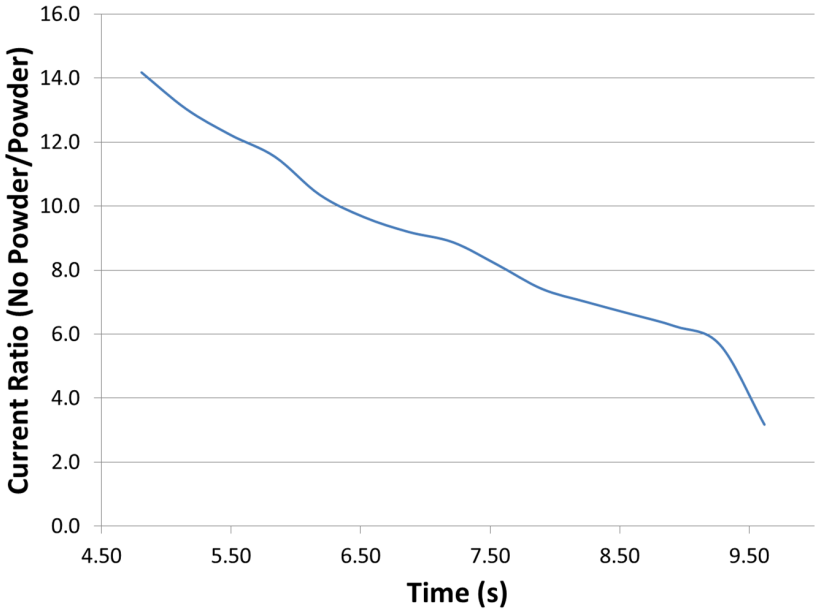

Figure 6.10: The ratio of current as a function of time when the linear fit shown in figure 6.8 is used.

where I_d is the depleted current, or current when powder is dispersed, and I_0 is the steady state current (including the linear fit portion). And since electron density is proportional to the electron saturation current, this is actually the percent of the electron population that is depleted. If all electrons are collected by the dust particles, then the depletion percentage would be 100%. This figure of merit will be used for the remainder of this chapter.

6.1.3.2 Depletion

Several important trends are observed regarding the electron depletion of the glow discharge related to shaker motor voltage, probe location, and the mass flux of powder dispersed into the discharge. These trends will be presented and discussed in this section.

Figure 6.11 shows typical current traces collected for varying shaker motor voltages. For each test, the shaker is turned on for approximately 5 seconds. Notice that the greatest depletion occurs for the 2.5 V case, followed closely by the 2.0 V case,

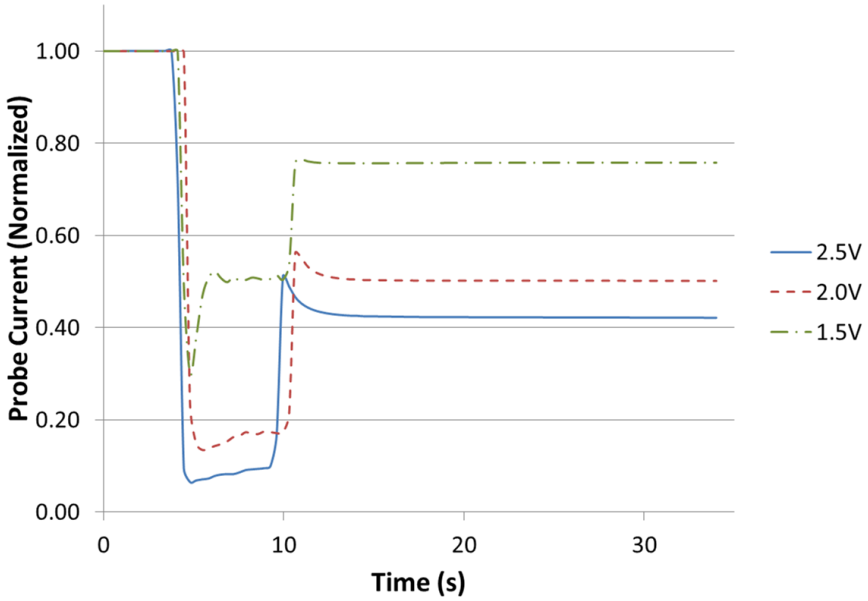

Figure 6.11: This figure shows typical current traces, all normalized, for shaker motor voltages ranging from 1.5 to 2.5 V.

and then the 1.5 V case, trailing significantly. This follows the expected trend since when 1.5 V is supplied to the shaker motors, the powder flux rate is significantly lower than both the 2.0 and 2.5 V case, as shown in figure 6.5.

Another interesting feature to notice is that the electron saturation current after the shaker turned off recovers more fully for the 1.5 V case. This is because, since not as much powder was dropped as in the 2.0 V and 2.5 V cases, not as much powder collected on the probe surface, resulting in greater electron saturation current recovery. Figure 6.12 shows a plot of the electron saturation current to the probe after a shaker test as a percentage of the initial electron saturation current, as a function of the mass flux of powder dispersed by the shaker. The percent of current recovered decreases approximately linearly with increasing powder mass flux.

Figure 6.13 shows the percent of electrons depleted as a function of the flux of powder dispersed by the shaker. One case shows the depletion for the top probe, while the other shows the case for the middle probe. In both cases, the shaker motors are supplied with 2.0 V. As expected, the electron depletion increases with powder

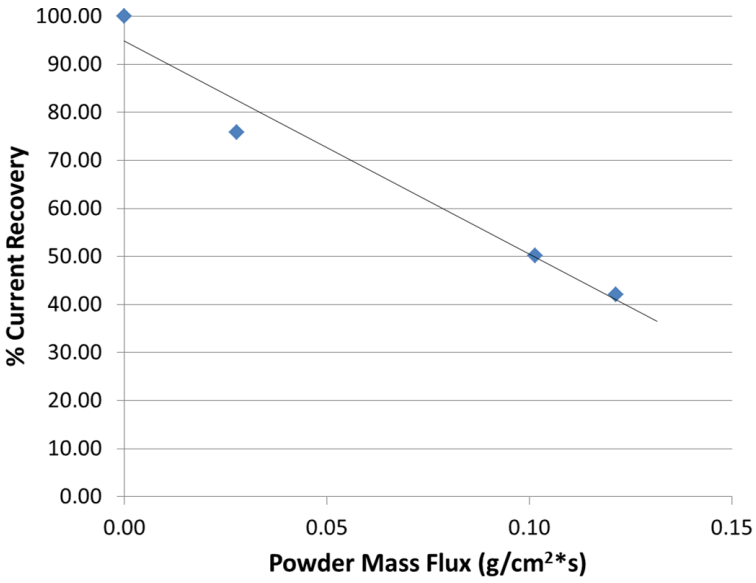

Figure 6.12: The percentage of current recovered decreases as function of increasing powder mass flux.

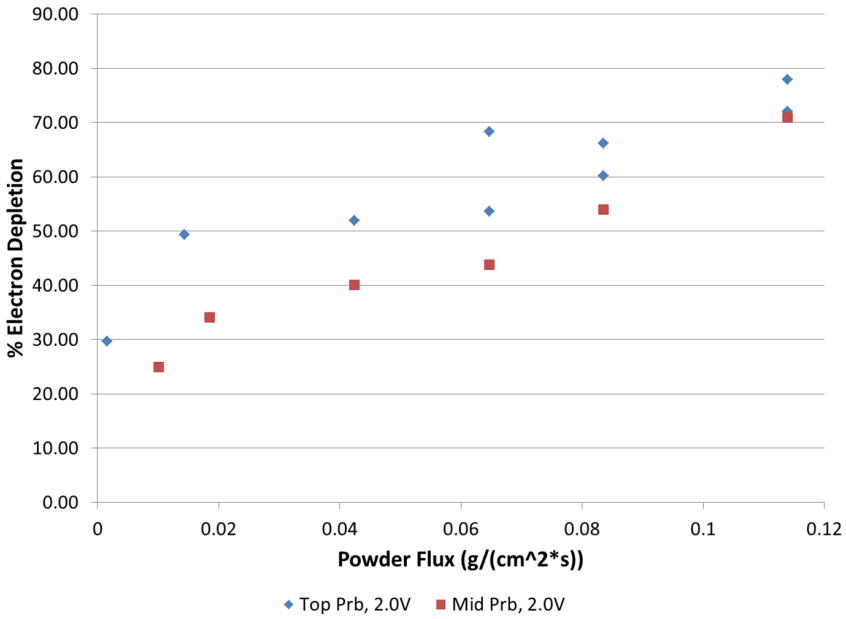

Figure 6.13: The percent of electron depletion plotted as a function of powder flux for the top probe and bottom probe.

flux for both cases. However, the electron depletion is greater for the top probe. This may be expected, however, since the top probe is much closer to the point where the powder is released into the discharge.

Powder particles can again be assumed to follow an approximately ballistic trajectory as they are dropped from the shaker, starting at the shaker exit with no vertical velocity. Particles will then pass by the top probe, 1 cm below the shaker exit, and middle probe, 6 cm below the shaker exit, approximately 45 ms and 111 ms, respectively, after being dropped from the shaker. While both of these times are significantly greater than the calculated particle charging time, found to be on the order of 0.2 µs from equation 2.20 in chapter III, particles passing by the top probe are just entering the glow discharge since the discharge is contained mainly within the cylindrical volume between the electrodes. However, particles passing by the middle probe have already been charging for at least 66 ms, and therefore should have already been fully charged. However, two factors must be taken into account. First, particles are continuously traveling through a small section of the plasma discharge directly below the shaker. Therefore, the first wave of particles dropped from the shaker will be the first to travel through this region, and will have already depleted many electrons by the time the second wave of particles enter. So subsequent particles will be traveling through a plasma that has a reduced electron density. The charging time for particles is inversely related to the electron current to the particle, and the electron current to the particle surface is directly related to the electron density, as shown in equation 2.20 on page 38. Therefore, since the electron density is reduced, the particle charging time will be increased. However, even if the electron density in this column is reduced by an order of magnitude, the charging time will be ~ 2.0 µs, much faster than 66 ms. The second factor that must be taken into account is that the particles, even after fully charged will still collect electrons and ions on the surface, and may provide a surface for electrons and ions to recombine and form neutral gas

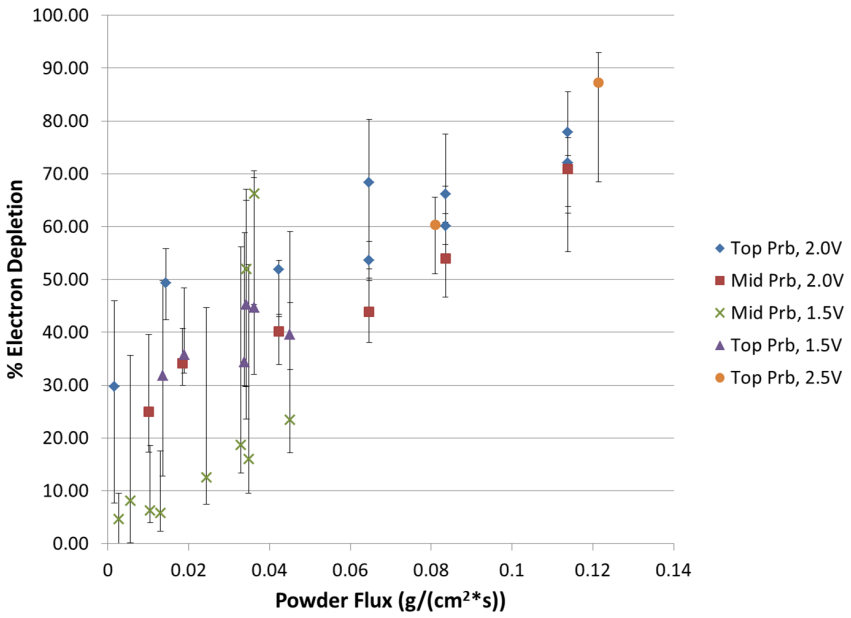

Figure 6.14: The electron depletion shows an approximately linear trend with respect to powder mass flux.

particles. Therefore, it is expected that even though particles have already reached their full charging potential when they pass by the middle probe, that the powder particles still deplete the plasma in this region.

Figure 6.14 shows the electron depletion as a function of the powder mass flux. Each data point on the plot is the average depletion over a five second period when the shaker was on and dispersing powder into the discharge. The error bars show the maximum and minimum measured depletion during each 5 second period of shaker operation. This relationship appears to be approximately linear, with depletion increasing with increasing powder dispersion. Notice the highest depletion test had an average depletion of 87% over the five second period, with a maximum measured depletion of 93% during this same period. This was acheived with the highest measured powder mass flux, at the top probe, with the shaker motor voltage set at 2.5 V.

The powder mass flux rate required to achieve an order of magnitude depletion of free electrons was 0.12 g/cm^2-s. The shaker opening was approximately 2 cm in diameter, resulting in a total mass ejection rate of 0.38 g/s of 45 micron diameter

alumina powder dispersed by the shaker. The depleted volume is assumed to be a cylindrical volume 2 cm in diameter and 10 cm long. Assuming that all particles are approximately spheres, the total number of particles dispersed per second is 2.04×10^{6}. The particles are allowed to free-fall for 1 cm before entering the glow discharge, and then must fall 10 cm through the plasma discharge, after which the particles will fall out of the discharge 105 milliseconds after entering the discharge. Assuming that the shaker releases particles at a perfectly constant rate, then the total number of particles present in the cylindrical depletion volume at any moment during steady state shaker operation is approximately 2.14×10^{5} particles, resulting in a particle density of 6.80×10^{3} particles/cm^{3}.

The total number of electrons expected to be removed from particle charging can then be estimated. The total net charge collected by each powder particle will be approximately 3.76×10^{-14} C, or 2.34×10^{5} electrons. Therefore, the total number of electrons collected per cubic centimeter will be 1.59×10^{15}! However, the plasma density to begin with is approximately 2.5×10^{8} cm^{-3}, therefore the particles have the capability to absorb all free electrons and still not reach the plasma floating potential. However, the particles in the depletion volume will be so close together that there will be a significant amount of sheath interference. That is, the particles are within one Debye length of each other, so the sheath of one particle will interfere with the sheath of its neighbors. This will prevent the particle from charging to the plasma floating potential, thereby reducing the number of electrons collected by each particle.

Therefore, powder dispersion has been shown to be capable of depleting the electron population of a plasma discharge by approximately an order of magnitude, and may be capable of greater depletion in more dense plasmas with the same powder flux rate. In these tests the initial plasma density, before depletion, was approximately 2.5×10^{8} cm^{-3}. This initial plasma has a cutoff frequency of 142 MHz. After depletion, the electron density was reduced to approximately 2.5×10^{7} cm^{-3}, reducing

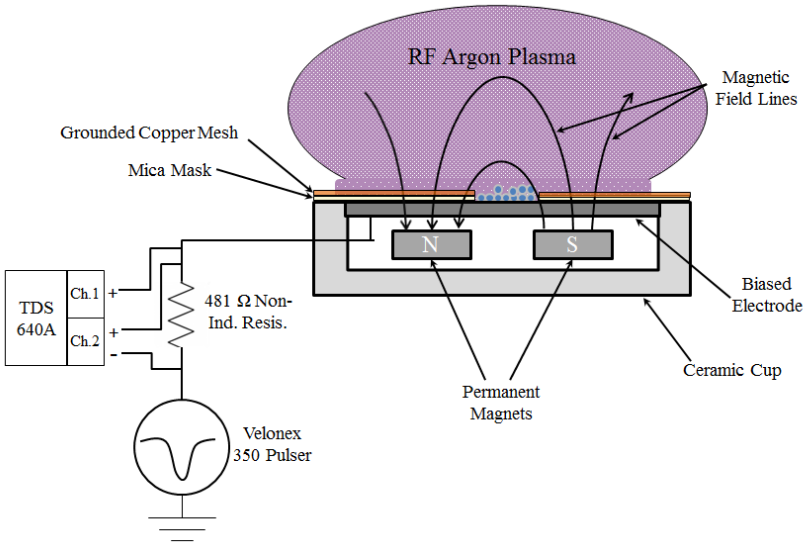

Figure 6.15: The basic experimental setup for plasma depletion measurements.

the cutoff frequency to below 45 MHz. While this plasma is on the lower side of the density of the reentry plasma layer experienced by hypersonic vehicles, it shows the capability to lower the plasma cutoff frequency by powder dispersion. If this method was deployed on an actual reentry flight when the reentry plasma density was near that measured in the glow discharge, blackout of the lower VHF band (45 MHz to 142 MHz) would be alleviated.

6.2 Plasma Depletion Via Cathode Spot Powder Dispersion

6.2.1 Experimental Procedure

The remainder of experiments were performed in the GEC reference cell, using the RF inductive discharge source described in chapter III. Figure 6.15 illustrates the basic setup for the density depletion measurements presented in this section. Additional diagnostic and triggering systems specific to the experiments performed will be shown in the appropriate sections below. The Velonex 350 pulser was used to supply a -1 kV pulse approximately 300 µs long to the electrode surface to initiate

cathode spots. For these experiments, a mica mask and grounded copper mesh mask were placed over the electrode, leaving only a small, circular open area, approximately 1.3 cm in diameter. This configuration limited the electrode surface area that was in contact with the overhead plasma and limited the region on the electrode surface where cathode spots could be initiated. This ensured that every cathode spot would eject powder in the vicinity of the probe measuring plasma density.

For these experiments, 8.0 sccm of argon was flowed into the vacuum chamber, with the turbopump valve throttled down to 8% open. At these settings, the background pressure in the chamber was 90 mTorr. While this pressure was significantly lower than the pressure experienced during blackout reentry, this pressure was required for efficient plasma production. Experiments were also operated at this pressure to prevent cathode spot arcing to nearby probe tips. Cathode spots are initiated by the voltage pulser. Two high voltage differential probes are used to measure the voltage on the electrode as well as the voltage across a non-inductive resistor with known resistance to calculate the cathode spot current. Typical cathode spot voltage (top) and current (bottom) waveforms are shown in figure 6.16.

There are several significant features of the waveform to note. The cathode spot current is considerably lower now, closer to 0.35 A, instead of the 1.0 A observed previously and reported in chapter IV. This is likely due to a difference in capacitance associated with the different power supplies used.

Also of note is that cathode spots do not ignite immediately when the voltage pulse arrives. This dead-period typically lasts between 15 and 150 µs. This may be related to pre-discharge events such as joule heating of microprotrusions on the electrode surface as discussed by Boxman.[14, 15] This delay could also be related to insulator charging at the surface of the dielectric powder layer.

Once the first cathode spot is ignited, the cathode spots burn for a majority of the time while the pulse voltage is supplied. Cathode spots dying and reigniting can

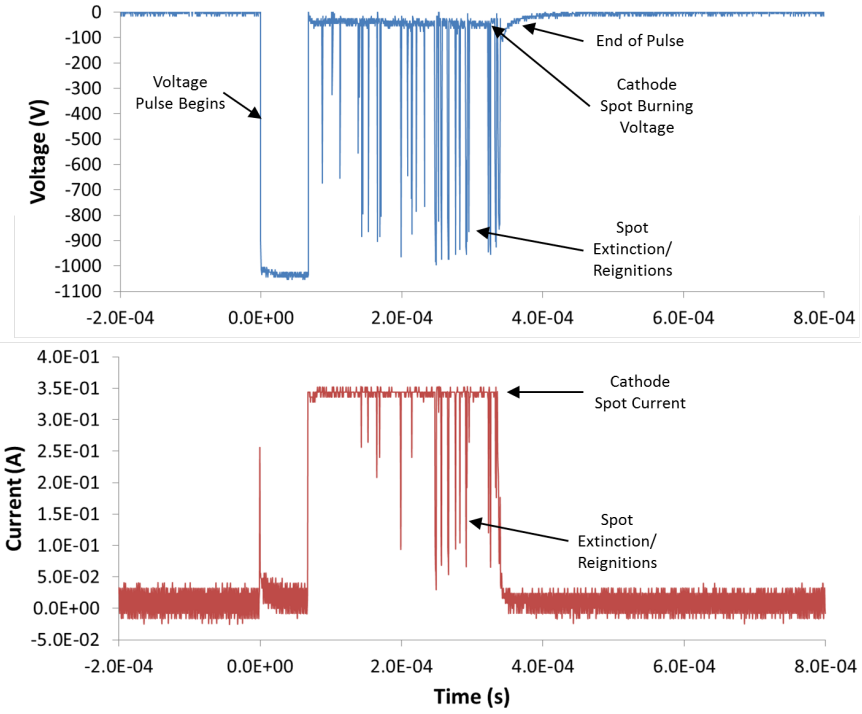

Figure 6.16: Typical cathode spot voltage (top) and current (bottom) waveforms for this experimental configuration.

be seen by the current and voltage spikes pointed out in figure 6.16. Notice that the current and voltage spikes correspond in most cases. In some instances, a spike is present in the voltage waveform, but not in the current waveform. This is most likely due to a slightly higher inductance in the current measurement, or a slower response time for the current trace. However, every time that a voltage spike drops below -800 V, a corresponding current spike is observed. The cathode spot burning voltage ranges from -25 to -55 V, with an average of about -40 V, slightly lower than cathode spots observed previously in this study.

As the pulse ends and the voltage on the electrode begins to fall, cathode spot activity continues until the voltage is no longer high enough to sustain cathode spots. This minimum voltage is around -100 V. Note that this is the minimum voltage required to ignite cathode spots reported in the initial cathode spot studies reported in chapter IV.

6.2.2 Hairpin Resonance Probe Measurements

6.2.2.1 Experimental Procedure

The goal of these studies was to employ a hairpin resonance probe to measure the electron depletion of the RF inductive plasma discharge. The inductively coupled hairpin resonance probe, discussed in chapter III, provides a relatively easy way to measure the plasma electron density in an RF discharge.

The main limitation of this diagnostic is the sweep time of the network analyzer, which depends predominantly on the number of datapoints taken in a sweep. For each measurement, three network analyzer sweeps were taken. The 'calibration' sweep was taken when the plasma was off and the chamber is at the operating pressure so that the probe's initial resonant frequency can be measured (when $\epsilon = 1$). For the calibration sweep there were no time constraints on the sweep time, so a very broad frequency sweep with many datapoints was taken. The same sweep settings were used for the 'plasma' sweep, when the overhead plasma was turned on and operating in steady state. The 'spot' sweep occurs a set time after the voltage pulse to initiate cathode spots is sent to the electrode. The spot sweep was limited to 11 datapoints in a very narrow frequency range, which still took 2.5 ms to complete. The hairpin probe resonance was expected to shift down in frequency with electron depletion.

It was previously argued that the required diagnostic should have time resolution on the order of the ejected particle time of flight ($\sim$ 20 to 300 ms), since the particles would be depleting the overhead plasma the entire time that they are in the discharge. An important consideration is that the network analyzer sweep, even with only 11 datapoints, still takes 2.5 ms to complete. The cathode spots and overhead plasma can change drastically within this time period. So while the plasma may be depleted when the sweep begins, it may not be by the time the sweep ends, or even when the sweep is partway through. Therefore, the spot sweep measurement is made over a 2.5

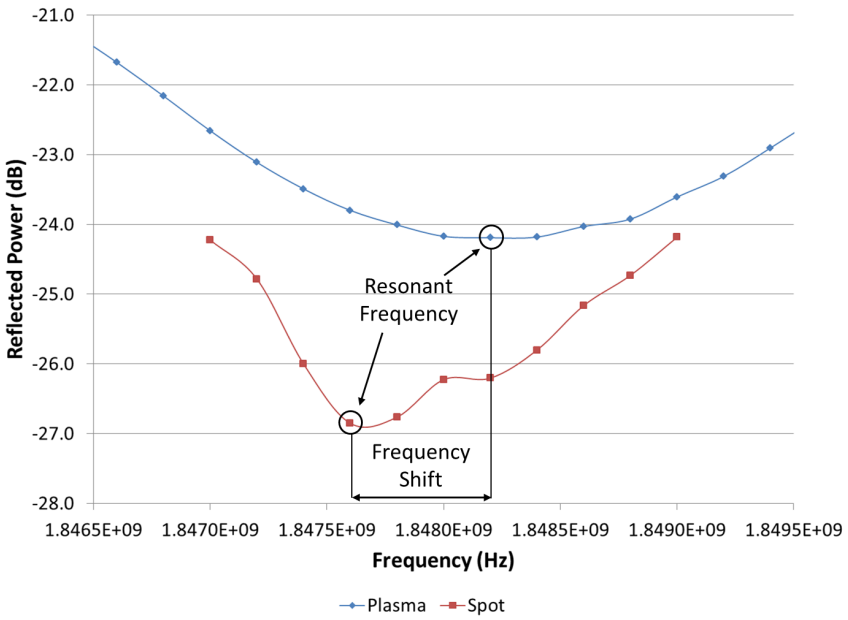

Figure 6.17: A typical 'spot' frequency sweeps with the 'plasma' sweep also shown.

ms time interval during which the overhead plasma density is changing. Ultimately, a diagnostic with much finer time resolution will likely be required.

Figure 6.17 shows both the plasma and spot sweep. Notice that the spot sweep resonant frequency shifted down with respect to the plasma sweep resonant frequency, indicating that the plasma electron density has been reduced.

In this case, the resonant frequencies for the calibration, plasma, and spot sweeps are 1.8434, 1.8482, and 1.8476 GHz, respectively. From the calibration and plasma resonant frequencies, the steady-state plasma electron density is calculated to be about 2.20×10^{8} cm^{-3}. The plasma density after the spot has dispersed powder is 1.92×10^{8} cm^{-3}, resulting in a 12.5% electron depletion. However, the correction factors for the magnetic field and sheath, outlined in chapter II, have not yet been taken into account. These correction factors are approximately 1.26 and 0.63, respectively, for both the plasma and spot sweep measurements. This results in a steady-state plasma density of 2.76×10^{8} cm^{-3}. The plasma density after cathode spot dispersion of the powder is 2.46×10^{8} cm^{-3}. The result is a 10.9% depletion in the electron

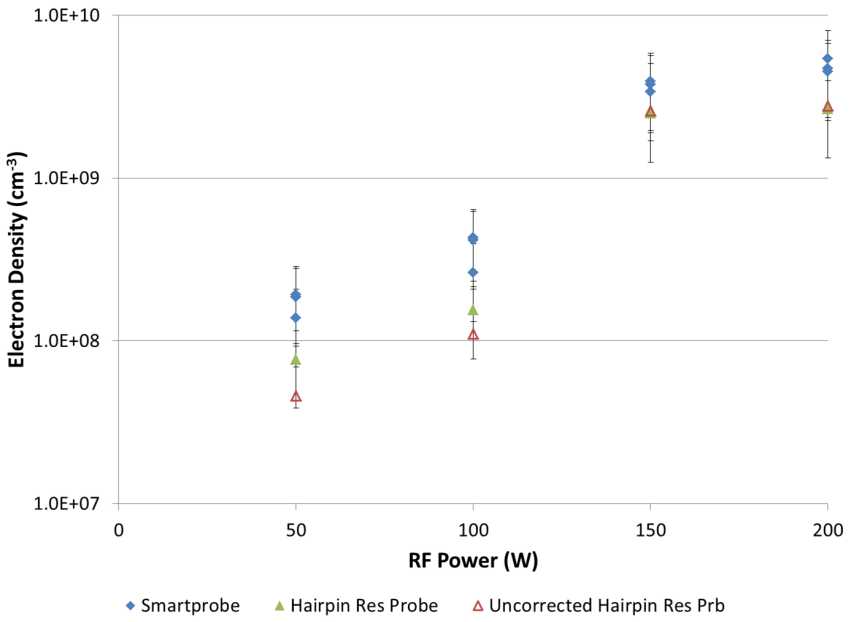

Figure 6.18: Comparison of electron density measurements with the Smartprobe Langmuir probe system and hairpin resonance probe.

population.

6.2.2.2 Comparison of Plasma Density Diagnostics

Before using the hairpin resonance probe for actual depletion measurements, the hairpin resonance probe was compared with measurements made by a commercial Langmuir probe system. The Smartprobe Langmuir probe system, specifically designed for RF systems such as the GEC cell, was used as a benchmark for measuring electron density. Figure 6.18 shows the density data collected for RF antenna powers ranging from 50 to 200 W at 90 mTorr of argon. The plasma transitions from the capacitive to inductive mode of operation between 100 and 150 W, resulting in a sharp increase in the electron density. The hairpin resonance probe magnetic field correction factor ranges from 1.24 to 1.26, and the sheath correction factor ranges from 0.47 to 0.84. The total correction factor (combining both sheath and magnetic field correction) ranges from 0.60 to 1.05, and increases with increasing density.

The hairpin resonance probe measurements of the electron density were on av-

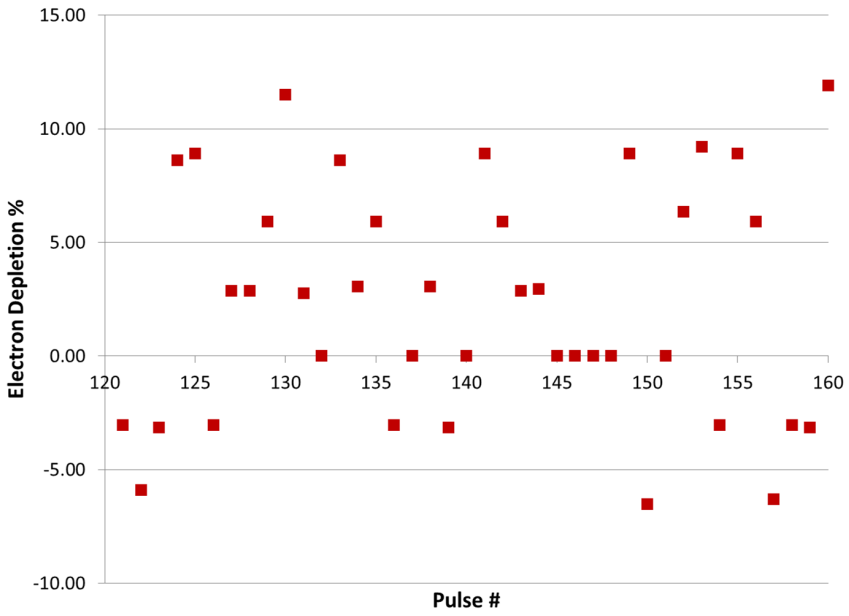

Figure 6.19: Typical shot-to-shot variation was large for measured electron depletion with the hairpin resonance probe.

erage slightly less than that measured with the Smartprobe over the power range investigated. The hairpin probe tracked measured trends as inferred from the Langmuir probe extremely well. That is, as the Smartprobe density increases, the hairpin resonance probe increases, and by similar proportions. Therefore, the hairpin resonance probe, despite *slightly* underestimating the electron density, is well within the error of the Smartprobe measurements and is a valid diagnostic for measuring plasma electron density.

6.2.2.3 Hairpin Resonance Probe Depletion Measurements

The hairpin resonance probe was used to measure electron population depletion as a result of powder dispersed by cathode spots ignited on the electrode surface. However, there was significant shot-to-shot variability for these measurements. Tests were taken in 'batches' of 40 pulses, attempting to obtain meaningful measurements through many measurements. Measurements were taken as a function of delay time between the voltage pulse and start of the network analyzer measurements.

Figure 6.19 shows the large shot-to-shot variation in one batch of 40 measurements. This test is the hairpin resonance probe measured electron depletion when the delay time was set to 10 ms, but is representative of all measurement sequences. The electrode had been pulsed 120 times since the last time the electrode was reloaded at the beginning of this test, and electron depletion was measured to be between -6.5% and 11.9% for all measurements. While the variation shows no particular trend, it is clear that there are significantly more datapoints that measured positive electron depletion. However, given the error in measurements, the average may not be an accurate estimate of the actual electron depletion. The convention is that *positive* electron depletion indicates a *decrease* in electron density, and vice versa.

This shot-to-shot variation is a result of several factors. First, the number and intensity of cathode spots varies from pulse to pulse. Furthermore, the number of particles ejected by each cathode spot varies depending on where the cathode spot forms, the number of cathode spots previously formed nearby, the powder layer coverage at the cathode spot location, and small variations in the powder layer placement on the electrode (variations in layer thickness, etc.) However, the most likely source of shot-to-shot variability lies in the limited hairpin resonance probe time resolution.

6.2.3 Langmuir Probe Depletion Measurements

It was clear from the prior discussion that the hairpin resonance probe diagnostic measurements had limited time resolution. In order to circumvent this issue, a Langmuir probe diagnostic was implemented. Here, variations in the electron saturation current are monitored.

6.2.3.1 Diagnostic Configuration

Figure 6.20 shows the diagnostic configuration for this series of experiments. The delay generator, in this case, is only used as an instrument to trigger the voltage

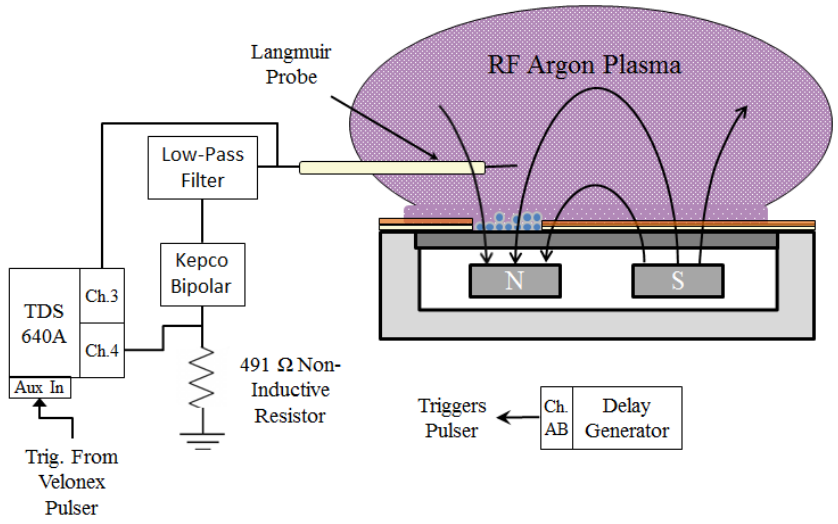

Figure 6.20: Experimental setup for Langmuir probe measurement of plasma depletion.

pulser. The pulser trigger, in turn was sent to the oscilloscope auxiliary trigger input. In this way, the oscilloscope could trigger at the beginning of the voltage pulse. Channels one and two were still used in conjunction with the differential probes to monitor cathode spot current and voltage. Channels three and four were dedicated to measuring the Langmuir probe voltage and current, respectively.

For these experiments, the Langmuir probe was placed approximately 5.0 mm from the surface of the electrode, immediately above the exposed electrode area, where powder was placed. A laser was used to precisely align the probe with the exposed electrode area. A Kepco bipolar power supply was used to provide a Langmuir probe bias. A low-pass filter was connected in series with the probe and power supply, along with a non-inductive resistor to measure Langmuir probe current. The low-pass filter produced a high impedance at frequencies of 13.56 MHz and above. The low-pass filter produced decent results, reducing probe current and voltage oscillations caused by the oscillating plasma potential. This reduced a potential source of significant Langmuir probe trace distortion.

For a majority of these experiments, the area of the electrode that the powder

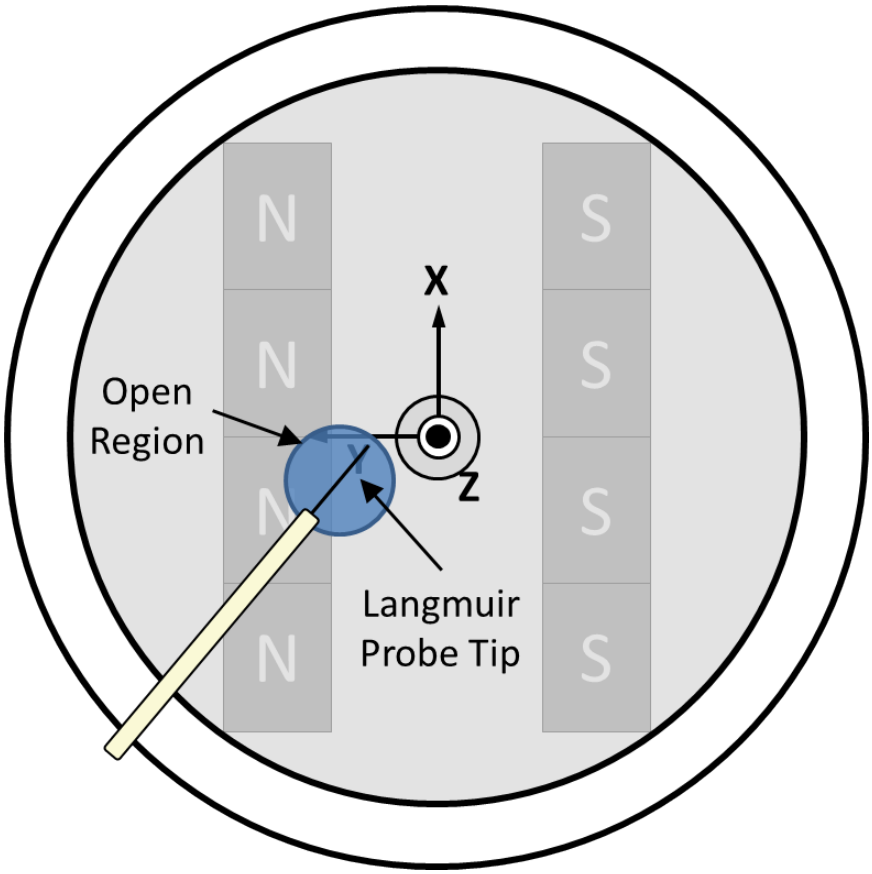

Figure 6.21: Schematic depicting the area of the electrode left open for powder placement and cathode spot formation and the Langmuir probe configuration.

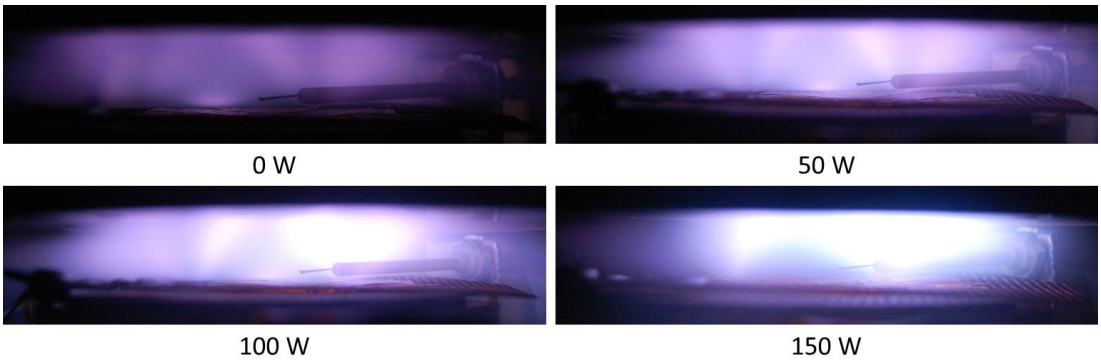

Figure 6.22: The GEC cell overhead plasma source operating on argon at 90 mTorr. The RF power levels are indicated.

was placed on was located almost directly over the magnet row. Observations suggest that conditions for cathode spot ignition are more favorable in this region. The approximate position and configuration of the open region as well as the Langmuir probe orientation is shown in figure 6.21.

6.2.3.2 Plasma Characterization

Langmuir probe use in an RF plasma is not trivial. To benchmark the Langmuir probe featuring an inline filter, plasma measurements were again compared with a commercial Smartprobe Langmuir probe system. Figure 6.22 shows an image of the discharge operating at each power level tested. Several Langmuir probe sweeps were performed at each power level.

Figure 6.23 shows that the Langmuir probe with an inline filter measures slightly higher electron density, particularly at low RF powers. In these tests, the Smartprobe is located at a location farther away from the quartz window and RF antenna. Therefore, it would be suspected that the Smartprobe may measure lower electron densities than our Langmuir probe, located at least 1 cm closer to the window. However, when the plasma transitions to the inductive mode between 50 and 100 W, an intense discharge in the shape of a ball forms below the quartz window that envelopes the tip of both probes. Therefore, the density measured by each probe when the discharge

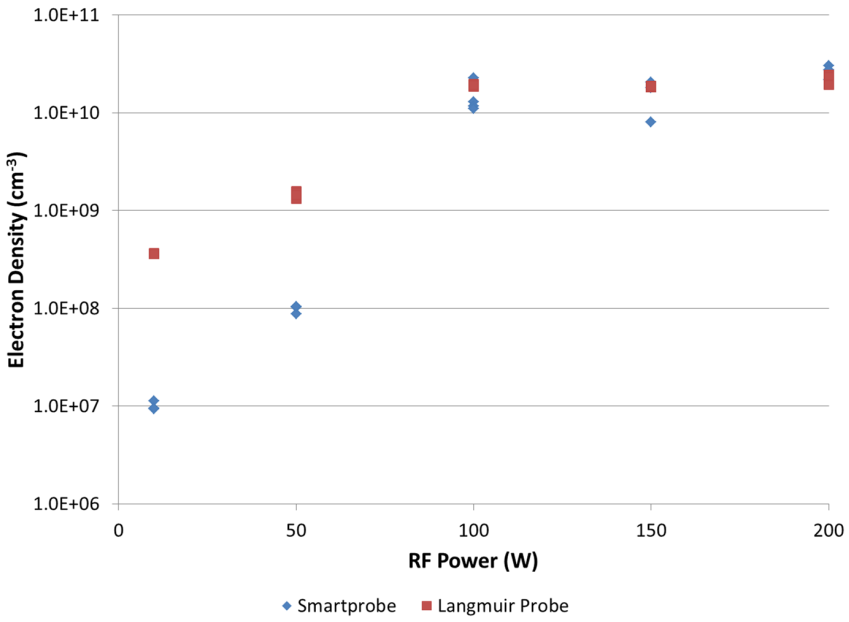

Figure 6.23: Comparison of measured electron density by the filtered Langmuir probe and Smartprobe.

operates in the inductive mode is similar.

The oscillation of the plasma potential and, as a result, the oscillation of the probe tip voltage with respect to the plasma, can cause large error in calculating the electron temperature of a discharge. Analysis of a time-averaged IV characteristic of a probe placed in an RF plasma with no filtering will result in an erroneously large electron temperature.[78, 118] Therefore, the Smartprobe is again used as a benchmark. The results of electron temperature calculated from the probe traces are shown in figure 6.24. The electron temperature is high in the case of the discharge operating in the capacitive mode, and drops significantly as the discharge transitions into the inductive mode. The Langmuir probe measurements match the Smartprobe measurements very closely over the entire range of interest.

Experiments presented herein were relatively straightforward in that for each discharge condition, a full I-V Langmuir probe trace was taken. The probe was then biased slightly above the plasma potential to collect the electron saturation current. A voltage pulse was then sent to the electrode, and the electron saturation current was

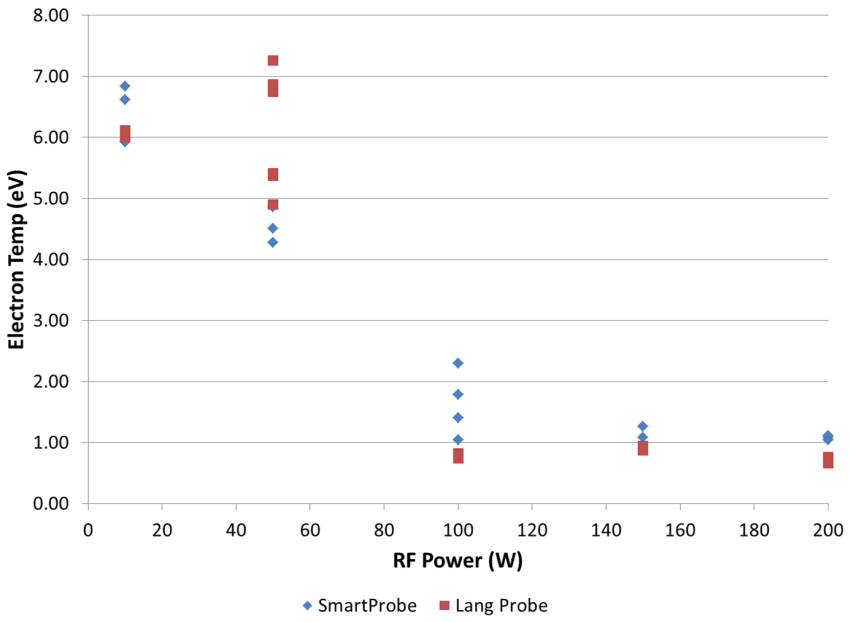

Figure 6.24: The electron temperature for the GEC RF discharge as measured by a filtered Langmuir probe and Smartprobe.

measured as a function of time from the oscilloscope traces. The probe was cleaned by biasing to a large positive voltage between each pulse to clear dielectric powder and other possible contaminants from the probe surface. In contrast to the dust shaker experiments discussed above, the probe collection surface was not observed to be affected by powder dispersion in these experiments during or after powder was dispersed. This is likely due in part to the fact that the thin wire cylindrical probe tip is harder for powder to stick to.

6.2.3.3 No Powder Case

A control set of experiments were performed, in which cathode spots were initiated with no powder on the electrode surface. While in previous experiments with a dc power supply, cathode spot formation was not possible without dielectric powder on the electrode surface, the fast rise time of the electrode voltage provided by the pulser *did* result in cathode spot formation without powder. In this case, it was found that a voltage of 1500 V or more was required to obtain similar cathode spots to that in

the cases with powder, where discharge voltages of a few hundred volts was required. No depletion was expected in this powder-free case.

Figure 6.25 shows the waveforms from a case where no powder was placed on the electrode and the discharge is at 50 W of power. From top to bottom, these oscilloscope traces are the electrode voltage, the cathode spot current, the Langmuir probe voltage, and the Langmuir probe current. The initial voltage pulse can be seen, and a rise in the cathode spot current is observed as the cathode spots are ignited. Note that in contrast to the above oscilloscope traces, these traces show no spikes as the cathode spots die out and reignite. However, this is simply due to the more broad time axis required, resulting in a lower sampling rate and lower time resolution of cathode spot voltage and current that cannot detect cathode spot extinction and ignition. The Langmuir probe voltage oscillates at 13.56 MHz, with peak-to-peak voltage of ~ 7 V. These relatively large oscillations ($> T_e$) in the Langmuir probe waveforms suggest that the electron temperature of the discharge may have been overestimated. The probe voltage cannot be sustained as the cathode spot is ignited. At the same time, the Langmuir probe collects a large amount of current from the cathode spot plume, and the current waveform becomes clipped. The current clipping was unavoidable in order to retain the resolution required for post-cathode spot measurements. However, once the voltage pulse is over, and cathode spots have been extinguished, the probe voltage recovers quickly, within approximately 200 µs. Meanwhile, the probe current does not relax immediately, but relaxes approximately 700 µs later, and continues to fall. This time is much longer than the plasma electron response time, and therefore is most likely lingering effects of the cathode spot plume on the bulk overhead plasma impedance. Other probe current oscilloscope traces have shown that the plasma fully recovers after approximately 5 ms.

So, while nothing about the overhead plasma is known while the cathode spots are ignited, the plasma response immediately following is monitored with extremely high

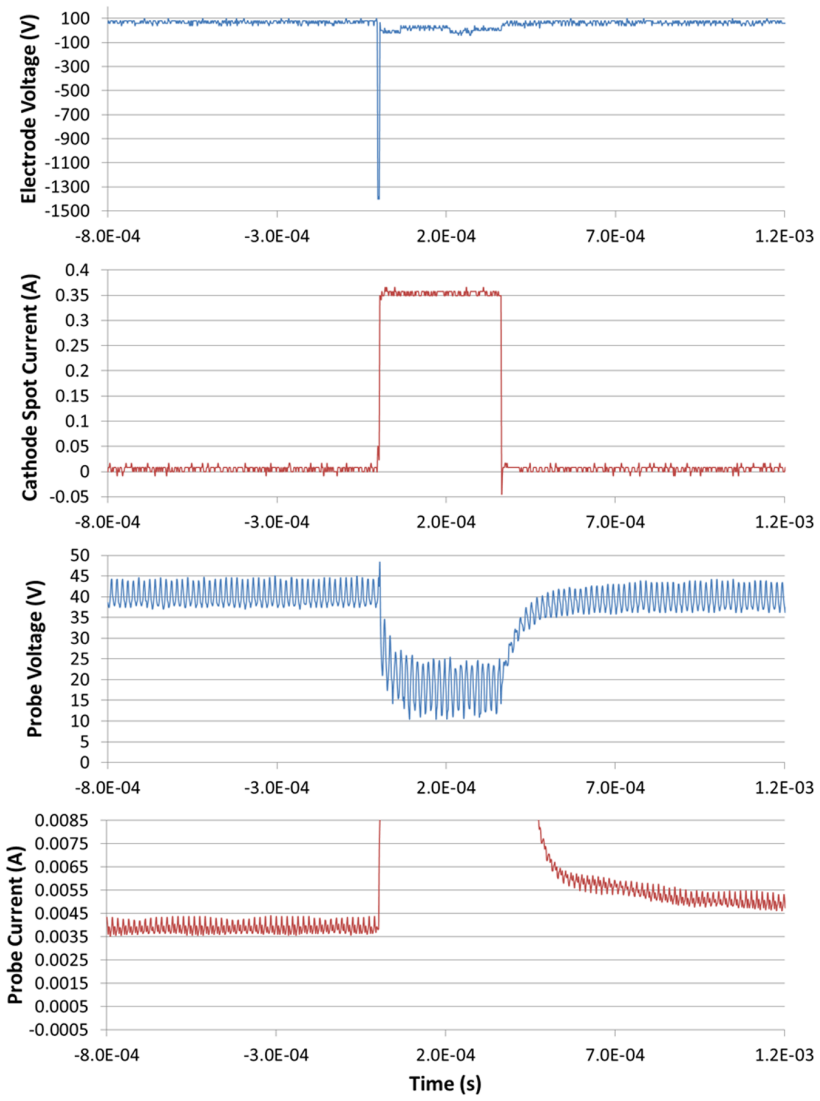

Figure 6.25: The oscilloscope traces for the no powder case of the cathode spot voltage and current, and Langmuir probe voltage and current of the overhead plasma.

time resolution from the oscilloscope traces. Beginning at 0.2 ms after the cathode spots die out, the probe voltage has recovered, and the plasma electron saturation current is measured with a time resolution of approximately 1 µs. In this case, there is not depletion, but rather a rise in electron density immediately following the cathode spot, most likely because the cathode spot plume ejected electrons.

Immediately after the cathode spots are extinguished and the probe voltage recovers, the probe current, and therefore the electron density is approximately 1.6 times the steady state discharge density. Therefore, no depletion is observed, rather an increase in electron density is experienced. This suggests that the cathode spot may have a significant effect on the overhead plasma and may be the reason for the long recovery time.

6.2.3.4 Dielectric Powder Current and Voltage Waveforms

Figure 6.26 shows an example of the same test discussed previously, but with 45 micron powder placed on the electrode, and with the overhead plasma operating at 10 W of RF power. Cathode spots are ignited after a 1000 V pulse is applied to the electrode. In this case the probe voltage again drops, this time below zero while the cathode spots are burning. Many electrons are collected at the probe surface, indicated by the probe current waveform. The waveform is clipped at 3 mA to show the structure after the cathode spot activity ceases. Even though the probe voltage drops to below zero with respect to ground, it is still positive with respect to the electrode, and therefore is attractive to electrons emitted from the electrode. After the cathode spots are extinguished, the probe voltage recovers quickly, again within about 0.2 ms. In this case, however, the current recovers very quickly, on the same time scale as the probe voltage. This is somewhat different from what was observed in the 'no powder' case discussed earlier. The current actually dips below the steady-state electron saturation current, then returns to a current level higher than the initial

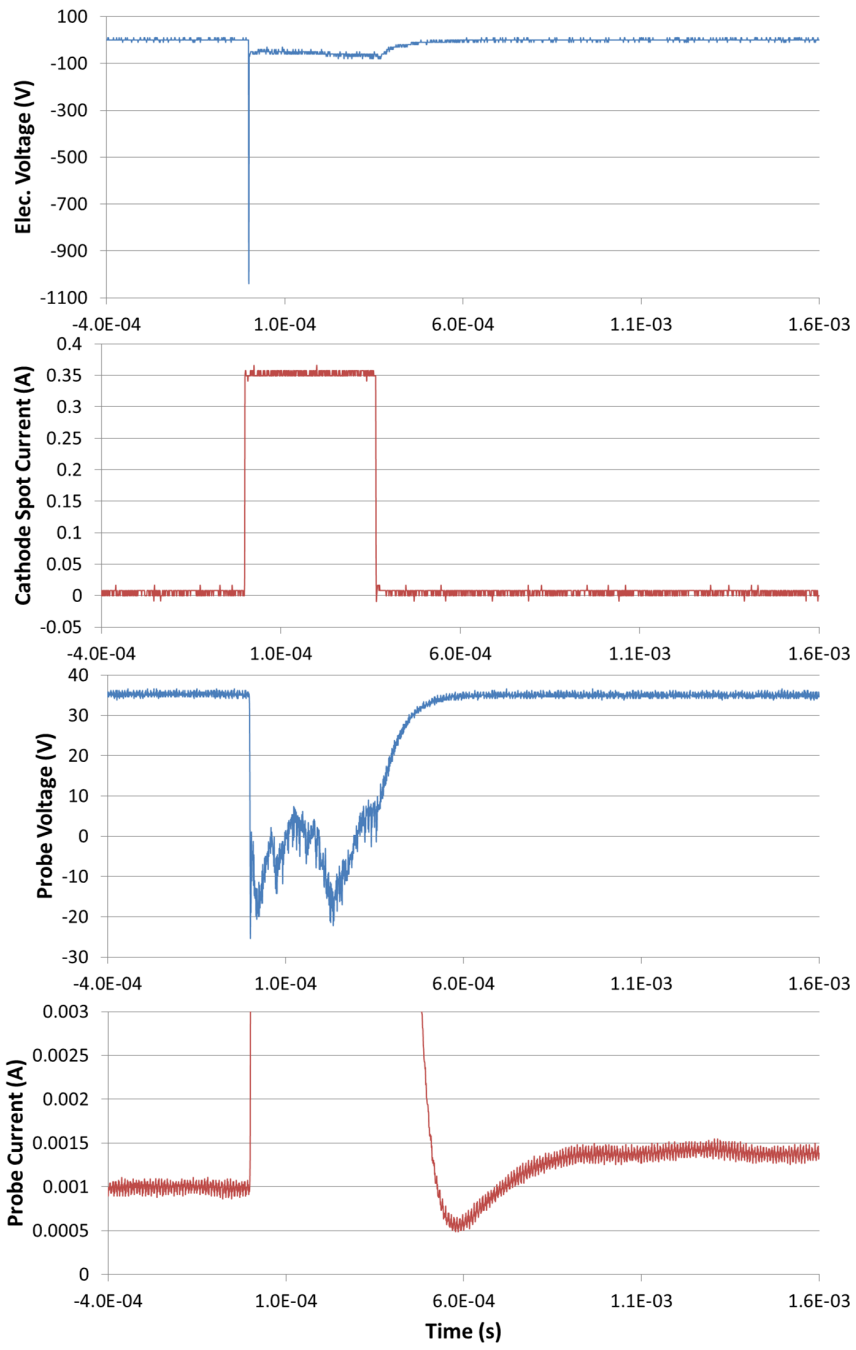

Figure 6.26: The oscilloscope traces for the 45 micron powder case of the cathode spot voltage and current, and Langmuir probe voltage and current of the overhead plasma.

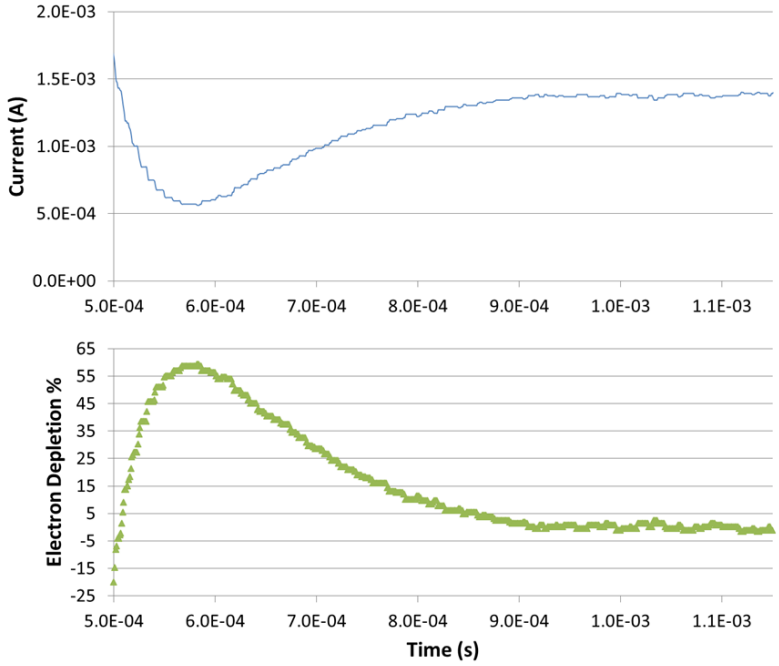

Figure 6.27: The smoothed current trace in the top half. The electron depletion percentage is plotted against time in the bottom half.

value. This occurs before finally decaying back to the initial steady state current after the trace has been cut off. While the case shown is for the 45 micron powder, similar behavior was observed for the case when the electrode is loaded with 0.1 micron powder.

Circuit inductance was minimized by the use of non-inductive resistors to ensure that the dip in the electron current is not due to inductance. Also, in the same experiments with no powder, no dip is observed. The dip in the electron saturation current is not observed in any trace when powder is not present on the electrode. The powder, when dispersed, is expected to cause depletion which is reflected in the dip in the measured electron saturation current. The presence of this dip in cases where the powder has been dispersed leads to the obvious conclusion that the powder is, in fact depleting the plasma.

After performing a moving average smoothing function to the electron saturation

current for the above data to remove RF oscillations, the electron depletion percentage can be plotted as a function of time. These plots are shown in figure 6.27. The electron depletion reaches a maximum of almost 60%, when the depletion is measured against the current level at the end of the trace. Although this current level is not the steady-state current level of the plasma, it was shown in the no powder case, that the probe saturation current would still be higher than the steady-state level at the end of the trace. So this depletion measurement is actually a conservative estimate. The full-width half maximum of this dip is approximately 1.69×10^{-4} s.

Though the example shown here is for 45 micron powder, tests were performed with 0.1 micron powder, and resulted in similar traces in terms of the electron depletion and time scales. Data and discussion comparing the 45 and 0.1 micron cases will be addressed later on.

The dip in the electron saturation current occurs approximately 250 µs after the cathode spots have been extinguished. Even if particles are assumed, as a very liberal assumption, to be ejected at the very beginning of the voltage pulse and are given the maximum observed velocity in the vertical direction (1.5 m/s from chapter V), the particles would only be approximately 0.9 mm from the surface of the electrode. These particles are still far from the Langmuir probe location, 5 mm above the electrode surface. The depletion mechanism is therefore somewhat unclear.

One possible explanation is related to the observation that the presence of the powder increases spot intensity. In this case, the intense plumes may 'blow' electrons out of the region being interrogated. However, these effects are likely minor due to the low density of both the background plasma and cathode spot plume at that height. Also, this is not observed in the powder free case.

The most plausible explanation can be demonstrated by considering a uniform density discharge model.[78] In the uniform density discharge model, a plasma of uniform density is considered, similar to this discharge. For the plasma discharge to

remain stable at a fixed discharge power, the ionization rate must be equal to the particle loss to the walls.[78]

$$n_0 u_B A_{eff} = K_{iz} n_g n_0 \pi R^2 \ell \tag{6.2}$$

where n_0 is the plasma density, u_B is the Bohm velocity, A_{eff} is the effective loss area, K_{iz} is the ionization rate constant, n_g is the neutral gas density, and R and ℓ are the size parameters of the discharge. In this model, charged particle losses are dependent on the effective loss area. However, with dust dispersion, additional loss surface is introduced in addition to the chamber wall surface. The surface of injected particles act as additional loss area. Therefore, with the inroduction of dust, at fixed input power, density drops because the ionization rate is inadequate.

The important thing to note from this proposed model is that the additional loss area decreases the *bulk* plasma electron density, and therefore the ionization rate in the *bulk* plasma. The discharge density can be calculated by:[78]

$$n_0 = \frac{P_{abs}}{e u_B A_{eff} \varepsilon_T} \tag{6.3}$$

where P_{abs} is the absorbed power and ε_T is the total energy lost per electron-ion pair lost from the system. So at fixed power with increased loss area, the bulk plasma density will necessarily decrease. This decrease in plasma electron density will be relatively independent of the location of the additional loss area; that is, bulk density depends on losses at the boundary. In this way, particles that are ejected from the electrode surface may still reduce the bulk discharge electron density at the probe location even though they physically have not reached that point.

The time for the bulk plasma near the Langmuir probe to 'see' this additional loss area is on the order of the time that an electron can travel from the Langmuir probe to the electrode surface. Assuming an electron temperature between 1 to 7

eV, electrons traveling at the thermal velocity can travel 5 mm in less than 10 ns. Therefore, the plasma near the Langmuir probe can be significantly affected on a very fast timescale due to boundary injection of powder particles.

It is suspected that the dip observed in the electron saturation current is due to the introduction of the additional dielectric particle surface plasma loss area, resulting in a decrease in the electron density. Since the RF power is constant, the ionization rate also remains approximately constant during this time. Once all of the ejected dielectric particles have charged to the plasma floating potential, the additional loss area is essentially removed. At this point the loss rate and ionization rate become equal again, and the plasma returne to steady state operation.

This discussion also has significant implications for the application of blackout mitigation. **It may not even be necessary for particles to reach the full thickness of the plasma layer for electron depletion.** Rather, the additional loss area introduced by particles may affect the plasma density at locations far from the particle location on a timescale much faster than the particle time of flight. In this case the input power producing plasma, which is dependent on the kinetic energy of the vehicle, is also quasi-constant. That is, the vehicle kinetic energy changes over relatively long timescales, on the order of several seconds to minutes.

6.2.3.5 Dielectric Powder Depletion

Many tests like those discussed earlier were carried out with no powder, with 45 micron powder, and with 0.1 micron powder loaded onto the electrode surface. These experiments were carried out for discharge powers varying between a 10 W up to 150 W, when the discharge is operating in the inductive mode.

Figure 6.28 shows the peak electron depletion observed for all discharge powers tested, for 0.1 micron powder and 45 micron powder cases. The no powder cases showed no plasma electron depletion. Each data point plotted is the result obtained

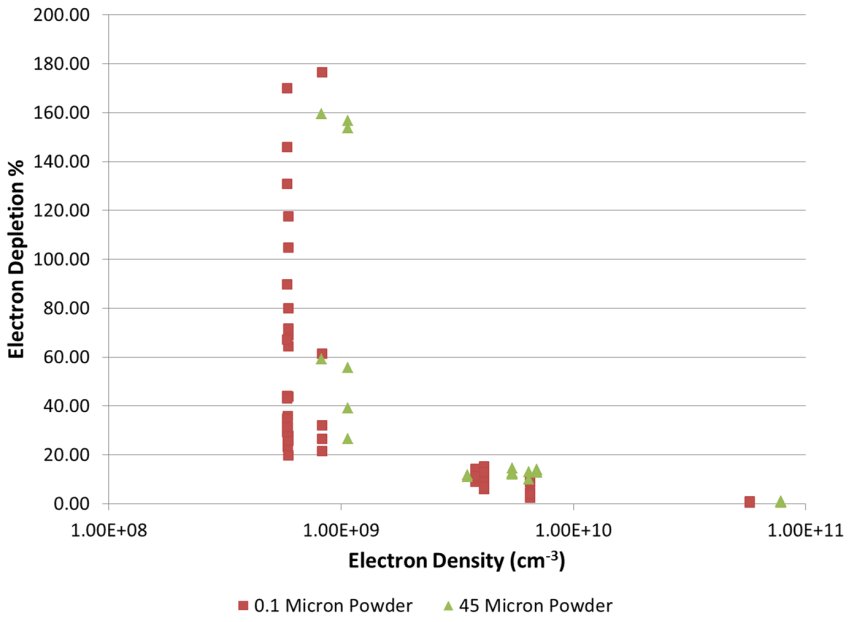

Figure 6.28: Electron depletion as a function of overhead plasma density for the 0.1 micron and 45 micron powder cases.

from separate experiments. The largest depletion occurs for the 10 W case, where the plasma density is lowest. In several instances, the electron saturation current was negative, resulting in depletion of over 100%. These cases are discussed below. The average depletion at 10 W is 93% and 62% for the 0.1 micron and 45 micron powders, respectively. However, there is a large spread in data for both cases, ranging from approximately 20% to 180% depletion. This disparity can be resolved when one considers the slight variation in the discharge settings between experiments, cathode spot shot-to-shot variation, shot-to-shot variation in the number of powder particles ejected, and variation due to error in the Langmuir probe measurements. These variations are less significant at higher discharge powers since the effect of powder injection is less significant. The depletion is approximately constant for the 50 and 100 W cases, with depletion around 10%, followed by very minimal depletion at 150 W, the most intense and dense overhead plasma. It is not clear whether the 0.1 micron or the 45 micron powder is a better performer in terms of plasma depletion. This issue will also be discussed below.

6.2.3.6 Magnetic Field Considerations

The observation of depletion greater than 100% is unphysical, suggesting that there may be other mechanisms at play. Obviously, it should not be possible to deplete more than 100% of the electrons, yet there are several cases where this is the calculated depletion. In the waveforms shown in figures 6.26 and 6.25, the ion saturation current was not subtracted from the electron saturation current because it is comparatively small. However, since the Langmuir probe is only 5 mm away from the electrode, almost directly over a magnet row, the magnetic field may play an important role in the collection of electron current.

If magnetic effects are significant, then the ratio of electron to ion saturation current deviates from the theoretical value given in chapter III. The ratio of electron saturation current to ion saturation current (without magnetic field effects and with equal ion and electron density), should be approximately 176. However, in experiments, extremely high ion saturation current relative to electron saturation current (factor $\sim$10 greater than expected) have been observed. This, along with a Hall parameter of approximately 28, suggests that the magnetic field is impeding electron current to the probe, and will almost certainly affect the plasma potential measurement as well.[116]

In these experiments, solely in the low power, 10 W case, the probe current has been observed to become negative during the depletion period. If the magnitude of the electron saturation current is impeded by the magnetic field so severely that it is on the order of the ion current, then negative current may be observed when the electron population is significantly depleted. Depletion as high as 175% has been observed, where depletion is measured as:

$$\text{Electron Depletion } \% = 100\left(1 - \frac{I_d}{I_0}\right) \tag{6.4}$$

where I_d is the depleted electron current to the probe, and I_0 is the unperturbed current at the plasma potential. However, both I_d and I_0 include the ion current since ions are produced at the plasma potential, so ions are collected at the probe at any potential up to the plasma potential. So if all of the electrons are collected by dust particles in a region, then the majority of current collected by the probe is ion current. Therefore, if the electron density is depleted such that the magnitude of the electron saturation current is less than the magnitude of the ion saturation current, then the current measured by the probe will be negative.

If the plasma potential rises just slightly due to the perturbation caused by the cathode spot injection of powder, then the electron current will be significantly lowered, and the electron current collected may be approximately equal to the ion saturation current. The plasma potential may rise when electrons are depleted, since the plasma will be left with a large population of positive ions, causing the plasma potential to be slightly more positive.

However, this raises a very important question: Is the depletion dip observed simply due to a rise in the plasma potential? Or due to electron depletion? Or both? One could argue that even if the depletion dip is due to a rise in the plasma potential, the rise in plasma potential is due to electron depletion. However, if this is in fact the case, it may be more difficult to quantify the electron depletion with these measurements since the probe is biased at a constant voltage. However, all experiments are carried out with the probe biased approximately 5 to 10 V above the plasma potential, so as long as the plasma potential does not rise more than 5 V, results should still be valid.

Magnetic effects can also skew interpretation of the relative changes in electron saturation current. In order to assess these effects, the ratio of ion to electron current collected by the probe must be calculated taking into account the magnetic field. Sugawara calculates the ratio of electron saturation current in a magnetized plasma to

non-magnetized plasma current for a planar probe oriented parallel and perpendicular to the magnetic field.[116] Since the probe in these experiments is oriented neither parallel nor perpendicular to the magnetic field, by calculating the ratio for both orientations, one can estimate the upper and lower limits of the magnetic field effect. These expressions are:

$$\frac{J_{e\perp}}{J_{e0}} = \frac{\pi\sqrt{\alpha}}{2K\left(k\right)} \frac{1+\frac{32\lambda_e}{3\pi r_0}}{1+\frac{16\lambda_e\sqrt{\alpha}}{3K(k)r_0}} \tag{6.5}$$

$$\frac{J_{e\|}}{J_{e0}} = \left[\left(1+\frac{32\lambda_e}{3\pi r_0}\right)\sqrt{\alpha}\right] \cdot \left[1+\frac{32\lambda_e}{3\pi r_0}\sqrt{\alpha}\right]^{-1} \tag{6.6}$$

where $J_{e\perp}$ and $J_{e\|}$ are the electron current density to the probe when oriented perpendicular and parallel to the magnetic field, respectively. The electron mean free path, λ_e, and a probe radius, r_0 is required. $K(k)$ is the complete elliptical integral of the first kind, where k and α are defined as:

$$\alpha = \left(1+\omega_c^2\tau_e^2\right)^{-1} \tag{6.7}$$

$$k = \sqrt{1-\alpha} \tag{6.8}$$

where ω_c is the electron cyclotron frequency and τ_e is the mean electron-neutral collision period.

This calculation is performed by selecting a probe radius such that the area of the cylindrical probe is equal to the area of a planar probe ($r_0 = 2.34$ mm). The electron collision period is found by assuming that the polarization collision frequency is approximately equal to the electron-neutral collision frequency (according to Lieberman), resulting in $\tau_e = 2.63\times10^{-9}$ s.[78] From this, and assuming an electron energy of 2 eV, the electron mean free path is found to be 2.2 mm. The magnetic field at the probe location is approximately 600 G, resulting in a cyclotron frequency of 1.06×10^{10} rad/s. Then α and k are equal to 1.30×10^{-3} and 0.9994, respectively. Plugging in

these numbers, the fraction of current collected by a probe oriented perpendicular and parallel to the magnetic field lines would be 0.045 and 0.136, respectively.

Because the Langmuir probe is oriented neither completely perpendicular or completely parallel to the magnetic field lines, these ratios provide the upper and lower limit for the electron saturation current collected by the probe. The ion saturation current is not as significantly effected by the magnetic field since the Larmor radius of ions is larger than the probe dimensions.

The ratio of electron to ion current for argon is expected to be 176. Taking into account the magnetic field effect on electron current collection, the electron saturation current would only be between approximately 8 to 24 times the ion saturation current. Therefore, rearranging the equation for electron depletion, equation 6.4, the maximum depletion that should be observed is 114% with the magnetic field present. This is true for the overhead plasma discharge at 10 W of RF power.

However, there are still several tests in which depletion well above 114% is observed. These observations are most likely due to uncertainty in the depletion measurements. Several of these sources of uncertainty have been mentioned previously. Any change in the plasma parameters, particularly the plasma potential during cathode spot operation will introduce significant uncertainty. An increase in the sheath size at low plasma densities may increase the effective probe area, therefore affecting current collection. Furthermore, the uncertainty associated with Langmuir probe measurements in general due to secondary electron emission, non-maxwellian electron populations, etc. must be taken into account. These sources of Langmuir probe error are present in the electron saturation current measurement, both before *and* after cathode spot ignition. Therefore, this source of error is significant. If the probe is not biased precisely at the plasma potential, the meausured electron saturation current may not be exactly proportional to the electron density. Therefore, while the uncertainty in these measurements is significant enough to explain measured elec-

tron depletion above 100%, it still remains clear that significant electron depletion is taking place.

6.2.3.7 Powder Particle Size

The results for the 0.1 and 45 micron powder are extremely similar, despite the fact that in chapter II, the 0.1 micron powder was expected to outperform the 45 micron powder particles. However, as was also shown and discussed in chapter II, the 0.1 micron powder tends to clump together, forming many clumps larger than 45 microns. Therefore, powder clumping may essentially be an inefficiency in terms of electron depletion. This is the likely cause of similar performance in terms of electron depletion. If powder clumping could be reduced then the 0.1 micron powder would be expected to perform better than the 45 micron powder.

For the 0.1 micron powder tests, 16.1 mg of powder was loaded onto the electrode. After 300 pulses 300 µs long, about half of the powder was removed. Therefore, the mass flux rate is calculated to be roughly 0.18 g/s, or 0.13 g/cm^2-s. This flux rate is within 10% of the flux rate estimated for the 90% depletion case in the shaker experiments. These cases also observed depletion on the order of 90%, and in some cases, depletion greater than this. Therefore, it is again reinforced by experimental evidence that particle flux is the most important factor for depleting the plasma, and cathode spot plume effects associated with powder dispersion does not significantly alter the required flux for plasma electron depletion. That is, even though the cathode spots are adding ionized material to the discharge, this does not decrease or significantly alter the measured electron depletion.

6.2.3.8 Electron Collection

Also of interest is the physics involved with solid particle collection of charge in the plasma. Figure 6.29 is a plot of the total number of electrons collected by all of the

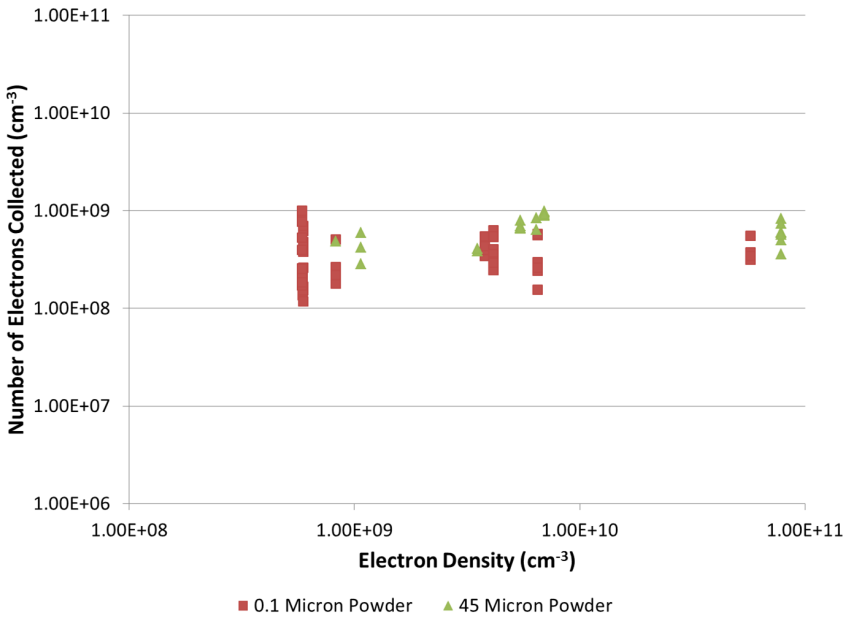

Figure 6.29: The number of electrons collected from the discharge as a function of plasma density is approximately constant.

particles ejected as a function of plasma density. This data was obtained by simply multiplying the electron depletion measured by the total electron density measured at steady state. There is no clear trend, except that for any given plasma density, the number of electrons collected is approximately constant. This is a significant result in that it suggests that for all cases, particles have become saturated with charge. This result also, again reinforces that by increasing particle flux, plasma depletion may also be increased. That is, the limiting factor for reducing the overhead plasma discharge is simply the number of particles injected.

Therefore, this is an important result for the ultimate application of this method for mitigating the communications blackout. This and several other results presented provide significant evidence that an increase in the number of particles injected will increase plasma depletion. Therefore, the amount of powder required during periods when the reentry plasma is more intense will require the injection of more particles, whereas fewer particles will be required when the reentry plasma layer is less intense.

6.2.3.9 Implications for Communications Blackout

Cathode spot injection has shown depletion of the electron population in a plasma discharge of over 90%. However, the discharge produced in these experiments are of significantly lower density than the most intense plasma experienced by hypersonic and reentry vehicles. The maximum discharge electron density in these experiments was less than 1.0×10^{11} cm^{-3}, and the maximum depletion acheived at this density was around 1%. Again, this is attributed to low particle flux. The maximum plasma layer density experienced during reentry can be as high as 1.0×10^{14} cm^{-3}.[16, 57, 11, 21, 34, 42, 43, 54, 55, 56, 80, 64, 68, 67, 75, 73, 74, 17, 105, 47, 108, 65, 113, 32, 22, 49, 58, 71, 30, 10, 102, 77]

However, it is important to note that in the shaker experiments, it was shown that with increased particle flux, the electron depletion can be increased as well. Therefore, by increasing particle flux, the depletion performance will increase.

Superior performance may also be achieved by using smaller particles that are not susceptible to clumping. Optimization of this method of plasma electron depletion may still be a viable option for plasma electron depletion, even for the most intense plasmas experienced during reentry.

The mass of powder required for a spacecraft during a typical three minute reentry flight can be roughly estimated. It has been shown that the measured flux of 0.12 g/cm^2-s can provide significant plasma layer depletion at relatively modest starting plasma layer densities on the order of 10^8 cm^{-3}. The approximate window size required for transmission through the plasma layer was found to be approximately 15 cm by 15 cm in chapter II. Therefore, the required flux for a 15 by 15 cm area, would be approximately 27 g/s. Over the course of a three minute spacecraft reentry, typical for Apollo missions, almost 5 kg of dielectric powder would be required for continuous use. Gemini 3 experiments injected approximately 7 kg of water in 10 seconds, and still did not observe full signal recovery.[108]

However, the method of cathode spot injection of dielectric powder has the distinct and important advantage of on-demand mitigation of the communications blackout plasma. That is, powder may be dispersed only when communications is required by simply igniting a cathode spot that will disperse powder. Therefore, consider the case when one 300 µs pulse is provided every second during flight, providing a window to transmit and receive communications through. In this case, the total powder mass required over a three minute vehicle atmospheric reentry is a mere 1.5 grams!

CHAPTER VII

Conclusions and Future Work

7.1 Conclusions

A novel method of mitigating the communications blackout experienced by hypersonic vehicles is proposed in this work. The dispersion of powder via cathode spot injection was studied as the method for blackout mitigation. The intense, dense, high velocity cathode spot flow accelerated powder particles into the overhead plasma used to simulate the blackout plasma. Powder particles, when ejected into the overhead plasma, will collect many electrons in reaching the plasma floating potential. The reduction of the electron density will allow communication signals to pass through the plasma layer commonly associated with communications blackout. This method of plasma layer depletion has been shown to be a feasible method of solving the radio communications problem.

However, at this time, communications blackout remains a critical problem for hypersonic vehicles traveling in the Earth's atmosphere, including spacecraft reentering the atmosphere, as well as missile, kinetic kill vehicles, and many defense systems.

Initial studies involved characterizing cathode spot operation in the presence of a static magnetic field on the surface of a metal electrode covered in dielectric powder. It was shown that cathode spots can be ignited when the electrode is biased negatively in the presence of an overhead or background plasma discharge. Cathode spots were

ignited at voltages of -100 V or higher. Cathode spots lasted for several microseconds before dying out and extinguishing. These cathode spots operated at currents as high as 1 A, and voltages on the order of 50 to 80 V. Intense electric fields on the electrode surface, enhanced by the placement of a dielectric powder layer, lead to the formation of cathode spots at the electrode surface. Cathode spots resulted in intense electrode heating, ultimately melting, vaporizing, and ionizing electrode material. A violent and intense cathode spot plume of high density and energy emanated from the cathode spot rooted at the electrode surface. In the process, powder particles from the dielectric powder on the electrode surface were ejected into the overhead plasma.

The first phase of this study demonstrated the ejection of powder via cathode spot ignition. It was also shown that the static magnetic field had a significant effect on the direction of cathode spot motion on the surface of the electrode. However, rather than following the expected Amperian direction, $\mathbf{J}\times\mathbf{B}$, cathode spots tended to follow the retrograde, or $\mathbf{-J}\times\mathbf{B}$ direction. Experiments showed repeatable patterns etched into the cathode surface that matched the calculated $\mathbf{-J}\times\mathbf{B}$ motion on the electrode surface. Particle flux was also measured using a witness plate to capture ejected particles. The ejection of particles from the electrode surface was found to be approximately 8.4 mg/s.

Subsequent experiments involved performing particle tracking and particle imaging velocimetry (PIV) techniques to calculate the velocity with which particles were ejected from the electrode surface. A fast frame-rate camera was used along with a laser to illuminate and capture particle motion as a function of time. From this, particle position and velocity as a function of time were determined to calculate the initial velocity with which particles were ejected.

Particle ejection velocity was important for determining the capability of particle penetration into the plasma layer for blackout mitigation techniques. Results showed that particles were ejected with velocities directed primarily in the vertical direction.

It was expected that particles would be ejected isotropically in the horizontal plane, with relatively small velocities. However, it was found that particles tended to gain a greater velocity in the direction that coincided with the retrograde direction of cathode spot motion on the electrode surface. It is suspected that this is due to cathode spots traveling in the retrograde direction, providing multiple boosts to particles traveling in the same direction, thereby increasing particle velocity in this direction. The resulting velocity distribution in the x-direction was a superposition of a small, isotropic velocity distribution centered at zero, along with a high energy tail. Ultimately, however, cathode spots ejected particles with a large component of velocity in the vertical direction, with a maximum of 1.5 m/s. The mean and median particle velocities in the vertical direction were 0.66 and 0.50 m/s, respectively. This shows that cathode spots are capable of injecting particles that can penetrate approximately 11.5 cm into the plasma layer assuming a maximum particle ejection velocity of 1.5 m/s in the vertical direction and a collisionless and ballistic particle trajectory after leaving the vicinity of the electrode.

Further experiments were aimed at elucidating the relationship between particle flux and overhead plasma electron depletion. Initial electron depletion experiments sought to determine the electron depletion capability in the presence of a glow discharge through direct injection of powder. It was found that electron depletion followed a linear trend with respect to the mass particle flux. Electron depletion of up to 90% was observed with a mass particle flux of approximately 0.12 g/cm^2-s.

The last phase of experiments involved measuring electron population depletion through cathode spot injection of dielectric particles. Relatively low time resolution and noisy results with hairpin resonance probe measurements did not provide sufficient data. Therefore a Langmuir probe biased at the plasma potential to collect the electron saturation current was employed. Results showed that following cathode spot initiation, the electron saturation current dropped significantly as electrons were

depleted from the overhead plasma. Results suggested that electron depletion may have been a result of the introduction of additional plasma loss area in the dielectric particle surface area. However, the electron depletion was observed in the bulk plasma, not only in the vicinity of the powder particles, and occurred on a timescale much shorter than the particle time of flight. This suggests that particle penetration of the plasma layer may not be required to deplete the electron population throughout the plasma layer.

Electron depletion above 95% in a low power RF plasma discharge was observed. It was also observed that there was little difference between depletion caused by particles 0.1 µm and 45 µm in diameter. This was likely due to particle clumping of the 0.1 micron powder particles, leading to an actual particle size distribution ranging from 0.1 µm to 0.5 mm in diameter. As the overhead plasma density was increased, electron depletion was reduced. However, it was shown that approximately the same number of electrons were collected by the injected particles, suggesting that increased particle flux in the presence of more dense overhead plasmas would result in similar electron depletion results.

7.2 Practical Application

It was shown that the plasma layer associated with communications blackout may be significantly depleted with only 1.5 grams of powder dispersed over a three minute period during reentry. However, experiments focused on loose powder particles placed on a stationary electrode. Therefore, a different method must be employed for the practical implementation of this novel method of blackout mitigation.

A relatively straightforward method would be to embed these dielectric particles in the ablative heat shield commonly placed on the surface of a blunt body during reentry. As the ablative shield burns away during reentry, the dielectric particles would be released. Or, rather, a small ablative shield with embedded dielectric par-

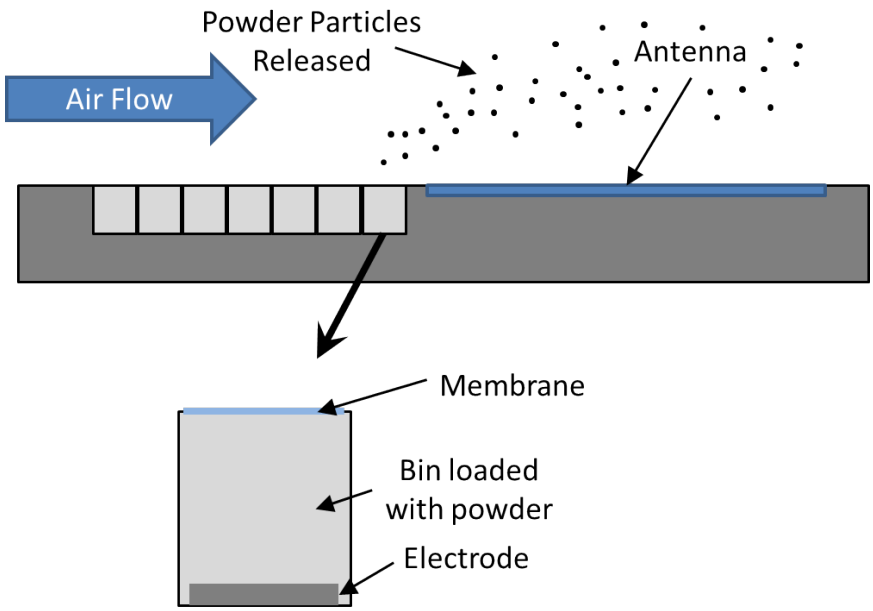

Figure 7.1: A schematic of a possible mitigation method using bins loaded with powder and a membrane that will be punctured by cathode spot ignition.

ticles could be placed near the antenna. Then particles would be released right next to the antenna, providing a small window for the antenna to receive and transmit signals through.

One possible method of implementation might be to place a layer of some sort of coating on an electrode or the transmitting antenna itself. This coating may be an epoxy that contains many dielectric particles suspended such that when a cathode spot is ignited, a portion of this epoxy is released, therefore injecting many dielectric particles to deplete the plasma layer.

Figure 7.1 shows another possible method of implementation that would involve the use of multiple bins loaded with loose powder. Each bin would have some sort of membrane that would be punctured by the cathode spot plume when a cathode spot is initiated, thereby releasing and injecting the dielectric particles. There may be several bins so that communications can be initiated multiple times during flight, and can be provided as needed with this on-demand method. Each bin would have a small electrode that would be powered when the release of powder in that bin is

required. Furthermore, this method would allow for great flexibility in terms of the amount of powder that is released, as each bin may be preloaded with the amount of powder required for a particular regime of the reentry trajectory. The particles, when injected, would then create a region almost completely void of electrons near the antenna, through which the antenna is able to transmit and receive communications signals.

Furthermore, it is speculated that cathode spot plumes themselves may be used as transmitting antennas that can penetrate through the plasma layer. Cathode spot plumes have been demonstrated to reach more than a centimeter into the overhead plasma. It was also shown that cathode spots will affect the response of a Langmuir probe, 5 mm away from the electrode surface, when cathode spots are ignited. Cathode spots produce extremely dense, highly conductive plumes of charged particles, behaving similar to a conducting wire. These plumes may act as virtual antennas, carrying and launching a radio frequency signal as the plume extends beyond the plasma layer. This is a method of practical implementation that requires further research.

7.3 Future Work

This work has formed the basis of a method which has the capability to mitigate the communications blackout experienced by hypersonic vehicles. However, this work should be continued in several areas:

- Basic Cathode Spot Research:

  There is still a great deal of research to be performed to answer many questions about the basic physics involved in cathode spot formation, operation, and extinction. Experiments could be performed to further investigate constraining cathode spot plumes emanating from the electrode surface with strong

transverse magnetic fields. By constraining the plasma jet, more efficient powder ejection may be achieved while minimizing perturbation of the overhead plasma. Furthermore, detection and characterization of macroparticle ejection from cathode spots would provide more insight into the actual density depletion mechanisms associated with the observed electron depletion.

- Optimize Magnetic Circuit:

  It has been shown that the magnetic circuit is capable of controlling areas of the electrode cleared of powder, as well as controlling the directionality of ejected particles. Several magnetic circuit configurations to reduce the distance traversed by retrograde type 2 cathode spots, for example, should be used to test the cathode spot and particle ejection response to magnetic field modifications.

- Optimize Particle Size and Mass Flux:

  The electron population depletion may be increased by finding the optimal particle size, capable of collecting the largest number of electrons. It is expected that smaller particles may produce the best results. Therefore dielectric powders composed of small particles that are not as susceptible to clumping should be tested. However, smaller particles may result in higher ejection velocities, and particle size should be selected to achieve maximum depletion up to the depth of the plasma layer thickness. It has also been shown that particle flux is the limiting factor for plasma layer depletion. Therefore efforts to improve particle collection of electrons, as well as increasing particle flux should be the main focus of this effort.

- Transmission of Electromagnetic Signals:

  This dust dispersion method of plasma layer mitigation should be further tested by showing that electromagnetic signals of interest may be passed through a plasma layer after dust dispersion. This would ultimately demonstrate that

this method is capable of providing the characteristics required in a plasma discharge for radio signal transmission.

- Practical Implementation Method:

  Test the powder injection approach in a way that may be practically implemented on a hypersonic vehicle, such as those methods mentioned above. The particle dispersion approach may be different for different specific hypersonic vehicle applications, depending on the hypersonic plasma layer and communications requirements.

BIBLIOGRAPHY

BIBLIOGRAPHY

[1] Wolfram alpha, July 2012.

[2] S. Aisenberg and K. Chang. a non-protruding conductivity probe system for re-entry plasma diagnostics. *NASA Special Publication*, 252:203, 1971.

[3] S. Aisenberg and P. Nien Hu. The removal of free electrons in a thermal plasma by means of rapidly evaporating liquid additives. *NASA Special Publication*, 252:617, 1971.

[4] N. Akey. Overview of ram reentry measurements program. *NASA Special Publication*, 252:19, 1971.

[5] B. S. S. Association. Melting temperature ranges for stainless steels, May 2012.

[6] A. Baird III and C. Lustig. The use of electroacoustic resonances to determine electron density profiles. *NASA Special Publication*, 252:57, 1971.

[7] S. Barengolts, E. Litvinov, E. Sadovskaya, and D. Shmelev. Motion of the cathode spot of a vacuum arc in an external magnetic field. *Technical Physics*, 43(6):668–672, 1998.

[8] I. Beckwith and D. Bushnell. Effect of intermittent water injection on aerodynamic heating of a sphere-cone at flight velocities to 18 000 feet per second. *NASA TM X-1128*, 1965.

[9] I. Beckwith and J. Huffman. Injection and distribution of liquids in the flow fields of blunt shapes at hypersonic speeds. *NASA TM X-989*, 1964.

[10] I. Belov and V. Borovoj. Investigation of remote antenna assembly for radio communication with reentry vehicle. *Journal of Spacecraft and Rockets*, 38(2):249–256, 2001.

[11] F. Blottner. Viscous shock layer at the stagnation point with nonequilibrium air chemistry. *AIAA Journal*, 7:2281–2288, 1969.

[12] L. Boufendi, A. Bouchoule, and T. Hbid. Electrical characterization and modeling of a dust forming plasma in a radio frequency discharge. *Journal of Vacuum Science Technology A: Vacuum, Surfaces, and Films*, 14(2):572 –576, Mar 1996.

[13] R. Boxman and S. Goldsmith. Macroparticle contamination in cathodic arc coatings: generation, transport and control. *Surface and Coatings Technology*, 52(1):39–50, 1992.

[14] R. Boxman, S. Goldsmith, and A. Greenwood. Twenty-five years of progress in vacuum arc research and utilization. *Plasma Science, IEEE Transactions on*, 25(6):1174 –1186, dec 1997.

[15] R. Boxman, D. Sanders, and P. Martin. *Handbook of vacuum arc science and technology: fundamentals and applications*. Materials science and process technology series. Noyes Publications, 1995.

[16] K. Chadwick. Plasma and flowfield induced effects on re-entry vehicles for l-band at near-broadside aspect angles. volume i. experimental measurements program summary and aerothermal data analysis. Technical report, DTIC Document, 1996.

[17] F. Chen. *Introduction to Plasma Physics and Controlled Fusion: Plasma physics*. Introduction to Plasma Physics and Controlled Fusion. Plenum Press, 1984.

[18] L. Christophorou and J. Olthoff. Electron attachment cross sections and negative ion states of sf61. *International Journal of Mass Spectrometry*, 205(1-3):27–41, 2001.

[19] P. Chung, L. Talbot, and K. Touryan. Electric probes in stationary and flowing plasmas. part i. collisionless and transitional probes. *AIAA Journal*, 12(2), 1974.

[20] S. Coulombe and J. Meunier. Importance of high local cathode spot pressure on the attachment of thermal arcs on cold cathodes. *Plasma Science, IEEE Transactions on*, 25(5):913 –918, oct 1997.

[21] R. Cowperthwaite, H. Myers, and E. Bialecke. Studies of electron attachment for the alleviation of radio communications blackout. *NASA Special Publication*, 252:559, 1971.

[22] W. Croswell and W. Linwood Jones Jr. Effects of reentry plasma on ram ci vhf telemetry antennas. *NASA Special Publication*, 252:183, 1971.

[23] W. Cuddihy, I. Beckwith, and L. Schroeder. Ram b2 flight test of a method for reducing radio attenuation during hypersonic reentry. *NASA TM X-902*, 1963.

[24] W. Cuddihy, I. Beckwith, and L. Schroeder. A solution to the problem of communications blackout of hypersonic reentry vehicles. In *Anti-Missile Research Advisory Council Meeting, Annapolis, Maryland,(October 22-24, 1965)*, 1963.

[25] J. E. Daalder. Components of cathode erosion in vacuum arcs. *Journal of Physics D: Applied Physics*, 9(16):2379, 1976.

[26] E. Daso, V. Pritchett, T. Wang, D. Ota, I. Blankson, and A. Auslender. Dynamics of shock dispersion and interactions in supersonic freestreams with counterflowing jets. *AIAA journal.*, 47(6):1313–1326, 2009.

[27] C. Davis, B. Gilchrist, and A. Gallimore. Density and spectral measurements using a 34 ghz interferometry system. In *35th Joint Populsion Conference*, 1999.

[28] W. Davis and H. Miller. Analysis of the electrode products emitted by dc arcs in a vacuum ambient. *Journal of Applied Physics*, 40(5):2212–2221, 1969.

[29] M. Drouet. The physics of the retograde motion of the electric arc. *Plasma Science, IEEE Transactions on*, 13(5):235–241, 1985.

[30] M. Dunn and S. Kang. Theoretical and experimental studies of reentry plasma. *NASA CR-2232*, 1973.

[31] D. Fang. Cathode spot velocity of vacuum arcs. *Journal of Physics D: Applied Physics*, 15:833, 1982.

[32] N. R. C. U. S. C. for the Decadal Survey of Civil Aeronautics, N. R. C. U. D. on Engineering, and P. Sciences. *Decadal survey of civil aeronautics: foundation for the future*. National Academies Press, 2006.

[33] J. Foster and E. Gillman. Observation of cathode-spot phenomena at the surface of a dielectric powder-covered electrode in the presence of a background plasma and applied magnetic field. *Plasma Science, IEEE Transactions on*, 37(5):637 –646, may 2009.

[34] A. Fuhs. Flight instrumentation for reentry plasma sheath. Technical report, DTIC Document, 1963.

[35] E. Gillman and J. Foster. Laser imaging and velocimetry of cathode-spot-ejected ceramic powder. *Plasma Science, IEEE Transactions on*, 39(10):2022 –2032, oct. 2011.

[36] G. Gogna and S. Karkari. Microwave resonances of a hairpin probe in a magnetized plasma. *Applied Physics Letters*, 96(15):151503–151503, 2010.

[37] B. Göksel and I. Rechenberg. Surface charged smart skin technology for heat protection, propulsion and radiation screening. In *Proceedings of the German Aeronautics Congress, Munich*, volume 3, 2003.

[38] Goodfellow. Ceramic - electrical properties, May 2012.

[39] Goodfellow. Ceramic - physical properties, May 2012.

[40] Goodfellow. Ceramic - thermal properties, May 2012.

[41] V. Gorelov. Computational and experimental investigations of ionization near hypersonic vehicles. *Journal of spacecraft and rockets*, 33(6):800–806, 1996.

[42] W. L. Grantham. Flight results of a 25,000-foot-per-second reentry experiment using microwave reflectometers to measure plasma electron density and standoff density. Technical Report D-6062, NASA Langley Research Center, 1970.

[43] W. L. Grantham. Reentry plasma measurements using a four-frequency reflectometer. Technical Report SP-252, NASA Langley Research Center, Oct. 1970.

[44] D. Griffiths. *Introduction to electrodynamics*. Prentice Hall, 1999.

[45] E. Hantzsche. A revised theoretical model of vacuum arc spot plasmas. *Plasma Science, IEEE Transactions on*, 21(5):419–425, 1993.

[46] R. Hartunian, G. Stewart, T. Curtiss, S. Fergason, R. Seibold, and P. Shome. Implications and mitigation of radio frequency blackout during reentry of reusable launch vehicles. *Proceedings of the AIAA Atmospheric Flight Mechanics Conference and Exhibit*, 2007.

[47] R. Hartunian, G. Stewart, S. Fergason, T. Curtiss, and R. Seibold. Causes and mitigation of radio frequency (rf) blackout during reentry of reusable launch vehicles. *Contractor Report ATR-2007 (5309)-1, The Aerospace Corporation, El Segundo, CA*, 2007.

[48] D. Hayes. An ablation technique for enhancing reentry antenna performance; flight test results. Technical report, DTIC Document, 1974.

[49] D. Hayes, S. Herskovitz, J. Lennon, and J. Poirier. Electrostatic probe measurements of chemical injection effects during a re-entry flight test. *Journal of Spacecraft and Rockets*, 11:388, 1974.

[50] R. Heimann. *Plasma-spray coating*. Wiley Online Library, 1996.

[51] W. Hinson, P. Gooderum, and D. Bushnell. *Experimental investigation of multiple-jet liquid injection into hypersonic flow*. National Aeronautics and Space Administration, 1970.

[52] H. Hodara. The use of magnetic fields in the elimination of the re-entry radio blackout. *Proceedings of the IRE*, 49(12):1825–1830, 1961.

[53] J. Hoffman. Control of plasma collision frequency for alleviation of signal degradation. *Communication Technology, IEEE Transactions on*, 14(3):318–323, 1966.

[54] P. Huber, U. S. N. Aeronautics, and S. Administration. *Deduction of Reentry Plasma Properties About Manned Orbital Spacecraft From Radio Signal Attenuation Data*. National Aeronautics and Space Administration, 1967.

[55] P. Huber, C. Chexnayder Jr, and J. Evans. Comparison of theoretical and flight-measured ionization in a blunt body re-entry flowfield. *AIAA Journal*, 9:1154–1162, 1971.

[56] Y. Inouye. Orex flight-quick report and lessons learned. In *Aerothermodynamics for space vehicles*, volume 367, page 271, 1995.

[57] C. Jones. Report from the workshop on communications through plasma during hypersonic flight. Technical report, DTIC Document, 2006.

[58] W. Jones and A. Cross. *Electrostatic-probe measurements of plasma parameters for two reentry flight experiments at 25000 feet per second*, volume 6617. National Aeronautics and Space Administration, 1972.

[59] D. W. Jordan. The adhesion of dust particles. *British Journal of Applied Physics*, 5(S3):S194, 1954.

[60] N. Jordan, Y. Lau, D. French, R. Gilgenbach, and P. Pengvanich. Electric field and electron orbits near a triple point. *Journal of Applied Physics*, 102(3):033301–033301, 2007.

[61] B. Jüttner. Vacuum breakdown. *Nuclear Instruments and Methods in Physics Research Section A: Accelerators, Spectrometers, Detectors and Associated Equipment*, 268(2):390–396, 1988.

[62] B. Jüttner and I. Kleberg. The retrograde motion of arc cathode spots in vacuum. *Journal of Physics D: Applied Physics*, 33:2025, 2000.

[63] S. Karkari, C. Gaman, A. Ellingboe, I. Swindells, and J. Bradley. A floating hairpin resonance probe technique for measuring time-resolved electron density in pulse discharge. *Measurement Science and Technology*, 18:2649, 2007.

[64] M. Keidar, M. Kim, and I. Boyd. Electromagnetic reduction of plasma density during atmospheric reentry and hypersonic flights. *Journal of Spacecraft and Rockets*, 45(3):445–453, 2008.

[65] M. Kim, M. Keidar, and I. Boyd. Analysis of an electromagnetic mitigation scheme for reentry telemetry through plasma. *Journal of Spacecraft and Rockets*, 45(6):1223–1229, 2008.

[66] M. Kim, M. Keidar, and I. Boyd. Electrostatic manipulation of a hypersonic plasma layer: Images of the two-dimensional sheath. *Plasma Science, IEEE Transactions on*, 36(4):1198 –1199, aug. 2008.

[67] M. Kim, M. Keidar, and I. Boyd. Two-dimensional model of an electromagnetic layer for the mitigation of communications blackout, 2009.

[68] M. Kim, M. Keidar, I. Boyd, and D. Morris. Plasma density reduction using electromagnetic e b field during reentry flight. In *International Telemetering Conference, Las Vegas, NV, International Foundation for Telemetering Paper*, pages 07–19, 2007.

[69] J. Laframboise. Theory of spherical and cylindrical langmuir probes in a collisionless, maxwellian plasma at rest. Technical report, DTIC Document, 1966.

[70] E. Langberg. Optical communication during hypersonic re-entry. *Communications Systems, IRE Transactions on*, 7(2):68–70, 1959.

[71] H. Legner. Plasma sheathing control using boundary layer stabilization and additives. Technical report, DTIC Document, 2006.

[72] R. Lehnert, B. Rosenbaum, U. S. N. Aeronautics, and S. Administration. *Plasma Effects on Apollo Re-entry Communication*. Citeseer, 1965.

[73] K. Lemmer. *Use of a helicon source for development of a re-entry blackout amelioration system*. PhD thesis, The University of Michigan, 2009.

[74] K. Lemmer, A. Gallimore, T. Smith, C. Davis, and P. Peterson. Experimental results for communications blackout amelioration using crossed electric and magnetic fields. 2009.

[75] K. Lemmer, A. Gallimore, T. Smith, S. Nguyen, D. Morris, C. Davis, and J. Zagel. Simulating hypersonic atmospheric conditions in a laboratory setting using a 15-cm-diameter helicon source. In *Pulsed Power Conference, 2007 16th IEEE International*, volume 1, pages 190–193. IEEE, 2007.

[76] E. Leung, M. Hilal, J. Parmer, and S. Peck. Lightweight magnet for space applications. *Magnetics, IEEE Transactions on*, 23(2):1331–1335, 1987.

[77] J. Lewis and W. Scallion. *Flight parameters and vehicle performance for Project Fire flight II, launched May 22, 1965*, volume 3569. National Aeronautics and Space Administration, 1966.

[78] M. Lieberman and A. Lichtenberg. *Principles of plasma discharges and materials processing*. Wiley-Interscience, 2005.

[79] C. Lim and F. Tay. Short notes on particle image velocimetry for micro/nano fluidic measurements. *Microfluidics and BioMEMS applications*, 10:307, 2002.

[80] W. Linwood Jones Jr and A. Cross. Electrostatic probe measurements of plasma surrounding three 25000 foot per second reentry flight experiments. *NASA Special Publication*, 252:109, 1971.

[81] Q.-Z. Luo and N. D'Angelo. Observations of dusty plasmas with magnetized dust grains. *Journal of Physics D: Applied Physics*, 33(21):2754, 2000.

[82] J. Madson. Plasma quench investigations-tungsten-oxide quenchants. In *AIAA, Aerospace Sciences Meeting*, volume 1, 1979.

[83] J. Marini. *On the decrease of the radar cross section of the Apollo Command Module due to reentry plasma effects(Radar cross section decrease of Apollo command module due to reentry plasma sheath effects)*, volume X-55824. National Aeronautics and Space Administration, 1967.

[84] F. Mitchell, W. Mahaffey, and R. Jacob. Modeling plasma effects on radar cross section of reentry vehicles. *IBM Journal of Research and Development*, 13(4):468–474, 1969.

[85] A. Modica, G. Stepakoff, and H. Rosenbaum. A shock tube study of plasma alleviation by oxide dust. *Recent developments in shock tube research*, pages 227–237, 1973.

[86] B. Moizhes and V. Nemchinsky. On the theory of the retrograde motion of a vacuum arc. *Journal of Physics D: Applied Physics*, 24:2014, 1991.

[87] R. Morris, P. Bench, K. Golden, and E. Sutton. Characterization and prediction of hypersonic plasma effects. *AIAA, Aerospace Sciences Meeting*, 1999.

[88] H. M. Mott-Smith and I. Langmuir. The theory of collectors in gaseous discharges. *Phys. Rev.*, 28:727–763, Oct 1926.

[89] S. Nazarenko, A. Newell, and V. Zakharov. Communication through plasma sheaths via raman (three-wave) scattering process. *Physics of plasmas*, 1(9):2827, 1994.

[90] C. Nelson. a brief history of the langley reentry communications program. *NASA Special Publication*, 252:1, 1971.

[91] G. Norris. Plasma puzzle: Radio frequency-blocking sheath presents a hurdle to hypersonic flight. *Aviation Week & Space Technology*, page 58, Mar. 2009.

[92] G. Norris. Telemetry lost during hypersonic test flight. *Aviation Week & Space Technology*, Aug. 2011.

[93] J. Olthoff. Gaseous electronics conference rf reference cell. *Journal of Research of the National Institute of Standards and Technology*, 100(4), 1996.

[94] R. Papa and R. Taylor. High-power electromagnetic transmission characteristics of a diffusing reentry plasma. *Journal of Applied Physics*, 45(2):684–696, 1974.

[95] E. Parmentier, K. Wray, and R. Weiss. Aerophysical plasma alleviation. *NASA Special Publication*, 252:579, 1971.

[96] R. Piejak, V. Godyak, R. Garner, B. Alexandrovich, and N. Sternberg. The hairpin resonator: A plasma density measuring technique revisited. *Journal of applied physics*, 95:3785, 2004.

[97] Y. Ralchenko, A. Kramida, J. Reader, and N. A. Team. Nist atomic spectra database. Online, June 2012.

[98] R. Rawhouser. Overview of the af avionics laboratory reentry electromagnetics program. *NASA Special Publication*, 252:3, 1971.

[99] C. Research. Boron nitride (bn) - properties and information on boron nitride, Nov. 2011.

[100] A. Robson. The motion of a low-pressure arc in a strong magnetic field. *Journal of Physics D: Applied Physics*, 11:1917, 1978.

[101] D. Rose, C. Thomas, and V. Sotnikov. Analysis of eaw and recomm communication schemes for hypersonic flight: Status report 1. Technical report, Voss Scientific, LLC, Dec. 2009.

[102] F. Russo and J. Hughes. Measurements of the effects of static magnetic fields on vhf transmission in ionized flow fields. *NASA TM X-907*, 26, 1964.

[103] J. Ryba. Nasa - space shuttle and international space station, February 2008.

[104] J. Rybak. Causes, effects and diagnostic measurements of the reentry plasma sheath. Technical report, DTIC Document, 1970.

[105] J. Rybak and R. Churchill. Progress in reentry communications. *Aerospace and Electronic Systems, IEEE Transactions on*, AES-7(5):879 –894, sept. 1971.

[106] B. L. Sands, N. S. Siefert, and B. N. Ganguly. Design and measurement considerations of hairpin resonator probes for determining electron number density in collisional plasmas. *Plasma Sources Science and Technology*, 16(4):716, 2007.

[107] W. Scallion, J. Lewis, U. S. N. Aeronautics, and S. Administration. *Flight Parameters and Vehicle Performance for Project Fire Flight 1, Launched April 14, 1964*. National Aeronautics and Space Administration, 1965.

[108] L. Schroeder and F. Russo. Flight investigation and analysis of alleviation of communications blackout by water injection during gemini 3 reentry. *NASA TM X–1521*, 1968.

[109] L. Scott, B. Bhat, and B. Rama Rao. Investigations on a cylindrical antenna as a diagnostic probe for isotropic and magnetized plasmas. *NASA Special Publication*, 252:47, 1971.

[110] J. Sherman, R. Webster, J. Jenkins, and R. Holmes. Cathode spot motion in high current vacuum arcs on copper electrodes. *Journal of Physics D: Applied Physics*, 8:696, 1975.

[111] T. Sims and R. Jones. Flight measurements of vhf signal attenuation and antenna impedance for the ram al slender probe at velocities up to 17,800 feet per second. *NASA TM X-760*, 1963.

[112] C. G. Smith. Cathode dark space and negative glow of a mercury arc. *Phys. Rev.*, 69:96–100, Feb 1946.

[113] D. Spencer. An evaluation of the communication blackout problem for a blunt mars-entry capsule and a potential method for the elimination of blackout. *Jet Propulsion Lab. TR*, pages 32–594, 1964.

[114] M. Steiger, L. Glatt, F. Fernandez, J. Fedele, and K. Golden. Re-entry communication: Theoretical analysis and flight test results. In *AIAA 8th Aerospace Sciences Meeting, New York, NY*, 1970.

[115] R. Stenzel. Microwave resonator probe for localized density measurements in weakly magnetized plasmas. *Review of Scientific Instruments*, 47(5):603–607, 1976.

[116] M. Sugawara. Electron probe current in a magnetized plasma. *Physics of Fluids*, 9:797, 1966.

[117] C. Swift, F. Beck, J. Thomson, and S. Castellow Jr. Ram c-iii s-band diagnostic experiment. *NASA Special Publication*, 252:137, 1971.

[118] J. Swift and J. Schwar. *Electrical probes for plasma diagnostics*. Iliffe Books, 1970.

[119] J. Visser. Van der waals and other cohesive forces affecting powder fluidization. *Powder Technology*, 58(1):1 – 10, 1989.

[120] G. Warwick. Darpa investigates hypersonic glider loss. *Aviation Week & Space Technology*, Apr. 2010.

[121] W. Weaver. Multiple-orifice liquid injection into hypersonic airstreams and applications to ram c-3 flight(oblique injection of water and electrophilic liquids through multiple-orifice nozzles into hypersonic airstreams with application to ram c-3 flight). *NASA-TM-X-2486*, 1972.

[122] S. Wright. Survey of technology on communication through the plasma sheath. *AFAL-TR-70-123*, 1970.

[123] H. Wroe. The magnetic stabilization of low pressure dc arcs. *British Journal of Applied Physics*, 9:488, 1958.